UNIVERSITY OF SOUTHAMPTON

FACULTY OF ENGINEERING, SCIENCE & MATHEMATICS

Optoelectronics Research Centre

Development and applications of dispersion controlled high nonlinearity microstructured fibres

by

Ming-Leung Vincent Tse

Thesis for the degree of Doctor of Philosophy

September 2007

UNIVERSITY OF SOUTHAMPTON

ABSTRACT

FACULTY OF ENGINEERING, SCIENCE AND MATHEMATICS
OPTOELECTRONICS RESEARCH CENTRE

Doctor of Philosophy

Development and applications of dispersion controlled high nonlinearity microstructured fibres

By Ming-Leung Vincent Tse

In this thesis I investigate aspects of dispersion controlled high nonlinearity all silica holey fibre, including design, fabrication, sample applications, and modelling.

Microstructured fibre fabrication allows for great flexibility in core and cladding structure designs, with the large available refractive index contrast between glass and air. This allows the control of waveguide dispersion across a wide wavelength range, which can be used to offset the material dispersion of the core glass. Therefore, this technology provides improved overall dispersion control via fibre design. This often requires a complex arrangement of air holes in the structure.

The full fabrication procedures for small-core holey fibres are presented. In particular, the fabrication of fibres with a graded-hole-size structure is reported. A structural accuracy of ±6% is achieved and improvements are proposed for future work.

A systematic study of the Supercontinuum Generation phenomenon is presented in this thesis. By using fibres with different dispersion profiles, pumping at 1.06 μm, the nonlinear effects such as Self-Phase-Modulation, Four-Wave-Mixing and Self-Soliton-Frequency-Shift, which dominate the spectral broadening in fibres with one or two zero-dispersion wavelengths are identified accordingly.

The latest work has been focussed on controlled structural variation of holey fibres along their length to obtain fibre with a longitudinal variation of dispersion and nonlinearity. I fabricated a dispersion-decreasing holey fibre and performed the first demonstration of soliton compression in a holey fibre. A compression factor of 2 has been achieved with pJ pulses at 1.06 μm. Further numerical modelling has been carried out from a holey fibre design contour map, to optimize holey fibre tapers for soliton compression at 1.55 μm. A compression factor of 6 is possible in a 15-m holey fibre taper with a loss of 0.1 dB/m.

Contents

List of Figures

List of Tables

Declaration of Authorship

I, Ming-Leung Vincent Tse

declare that the thesis entitled:

Development and applications of dispersion controlled high nonlinearity microstructured fibres

and the work presented in the thesis are both my own, and have been generated by me as the result of my own original research. I confirm that:

- this work was done wholly or mainly while in candidature for a research degree at this University;
- where any part of this thesis has previously been submitted for a degree or any other qualification at this University or any other institution, this has been clearly stated;
- where I have consulted the published work of others, this is always clearly attributed;
- where I have quoted from the work of others, the source is always given. With the exception of such quotations, this thesis is entirely my own work;
- I have acknowledged all main sources of help;
- where the thesis is based on work done by myself jointly with others, I have made clear exactly what was done by others and what I have contributed myself;
- parts of this work have been published as: [See *List of Publications*].

Ming-Leung Vincent Tse

September 2007

Acknowledgements

I would like to thank my supervisor, Professor David Richardson for his constant guidance and encouragement.

In addition, I would like to thank those who have directly helped with the work presented in this thesis. I acknowledge the contribution of all my co-workers for the highly nonlinear holey fibre development. In particular, I thank Dr. Peter Horek, who helped me in the numerical modelling presented in this thesis. I thank Dr. Francesco Poletti, who provides theoretical support throughout my PhD. Many thanks to Dr. Eleanor Tarbox for giving constant advices on all aspect of my PhD. I thank Dr Neil Broderick, Dr Tanya Monro and Dr. Joanne Flanagan for additional guidance and support. Special thanks to Mr. John Hayes and Dr. Kentaro Furusawa for kick-starting my project by showing the ropes in holey fibre fabrication techniques, and providing continuous guidance in the cleanroom. I thank Dr. Jonathan Price Dr. Andrew Malinowski and Fei He for helping with many of the holey fibre experiments.

I thank the other members of Prof. Richardson's group with whom I have had the pleasure of discussing ideas, borrowing equipment and who generally helped with holey fibre characterisations: Dr. Periklis Petropoulos, Dr. Micheal Roelens, Dr. Francesca Parmigiani, Chun Tian and Symeon Asimakis.

I am also grateful to Dr Rüdiger Paschotta of ETH Zurich for enabling me to use his numerical modelling program 'ProPulse'.

I thank Dr. John Mills for assistance in the FASTlab. I thank Chris Nash for his help with preparing posters for presentations. I thank David Oliver and Kevin Sumner for their cheerful help with computer troubles. I thank Professor Rob Eason and Eve Smith for being so energetic and friendly in their support of the ORC PhD students, and anyone in the admin and finance offices

I acknowledge the support of an EPSRC studentship.

I would like to thank my family for their support throughout my studies.

Abbreviations

DDHF	Dispersion Decreasing Holey Fibre
DDF	Dispersion Decreasing Fibre
DMDHF	Dispersion and Mode area Decreasing Holey Fibre
EOP	End Of Pull
FWM	Four Wave Mixing
FWHM	Full Width Half Maximum
GVD	Group Velocity Dispersion
HF	Holey Fibre
HNSC	Highly Nonlinear Small Core
IR	Infra Red
ID	Inner Diameter
LMA	Large Mode Area
MCVD	Modified Chemical Vapour Deposition
MOF	Microstructured Optical Fibre
MFEOP	Metre From End Of Pull
NA	Numerical Aperture
NLS	NonLinear Schödinger
OD	Outer Diameter
ORC	Optoelectronics Research Centre
OSA	Optical Spectrum Analyser
PBG	Photonic Bandgap
PCF	Photonic Crystal Fibre
PhD	Doctor of Philosophy
RGB	Red Green Blue
SBS	Stimulated Brillouin Scattering
SC	SuperContinuum
SEM	Scanning Electron Microscope
SHG	Second Harmonic Generation
SMF	Single Mode Fibre
SOP	Start Of Pull
SPM	Self Phase Modulation
SRS	Stimulated Raman Scattering
SSF	Split Step Fourier

SSFS	Soliton Self Frequency Shift
TIR	Total Internal Reflection
TOD	Third Order Dispersion
UV	UltraViolet
WDM	Wavelength-Division Multiplexing
ZDW	Zero Dispersion Wavelength

In the memory of my grandmother and

for all of my friends and family.

Chapter 1

Introduction

1.1 Holey fibre overview

Since the proposal of microstructured optical fibres (MOFs) in 1995 [Birks, 1995] and the first experimental demonstrations of such fibres in 1996 [Knight, 1996], the associated unusual optical properties and the developing fabrication techniques have attracted significant interest and are undergoing intense research. The fibre structure typically consists of an arrangement of air holes that are introduced in the cladding region, which extends along the fibre length. MOFs are also known as *Photonic Crystal Fibres* (PCFs) and *Holey Fibres* (HFs). Note that the idea of introducing air holes within the fibres dates back to the 1970's [Kaiser, 1974]. However, due to the technical difficulties in realising such structures and the lack of interesting optical properties discovered within such structures at the time, this topic was not properly explored until the mid 1990's. A recent on-line scientific search shows that over 8000 articles have been published on the topic between 1995 and 2007.

1.2 Guidance effects in microstructured optical fibres

1.2.1 Index guiding holey fibre

For guidance to occur along an optical fibre, light must be confined to a central core, or to several cores, by effective internal reflection from the cladding (that has a lower effective index). In a conventional 'solid' optical fibre this is achieved by doping the core region with a material of higher refractive index than the surrounding silica cladding. There is a class of microstructured fibres which also guide light via the *index-guiding* mechanism. Similar to conventional optical fibres, the effective refractive index in the cladding region is lowered, however in this case due to the presence of air holes – effectively creating a step-index optical fibre. Light is guided in the higher index solid core via a modified form of total internal reflection. Fig. 1.1 shows a typical structure of a holey fibre and a typical structure of a conventional fibre. Although, in practice, the holes are typically arranged on a hexagonal lattice, strict periodicity is not required for the confinement of light, and the holes need not

necessarily be positioned in a lattice. One example is the random holes holey fibre [Monro, 2000].

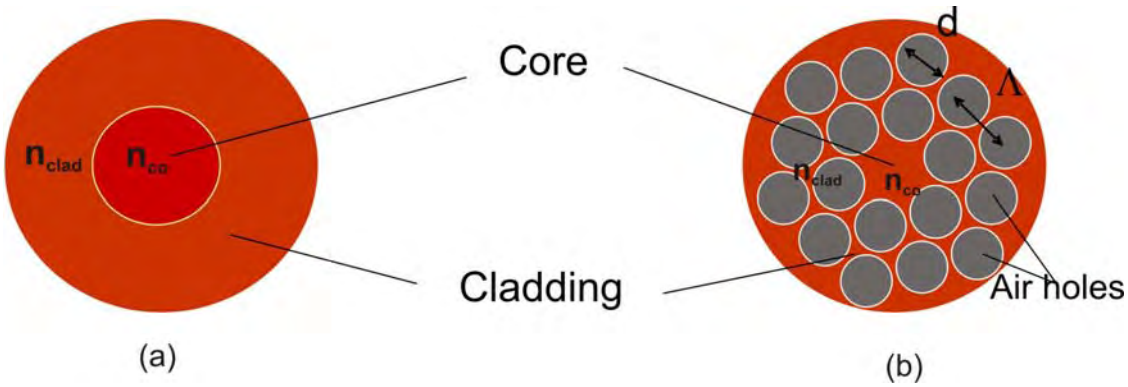

Fig. 1.1 The typical structural arrangement of (a) a conventional optical fibre and (b) a typical two-rings highly nonlinear holey fibre.

Although holey fibre behaves in many ways like standard step-index fibres (which are typically made of a germanium-doped higher index core (n_{co}) surrounded by a pure silica cladding (n_{clad})), they can have a number of advantages. Holey fibres can be made entirely of undoped silica, which potentially provides very low propagation losses, sustains high powers and higher temperature levels. Moreover, depending on the fibre design, the amount of air in the cladding may be utilized to yield fibres with extremely low or extremely high effective index steps, offering a host of new device opportunities.

1.2.2 Guidance via photonic bandgap effects

All conventional optical fibres guide light by total internal reflection (TIR), which requires that the core has a higher refractive index than the cladding. TIR is advantageous in that it causes no loss other than the intrinsic absorption and scattering losses of the materials which make up the fibre. Even these losses could be largely avoided if light can be made to travel in a hollow core. However, this is not possible via TIR, because no solid cladding material exists with a refractive index lower than that of air.

Light can be guided in a microstructured fibre if the air holes are arranged on a periodic lattice in the cladding region. A perfectly periodic structure can exhibit a photonic bandgap effect [Yablonovitch, 1987, John, 1987] at particular operating frequencies. These frequencies are thus forbidden to propagate within the cladding [Birks, 1995, Broeng, 1999(a)]. By breaking the periodicity of the cladding, namely by adding an extra air hole to form a low-index defect, it is possible to confine light within this defect [Cregan, 1999]. Such a defect can act as a core and guide light within well-defined frequency windows. These fibres are known as photonic bandgap (PBG) fibres, a typical structure of a PBG fibre is shown in Fig 1.2. They can be designed to have transmission windows centred at near- and mid-infrared wavelengths, as material absorption at these wavelengths is negligible in the air core [Broeng, 1999(b)].

Such fibres have a range of interesting and completely novel properties and represent an area of acute research interest at present. Although many of the fabrication techniques I used/developed are relevant to the production of these fibres, I did not actually produce any PBG fibres during my thesis studies and therefore I will not consider this form of fibre further in this thesis.

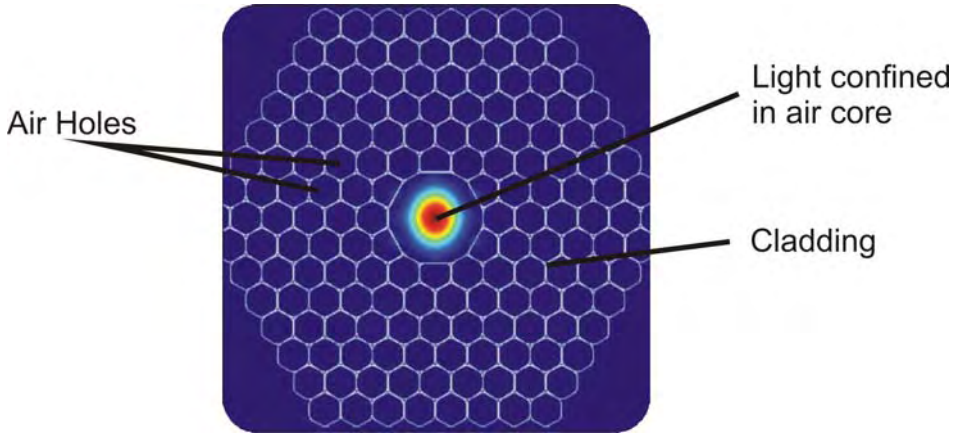

Fig. 1.2 A schematic of a typical structure of a photonic bandgap fibre.

1.3 Optical properties of index guiding fibres

1.3.1 Single mode operation

In a conventional step-index fibre, the number of guided modes is determined by the normalised frequency V [Snyder, 1996]; it may be expressed in terms of the numerical aperture NA:

$$V = \frac{2\pi}{\lambda} a(NA) \qquad \text{or} \qquad V = \frac{2\pi a}{\lambda}\sqrt{n_{co}^2 - n_{cl}^2} \ . \qquad \text{Eqn. 1.3:1}$$

The normalised frequency is a dimensionless parameter and is sometimes referred to as the V number, or V value, of the fibre. It combines, in a useful manner, the information from four important design variables for the fibre: namely, the core radius a, the refractive indices of the core n_{co} and cladding n_{cl}, and the operating wavelength λ. The V value must be less than 2.405 for the fibre to be single mode. Thus conventional single-mode fibres, in which the core and cladding indices are weakly wavelength dependent, are in fact always multimode for light of sufficiently short wavelength.

In a HF, the effective refractive index of the cladding is strongly wavelength dependent [Knight, 1998]. Therefore the effective V value for a pure silica HF can be written as:

$$V_{eff} = \frac{2\pi\Lambda}{\lambda}\sqrt{n_{silica}^2 - n_{eff}^2(\lambda)}\ , \qquad \text{Eqn. 1.3:2}$$

where V_{eff} is the effective normalised frequency, Λ is the hole-to-hole spacing, n_{silica} is the refractive index of the silica core and n_{eff} is the effective refractive index of the cladding.

A holey fibre can be single-mode over a wide range of wavelengths, which is not possible in conventional fibres. Consider the effective refractive index of the cladding $n_{eff}(\lambda)$, which can also be assumed as the average index in the cladding weighted by the intensity distribution of the light. At shorter wavelengths, the overlap between the mode and the cladding region decreases, thus the field becomes more concentrated in the silica regions and avoids the holes; light is more confined within the core and therefore the effective cladding index decreases. It can be shown that the effective $NA \approx \sqrt{n_{silica}^2 - n_{eff}^2(\lambda)}$ scales in proportion to λ as $\lambda \to 0$ and hence, from Eqn. 1.3:2, V_{eff} can be kept almost constant in this limit. By engineering the air ratio in the cladding (typically $d/\Lambda < 0.4$), the cladding index can be controlled, and if $V_{eff} < V_{cut\text{-}off}$, where $V_{cut\text{-}off}$ is the cut-off normalised frequency for single-mode guidance, the fibre is *endlessly single-mode* [Birks, 1997].

1.3.2 Large Mode Area and Highly Nonlinear Small Core fibres

Index guiding silica holey fibres can be broadly categorised into Large Mode Area (LMA) and Highly Nonlinear Small Core (HNSC) fibres. The classification and properties are essentially determined by the geometry, the hole-to-hole spacing or the pitch, Λ, of the lattice, and the hole diameter, d. All-silica LMA HFs are typically composed of a large pitch ($\Lambda > 5$ μm) and/or a small air-filling fraction ($d/\Lambda < 0.3$), HNSC HFs typically have $\Lambda \sim 1$ μm and $d/\Lambda > 0.9$.

In a conventional fibre, one creates large mode areas either by increasing the core size or by reducing the NA. For any given core size and wavelength there exist a maximum NA that will result in single-mode guidance. Conventional techniques for reducing the NA rely on the ability to control dopant concentrations accurately, which in conjunction with the onset of bend-loss ultimately limits the maximum mode size that can be created, especially for short-wavelength operation. In a HF, large mode area can be engineered either by increasing Λ or by decreasing d. Increasing Λ is analogous to enlarging the core size, while decreasing d allows the field to penetrate farther into the cladding. Thus, the cladding parameters and the hole arrangement give HFs extra degrees of design freedom relative to conventional fibres. Moreover, endlessly single-mode guidance offers advantages for broadband applications and could also offer a simpler way of manufacturing single-mode fibres with large mode areas at visible and ultraviolet wavelengths.

In a HNSC HF, light is strongly confined within a core of a size of order λ, which provides for high nonlinear effects [Broderick, 1999], and a large NA. HFs with effective mode area, A_{eff}, of less than a few μm^2 are practically feasible at telecoms wavelengths, the minimum effective mode area value was given to be ~1.7 μm^2 at 1.55 μm wavelength [Finazzi, 2003]. Many optical processing applications can be realised using the nonlinear effects, including optical demultiplexing [Hansryd, 2002], wavelength conversion [Lee, 2003], data regeneration [Petropoulos, 2001], and Raman amplification [Yusoff, 2002]. Also, supercontinuum generation has been studied intensively [Ranka, 2000], which can be used in optical coherence tomography [Hartl, 2001], metrology [Diddams, 2001] and spectroscopy [Nagarajan, 2002].

The majority of fabricated holey fibres reported to date exhibit uniform pitch and hole sizes. Many designs with different hole sizes have been studied for different applications, and have not been practically realised. The first generation of small core HFs have been fabricated based on regular pitch and hole size designs. However, they were generally aimed at achieving the best possible nonlinearity (γ) or dispersion (D) values within certain wavelength ranges. The exact target design of the feature sizes could not always be realised, but good results were still achieved. Fabrication techniques for the second generation small core HFs with improved and accurately controlled feature sizes, and thus, dispersive and nonlinear properties, were investigated in this PhD project. Special fibres with specific dispersion characteristic, such as dispersion-flattened and dispersion-decreasing properties, often involve designs with a different hole size, varied either radially or along the length of the fibre.

One attractive application for a nonlinear dispersion-flattened and/or dispersion-decreasing holey fibre is supercontinuum (SC) generation [Tse, 2006(a), Kudlinski, 2006]. The generation of a SC using microstructured fibres is being studied intensively; as the pulse energies required to generate a SC in HFs are low compared to that of a conventional optical fibre [Foster, 2004], while they retain a relatively high spatial purity and intensity of the SC [Husakou, 2002]. Historically, a spectrum spanning 300 nm from femtosecond-distributed soliton spectra using picosecond pump pulses in the anomalous dispersion regime of a conventional fibre is possible [Islam, 1989]. Since then, a SC spanning over 600 nm has been demonstrated by using dispersion shifted fibre and high power input pulses [Mori, 1995]. However, HFs can offer much wider spectrum generation. An ultra-broadband continuum generation extending from 390 to 1600 nm, in all-silica HFs, was reported for the first time in 2000 [Ranka, 2000] (Note that, others have more recently produced octave spanning SC in conventional solid highly nonlinear fibres [Westbrook, 2005]). Moreover, dispersion-decreasing fibres can be used for good quality soliton compression, which is important for ultrahigh-data-rate optical communications [Chernikov, 1991]. In contrast to conventional fibres, holey fibres can be

fabricated with, simultaneously, significantly decreasing dispersion and effective mode area over shorter fibre lengths, leading to enhanced compression factors.

In the years before my PhD study, many works have been done to use highly nonlinear small core holey fibres to achieve high values of nonlinearity with little dispersion control. The aim of my thesis was to achieve simultaneously high nonlinearity and dispersion control in HNSC HFs, and to investigate some of their applications.

1.4 Thesis outline

Chapter 2 describes the general background on the nonlinear and dispersive effects in conventional and holey fibres. Nonlinear effects such as Stimulated Raman Scattering (SRS) and Self-Phase Modulation (SPM) are reviewed. An understanding of these effects is essential in order to understand the nonlinear phenomena in optical fibres such as Supercontinuum generation, which is studied in detail in this thesis. Soliton effects in optical fibres are also reviewed, and they are important in both SC generation and soliton compression. All simulations in this thesis were done using the Split Step Fourier (SSF) method, and I explain this method within this chapter. The concept of using a design map for designing a holey fibre is also introduced.

One of the main points of the work reported herein is to document the fabrication procedures for holey fibre. In Chapter 3, the general procedures for small-core holey fibre fabrication are presented. I learnt the majority of the techniques presented in the chapter from other researchers within the ORC (taught by Mr. J. Hayes and Dr. K. Furusawa). Fabrication techniques presented in the chapters thereafter were mostly developed and implemented by me. Nevertheless, the early fabrication steps such as capillary preparation were crucial to the success of holey fibre production, and these steps were always followed rigorously.

In an attempt to fabricate dispersion-flattened holey fibres with varying hole size structure, I initially followed the general fabrication methods presented in Chapter 3, and results are presented in Chapter 4. They showed that when the general fabrication methods were followed, it was not possible to control or predict the variations of the cladding parameters (Λ and d) during the fibre drawing process. In order to investigate the structural distortions which arise from the general method, experiments on the variation of fabrication techniques were carried out and presented in the chapter. It concluded that the fabrication of such fibre was not possible using the technology available at the time and that further innovation was needed. Alternative fibre designs were suggested and discussed. However, the experiments ceased at that point, and readers of this thesis may feel that this work was slightly incomplete. This was due to the unfortunate event of the Mountbatten building fire on the 30th Oct 2005, which

destroyed all of the fibre fabrication facilities within the ORC, and most of the fibres fabricated by me and curtailed any further fabrication work by me. Note that this PhD project began in October 2003.

Chapter 5 demonstrates supercontinuum generation in holey fibres with different dispersion profiles. The design and fabrication procedures for fibres with two zero-dispersion-wavelengths (ZDWs) are reported. The experimental results were fully supported by numerical simulations, and are reported in full. The dominating nonlinear effects at different stages of the SC generation in the fibres were identified and discussed. The effects were very different depending on whether the fibres have two closely spaced ZDWs or wider ZDWs spacing, and the value of the anomalous or normal dispersion at the pump wavelength region.

The same fabrication methods were used to produce the dispersion-decreasing holey fibre for soliton compression, which is demonstrated in Chapter 6. This was the first demonstration of high quality soliton compression in a dispersion-decreasing holey fibre. This was achieved by a fibre with both the dispersion-flattened and decreasing properties at the same time. The experiment shows a compression factor of 2 at 1.06 μm wavelength at low pulse energy. The effects are discussed in the chapter, and the experimental results are supported by numerical simulations. I intended to demonstrate a larger compression factor from a dispersion-decreasing holey fibre with an improved design, but again, the work was held back by the Mountbatten fire.

Due to the loss of the fabrication facilities, I focused on numerical modelling for the later part of my PhD project. Chapter 7 presents the simulation results for optimising tapered holey fibre, with simultaneously varying dispersion and effective area profile, for enhanced soliton compression at 1.55 μm. The problem was explored from a design map containing contours for dispersion, dispersion slope and effective area in the (d/Λ, Λ) grid. Many paths on the map were investigated, and the major concerns when designing such fibres were identified and addressed. I proposed tapered holey fibre designs, with a short fibre length, capable of delivering good quality soliton compression by factors of between 5 and 10.

The thesis concludes with Chapter 8, where I summarise the results and discuss possible directions for future work.

Chapter 2

A review of nonlinear and dispersive effects in conventional and holey fibres

2.1 Introduction

Historically, nonlinear processes in conventional optical fibres such as stimulated Raman- and Brillouin-scattering [Stolen, 1972, Smith, 1972], four-wave mixing [Stolen, 1975], and self-phase modulation [Stolen, 1978] were studied since the 1970s. However, the field of nonlinear fibre optics only took off during the early 1980s with the development of low loss silica fibres. Soliton pulses were also observed experimentally in optical fibres during the same period [Mollenauer, 1980]. Pulse compression and optical-switching techniques that exploited the nonlinear effects in fibres were developed [Nakatsuka, 1981, Doran, 1988]. During the 1980s, the development of single-mode rare-earth doped optical fibres was also rapidly advancing for the development of diode pumped amplifiers and lasers [Payne, 1986], two decades after the initial study of lamp pumped fibre amplifiers [Koester, 1964].

The field of nonlinear fibre optics continued to grow in the 1990s, with much focus on the development of highly nonlinear fibres and their applications in optical signal processing, and the development of amplifiers based on Raman Scattering and Four-Wave-Mixing capable of operating in any spectral region. After 2000, with the advent of holey fibres, new device opportunities arose due to the unique properties these fibres offered. Structural changes in holey fibres affect their dispersive as well as nonlinear properties. In particular, they offer the ability to shift the zero group-velocity dispersion wavelength from the near-infrared region toward the visible region. Some fibres exhibit two or three such wavelengths. At the same time, the nonlinear effects are enhanced considerably because of the relatively small core size. This combination leads to dramatic nonlinear effects such as supercontinuum generation, a phenomenon in which the optical spectrum of ultrashort pulses is broadened by a factor of more than 200 over a length of 1 m or less [Ranka, 2000]. HFs have now been used to realise a variety of nonlinear optical devices including high gain Raman amplifiers [Yusoff,, 2002], regenerators [Chow, 2005], demultiplexers [Siahlo, 2003], parametric amplifiers and oscillators [Harvey, 2003] amongst others.

In this chapter, I will review the relevant nonlinear and dispersive effects in conventional and holey fibres. Sections 2.2 to 2.9 describe the main effects in the conventional case, following the book by Agrawal [Agrawal, 2007]. Description of the modelling approach used is presented in Section 2.10. Sections 2.11 to 2.13 describe the main effects in holey fibres. Conclusions are in Section 2.14.

2.2 Chromatic dispersion

Chromatic dispersion is related to the characteristic resonance frequency at which the medium absorbs electromagnetic radiation through oscillations of bound electrons, it manifests itself through the Kramers-Kroning relation as a frequency dependence of the refractive index $n(\omega)$ [Agrawal, 2007].

Fibre dispersion plays a critical role in the propagation of short optical pulses because different spectral components associated with the pulse travel at different speeds. The effects of fibre dispersion can be studied mathematically by expanding the mode-propagation constant β in a Taylor series

$$\beta(\omega) = n(\omega)\frac{\omega}{c} = \beta_0 + \beta_1(\omega-\omega_0) + \frac{1}{2}\beta_2(\omega-\omega_0)^2 + \frac{1}{6}\beta_3(\omega-\omega_0)^3\cdots \qquad \text{Eqn. 2.2:1}$$

β_2 represents dispersion of the group velocity and is responsible for pulse broadening. β_3 is the third-order-dispersion (TOD) coefficient. Such higher-order dispersion effects can distort ultrashort optical pulses (width < 1 ps) both in the linear and nonlinear [Agrawal, 1986] regimes. Their inclusion is usually necessary only when the wavelength λ approaches the zero-dispersion wavelength λ_0, where β_2 vanishes.

A pulse envelope moves at the group velocity $v_g=1/\beta_1$ while the effects of group-velocity dispersion (GVD) are governed by β_2. The GVD parameter β_2 is positive in the normal-dispersion regime and is negative in the anomalous-dispersion regime. In standard silica fibres, $\beta_2 \sim 50$ ps^2/km in the visible region but becomes close to -20 ps^2/km near wavelengths ~ 1.5 μm, the change in sign occurring in the vicinity of 1.3 μm. The dispersion parameter D, defined as $d\beta_1/d\lambda$, is also used in practice. It is related to β_2 and n as

$$D = \frac{d\beta_1}{d\lambda} = -\frac{2\pi c}{\lambda^2}\beta_2 \qquad \text{Eqn. 2.2:2}$$

2.3 Dispersion-induced pulse broadening

Dispersion induces pulse broadening because different frequency components of a pulse travel at slightly different speeds along the fibre. Any time delay in the arrival of different spectral components leads to pulse broadening. GVD also changes the phase of each spectral component of the pulse by an amount that depends on the frequency and the propagated distance, *z*. This does not affect the pulse spectrum, but can modify the pulse shape.

As the phase $\phi(z, T)$ is time dependent, the instantaneous frequency differs across the pulse from the central frequency ω_0. Thus a fibre imposes a linear frequency chirp on the pulse. The chirp $\delta\omega$ depends on the sign of β_2. In the normal-dispersion regime, $\delta\omega$ is negative at the leading edge and increases linearly across the pulse; the opposite occurs in the anomalous regime. The instantaneous frequency increases linearly from the leading to the trailing edge and is commonly referred to as a positive chirp, the opposite is true for a negative chirp. In general, a pulse with steeper leading and trailing edges broadens more rapidly with propagation because such a pulse has a wider spectrum to start with.

For ultrashort pulses ($T_0 < 1$ ps), it is necessary to include the β_3 term even when $\beta_2 \neq 0$ because the expansion parameter $\Delta\omega/\omega_0$ is no longer small enough to justify the truncation of the expansion in Eqn. 2.2:1 after the β_2 term [Miyagi, 1979]. TOD distorts the pulse such that it becomes asymmetric with an oscillatory structure near one of its edges [Agrawal, 2007].

2.4 Nonlinearity

In an optical fibre, the response to light becomes nonlinear for intense electromagnetic fields. The total polarisation **P** induced by electric dipoles is not linear in the electric field **E**, and follows the general relation [Agrawal, 2007]

$$\mathbf{P} = \varepsilon_0(\chi^{(1)} \cdot \mathbf{E} + \chi^{(2)} \cdot \mathbf{E}^2 + \chi^{(3)} \cdot \mathbf{E}^3 + \cdots), \qquad \text{Eqn. 2.4:1}$$

where ε_0 is the vacuum permittivity and $\chi^{(j)}$ (j=1, 2, …) is jth order susceptibility. The linear susceptibility $\chi^{(1)}$ represents the dominant contribution to **P**. Its effects are included through the refractive index n and the attenuation coefficient α. The second-order susceptibility $\chi^{(2)}$ is responsible for nonlinear effects in media that lack an inversion symmetry at the molecular level. Silica optical fibres do not normally exhibit second-order nonlinear effects, as SiO_2 is a symmetric molecule.

The most common nonlinear effects in optical fibres originate from the third-order susceptibility $\chi^{(3)}$, which is responsible for phenomena such as nonlinear refraction, third-

harmonic generation and four-wave mixing. Nonlinear refraction refers to the intensity dependence of the refractive index, and the nonlinear refractive index can be written as

$$n(\omega, I) = n(\omega) + n_2 I \,, \qquad \text{Eqn. 2.4:2}$$

where $n(\omega)$ is the linear refractive index and I is the optical intensity inside the fibre, and n_2 is the nonlinear-index coefficient related to $\chi^{(3)}$. This leads to nonlinear effects such as self-phase modulation (SPM); where an optical field experiences a self-induced phase shift during its propagation in optical fibres.

Stimulated Raman scattering (SRS) and stimulated Brillouin scattering (SBS) are another class of nonlinear effects found in optical fibres [Stolen, 1972, Ippen, 1972]; they result from stimulated inelastic scattering relating to vibrational excitation modes of silica. The main difference between the two is that optical phonons participate in SRS while acoustic phonons participate in SBS.

2.5 Generalized nonlinear Schrödinger equation

The propagation of a generic optical field can be described by starting from the evolution of its electric and magnetic fields in a fibre via Maxwell's equations. Without attempting to describe any of its derivation (see [Agrawal, 2007]), I present the main elements of the analysis and notation here.

Assuming the fundamental mode of the electric field is linearly polarised in the x or y direction, while z is the propagation direction, the electric field $E'(x, y, z, t)$ can be written as:

$$E'(x, y, z, t) = \frac{1}{2}\left\{E(x, y, z, t)\exp\left[i(\beta_0 z - \omega_0 t)\right] + c.c.\right\} \qquad \text{Eqn. 2.5:1}$$

Where $E(x,y,z,t)$ is the envelope of the waveform, which is a slowly varying function of time t, β_0 is the propagation constant and ω_0 is the carrier frequency. This approximation is valid for a spectral width $\Delta\omega$ such that $\Delta\omega/\omega_0 << 1$.

For a single mode fibre, using the method of separation of variables, it is possible to separate the longitudinal and temporal evolution of the electric field, $A(z,t)$, from the transverse evolution, $F(x,y)$:

$$E(x, y, z, t) = F(x, y)A(z, t). \qquad \text{Eqn. 2.5:2}$$

$F(x,y)$ corresponds to the modal distribution of the fundamental fibre mode, often approximated by a Gaussian distribution. $A(z,t)$ is the pulse envelope variation It is under the influence of both linear and nonlinear effects, and is described by the nonlinear Schrödinger

(NLS) equation. In the general form, the NLS can be expressed as follows [Frosz, 2005] (see [Agrawal, 2007] for steps that lead from the Maxwell's equations to the NLS equation):

$$\frac{\partial A}{\partial z} = -\frac{\alpha A}{2} + i\sum_{m\geq 1}\frac{i^m \beta_m}{m!}\frac{\partial^m A}{\partial t^m} + i\gamma\left[1+\frac{i}{\omega_0}\frac{\partial}{\partial t}\right]\left[A(z,t)\int_0^\infty R(t')\left|A(z,t-t')\right|^2 dt'\right], \quad \text{Eqn. 2.5:3}$$

loss dispersion SS Kerr + Raman

where the nonlinear response function, $R(t)=(1-f_R)\delta(t-t_e)+f_R h_R(t)$, t_e accounts for a negligibly short delay in electronic response and f_R represents the contribution of the delayed Raman response to nonlinear polarization P_{NL}, and $h_R(t)$ is the Raman response function. Eqn. 2.5:3 includes the effects of loss (absorption coefficient α), higher order dispersion, Kerr nonlinearities (γ), self-steepening (SS) and Raman gain. This was the standard NLS equation used in all the simulation carried out in this thesis via commercial software ('Propulse' by R. Paschotta).

2.6 Propagation regimes

Depending on the initial width T_0 and the peak power P_0 of the incident pulse, either dispersive or nonlinear effects may dominate along the fibre. Consider the dispersion length L_D and the nonlinear length L_{NL} defined as [Agrawal, 2007, Shen, 2003(a)]

$$L_D = \frac{T_0^2}{|\beta_2|}, \qquad L_{NL} = \frac{1}{\gamma P_0}, \qquad \text{Eqn. 2.6:1}$$

where γ is the nonlinear parameter related to n_2 and the effective core area of the fibre (see Eqn. 2.11:1). The dispersion length and the nonlinear length provide the length scales over which dispersive or nonlinear effects become important for pulse evolution. For fibre length L such that $L << L_{NL}$ and $L << L_D$, neither dispersive nor nonlinear effects play a significant role during pulse propagation. As a result, the pulse maintains its shape during propagation. As pulses become shorter and more intense, L_D and L_{NL} become smaller. For example, L_D and L_{NL} are ~ 100 m for T_0 ~ 1 ps and P_0 ~ 1 W. For such optical pulses, both dispersion and nonlinear effects need to be included if the fibre length exceeds a few meters. If $L << L_D$ and $L \sim L_{NL}$, the pulse evolution in the fibre is governed mainly by SPM that leads to spectral broadening of the pulse. If $L << L_{NL}$ and $L \sim L_D$, the pulse evolution is then governed by GVD.

2.7 Stimulated Raman Scattering

SRS is scattering of a photon by one of the molecules to a lower-frequency photon, while the molecule makes a transition to a higher-energy vibrational state. A photon of the incident field (pump) is annihilated to create a photon at a lower frequency (Stoke's wave) and a phonon with the right energy and momentum to conserve the energy and the momentum. The same is true of a higher energy photon at a higher frequency (anti-Stoke's wave). For SRS, the initial growth of the Stokes wave can be described by the relation

$$\frac{dI_s}{dz} = g_R I_P I_s \,, \qquad \text{Eqn. 2.7:1}$$

where I_p is the pump intensity, I_s is the Stokes intensity, and g_R is the Raman gain coefficient. Moreover, significant conversion of pump energy to Stokes energy occurs only when the pump intensity exceeds a certain threshold level (Raman threshold) [Smith, 1972]. SRS leads to the generation of a Stokes wave whose frequency is determined by the peak of the Raman gain. The corresponding frequency shift is the Raman or Stokes shift.

In silica fibres, the Raman-gain spectrum $g_R(\Omega)$, where Ω represents the frequency difference between the pump and Stokes waves, extends over a large frequency range (up to 40 THz) with a broad peak located near 13 THz [Stolen, 1972]. This behaviour is due to the noncrystalline nature of silica glass. In amorphous materials such as fused silica, molecular vibrational frequencies spread out into bands that overlap and create a continuum. As a result, it extends continuously over a broad range in silica fibres. Thus, optical fibres can be used to amplify a weak signal if that signal is launched together with a strong pump wave such that their frequency difference lies within the bandwidth of the Raman-gain spectrum [Agrawal, 2007].

The vibrational or Raman response occurs over a time scale of 60 – 70 fs, approximately valid for pulse widths >1 ps. For ultrashort pulses whose width ≤ 1 ps with a wide spectrum (> 0.1 THz), the Raman gain can amplify the low-frequency components of a pulse by transferring energy from the high-frequency components of the same pulse. As a result, the pulse spectrum shifts toward the low-frequency side as the pulse propagates inside the fibre, this phenomena is known as the self-frequency shift [Mitschke, 1980].

For Stimulated Brillouin scattering (SBS), the input power levels for it to occur in optical fibres are much lower than those needed for SRS. It manifests through the generation of backward-propagating Stokes wave that carries most of the input power, once the threshold is reached. One of the major differences between SBS and SRS is that the Stoke wave propagates

backward when SBS occurs in a single-mode optical fibres, in contrast to SRS that can occur in both directions.

2.8 Self-Phase Modulation

2.8.1 Spectral broadening

SPM can lead to spectral broadening of optical pulses [Ippen, 1974, Stolen, 1978]. It gives rise to an intensity-dependent phase shift but the pulse shape remains unaffected. The SPM-induced spectral broadening is a consequence of the time dependence of the nonlinear phase shift ϕ_{NL}. A temporally varying phase implies that the instantaneous frequency differs across the pulse from its central value ω_0.

SPM induces frequency chirping, where new frequency components are generated continuously as the pulse propagates down the fibre, and thus broadens the spectrum [Oberthaler, 1993]. The chirp $\delta\omega$ is linear and positive over a large central region of a Gaussian pulse; it is negative near the leading edge (red shift) and becomes positive near the trailing edge (blue shift) of the pulse. The chirp is considerably larger for pulses with steeper edges.

In the case of intense ultrashort pulses, the broadening spectrum can extend over more than 100 THz, especially when other nonlinear processes such as stimulated Raman scattering and four-wave mixing are also involved and this can lead to supercontinuum generation. For shorter pulses, where the dispersion length becomes comparable to the fibre length, it is necessary to consider the combined effects of GVD and SPM [Fisher, 1975]. SPM generates new frequency components that are red-shifted near the leading edge and blue-shifted near the trailing edge of the pulse. As the red components travel faster than the blue components in the normal-dispersion regime, SPM leads to an enhanced rate of pulse broadening compared with that expected from GVD alone.

In the anomalous-dispersion regime, the two phenomena can cooperate in such a way that the pulse propagates as an optical soliton [Drazin, 1993]. Consider a sech^2 pulse when $L_D \sim L_{NL}$, in the anomalous-dispersion regime. In this case, the pulse broadens initially at a rate much lower than that expected in the absence of SPM and then reaches a steady state. At the same time, the spectrum narrows rather than broadens as expected by SPM in the absence of GVD. This is because the SPM-induced chirp is positive while the dispersion-induced chirp is negative. The pulse shape adjusts itself during propagation to make such cancellation. Thus, GVD and SPM cooperate with each other to maintain a chirp-free pulse in the form of a soliton.

2.8.2 Self-steepening

For an ultrashort pulse, the higher-order nonlinear effects such as self-steepening and intrapulse Raman scattering must be considered. Self-steepening results from the intensity dependence of the group velocity, such that the peak of the pulse moves at a lower speed than the wings [Jonek, 1967, Grischkowsky, 1973]. It leads to an asymmetry in the SPM-broadened spectrum of an ultrashort pulse [Fork, 1983, Mestdagh, 1987]. As the peak of the pulse is shifting toward the trailing edge, it becomes steeper and steeper with distance of propagation, eventually it creates an optical shock. There is also a spectral asymmetry as the red-shifted peaks are more intense than blue-shifted peaks, and spectral broadening is larger on the blue side than the red side.

2.9 Solitons

2.9.1 Introduction

Solitons, or solitary waves, are localised wave entities that propagate undistorted. Spatial and temporal optical solitons refer to solitary waves that retain, respectively, their spatial and temporal profiles while propagating. In the spatial domain, light travels through a nonlinear material, and changes the index of refraction of the medium, leading to self-focusing. This self-focusing competes with diffraction effects, and at sufficient intensities can lead to the development of a structure for which diffraction and self-focusing exactly balance – a spatial soliton.

2.9.2 Modulation Instability

In the anomalous dispersion regime, Modulation Instability leads to a spontaneous temporal modulation of a CW beam and transforms it into a pulse train [Itoh, 1989, Wang, 1989]. Modulation instability can be interpreted in terms of a four-wave-mixing process that is phase-matched by SPM. The energy of two photons from the intense pump beam at a pump frequency w_0, is used to create two different photons, one at the probe frequency w_1 and the other at the idler frequency $2w_0 - w_1$. The case in which a probe is launched together with the intense pump wave is referred to as *induced* modulation instability. It can be used to create optical sources capable of producing periodic trains of ultrashort pulses at high and controllable repetition rates. Several experiments have used dispersion-decreasing fibres for this purpose.

2.9.3 Fundamental solitons

The soliton order is characterised by the parameter *N*, it is introduced as

$$N^2 = \frac{L_D}{L_{NL}} = \frac{\gamma P_0 T_0^2}{|\beta_2|}. \qquad \text{Eqn. 2.9:1}$$

The first-order soliton (N =1) is referred to as the fundamental soliton, and its shape does not change on propagation; it has a pulse form of $\text{sech}^2\, e^{i\phi}$. A soliton is characterised by four physical parameters: amplitude, frequency, position, and phase. The latter three can be mathematically and physically engineered and become less important for a fundamental soliton [Agrawal, 2007]. The inverse relationship between the amplitude and the width of a soliton is the most crucial property. Fundamental solitons can be formed in optical fibres at moderate power levels available from, for example, a semiconductor laser. The peak power necessary to launch the Nth-order soliton is N^2 times that required for the fundamental soliton.

2.9.4 Higher Order Solitons

For all higher-order solitons, periodic evolutions occur. The soliton period z_0 can be written as

$$z_0 = \frac{\pi}{2} L_D = \frac{\pi}{2} \frac{T_0^2}{|\beta_2|} \approx \frac{T_{FWHM}^2}{2|\beta_2|} \quad . \qquad \text{Eqn. 2.9.2}$$

As the pulse propagates along the fibre, it first contracts to a fraction of its initial width, splits into two distinct pulses at $z_0/2$, and then merges again to recover the original shape at the end of the soliton period at $z = z_0$. This pattern is repeated over each section of length z_0. It is the mutual interaction between the GVD and SPM effects, similar to the ones mentioned earlier, that is responsible for the evolution pattern. In the case of a fundamental soliton, GVD and SPM balance each other in such a way that neither the pulse shape nor the pulse spectrum changes along the fibre length. In case of higher-order solitons, SPM dominates initially but GVD soon catches up and leads to pulse contraction.

2.9.5 Soliton preservation within optical fibres

Since solitons result from a balance between the nonlinear and dispersive effects, the pulse must maintain its peak power if it has to preserve its soliton character. Fibre losses are disadvantageous because they reduce the peak power along the fibre length. As a result, the width of a fundamental soliton also increases with propagation power loss, and the soliton is thus reduced in amplitude.

A scheme to restores the balance between GVD and SPM in a lossy fibre was demonstrated by changing the dispersive properties of the fibre [Tajima, 1987]. Dispersion-decreasing fibres (DDFs) are used for this purpose because their GVD must decrease in such a way that it compensate for the reduced SPM experienced by a soliton as its energy is reduced by the fibre

loss. Another scheme to overcome the effect of fibre losses is to amplify the solitons periodically so that their energy is restored to its initial value [Hasegawa, 1982, Nakazawa, 1990].

Higher-order nonlinear and dispersive effects such as TOD, self-steepening, and intrapulse Raman scattering are again becoming important for ultrashort pulses; the three parameters vary inversely with pulse width. TOD slows down the soliton and, as a result, the soliton peak is delayed by an amount that increases linearly with distance [Hasegawa, 1995]. Whereas intrapulse Raman scattering leads to the phenomenon of Soliton Self-Frequency Shift [Mitschke, 1986, Gordon, 1986]. As mentioned earlier, an energy transfer appears as a red shift of the soliton spectrum, with the shift increasing with distance. Furthermore, the shift scales with the pulse width as T_0^{-4}, thus, it can become quite significant for ultrashort pulses. Soliton decay occurs within a soliton period, the main peak shifts toward the trailing side at a rapid rate with increasing distance. This temporal shift is due to the decrease in the group velocity ν_g occurring as a result of red shift of the soliton spectrum. Finally, the combined effect of TOD, self-steepening, and intrapulse Raman scattering on a higher-order soliton is to split it into its constituents [Agrawal, 2007, Beaud, 1987].

2.10 Split Step Fourier Method

The nonlinear Schrödinger equation, Eqn. 2.5:3 can be approximated by

$$\frac{\partial A}{\partial z}+\frac{\alpha}{2}A+\frac{i\beta_2}{2}\frac{\partial^2 A}{\partial T^2}-\frac{\beta_3}{6}\frac{\partial^3 A}{\partial T^3}=i\gamma\left(|A|^2A+\frac{i}{\omega_0}\frac{\partial}{\partial T}\left(|A|^2A\right)-T_R A\frac{\partial|A|^2}{\partial T}\right), \quad \text{Eqn. 2.10:1}$$

where $T_R \equiv \int_0^\infty tR(t)dt$ and $\int_0^\infty R(t)dt = 1$. A frame of reference moving with the pulse at group velocity ν_g is used by making the transformation

$$T = t - z/\nu_g \equiv t - \beta_1 z\,. \quad \text{Eqn. 2.10:2}$$

The NLS equation can be analytically solved only in some particular cases, in the general case, the NLS equation is not a solvable differential equation, therefore, a numerical approach is often necessary. A robust method that has been used extensively to solve this pulse propagation problem is the Split-Step Fourier (SSF) method, which is presented in here. This numerical tool is important for the comprehension of the physical phenomena affecting a pulse during its propagation. The simulation results presented in this thesis will all be calculated using this method.

The SSF method obtains an approximate solution by assuming that in propagating the pulse over an extremely small distance h, the dispersive and nonlinear effects act independently. It is useful to write Eqn. 2.10:1 in the form:

$$\frac{\partial A}{\partial z} = (\hat{D} + \hat{N})A, \qquad \text{Eqn. 2.10:3}$$

where $\hat{D}$ is the differential operator, which describes the dispersion and attenuation in a linear medium and $\hat{N}$ is the nonlinear operator, which describes the nonlinear effects in the fibre. These operators are given by:

$$\hat{D} = -\frac{i\beta_2}{2}\frac{\partial^2}{\partial T^2} + \frac{\beta_3}{6}\frac{\partial^3}{\partial T^3} - \frac{\alpha}{2}, \qquad \text{Eqn. 2.10:4}$$

$$\hat{N} = i\gamma\left(|A|^2 + \frac{i}{\omega_0}\frac{1}{A}\frac{\partial}{\partial T}(|A|^2 A) - T_R\frac{\partial|A|^2}{\partial T}\right). \qquad \text{Eqn. 2.10:5}$$

A formal solution of Eqn. 2.10:3, assuming that $\hat{N}$ is independent of z, is given by

$$A(z+h,T) = \exp[h(\hat{D} + \hat{N})]A(z,T), \qquad \text{Eqn. 2.10:6}$$

An approximate solution of Eqn. 2.10:6 can be obtained by assuming that the linear and nonlinear effects can be considered independent over the distance h, thus Eqn. 2.10:6 can be rewritten as:

$$A(z+h,T) \approx \exp(h\hat{D})\exp(h\hat{N})A(z,T). \qquad \text{Eqn. 2.10:7}$$

The propagation along h is carried out in two steps. In the first step, only the nonlinear operator $\hat{N}$ acts ($\hat{D}$ = 0) in Eqn. 2.10:7. The problem can then be easily solved in the time domain after an interval h. Let

$$B(z,T) \approx \exp(h\hat{N})A(z,T). \qquad \text{Eqn. 2.10:8}$$

In the second step, only the linear operator $\hat{D}$ acts ($\hat{N}$ = 0) in Eqn. 2.10:7. The problem can then be solved in the spectral domain:

$$\tilde{B}(z+h,\omega) \approx \exp(h\tilde{\hat{D}}(i\omega))\tilde{B}(z,\omega), \qquad \text{Eqn. 2.10:9}$$

where $\tilde{B}(z,\omega)$ is the Fourier transform of *B(z,T)* and $\tilde{\hat{D}}(i\omega)$ is the Fourier transform of $\hat{D}$. In particular, $\tilde{\hat{D}}$ is obtained from Eqn. 2.10:4 by replacing the differential operator $\partial/\partial T$ by $i\omega$ in the frequency domain. After making the substitutions, the evaluation of Eqn. 2.10:9 is straightforward. Finally, it is possible to go back to the time domain by simple carrying out the inverse Fourier transform:

$$\exp(h\hat{D})B(z,T) = F^{-1}\left(\exp(h\tilde{\hat{D}}(i\omega))\tilde{B}(z,\omega)\right). \qquad \text{Eqn. 2.10:10}$$

By iterating these two steps a large number of times, the electric field evolution along a fibre can be obtained.

To improve the accuracy of the method a slightly different procedure can be carried out. The main difference compared to the previous case is that the effect of the nonlinearity is included in the middle of the distance segment rather than at the segment boundary. In other words, the pulse propagates over the distance h/2 where only the dispersive effects are considered, then the effects of nonlinearity are included at the middle of the segment (h) and finally the dispersive effect are included in the last h/2 of the segment. In this procedure Eqn. 2.10:7 is replaced by

$$A(z+h,T) \approx \exp\left(\frac{h}{2}\hat{D}\right)\exp\left(\int_z^{z+h}\hat{N}(z')dz'\right)\exp\left(\frac{h}{2}\hat{D}\right)A(z,T). \qquad \text{Eqn. 2.10:11}$$

2.11 Nonlinearity and effective mode area in holey fibres

Nonlinear properties can be found in all-silica optical fibres if the intensities of light are high within the core. When high values of effective nonlinearity per unit length are achieved in an optical fibre, the device lengths and the optical power required are greatly reduced. Such high nonlinearity can be found in small core holey fibres.

The effective nonlinearity γ, is given by

$$\gamma = \frac{2\pi}{\lambda}\frac{n_2}{A_{eff}}, \qquad \text{Eqn. 2.11:1}$$

where n_2 is the nonlinear coefficient of the material, A_{eff} is the effective mode area, and λ is the optical wavelength. For standard telecommunications fibre with n_2 of 2.2×10^{-20} m^2/W for silica, and an A_{eff} of 90 μm^2 at 1550 nm, γ is ~1 W^{-1}km^{-1}. By reducing the core diameter and modifying the composition of a silica fibre, for example, the addition of Ge to the fibre core, thus increases n_2 and the NA, the effective mode area can be reduced. For a small-core conventional fibre, the largest γ that is possible is ~26 W^{-1}km^{-1} with an A_{eff} of ~8 μm^2 [Okuno, 1999].

The large index difference between silica and air allows the production of HFs with a very high NA. Therefore, tighter mode confinement can be achieved. As the diameter of the core is

reduced, the mode becomes more confined and the effective mode area decreases. When the core size becomes significantly smaller than the optical wavelength, it is harder to confine light sufficiently, and the mode expands again. Hence, for a given wavelength, there is a minimum effective mode area, which depends on the index difference. Pure silica HFs with A_{eff} as small as 1.7μm^2 at 1550nm have been designed by the authors in reference [Finazzi, 2003]. In the extreme case, when a silica rod is surrounded by air, the minimum effective mode area is ~1.48 μm^2.

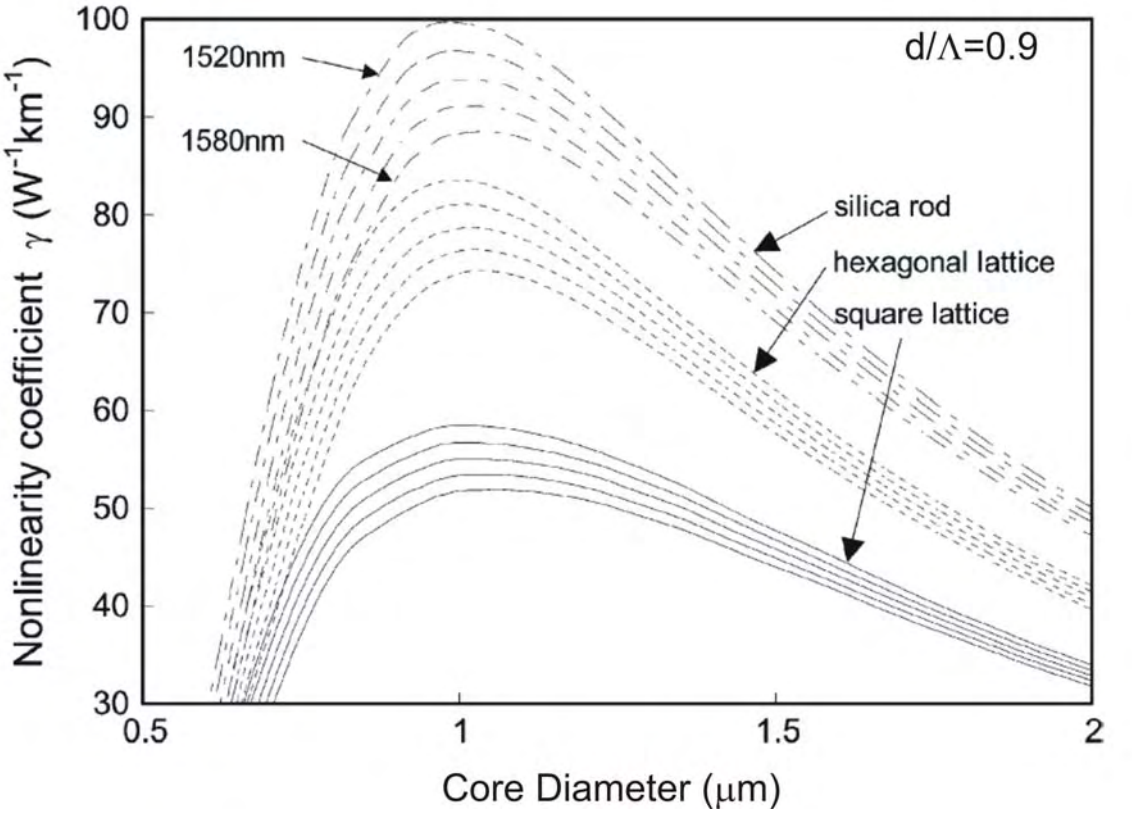

Fig. 2.1 Nonlinearity coefficient as a function of the core diameter for a silica rod (dashed–dotted line), and the square lattice (solid line) and hexagonal lattice HF (dotted line) with d/L= 0:9; for each type, the characteristics of five wavelengths between 1520 and 1580 nm increasing in 15-nm steps are plotted, after reference [Hainberger, 2005].

Changing the mode size alters the effective nonlinearity of the fibre by varying the intensity inside the fibre, thus, varying the nonlinear phase change that is experienced by light during propagation. Figure 2.1 shows the nonlinearity coefficient as a function of the core diameter for a typical hexagonal lattice HNSC HF and for a silica rod. Nonlinearity as high as ~70 W^{-1}km^{-1} is possible in HFs, more than 70 times higher than in standard telecommunications fibre, and over 2.5 times higher than in the large-NA conventional fibres described above.

One way to enhance the nonlinearity is to raise the index of the core even further by using Ge-doped cores [Fuochi, 2003]. A more direct way is by filling the holes in HFs with a suitable nonlinear material. This is attractive only when a large fraction of the mode can

propagate in the air; which can be found in HFs with a hole spacing less than the wavelength of the light [Monro, 2001].

Note that in holey fibres, the nonlinearity and/or the effective area are determined by the fibre parameters, namely, pitch (Λ), air hole size (d) and air-filling fraction (d/Λ). The concept of using a design map for designing a holey fibre is introduced in a later part of this thesis. Optimising holey fibre designs for various nonlinear applications can be done from contours maps in the (d/Λ, Λ) grid. For example, a design map could contain contours presenting the values of nonlinearity, dispersion, dispersion slope and effective area in the (d/Λ, Λ) grid, see Fig. 2.2. Many paths on the map are then investigated and the optimum Λ and d/Λ profiles are identified. This is a flexible method for designing holey fibres that are used in nonlinear applications such as tapered designs for soliton compression (see Chapter 7).

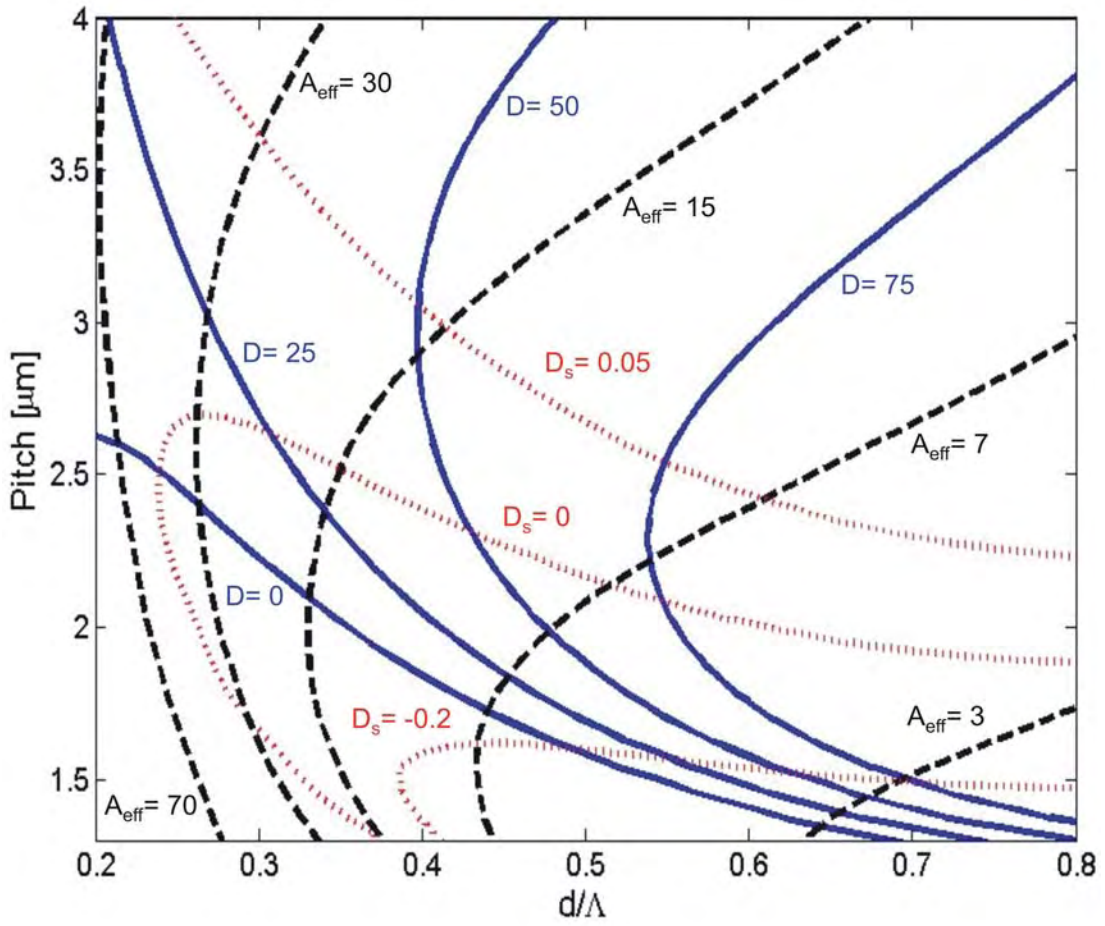

Fig. 2.2 Contour map for dispersion (ps/nm/km), dispersion slope (ps/nm^2/km) and effective area (μm^2) versus pitch Λ and d/Λ for holey fibres of hexagonal geometry at 1.55 μm wavelength.

2.12 Dispersion management in holey fibres

2.12.1 Shifts of zero-dispersion wavelength

It is possible to tailor both the magnitude and the sign of the dispersion over a wide range of wavelengths by modifying the fibre structure parameter profiles. The dispersion for a one-ring structure differs significantly from that of a structure with two rings of holes. However, it has been shown that structures with two or more rings have similar dispersion values [Finazzi, 2003].

The overall group velocity dispersion (GVD) has two contributions, the material dispersion (which is a given function of wavelength for all silica fibres and is zero at λ=1.27 μm) and the waveguide dispersion (which in a conventional single-mode fibre shifts the zero of the net GVD to 1.31 μm). The strong wavelength dependence of the effective-index difference between the core and the cladding in HFs results in a range of unique dispersion properties. In an index-guiding HF, very strong waveguide dispersion is attainable; the overall fibre dispersion can be made anomalous at wavelengths where the GVD of a conventional single-mode fibre is normal [Knight, 2000]. Moreover, it can be designed to be simultaneously single mode with anomalous waveguide GVD, whereas conventional step-index fibres are always multimode when the waveguide GVD is anomalous.

It has been shown that a wavelength of zero dispersion can be altered over a very broad range simply by changing the air hole size or the pitch [Sinha, 2003]. There can be a shift of zero dispersion wavelengths from the IR region of the spectrum towards the UV region, which is unattainable in conventional optical fibre. Fig. 2.3 shows examples of the dispersion profiles for different holey fibre designs. It shows designs having anomalous dispersion at wavelengths below 1.27 μm, two zero dispersion wavelengths, and ultraflattened dispersion at 1.55 μm.

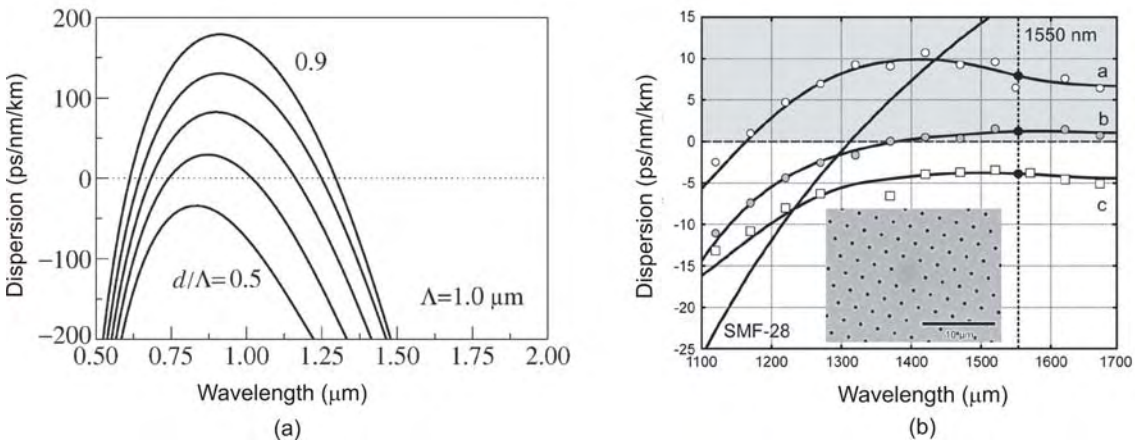

Fig. 2.3 (a) Variation of dispersion with wavelength for HFs designed with different values of d/Λ when Λ= 1 μm, after reference [Saitoh, 2005(a)]. (b) Dispersion profiles against wavelength for three different HFs designed to have low-level ultraflattened dispersion, and the curve of a standard conventional single mode fibre, Corning SMF-28, after reference [Russell, 2006].

2.12.2 Dispersion compensation

Any chromatic dispersion in single-mode fibres limits the data transmission rate [Glass, 2000]. With large air holes, giving a large index contrast, large normal dispersion in HFs can be obtained not only at a single wavelength, but also for a wide range of wavelengths. It is possible to obtain normal dispersion of as much as -584.7 ps/nm-km (at 400 nm), -1600 ps/nm-km (at 1300 nm), and -1350 ps/nm-km (at 1550 nm) by varying the core diameter [Sinha, 2003]. These large values of negative dispersion could be used to compensate the anomalous dispersion of conventional single-mode fibre. For example, this can cancel the small anomalous material GVD at 1550 nm (~20 ps/nm-km) for a standard single-mode telecom fibre. The larger the normal dispersion of the compensating fibre, the shorter the length that is required.

In a simple step-index dispersion-compensating fibre, the core must be heavily doped to obtain a large index contrast, making the fibre lossy, because of the thermal mismatch between the core and cladding [Ainslie, 1986]. This problem does not occur in HF technology where a single and undoped material can be used. Dispersion values exceeding -2000 ps/nm-km at 1550 nm are reported [Birks, 1999], 20 times larger than that of a typical conventional dispersion compensating fibre, thus this fibre could compensate for the anomalous dispersion of over 100 times its length of standard fibre. Unfortunately, its core effective area is only around 1 μm^2; and in typical HFs, large negative dispersion is always associated with very small A_{eff}, leading to undesirable nonlinear effects during optical signal transmission. A novel "dual-core" design is proposed [Ni, 2004], which has an A_{eff} of 12 μm^2 and a dispersion as large as -18000 ps/nm-km at 1.551 μm.

2.12.3 Dispersion-flattened designs

Flattened fibre-dispersion behaviour is crucial for communication systems, in both linear and nonlinear regimes [Nakazawa, 1998]. For example, in ultrashort (<1ps) optical soliton dispersion-managed systems the existence of significant third-order dispersion can lead to strong instabilities that destroy soliton-pulse transmission features [Agrawal, 2007].

Conventionally, dispersion-shifted W-type fibres are used to generate flattened behaviour mainly in the telecommunication wavelength window (dispersion below 2 ps/nm/km over the 1.3 μm - 1.6 μm wavelength range has been achieved with W fibre). In holey fibre technology, configurations of the basic structure (hole-to-hole spacing and the air filling fraction) can provide wider flattened dispersion over different wavelength windows [Ferrando, 1999].

A trial-and-error manual procedure for designing HFs with zero ultraflattened dispersion is given in reference [Ferrando, 2000, Monro, 1999]. Since the material dispersion D_m curve is fixed, by modifying the waveguide or geometric dispersion D_g by designing the two structure

parameters, hole size (d) and pitch (Λ), one can achieve a D_g curve which exactly cancels out the D_m curve over a range of wavelengths. It is assumed that the material refractive index is wavelength independent, and the dependence of D_g on λ arises solely from the geometric configuration of the fibre. The authors in reference [Ferrando, 2000] provide the basic behavioural trend of D_g when varying the simultaneous scale transformation (M), of d and Λ, and the ratio d/Λ: A change in M results in a shift of the near linear part of the D_g curve along the λ axis along with a change in its slope. When the d/Λ ratio is modified, the D_g curve is shifted along the λ axis without significant changes of the slope of the linear central region. With this scheme, near zero ultraflattened dispersion around 1.55 μm was achieved over a range of 428 to 543 nm. Since then, many dispersion-flattened holey fibre designs have been proposed, in particular, the five-ring multi hole-size designs shown to be the most effective [Saitoh, 2003, Poletti, 2005].

2.12.4 Dispersion-decreasing designs

Conventional Dispersion-Decreasing Fibres (DDFs) are fabricated where the core diameter of a single-mode fibre is varied through tapering the fibre during the drawing process, and hence changing the waveguide contribution to the second-order dispersion. The dispersion is monotonically and smoothly decreased from an initial value to a different value at the end of the length according to some specified profile. The use of fibres with variable dispersion is viewed as an effective method to control optical solitons in soliton communication systems. DDF's have been recognized to be useful for high-quality, stable, adiabatic soliton pulse compression and soliton train generation, [Mamyshev, 1991, Ivanov, 1992]. These processes typically required 10m - 100m of conventional DDFs.

Because of the increased design flexibility (fibre diameter, Λ and d/Λ along the fibre) provided by holey fibres with small effective mode area and corresponding large nonlinearity, shorter fibre length can be used, and HFs are also able to operate in other wavelength ranges outside that of the telecommunication windows. These fibres can be designed using contour maps as mentioned earlier. The main applications are UV-to-IR supercontinuum generation, [Kudlinski, 2006] and pulse compression [Hu, 2006].

2.13 Loss mechanisms

The total loss of optical fibres is a combination of many different factors. In general, they are confinement loss (α_C), intrinsic material absorption (α_M), in particular the losses due to the electron transition in the ultraviolet and multi-phonon absorption in the infrared, and scattering loss (α_S). Also, losses induced by the impurities (α_{IM}), such as water contamination that causes

unwanted absorption. There is an additional bend loss (α_{BEND}) to be considered in devices, especially for large-mode area HFs.

The total loss, α_{TOL}, can be written as:

$$\alpha_{TOL}(\lambda) = \alpha_S + \alpha_C + \alpha_M + \alpha_{IM} + \alpha_{BEND.} \quad \text{Eqn. 2.13:1}$$

All the loss components (except for α_M) in microstructured fibres are quite different from those of conventional fibres [Furusawa, 2003]. The presence of glass/ air interface in HFs introduces new mechanism for the incursion of loss. Impurity occurring at the interfaces during the fibre draw may increase the loss due to absorption, or may act as centres of formation for crystallites which add to the scattering loss. These loss contributions can be reduced or eliminated by technological improvement of fibre fabrication. The ultimate loss limit is determined by surface roughness caused by thermally-driven capillary waves, which are present at all length scales. These interface ripples freeze in when the fibre cools, so that it can not be substantially reduced by technological improvement, and introducing high scattering losses for modes that are extended across the interfaces [Roberts, 2005].

2.13.1 Scattering loss

Rayleigh scattering is applicable when the scattering particles are much smaller than the wavelength of the incident light. In an optical fibre, the scattering is caused by nanometer-scale refractive index variations inside the glass due to its random molecular structure.

In HFs, fluctuations in the fibre geometry along the fibre length perturb the guided modes; in particular, a longitudinal variation of the structure promotes modal coupling to high order or radiation modes, thus, imperfection loss may be induced.

Since a typical HF is composed only of pure silica glass, Rayleigh scattering and infrared absorption losses are estimated to be less than that of a conventional single-mode fibre. Nevertheless, a high Rayleigh scattering coefficient is commonly found in HFs [Tajima, 2002], and it is the major contribution to the overall losses. In order to realise low-loss HFs, a pure silica glass with low Rayleigh scattering loss and low absorption loss should be used and the surface roughness of the holes should be minimized. With certain glass polishing and etching techniques, a HF with a total loss of 0.18 dB/km at 1550 nm has been reported [Tajima, 2007]. Moreover, the scattering loss is dependent on core size, see Fig. 2.4, a study of this topic is found in [Furusawa, 2003]. The loss of solid core HFs is found to increase as the core size decreases, a property which has been ascribed to the increased field strength at the hole interfaces leading to a larger roughness scattering loss component.

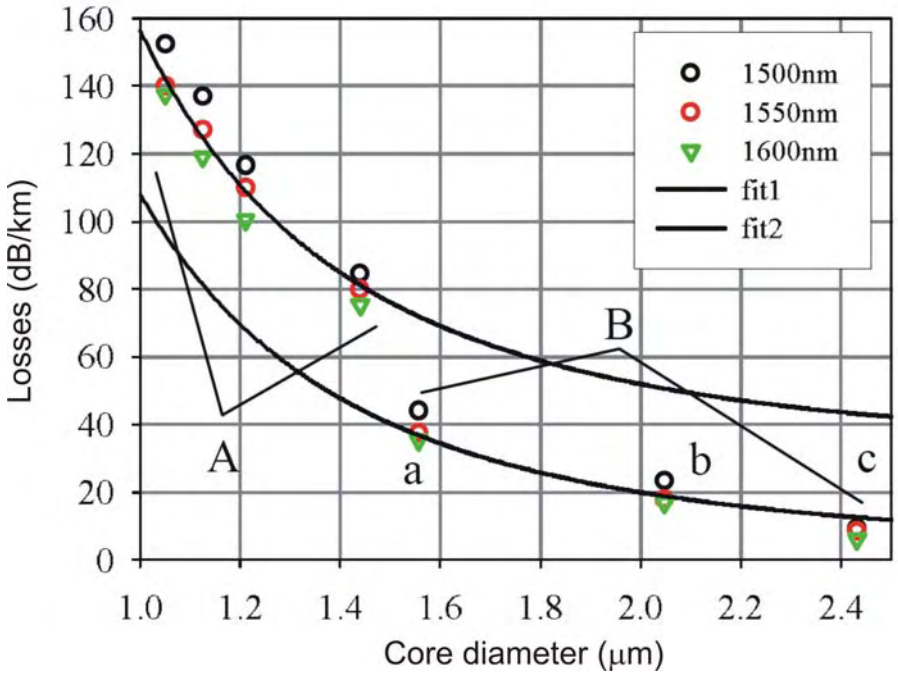

Fig. 2.4 The loss versus core diameter of various holey fibres drawn from two preforms (A and B), with similar air-filling fraction, d/Λ> 0.9, after reference [Furusawa, 2003].

2.13.2 Confinement loss

Confinement loss is a unique form of loss that occurs in HFs composed of a single-material. Owing to the finite numbers of air holes, in an all-silica HF the core possesses the same refractive index as the material beyond the finite holey cladding region and causes the modes to be leaky, and often behave as very lossy guided modes rather than radiation modes [Senior, 1992]. These losses occur even in the absence of material absorption or scattering losses. Leaky modes have oscillatory fields in the cladding, allowing power to leak out of the fibre, whilst bound modes that are usually found in conventional fibres, are radially evanescent in the depressed cladding layer.

In general, by increasing the number of rings of air holes in the cladding, thereby physically increasing the separation between the core and the outer cladding, confinement loss can be reduced [White, 2001]. Moreover, by careful design of the geometry of the fibre structure, these losses can be reduced further [Finazzi, 2003]. For example, Fig. 2.5 shows the confinement loss against the pitch size Λ, for different air-filling fraction d/Λ and different number of rings. Certain criteria have been identified in order to reduce the confinement loss of small-core HFs to a level comparable to conventional fibres. It has also been shown that HFs with a nonlinearity as high as 45 W^{-1} km^{-1} and with a confinement loss of less than 0.2 dB/km, are possible by using only four rings of holes; these designs are highly practical.

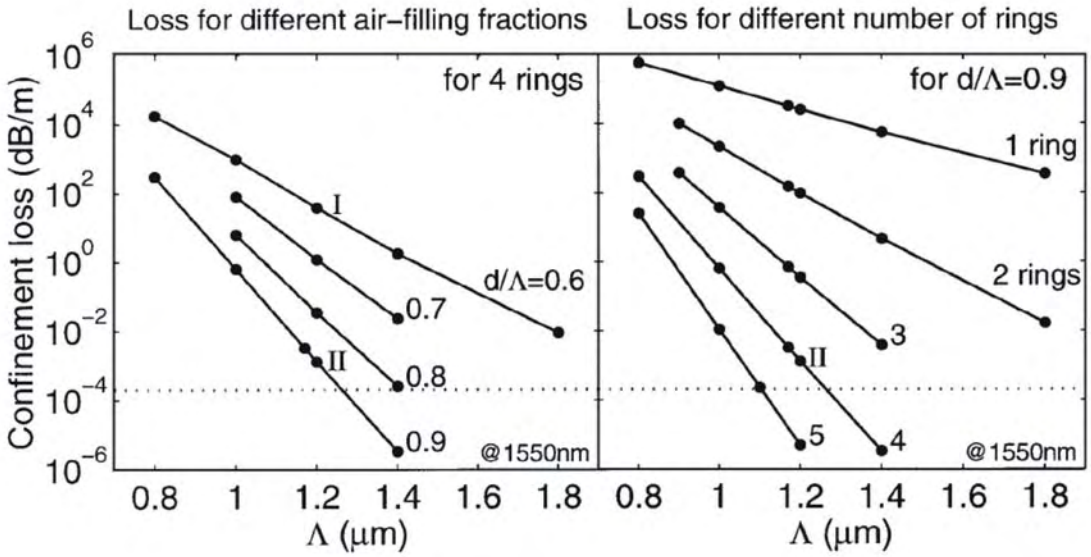

Fig. 2.5 Confinement loss for different air-filling fractions (left) and different number of rings of holes (right) as a function of Λ. The dotted line represents the loss of conventional fibers (0.2 dB/km), after reference [Finazzi, 2003].

2.13.3 Bend loss

Like conventional fibres, HFs exhibit a bend loss edge at long wavelengths due to the fact that the mode extends further into the cladding, resulting in a more weakly guided mode that suffers a greater perturbation in response to bending.

As shown in Eqn. 1.3.2, n_{eff} has a strong wavelength dependency due to the air hole arrays. At short wavelengths, the field is mainly confined to the silica core, whereas at long wavelengths it has an effective index determined by the air-filling fraction of the cladding. This implies that the refractive-index difference decreases with decreasing wavelength, and that the field confinement factor of a guided mode will decrease, resulting in the unusual property of high bend losses at short wavelengths in HFs.

Pure bend loss is a continual loss of radiation that occurs along any curved section of a fibre and is separated into two regimes: *macro-bending* and *micro-bending* losses. Macro-bending losses result from bends that are significantly greater in scale than the fibre core, while micro-bending losses occur for small-scale bends, along which the mode distorts continuously. Micro-bend losses can be reduced through careful processing and handling of the fibre. On the other hand, macro-bend loss has been further studied with full theoretical treatment [Baggett, 2003, Sorensen, 2001, Nielsen, 2004].

If the hole-to-hole spacing is large compared with the wavelength, when the fibre is bent, the guided mode can escape through the solid silica bridges between neighbouring holes. Thus bend losses are particularly significant in large mode area HFs, which are realised either by increasing the hole-to-hole spacing or by decreasing the hole diameter, or both. It has been shown that HFs can possess bend losses at 1.55 μm that are comparable to those of similarly

sized conventional fibres [Baggett, 2001], the largest mode areas that are practically feasible are ultimately determined by bending losses.

The fibres used for this thesis were all small core holey fibres, thus the bend losses in these fibres were less significant and were neglected.

2.13.4 Coupling Loss

As HF becomes more widely used, there is an increasing need for effective cleaves, low-loss splices, and mode-area transformers. HFs cleave cleanly using standard tools, showing slight end face distortion only when the core is extremely small ($\Lambda \sim 1\ \mu m$) and the air-filling fraction is very high (> 0.5). Solid glass end caps can be formed by collapsing the holes at the fibre end to form a coreless structure through which light can be launched into the fibre. A solid-core HF can be fusion spliced successfully both to itself and to step-index fibre using resistive heating elements. The two fibre ends are placed in intimate contact and heated to softening point. With careful control, they fuse together without distortion. Provided the mode areas are well matched, splice losses of <0.2 dB can be achieved, except when the core is extremely small.

It is important to be able to change the mode area without losing light. This can be obtained by scanning a heat source along the fibre. This causes the holes to collapse, with the degree of collapse depending on the dwell time of the heat. Drawing the two fibre ends apart at the same time provides additional control. Graded transitions can fairly easily be made, and mode diameter reductions as high as 5 :1 have been realised with lowloss [Town, 2001].

2.14 Conclusions

This chapter gives a brief overview of the main nonlinear and dispersive effects in optical fibres, and the design approaches, that need to be considered for a detailed understanding of the thesis, especially for Chapters 5, 6 and 7, where the nonlinear processes such as SPM, Raman scattering, soliton formation, and four-wave-mixing are used to describe the origin of the nonlinear effects seen in applications.

Chapter 3

A guide to fabrication of small-core holey fibres

3.1 Introduction

This chapter describes a general method for the fabrication of small-core silica holey fibres. To date, there are limited publications describing the exact procedures for the fabrication of microstructured fibres (MOFs). This information can be found in PhD theses, for example in [Furusawa, 2003]. The most commonly used method is by stacking glass capillaries, due to its flexibility and low capital cost. This method is reported here, and largely followed in the rest of this thesis when specialised fibres are fabricated. Other methods such as casting [Zhang, 2006, Windeler, 2005], extrusion [Ebendorff-Heidepriem, 2007] and direct drilling [Barton, 2004, Mukasa, 2006] have also been used to produce structured preforms.

Preform preparation is a major part of the entire fabrication procedure for the production of conventional and microstructured optical fibres. For the latter, this usually includes drawing capillaries from glass tubes, then cleaning and stacking them. Small core silica holey fibres are generally fabricated in a two-stage pulling process, where in the first stage the stacked preform is drawn into cane. In the second stage, the cane is inserted into a jacket tube and pulled to fibre.

To achieve high quality conventional optical fibre, the most important part of the fabrication process is the preparation of the preform. By carefully synthesising the preform, very low transmission losses have been achieved, with various active and passive dopants in the core. Moreover, the drawing process has been considered as a trivial problem. The dimension of the fibre drawn from a solid preform follows a simple mass conservation law

$$\left(\frac{FinalOD}{InitialOD}\right)^2 = \frac{u_f}{u_d} = \eta\,, \qquad \text{Eqn. 3.1.1}$$

where *FinalOD* and *InitialOD* are the outer diameters of the fibre and the preform, u_f and u_d denote the feed and draw speeds, respectively, η is the volume reduction ratio. The outer diameter (OD) of the fibre can be controlled by optimising either feed or draw speed. The core

diameter/ the fibre OD ratio, determined at the preform preparation stage, is retained. This is not true in the case of MOFs, due to the existence of air holes that may be unintentionally collapsed or expanded during the drawing process, by the combined effects of the viscosity and the surface tension of the glass.

In Section 3.2, the operation and limitations of the fibre draw tower are reviewed. Section 3.3 describes the capillary preparation technique. The preform stacking method and cleaning precedures are given in Section 3.4. Caning and fibre drawing procedures are presented in Section 3.5 and 3.6, respectively. Conclusions are presented in Section 3.7.

3.2 Fibre draw tower

3.2.1 Feeder and furnace

A 5 m fibre draw tower was used for the fabrication of all the fibres that I made during my PhD period. In this section, the configuration of the tower is outlined; the limits and practical ranges of the fibre draw parameters available on the tower are discussed. (Note that, all the fabrication works carried out by me were done before and up to the Mountbatten fire of 30 Oct'05 during which the tower was destroyed) The schematic of the fibre draw tower is shown in Fig. 3.1.

The preform is clamped by the preform feeder chuck, which has a reliable speed range between ~0.4 mm/min and ~15 mm/min. The lower limit is given by the minimum step size of 0.1 mm/min of the motor control, and the maximum is limited by the mechanics of the motor driver.

The hot zone of the furnace is located ~150 mm below the top iris and the length of the furnace element is ~50 mm. The distance between the top and the bottom iris is ~300 mm. Before each draw, the furnace is purged with argon, in order to avoid any oxidation of the furnace carbon elements, especially at high temperature, and to prevent impurities that may have been in the furnace being incorporated into the glass. The temperature control and the pyrometer provide a relative temperature adjustment and reading with high accuracy, but not the absolute temperature. Therefore, it is usual practice to record the temperature values with reference to the initial drop temperature when the fibre draw is initiated. The subsequent temperatures during draw require high stability, any temperature variation leads to fibre diameter fluctuations due to the changes in viscosity, and therefore fibre tension. A diameter gauge is placed between the bottom of the furnace and the coating cup, to monitor the fibre diameter during the draw, and to provide feed back to the system for automatic diameter control by varying the draw speed. Typical diameter fluctuations observed for both

conventional and holey fibres drawn on the tower are <1%, with or without automatic diameter control.

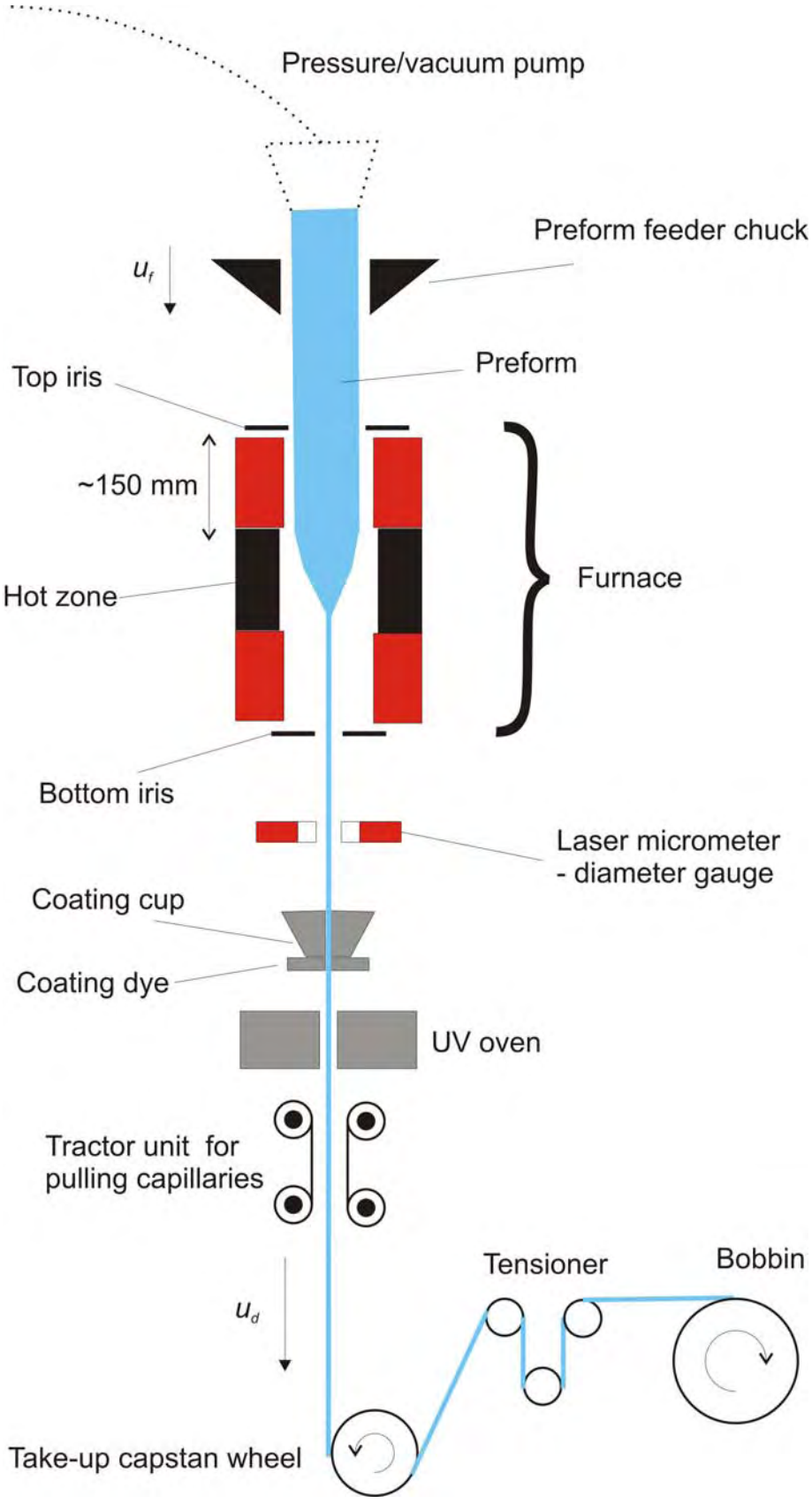

Fig. 3.1. The schematic of the fibre draw tower

3.2.2 Polymer fibre coating

An acrylate coating is applied on the surface of the fibre and UV cured in order to protect the fibre and to provide strength. The open coating cup, together with a coating dye, is placed below the diameter gauge. The cup contains the polymer resin, which is extruded through the coating dye. The coating material is then immediately cured through the UV curing oven. The optimum thickness of the coating depends on the fibre diameter, the coating material and the curing quality. A thickness of ~40% of the fibre diameter is typically good enough for laboratory use for most fibres. For a fibre of 125 μm OD, a coating dye with a minimum hole size of 250 μm diameter is used which, under typical conditions, would produce a good quality coating of ~50 μm thickness.

High index coating polymer (Desotech: DSM 3-14) is used for all of my fibres. It is very important for the fibre to have good quality coating to provide enough mechanical strength to at least be able to withstand the fibre take-up process by the capstan and the bends during the fibre winding process without breakage. There are a few factors that need to be taken into account to apply a good coating. The first factor is the volume shrinkage of the coating during curing. This depends and is controlled by the curing time and the power of the UV lamp. The second factor is the viscosity of the polymer, which determines the maximum u_d for a given die size. If the die is too large compared to the fibre diameter, the polymer slips at the die, resulting in patchy coatings. Also there is the issue of the formation of air bubbles in the polymer resin within the coating cup, and extruded through the coating dye, which weaken the coating locally (note, this can be solved by using a pressurised coating die).

The other factor is the surface temperature of the fibre when applying the coating. It must be sufficiently cooled as it enters the coating cup. If the temperature is too high, it may result in a fire or slippage of the polymer due to locally increased viscosity of the polymer. Because the heat removal primarily depends on the distance between the furnace and the coating cup, the height of the fibre draw tower ultimately determines the fastest u_d. For the 5 m tower, the highest possible u_d was ~20 m/min, without using a pressurised coating system or actively cooling the fibre.

3.3 Capillaries Preparation

3.3.1 Analytical model for capillary drawing

Capillary drawing is one of the most important processes in MOF fabrication. The success of the production of holey fibres with a specific design can depend greatly on this fundamental process. The precise control of capillary dimensions and the uniformity of capillaries are essential for structuring regularly arranged air holes within the stacked preform. As mentioned

previously, this is not a trivial problem because of the possible contraction or expansion of air holes during the drawing process. A mathematical study for the capillary drawing process is given in [Fitt, 2002, Furusawa, 2003]. In the reports, an isothermal fluid dynamics model was considered, and both numerical and analytical approaches were examined to solve the problem. The major analytical results are extracted from the reports and summarised in the following.

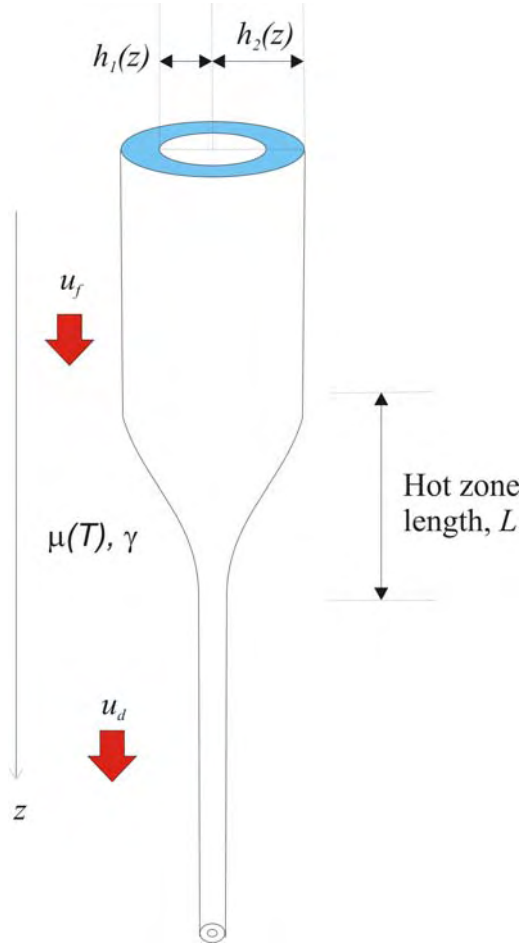

Fig. 3.2. Definitions used for the analytical model of capillary drawing.

The physical model and the parameters used in the study are illustrated in Fig. 3.2. The boundary conditions are given by the u_f and u_d, while the initial conditions are the inner and the outer radii $h_1(0)$ and $h_2(0)$ of the glass tube, respectively, where the origin is taken to be the top of the hot zone. The viscosity $\mu(T)$, surface tension γ, and the hot zone length L are also included in the model. It is assumed that no deformation of the glass occurs outside the hot zone. The temperature dependence of the viscosity for silica at a temperature T ^{0}C is approximated by the equation,

$$\log(\mu) = \frac{-6.24 + 2.69 \times 10^4}{(T + 273))}, \qquad \text{Eqn. 3.3.1}$$

in the temperature range (1600 to 2500 ^{0}C) of interest for silica with small amount of OH content ($3x10^{-4}$ wt%). The collapse ratio of the tube can be defined as

$$C = 1 - \frac{h_1 h_2(0)}{h_2 h_1(0)} \cong \frac{\gamma L}{\mu u_f \ln(u_d / u_f)} \left[\frac{1}{h_1(0)} + \frac{1}{h_2(0)} \right], \qquad \text{Egn. 3.3.2}$$

where γ is the surface tension coefficient, and is estimated to be ~0.3 N/m. C is a measure of the change in capillaries geometry during the draw and reflects the sensitivity of the collapse to the relevant draw parameters. Note that when C= 0, the ratio of the inner and outer diameter is preserved during and after the draw. And when C= 1, this represents a complete collapse of the air hole. Although, the effect of the surface tension becomes more significant as the radius of the capillary decreases, the viscous force that originates from the longitudinal tension applied by the continuous pulling action increases more rapidly with the reduced capillary dimensions. Therefore, the influence of the surface tension becomes less significant as the tube diameter decreases over the neck-down region. Also, Eqn. 3.3.2 shows that a shorter hot zone length, L, can help to avoid collapse, and that any collapse occurs mainly in the upper part of the hot zone, therefore the geometry of the capillaries is nearly constant over most of the neck-down region. Moreover, C is more sensitive to u_f than to u_d, therefore, by using a larger u_f , and increasing the viscosity, thus using a lower temperature, can also help to avoid collapse.

3.3.2 Capillary drawing

High-grade, low OH content silica glass tube such as ‘Heraeus: Suprasil F300’ is commonly used for the production of capillaries. It possesses better initial uniformity, where the diameter deviation is typically ±~0.2 %/m. However, due to the limited accuracy of the draw parameters, some transverse deformation induced through the drawing process degrades the uniformity of the capillaries to the level of ~0.5 %/m. This glass material was used for the production of all of the holey fibres that I have fabricated. Large tubes that have outer diameters typically of the order of 25 to 28 mm are used for production of capillaries. A tube is chosen with the inner/outer diameter ratio, d/D, closest to the desired d/Λ of the structure in the stack. Note that the ratio d/Λ here is not necessarily the same as the one required in the final fibre, due to the expansion and contraction of hole sizes during the caning and the final fibre pulling stages.

Capillary elements are drawn down to size from a large tube on a drawing tower (see Fig. 3.1) located in a ’10,000-class’ cleanroom laboratory. First, a low grade drop rod or tube is attached to one end of the ‘F300’ tube; this is done on a glass lathe. On the draw tower, the tractor unit is used; the draw speed determines the outer diameter of the capillaries. It is important to spend some time on adjusting the x-y position of the tube to make sure that it is located at the centre of the furnace. The pulling is usually done at or slightly below the drop temperature (~2050 to

~2010 ^{0}C); this is the temperature at which the tube (with a drop rod attached) itself is softened and able to be stretched under gravity alone.

The model in Section 3.3.1 provides valuable information on the draw parameters. The draw is unstable when u_f is below 2 mm/min, a slight change in u_f leads to a significantly different ID/OD ratio. High drawing temperatures lead to low viscosity, therefore more collapse for a given u_f. However, when the draw temperature is too low, the circularity of the capillaries can be degraded, possibly due to the very high tension. Nevertheless, it is clear that the ID/OD ratio approaches that of the original value of the tube by either reducing the temperature or increasing u_f.

Any surface scratches or defects can be eliminated by fire-polishing or baking the tube (see Section 3.5 and 3.6). Although the draw process itself involves heating the glass tube but, as discussed before, the capillaries have to be pulled at reasonably low temperatures and using high feed speed, in order to preserve the geometry and to ensure stability. This makes it difficult to improve the surface quality during the draw.

Although, it is possible to control the amount of collapse of the capillary geometry by either tuning the temperature or u_f alone, the process control is much simpler when applying a small amount of pressure. In practice, by applying additional pressure to the inside of the tube and/or tuning the drawing temperature, u_f and u_d, the inner diameter can be altered until the required d/Λ is reached.

Therefore, the feed speed is estimated initially by a simple conservation of volume method (see Eqn. 3.1.1). For example, drawing capillaries of diameter ~1.15 mm from a 25 mm OD tube at a chosen draw speed of 2 m/min, the calculated feed speed is 4.2 mm/min. The diameter gauge on the tower is used to monitor the final OD of the capillary whilst the final inner diameter, ID, is measured under the optical microscope, and both of these are calibrated using vernier calliper. Due to the relatively long distance between the drawing tractor and the neck-down region, the capillary may be slightly perturbed transversely by the ambient air turbulence in the clean-room during draw, affecting the uniformity along the length. This is more significant when drawing either with high temperature or low u_d.

3.3.3 Capillary sealing and cleaning

Only clean capillaries are used for the construction of the preform, to avoid as much contamination as possible. Any residue in the preform can be burnt in the furnace during draw and some elements can diffuse into the glass, which leads to high propagation losses. It is difficult to clean the inner wall of the capillaries because of their small inner diameter; if ultra-low loss fibre is required, extra polishing and cleaning steps are carried out for the large tube before it is reduced into capillary sizes. Therefore, only the outer surface of the capillaries is cleaned individually using methanol and acetone with a lens tissue. To ensure that the

methanol and acetone residue is completely evaporated from the capillaries, a nitrogen gun is used to dry the surfaces. Alternatively, the capillaries can be set-up and held on a glass lathe and then purged them with dried gas flow from a MCVD system.

From Eqn. 3.3.2, a tube with larger dimensions is expected to experience less collapse. This applies to the individual capillary elements within a preform stack, where the capillaries are more collapsed than the holding jacket tube. Therefore, the structured lattice may not be maintained during the caning process because the capillaries can freely move within the jacket tube. This issue can be overcome by pressurising the individual capillaries so that the inner structure is less collapsed than the jacket tube, and this can be achieved by sealing the capillary ends. The inner structure can then be fitted to the jacket, preserving the structure.

The capillaries (preform length) are typically 250 to 400 mm in length; this depends on the amount of canes that are required, and the amount of preform that is needed to establish stable draw conditions. At least one end of the capillaries is required to be sealed. The air inside the capillaries provides a natural pressure to prevent the holes from collapsing during the caning stage. The sealing process can be done using a low flame hydrogen/oxygen burner. Care must be taken so that the diameter of the sealed end is not greater than the capillary diameter since overheating leads to globule formation, which prevents neat hexagonal stacking.

3.4 Preform stacking

The balance between the pressure within the air holes and the mechanical forces within the glass are the primary factors determining the resultant geometry. The pressure within the capillaries is inversely proportional to the length of the remaining preform. Since most of the pressures are cancelled out by the adjacent air holes, the net pressure imposed on the jacket tube is not determined by the total volume of the air holes but by the dimensions of a single air hole. Therefore, the pressure built up within the preform can be well compensated by either the use of a thick enough jacket or by having a large number of capillaries to reduce the size of the air holes. However, when the air holes of the capillaries are small (<1 mm), the pressure decay along the length of the capillaries can become significant due to the temperature gradient along the preform length. This effect can be reduced by sufficiently warming up (baking) the preform in the furnace before pulling it.

In the following section, I will discuss the absolute dimensions of the preform, and the techniques and practical issues for the preform assembly.

3.4.1 Jacket tube selection and preparation

The preform dimensions are determined by the capillary sizes and the number of rings of holes required. The maximum OD of the preform is physically limited by the bore size of the

furnace. For example, if 2 mm OD capillaries are stacked to form a 8-rings lattice, the ID of the jacket tube has to be at least 34 mm. The bore size of the furnace used for the work in this thesis is 35 mm in diameter. Therefore, the jacket thickness must be less than 0.5 mm, which will cause a problem because of the possible expansion of the preform due to the residual pressure of the sealed capillaries. Thus, using smaller capillaries would help, as more rings/capillaries can be stacked. However, it becomes increasingly difficult to assemble them as their dimensions are reduced. The thinnest capillaries used to date for stacking had OD of ~0.5 mm.

More importantly, the transverse thermal gradient within the preform, when it is in the furnace, causes issues for the preservation of the lattice. Large preforms are significantly affected by the temperature difference between the vicinity of the core and that of the jacket tube; the latter is hotter and tends to be unstable. The slight difference in viscosity leads to a significant transverse deformation; the air holes near the jacket tube collapse more than those nearer the centre. As the preform size increases, not only the thermal gradient causes problems, but it also typically requires more time to stabilise the draw process due to the increased glass volume. Therefore, it is always better to use a long length and a relatively small jacket tube/preform (<20 mm OD).

A tube of reasonable dimensions (OD:ID= 20:16 mm) is chosen as the holding jacket tube of the stack. This should accommodate 7 rings of capillaries with OD~1 mm. The tube is cleaned thoroughly in an ultrasonic bath with de-ionised water and ‘Microclean (Micro-90)’ solution for 30 minutes and finally washed with acetone to remove the grease, finger prints (not by me) and other contaminants.

3.4.2 Stacking techniques

The capillaries are arranged hexagonally inside the jacket tube as shown in Fig. 3.3, all the sealed ends are facing one direction. This is done by a repetitive capillary and rod substitution method. To help shape the hexagonal ring structure, and to fix the stack neatly to the jacket, additional rods of the same material and different sizes are inserted into the space between the inner wall of the jacket tube and the outer ring of the capillaries. By creating a scaled sketch of the structure using computing graphics software, the sizes of the packing rods can be estimated, to provide the best possible fit. A rod of the same size as the capillaries is used to form the core in the centre of the stack. The rods are drawn and prepared using a similar process to the capillaries. They are also useful for preventing any unexpected shrinkage or expansion of air holes, in the outer rings near the jacket tube, that may occur due to the thermal gradient.

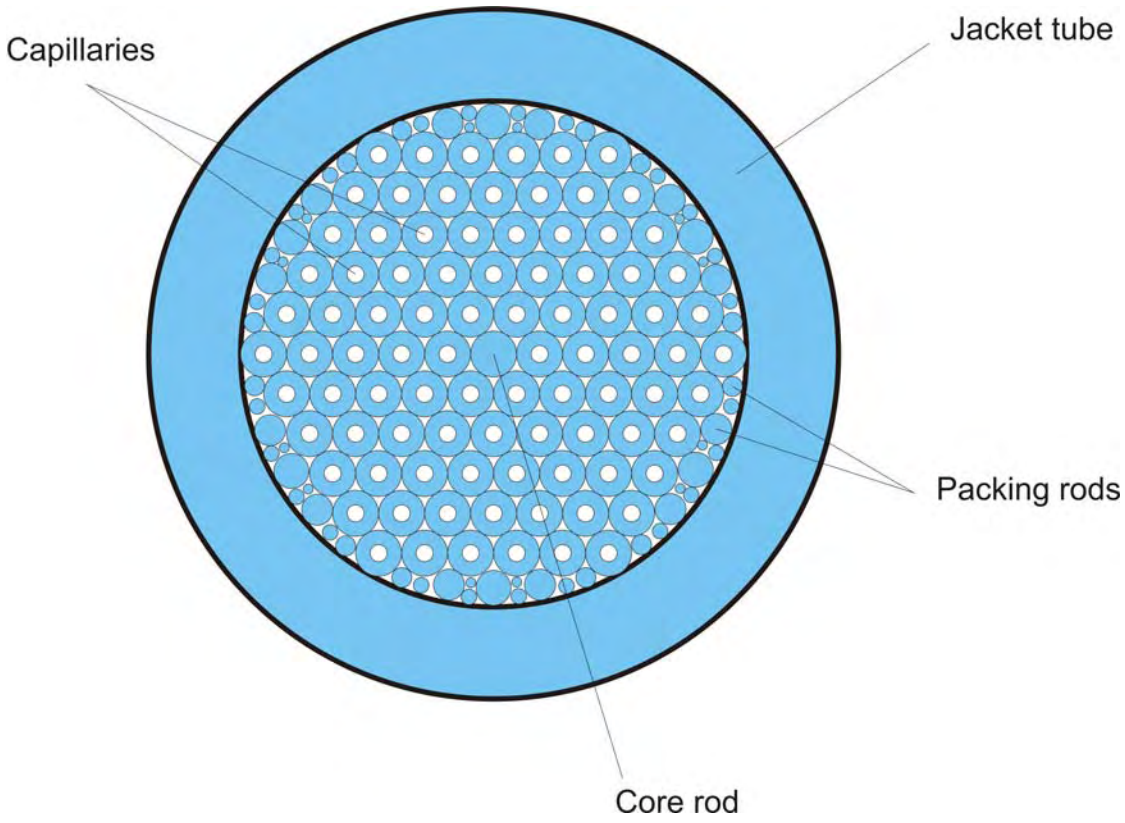

Fig. 3.3. End view of the structural arrangement of a 5-ring holey fibre preform stack.

Additional care, that should be taken during the preform assembly includes: minimising accidental scratches and breaks, and aligning the capillary bundle without any twists. The capillaries need to be held at the sealed end, each one is aligned in the same position so that there is no significant pressure difference between the capillaries during the draw.

3.4.3 Cleaning stacked preform

Once the capillaries are tightly stacked within the jacket tube, it is ready to be cleaned again with an oxygen gas purge at a temperature of ~1050 ^{0}C. This is done in a glass lathe by passing oxygen through the stack; the set up is shown in Fig. 3.4. Care needs to be taken when attaching the connection tubes either side of the preform. This is done either using the oxy-hydrogen burner or a more precise hand-held flame torch (Fig. 3.4(i)). During the heat-up stage for joining the tubes, the capillary bundle in the stack should not be heated or disturbed in any way.

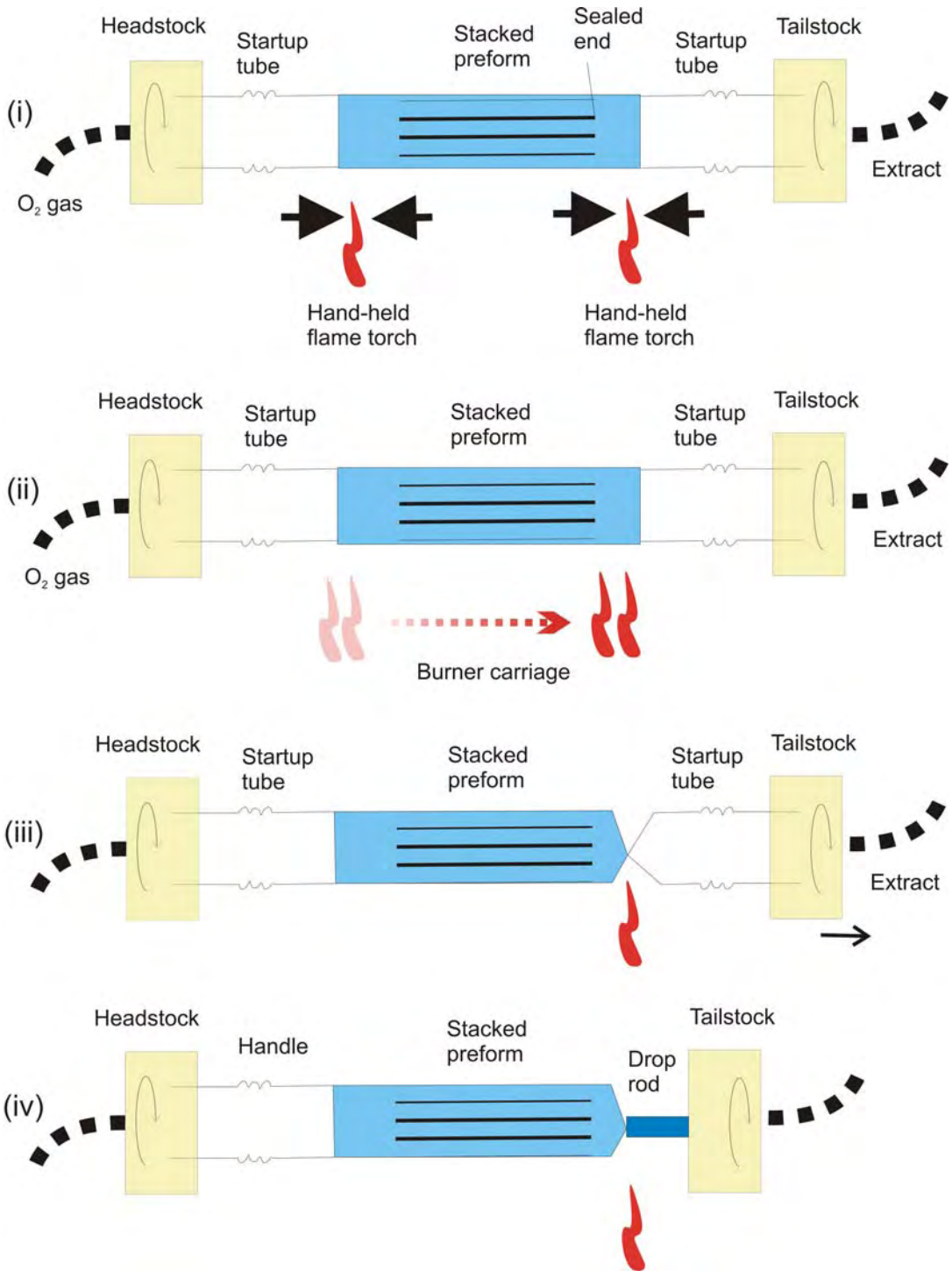

Fig. 3.4. Step-by step schematics to show the procedures to clean a stacked preform.

Typically a gas flow rate of 100 sccm (standard cubic cm per minute) is used, so that no great pressure is built up, and to prevent any loose capillaries from being pushed out of the stack. The rotation of the headstock and tailstock of the lathe is set to 30 per minute. The burner carriage is set to run automatically (100 mm/min) for 10 to 15 passes (Fig. 3.4(ii)). This process is necessary to remove any excess metal or organic residues and to dry the preform

thoroughly. If the fibre is required to have low water content, a dehydration step can be applied to the preform using chlorine during the oxygen treatment.

3.5 Drawing canes from stacked preform

Microstructured cane is drawn first from the preform, and is then pulled again by jacketing with another tube (see Section 3.6). This two-step approach is particularly effective for obtaining the small structures with $\Lambda < 2$ μm, the reason for which can be understood by considering the maximum draw ratio required to achieve the small scale structures.

Consider the smallest capillaries that can be practically stacked to have OD of ~0.5 mm, the volume reduction ratio η has to be ~10^{-7} to achieve Λ~1.5 μm, for instance. However, u_f must be fast enough to preserve the structure as discussed earlier. This requires an extremely fast draw speed (u_d>>100 m/min) for a single step draw, which is not possible due to the height restriction of the fibre draw tower used. The net volume reduction factor is the product of that of the two steps, $\eta_n = \eta_1 \eta_2$, where the subscript number corresponds to each step. As discussed, a smaller η exhibits a smaller collapse ratio, thus the structure is better preserved. Moreover, the collapse ratio is inversely proportional to the initial dimensions. Therefore, it is intuitive that η_2 should be as small as possible since the size of the structure in the second step is small. Therefore, canes with diameters of between 1 to 2 mm are usually drawn; the typical cane yield from a 250 mm long stacked preform is around 20 m, with each cane cut to a ~1 m long length during the draw.

It is good practice to draw the preform into canes once it is cleaned and dehydrated, to prevent additional stresses and contaminants being introduced. In other words, the oxygen treatment, which is done on a glass lathe, is applied on the same day as the caning process takes place. The preform is kept on the lathe with oxygen passing through it for as long as possible before it is moved to the drawing tower for caning, this will ensure that the preform is free from contaminants, and dried at all times. However, if it is kept on the lathe for too long, the stresses introduced by gravity and the clamping points of the end stocks of the lathe may cause damage to the fragile glass preform.

A drop rod is attached to the bottom of the preform; this is done on the lathe as shown in Fig. 3.4(iii) and (iv). The low grade start-up tube attached on the other end of the preform is kept, and acts as a handle, which is clamped by the chuck on the draw tower. The diameter of the handle tube should ideally be the same as that of the jacket tube, since it provides a smooth transition in diameter through the furnace, and it does not require any changes of the iris aperture during draw, thereby minimising the temperature instability.

The caning process is similar to the capillary production stage; sealed ends are at the top end of the preform. Here a moderate vacuum (~30 mbar) can be applied to the preform to eliminate interstitial holes. The strength of the vacuum should not be too great otherwise the holes in the lattice will be expanded. In addition, the preform is baked in the furnace at an intermediate temperature, just below 1700 ^{0}C for 15 minutes, before the drop/draw stage takes place. This allows the preform to experience a uniform heat distribution throughout, and release any stress that may have been introduced during any work done on the lathe. The baking process greatly improves the surface quality of the preform. The choice of temperature for this process is important, if the temperature is too high (~1750 ^{0}C), air can be trapped within the scratch, forming bubbles that are difficult to eliminate. If the temperature is too low (~1600 ^{0}C), no changes are made to the surface since the viscosity of the glass is too high.

It is possible that pressure can build up within the air holes during the baking stage, and so there is a possibility of blowing up the preform in the period when the temperature is increasing to the drop temperature. Therefore, a drop rod of reasonable weight should be used for a given preform dimensions to apply sufficient tension to counteract the increased internal pressure. Also, a vacuum may be applied to the inside of the preform to reduce the pressure. A picture of a typical cane with a 7-rings structure is shown in Fig. 3.5(a).

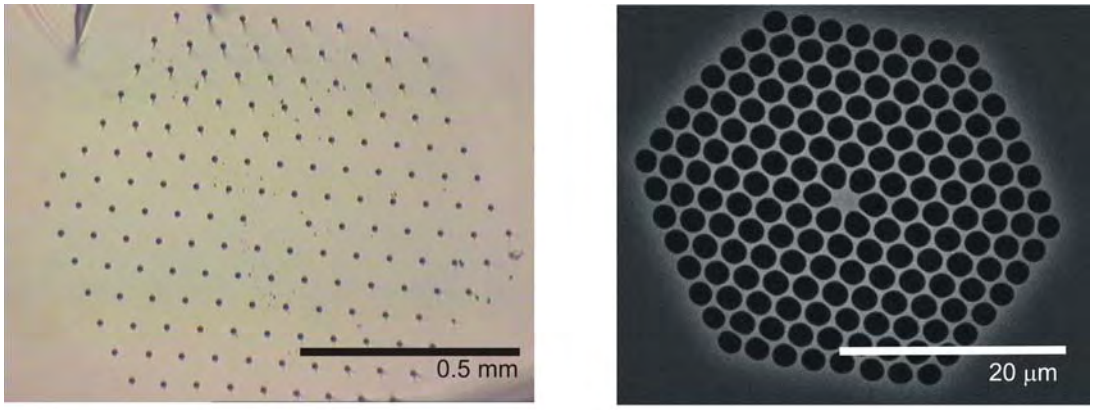

Fig. 3.5 (a) An image of a typical cane with a 7-rings structure taken under an optical microscope. (b) A SEM picture of a typical HNSC HF with 7 rings of holes.

3.6 Drawing fibre from canes

3.6.1 Jacket tube/preform preparation

In order to reduce the tension on the fibre during the second stage of the drawing process, a small preform/jacket (<10 mm) is used, so that it is more uniformly heated in the centre of the bore of the furnace. The use of a low speed draw is also important. By drawing small canes, it

is possible to set u_d at less than 10 m/min. At this speed, the fibre tension is low enough to allow low temperature (~180 to 200 ^{0}C below the drop temperature) fibre pulling.

Since the cane must be sealed to prevent the air holes within the cane structure from collapsing, care must be taken at the second draw step to achieve good structural control. The pitch within the cane structure can be used as a guide to determine the initial draw parameters by comparing it to the pitch required within the target fibre structure.

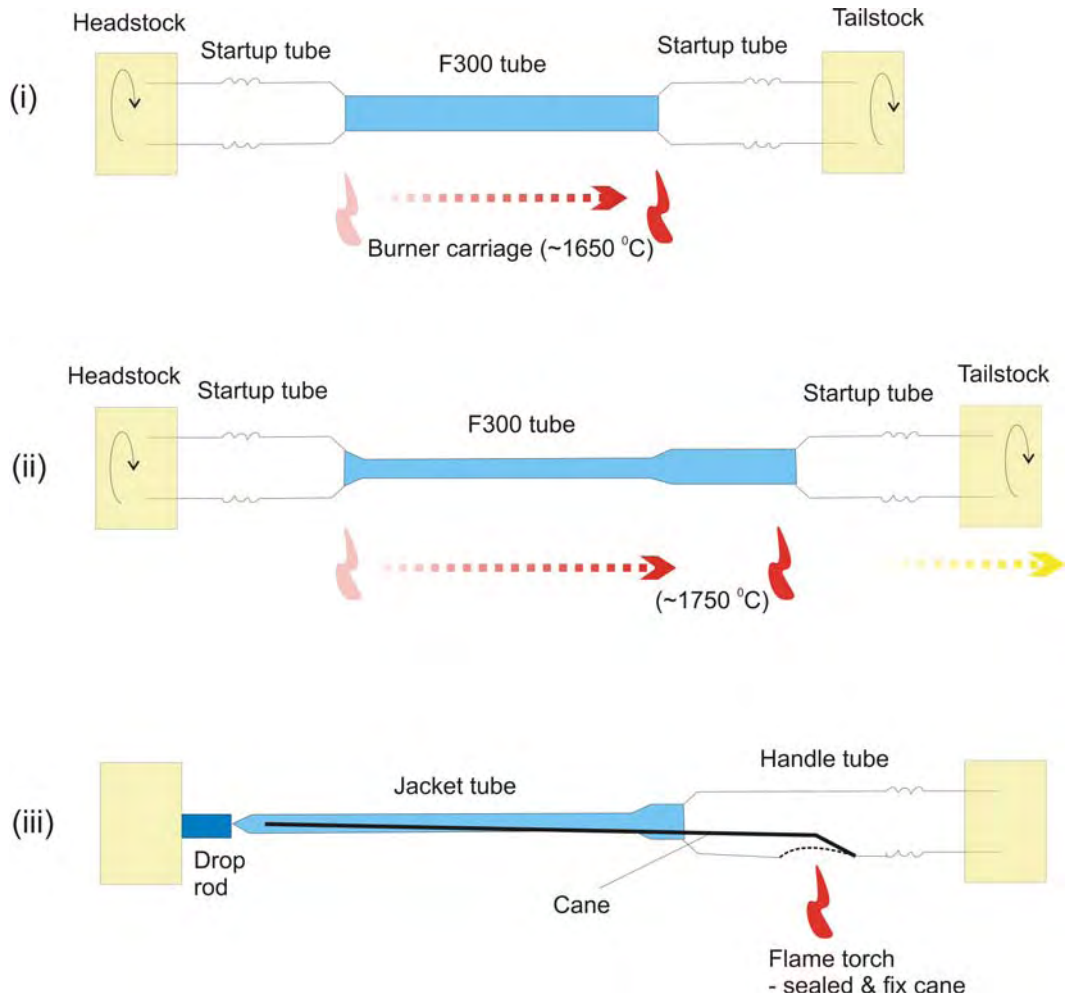

Fig. 3.6. Step-by step schematics to show the procedures to stretch a 12 mm OD 'F300' tube into a jacket tube, and inserting the cane.

A cane is selected, sealed and inserted into another jacket tube, and finally pulled to fibre. The jacket tube is often made from a 12:4 (OD:ID) mm 'F300' tube. It is cleaned in the same way as the stack holding tube. It is fire-polished (at ~1650 ^{0}C) (Fig. 3.6(i)) and then stretched on a glass lathe to a 8.5:2.8 (OD:ID) mm tube (Fig. 3.6(ii)). The stretch speed is calculated using the following volume conversion equation.

$$\left(\frac{Diameter.After(D)}{Diameter.Before(d)}\right)^2 = 1 - \frac{Tailstock.Speed(V_T)}{Carriage.Speed(V_B)} \qquad \text{Eqn. 3.6.1}$$

The temperature used for the stretch is typically between 1700 and 1800 ^{0}C, to preserve the tube ID/OD ratio, and the carriage transverse speed is chosen to be 100 mm/min. Since the tailstock speed is limited to 20 mm/min, the tube needs to be stretch over 2-3 passes before the required diameter is reached.

A low graded glass 'start-up' tube is left attached to the jacket tube, where the preform is held by the feed chuck onto the draw tower. The selected cane is inserted and fix to the handle tube as shown in Fig. 3.6(iii). Note that the inner diameter of the jacket tube does not need to be an exact fit to the cane, for reasons described below.

The collapse ratio of the jacket is nearly zero at a low temperature. Thus, the cane must be tightly fitted within the jacket. Otherwise, the sealed cane can expand during drawing while preserving the glass volume according to Eqn. 3.1.1. However, because of the small cane size (~1 mm OD), it is difficult to prepare a jacket tube so that it perfectly fits the cane. To overcome this problem, the fibre is pulled by using a relatively loose jacket, and applying vacuum (~200 to 500 mbar) to the inside of the preform to intentionally collapse the jacket to allow it to fit onto the cane. Therefore, the expansion of the cane structure is determined by the vacuum and temperature, for a given thickness of the jacket, at a given draw speed. The balance between these factors controls the final Λ and d/Λ in the fibre.

3.6.2 Fibre drawing techniques

Although the jacket can be made to fit the cane well by applying vacuum, the cane structure is still expanded, depending on the jacket thickness, particularly when the vacuum is too high. The reason may be due to the fact that the cane starts expanding before the jacket shrinks because of the low pressure. Thus, there is an optimum pressure, where the jacket is sufficiently collapsed while suppressing the expansion of the cane. The draw-speed controls the final diameter or the pitch of the fibre. All the other control variables, including feed speed, need to be optimised in real time during the pulling process, in order to achieve fibres with structure that is comparable to the idealised design. For a new fibre design, it may require a sequence of 'blind' pulls to iterate to the desired structure. This may involve a few fibre draws from the same preform to study how the fibre reacts to the changes of draw parameters.

High-index coatings are usually applied to the fibre, for added strength to the fibre, and help to eliminate cladding modes. Care needs to be taken when adding coating resin into the coating cup. It should be done before the lowering of furnace temperature from the drop temperature (~2040 ^{0}C), as the fibre is pulled under very high tension. Also, if the bare fibre is scratched slightly against the metal coating cup, then breakage of the fibre either around the coating cup or on the drum is likely to occur before the resin is added.

Typical draw speeds are between 5 to 8 m/min, which is slow compared to a conventional fibre draw. The initial feed speed is estimated accordingly using Eqn. 3.1.1, for example, fibres

with a diameter of 125 μm, drawn from a 8.5mm preform, required a feed speed of ~1.5 mm/min, thus for a 300 mm long preform, the fibre draw period can take over three hours. Note that fibre drawing on a 5m tower can be done up to 60 m/min, but is limited by the cure rate of the acrylete coating. A SEM picture of a typical highly nonlinear small core holey fibre with 7 rings of holes is shown in Fig. 3.5(b).

3.7 Conclusions

General guidelines for the preform preparation, caning, and fibre drawing have been presented. A simple capillary drawing model is used to determine the initial draw parameters, and can be practically tuned thereafter. Based on observations, the dynamics of the two-stage fibre drawing process were discussed. The challenges of the fabrication of small core silica holey fibres are pointed out, and they have been tackled by optimising the draw parameters to reduce the fibre tension and by improving the quality of the jacket tube and capillaries.

Special fibres such as fibres with graded hole sizes in the structure or fibres with varying hole size along the fibre, required additional fabrication steps that are tailored to the designs. Investigation into the new challenges and limitations of the fabrication of these fibres are presented in Chapter 4, 5 and 6.

Chapter 4

Dispersion-flattened holey fibres

4.1 Introduction

The use of low-loss glass fibre for communication was first proposed in 1966 [Kao]. At the time, the best such fibres had losses of 1000 dB/km. With the advent of vapour deposition proceses of silica glass in the 1970s [Kapron, 1970, MacChesney, 1974], fibres with loss of 0.2 dB/km was achieved. The initial fibres produced were multimode guides having a core diameter of 62.5 μm to facilitate splicing and light launched from low-cost light-emitting diodes. However, single-mode fibre having a small core diameter (less than ~10 μm) became dominant because of its higher bandwidth and the development of splicing and connector technology. Single-mode fibre designs remained relatively unchanged throughout the 1980s as optical networks were installed around the world. These networks used commercially available lasers operating at 1.3 μm, the zero-dispersion point of this standard fibre. As 1.55 μm laser, corresponding to the lowest loss region of silica fibre, became available, new dispersion-shifted fibre, simultaneously offering both zero dispersion and low loss at 1.55 μm, was developed.

Since the invention of erbium-doped fibre amplifiers (EDFA) in 1987 [Mears, 1987], new fibre designs emerged to accommodate the broad range of wavelengths required for dense wavelength-division multiplexing (WDM) transmission systems, and dispersion-compensating fibre was developed to minimize the deleterious effects of dispersion. Optical fibres designed for use in high-bit-rate transmission require low attenuation loss, small dispersion (D), a low dispersion slope (D_s) and low nonlinearity (γ), these must be accomplished across the entire wide spectrum for WDM systems. [Glass, 2000]. Therefore, fibres with large effective areas and dispersion-flattened profiles have been studied intensively in the past. Dispersion below 2 ps/nm/km over the 1.3 μm - 1.6 μm wavelength range has been achieved with W fibre or quadruple clad fibre [Lundin, 1994, Cohen, 1982]. Multi-clad fibre design can offer dispersion of ±0.95 ps/nm/km with three zero-dispersion wavelengths over the same wavelength range, with an effective area of ~60 μm^2 [Lu, 1989]. More recent fibres such as Belllab's TrueWave-RS (Reduced Slope) and Corning's LEAF were specifically designed for use with both single and multiple-channel high speed dense wavelength division multiplexing (DWDM) systems

operating in the C and L Bands, ideal for high-data-rate, long-haul and terrestrial networks. Here, low dispersion is not desirable in the DWDM systems due to the effect of FWM, hence, dispersion of around 8 ps/nm/km at the operating wavelengths is targeted as a compromise.

However, low dispersion in highly nonlinear fibres is desirable for utilising four-wave mixing, and in low walk off Kerr devices, as well as continuum generation. Fibres with nonlinear coefficients as high as ~10 $W^{-1}km^{-1}$ and nearly flat dispersion slopes (0.0002 $ps/nm^2/km$) at the telecommunication window have been fabricated conventionally [Okuno, 2003].

Early work in small core holey fibre design has been focused on achieving high nonlinearity (γ) with little attention of controlling the dispersion slope. The next generation of nonlinear holey fibres presented in this chapter have improved dispersion properties. Dispersion profiles of holey fibres have been modelled extensively by many authors [Mogilevtsev, 1998, Monro, 1999, Sinha, 2003]. Significant interest was focused on designing ultra-flattened zero dispersion fibres in a wide wavelength range (~500 nm) in the C-Band with low loss. Triangular lattice cladding structure designs with 8 to 11 rings of constant diameter air holes have been proposed, and experimentally realised, either in silica [Reeves, 2002] or with a germanium doped core [Hansen, 2003]. The fabrication of these fibres was labour intensive, as a large number of air holes, with near ideal dimensions, is required in order to achieve the desired dispersion profile and low confinement losses.

Since 2003, it was clear that improved dispersion control was possible with complex multi-hole size/ pitch varying structures [Saitoh, 2003]. Five-ring designs with graded hole-size have been proposed with a flattened dispersion of 0 ± 0.4 ps/nm/km in a wavelength range between 1.23 and 1.72 μm, and 0 ± 0.1 ps/nm/km in a range between 1.5 and 1.6 μm, in both cases having the A_{eff}~ 8.5 μm^2 at 1.55 μm [Poletti, 2005]. Similar performances can be achieved in the wavelength range between 1.3 and 1.9 μm by selectively filling the holes with index-matching liquids, thus effectively reducing the hole size [Gundu, 2006]. Note that, holey fibre designs offer comparable nonlinearity and a dispersion-flattened wavelength range in the telecommunication windows when compared to the conventional designs, but holey fibre are superior in the wavelength range outside of the telecommunication bandwidth. However, at present, holey fibre technology suffers higher splice loss and attenuation.

This chapter presents a study of the fabrication of the graded hole-size fibres with the aim to reach the design target set by the authors in the literature mentioned above. The process limitations in the fabrication of these fibres are identified, and the performance of the fabricated fibres is presented. In Section 4.2, the chosen target design and the corresponding dispersion profile are presented. The fabrication methods and results are shown in Section 4.3. The characterisation results, such as dispersion measurements of the fabricated fibres, are

presented in Section 4.4. The structural tolerance analysis of the target fibre is given in Section 4.5. The conclusions are in Section 4.6.

4.2 Target design

A novel design has been chosen in which it is possible to have a five-ring HF structure with a flattened dispersion [Saitoh, 2003]. In this design, the size of air-holes is different for each ring of holes; increasing in size radially outward from the centre of the fibre, as shown in Fig. 4.1. The unusual graded hole-size structure was modelled by a manual trial which followed a tested design method. The design is such that, in the short wavelength limit, the guided mode is well confined into the core region and the dispersion property is affected by the inner air-hole rings while, in the long wavelength limit, the effective core area is increased and the dispersion property is affected by both the inner and outer rings. Moreover, the very large air holes in the outer rings are beneficial for not only dispersion control but also for reducing the confinement loss, thus allowing designs with only a small number of rings. The target dispersion profile from this design is extracted from the literature and shown in Fig. 4.1(b).

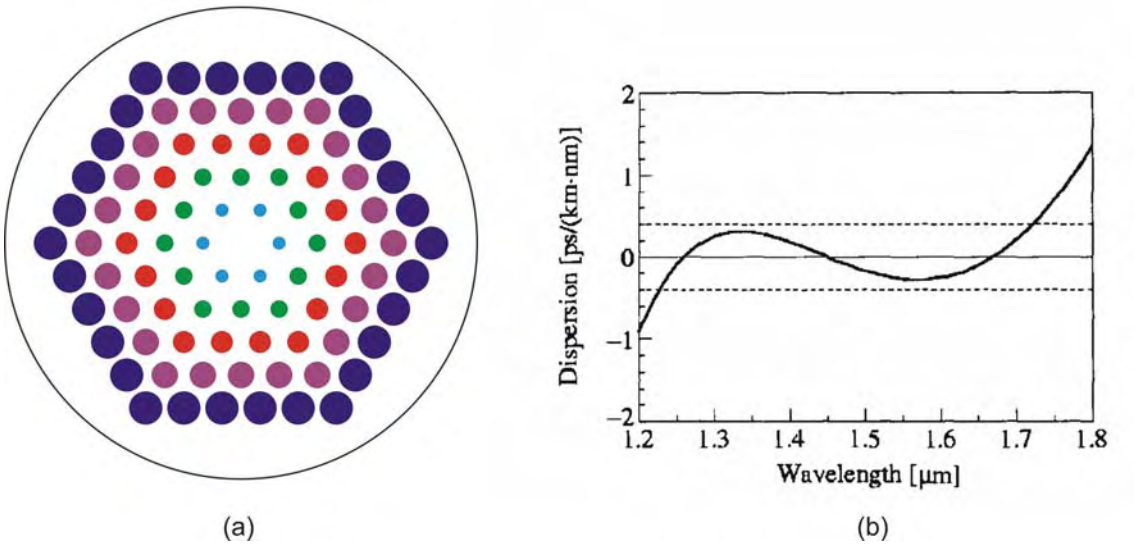

Fig. 4.1. (a) Five-rings, dispersion-flattened HFs design with pitch Λ=1.58 μm and air-filling ratio d/Λ= 0.31, 0.45, 0.55, 0.63 and 0.95. (b) The predicted dispersion profile after reference [Saitoh, 2003].

4.3 Fabrication of graded-hole-size fibres

4.3.1 Iteration one

The aim of this project was to fabricate the fibre with the complex structural design shown in Fig. 4.1. As a first attempt to fabricate a five-ring structure holey fibre with five different hole sizes, the initial capillary dimensions were chosen based on the experience collected in the past for regular pitch and hole size structures.

The fabrication procedures for this fibre were similar to the ones described in Chapter 3. The preform was stacked using silica capillaries with the same outer diameter (1.45 mm), and different inner diameters for each ring. The initial capillary dimensions were as follows: the first innermost ring d_1/D_1= 0.31, second ring d_2/D_2= 0.41, third ring d_3/D_3= 0.5, fourth ring d_4/D_4= 0.58 and fifth ring d_5/D_5= 0.69. In general, if the outer diameter of the capillaries is constant; the expansion of holes is greater for a larger initial inner diameter, where the volume-to-surface area ratio is larger. Therefore, for the first ring, d_1/D_1 was chosen to be the same as the d_1/Λ_1 from the target fibre design, and the chosen starting (d/Λ)s in rings 2 to 5 were slightly smaller than the required ones in the target design; this allows the expansion of holes to the target value during the fibre draw. According to Eqn. 3.3.2, the larger holes would expand more; therefore, capillaries in the outer rings had relatively smaller d/Λ compared to that in the design than the capillaries in the inner rings. From this preform, a number of fibres were drawn using slightly different draw parameters. The behaviour of the preform and the structural variation during the fibre draw under the different conditions were observed.

The first step was to draw the stacked preform into canes. The d/Λ ratios in the cane were almost preserved, the outer ring suffered slightly greater shrinkage. The pitch size in the cane structure was ~88 μm, and the air-filling fractions for the five rings were measured as d_1/D_1= 0.32, d_2/D_2= 0.42, d_3/D_3= 0.52, d_4/D_4= 0.57 and d_5/D_5= 0.63. To measure the pitch and hole sizes, I simply took a picture of the image under an optical microscope (Fig. 4.2), and used a ruler, together with the given scales from the microscope, to work out the feature sizes. This was not the most accurate method to measure the absolute feature sizes but, since this was a study of the effect of the fibre draw on the relative hole size variation, it was the simplest method. The same method was used for measuring the feature sizes in the fibres from SEM micrographs. A more accurate method is presented in Chapter 5, for fibres with regular hole size.

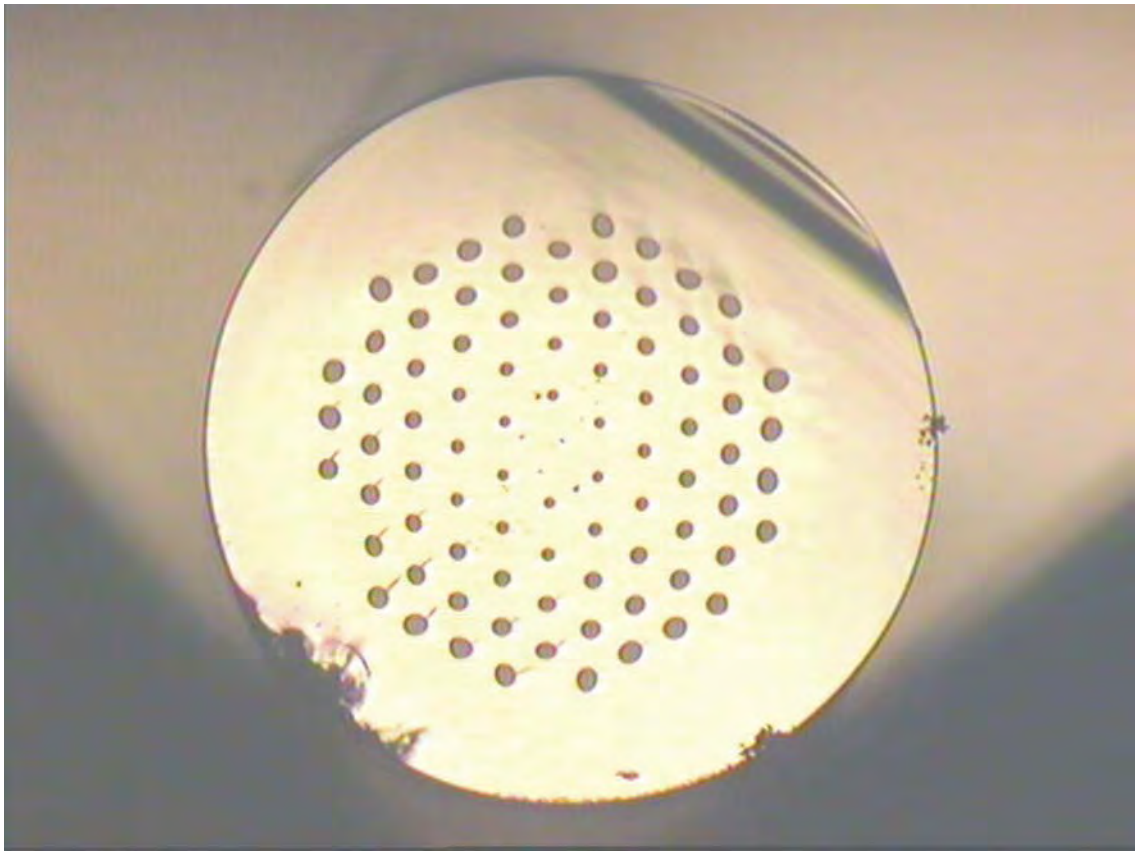

Fig. 4.2. A structural image of the cane under an optical microscope in the transmission state.

The SEM micrographs of the microstructure region of the fibres pulled from the above preform are shown in Fig. 4.3. The draw parameters and the values of (d/Λ)s of the fibres are summarised in Table 4.1. The feed speed was determined according to the jacket tube diameter, larger preform produced higher yield, but required lower feed speed and higher draw temperature (lower vacuum). The resulting fibres show that the inner holes expand more than the ones in the outer rings; on average d_1/Λ_1 increases by 74%, d_2/Λ_2 increases by 51%, d_3/Λ_3 increases by 46%, d_4/Λ_4 increases by 41% and d_5/Λ_5 increases by 29% with respect to the initial capillary stack. Thus, the capillary dimensions for the next iteration to optimise the design could be adjusted accordingly. The comparison of the average hole and pitch sizes for these fibres with the target design are presented graphically in Fig. 4.4.

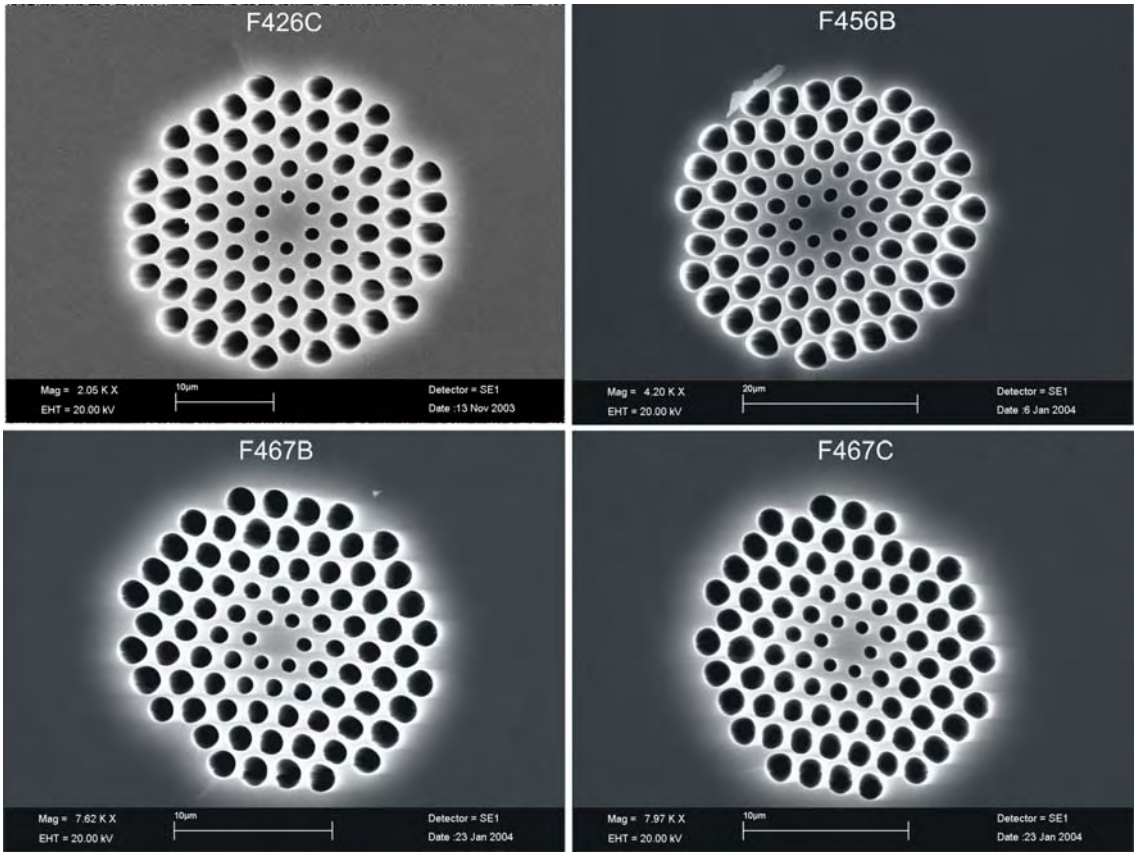

Fig. 4.3. First iteration SEM micrographs of graded hole size HFs labelled 'F426C', 'F456B', 'F467B' and 'F467C' in chronological order.

Fibre	Draw Temp. (^{0}C below drop temp.)	Feed Speed (mm/min)	Vacuum (mbar)	d/Λ
F426C	**160**	**6**	**500**	**0.4, 0.6, 0.7, 0.8, 0.9**
F456B	**160**	**6**	**500**	**0.5, 0.6, 0.8, 0.8, 0.91**
F467B	**140**	**3**	**120**	**0.54, 0.69, 0.78, 0.86, 0.9**
F467C	**140**	**3**	**120**	**0.54, 0.62, 0.73, 0.77, 0.86**
Target design				**0.31, 0.45, 0.55, 0.63, 0.95**

Table 4.1. Summary of the air-filling fractions (d/Λ)s for different graded hole size fibres.

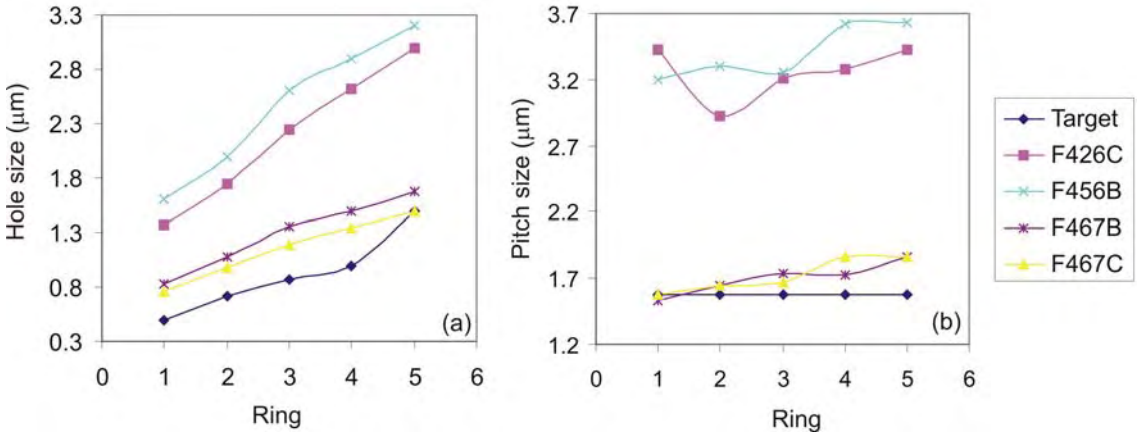

Fig. 4.4. (a) Average hole sizes and (b) average pitch sizes for each ring in the fibres.

4.3.2 Iteration two

The results from the first iteration showed that smaller holes expand more, which is opposite to the previous prediction, a possible explanation is given in Section 4.6. Therefore, holes in the first ring expand more than the holes in the second ring, which expand more than the holes in the third ring etc. The capillary dimensions for this iteration were chosen based on the average percentage expansion of holes in each ring, found in Section 4.3.1. For example, in ring 1, the average d_1/Λ_1 expansion was 74%, assuming the d/Λ value for the next fibre in ring 1 would also expand by the same amount. In order to achieve the target $d_1/\Lambda_1 = 0.31$, then the initial capillaries for ring 1 should now be $\frac{d_1}{D_1} = \frac{0.31}{(1+0.74)} = 0.18$. Similar calculations were carried out for rings 2 to 5. For the second iteration, the initial capillary dimensions were as follows: the first innermost ring $d_1/D_1 = 0.18$, second ring $d_2/D_2 = 0.30$, third ring $d_3/D_3 = 0.38$, fourth ring $d_4/D_4 = 0.45$ and fifth ring $d_5/D_5 = 0.73$. Thus, if the percentage expansion of holes in each ring is the same as before, the final fibre would yield the target design.

Two separate canes were drawn to fibres, the pitch size in the cane structure for fibre 'F573' was ~88 µm, and air-filling fractions for the five rings were measured as $d_1/D_1 = 0.16$, $d_2/D_2 = 0.28$, $d_3/D_3 = 0.34$, $d_4/D_4 = 0.41$ and $d_5/D_5 = 0.58$. And for fibre 'F585', $d_1/D_1 = 0.13$, $d_2/D_2 = 0.24$, $d_3/D_3 = 0.30$, $d_4/D_4 = 0.35$ and $d_5/D_5 = 0.58$.

The SEM micrographs of the microstructure region of the fibres pulled from the preform are shown in Fig. 4.5. The draw parameters and the values for d/Λ of the fibres are summarised in Table 4.2. Here, it was found that the expansion of d/Λ in each ring was not the same as the ones observed in the first iteration, further investigation is carried out in the next section. The comparison of the average hole and pitch sizes for these fibres with the target design are presented graphically in Fig. 4.6; although this shows an improvement towards achieving the target design, it was still far from ideal.

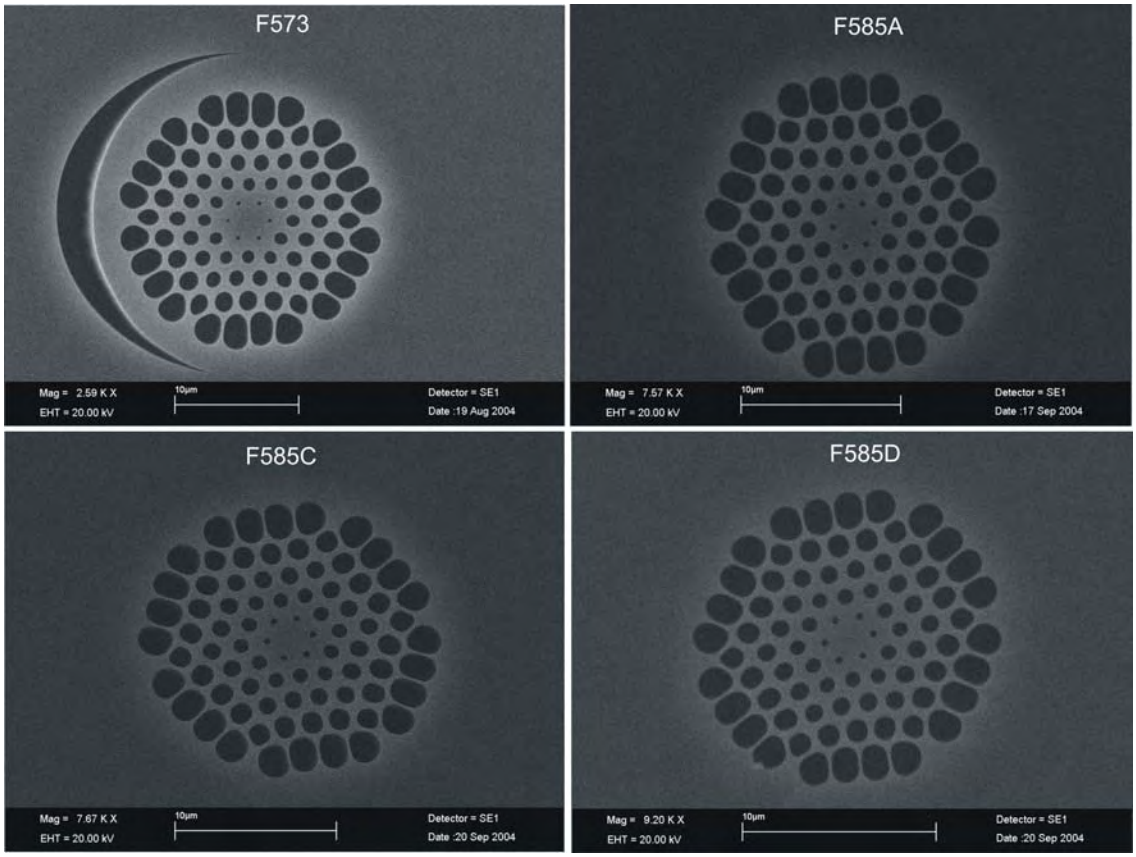

Fig. 4.5. Second iteration SEM micrographs of graded hole size HFs

Fibre	Draw Temp. (^{0}C below drop temp.)	Feed Speed (mm/min)	Vacuum (mbar)	d/Λ
F573	**50**	**2**	**300**	**0.17, 0.56, 0.62, 0.73, 0.9**
F585A	**60**	**2**	**340**	**0.29, 0.63, 0.66, 0.78, 0.93**
F585C	**70**	**2**	**340**	**0.29, 0.61, 0.66, 0.78, 0.9**
F585D	**80**	**2**	**340**	**0.27, 0.56, 0.63, 0.73, 0.88**
Target design				**0.31, 0.45, 0.55, 0.63, 0.95**

Table 4.2. Summary of the air-filling fractions (d/Λ)s for fibres ‘F573’ and ‘F585’

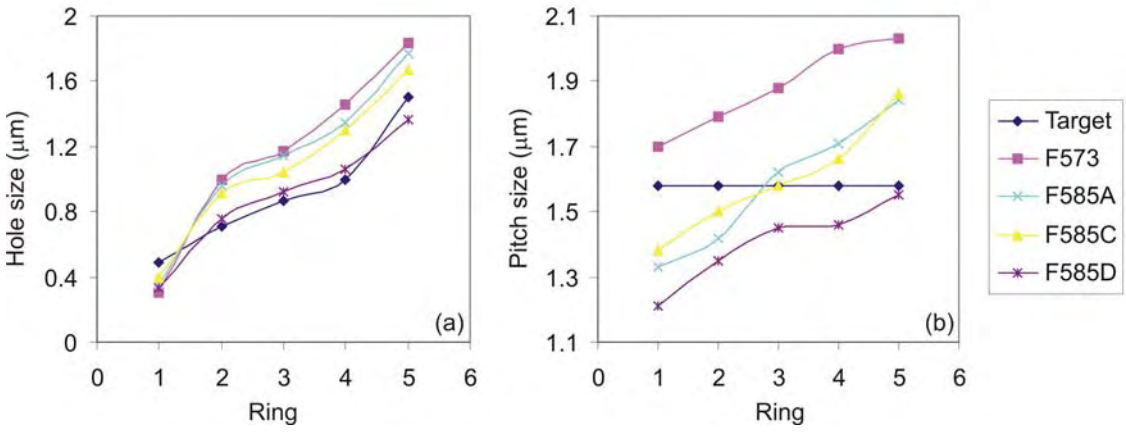

Fig. 4.6. (a) Average hole size and (b) average pitch size for each ring in fibres ‘F573’ and ‘F585’.

4.3.3 Fibre analysis

The fibre SEMs show that the microstructured region, or indeed the fibre itself, was slightly elliptical (see Fig. 4.7); this was mainly due to the fibre drawing techniques employed. In this method, the cane was not held in the centre of the jacket tube (see Fig. 3.5(iii)) during the final fibre pulling stage. A strong vacuum was required to get rid of the spacing between the cane and jacket, thus the cane itself was expanded near the hot zone of the furnace just above the neck-down region. If the cane is not kept in the centre of the jacket tube, the cane experiences asymmetric heating during the draw, thus the cane is stretched more on one axis. This caused distortion in the fibre structure, especially variation in the hole-sizes. This effect was captured in the SEM for fibre ‘F573’; the corresponding picture in Fig. 4.5 shows that one side of the cane merges with the jacket tube before the other side, thus showing the initial cause of the elliptical distortion.

In order to have a better understanding of whether it is during the caning stage or the fibre drawing stage, or both, when the distortions appeared, I also investigated the structural information of the canes. Fig. 4.8 shows an optical microscope picture of the cane structure, the scaled arrangement of the capillary stack that the cane was collapsed from, and an overlay of the two. The holes in the outer-most ring appeared to be less circular; this is due to the irregular spacing in the packing rods region of the stack. However, other parts of the structure appeared well matched to the stacking arrangement. The first 4 rings of hole and pitch size measurements for the cane of fibre ‘F467B’ are summarised in Table 4.3. It is shown that the collapsing process of the cane from the capillary stack was done in a well behaved and controllable manner; all the holes were collapsed by the same ratio, this is also true for the pitch sizes, thus d/Λ is essentially preserved.

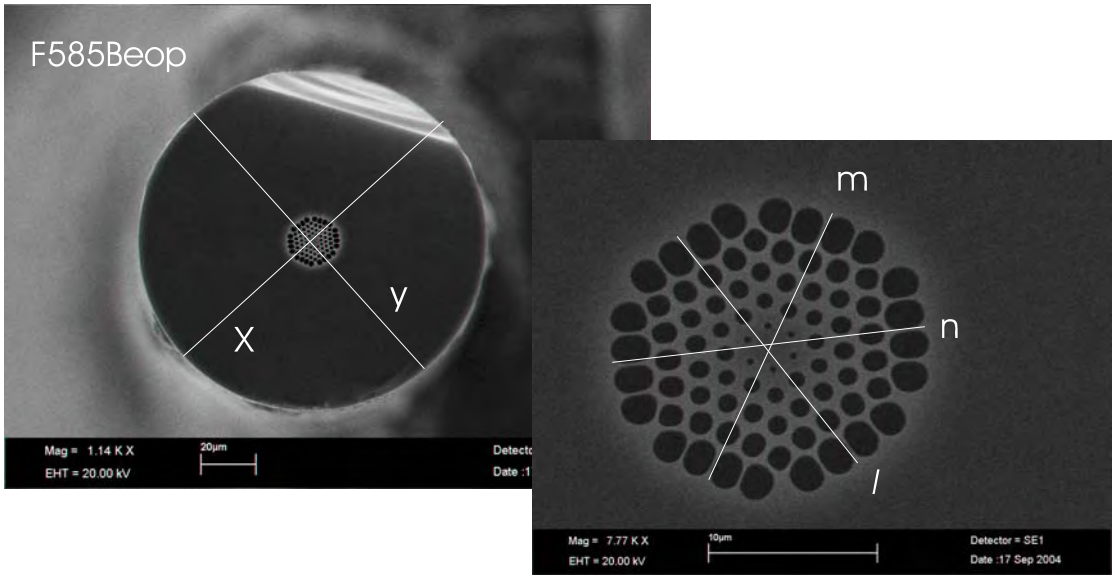

Fig. 4.7. SEM micrograph of fibre 'F585B', indicates an elliptical fibre. x= 127.4µm, y= 124.6µm; ratio (1.02 : 1). m= 17.3 µm, n= 18.6 µm and *l*= 17.4 µm; ratio (1 : 1.08 : 1.01)

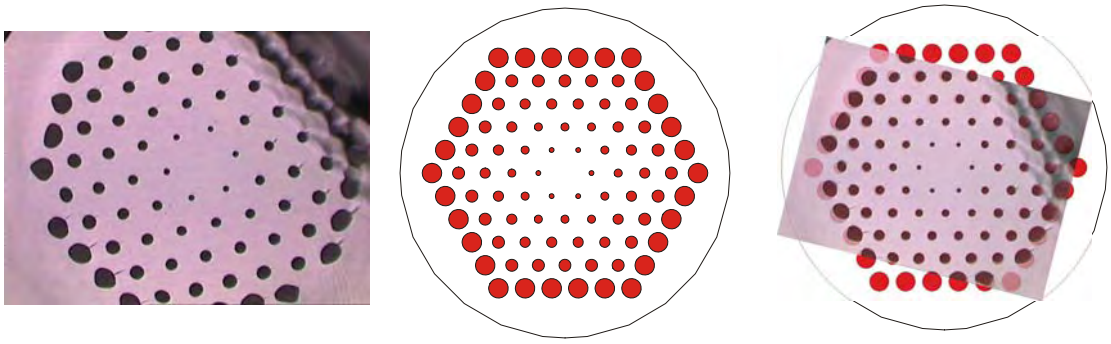

(a) (b) (c)

Fig. 4.8. (a) Optical microscope image of the cane from the second iteration. (b) Scale drawing of the capillary stack from the second iteration. (c) Overlay of (a) and (b)

The major cause of structural distortion arises during the final fibre pulling from the cane and jacket. In Fig. 4.4(a) and 4.6(a), the graphs of the different fibres were shown to vary in a similar way in each case, suggesting that the holes from each ring were reduced by a similar ratio during caning and fibre pulling. It is not the case for the pitch sizes, the shape of the graphs in Fig 4.4(b) and 4.6(b) are quite different in each case. This was identified as the major problem when fabricating fibres with different sizes of holes; and a considerable amount of pitch variation was found.

	Capillary stack		Cane		Fibre 'F467B'				
Ring	Hole size (μm)	Pitch size (μm)	Hole size (μm)	Pitch size (μm)	Hole size (μm)	Pitch size (μm)	Ratio of cane/stack hole size	Ratio of cane/stack pitch size	Ratio of fibre/cane hole size
1	450	1450	26	86.5	0.83	1.53	0.06	0.06	0.03
2	600	1450	35	86.5	1.08	1.65	0.06	0.06	0.03
3	730	1450	42	86.5	1.36	1.74	0.06	0.06	0.03
4	820	1450	47	86.5	1.49	1.73	0.06	0.06	0.03

Table 4.3. Hole and pitch sizes for the stack, cane and fibre 'F467B'

Another interesting observation is that lower drawing temperatures offered a slightly lower pitch variation. Fibres 'F585A, C and D' were drawn at slightly different temperatures during the same pull, where 'D' was drawn at 20^0C below that of 'A'. From Figure 4.6(b), a slightly different gradient can be seen between the two.

Although, the target design was not achieved, it is interesting nevertheless to study the performance of these fibres in terms of dispersion, loss, birefringence and nonlinearity. In the next section, the results of the characterisation of some of these fibres are presented.

To conclude this section, it was clear that from the initial fabrication trials, the radial distortion (in Λ and d/Λ) arises during fibre draw was very problematic, and the ellipticity of the fibres added further complications. Further investigation of structural distortion is presented in Section 4.6, using fibres made by various fabrication techniques.

4.4 Characterisation of graded-hole-size fibres

4.4.1 Chromatic dispersion measurement

Chromatic dispersion measurements were carried out in the 1.55 μm narrow-band region using a tunable external-cavity laser [Horiuchi, 1989] (many thanks to Dr. M. Roelens and Dr. F. Parmigiani for assistance). Both ends of the fibres were spliced to an intermediate Ge-doped, high NA conventional fibre, single mode at 1.55 μm, which were then spliced to standard patch cables. A splice loss of around 1 dB between the HF and the high NA single mode fibre was achieved by using the 'repeated arc discharges' technique, which is comparable to the result reported in [Xiao, 2007].

The group delays were measured, and the data was fitted with a quadratic curve; the dispersion profile was then calculated from the fitted curve. An example of this is shown in Fig. 4.9 and the dispersion profiles found for the other fibres are shown in Figure 4.10.

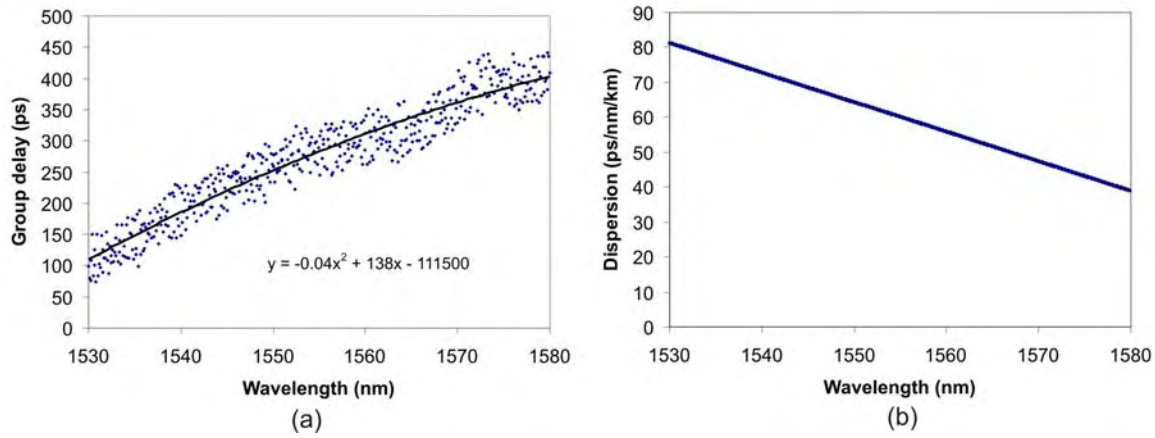

Fig. 4.9. (a) Group delay + fitted curve (b) Chromatic dispersion profile of fibre 'F467C'.

Fibre 'F585C' was the best fibre fabricated so far; the d/Λ of the first ring is ~6% too low compared to the target design, and the pitch size was engineered correctly at the third ring. Indeed this fibre has shown the lowest dispersion. The measured dispersion at 1550 nm was ~10 ps/nm/km, which does not agree with the predicted value of 19 ps/nm/km, calculated by F. Poletti for an idealised structure with the average measured fibre structure parameters, this may also be due to the distortion of the structure itself. For a more reliable dispersion measurement, other techniques should be used, for example, by low-coherence interferometry [Tateda, 1981].

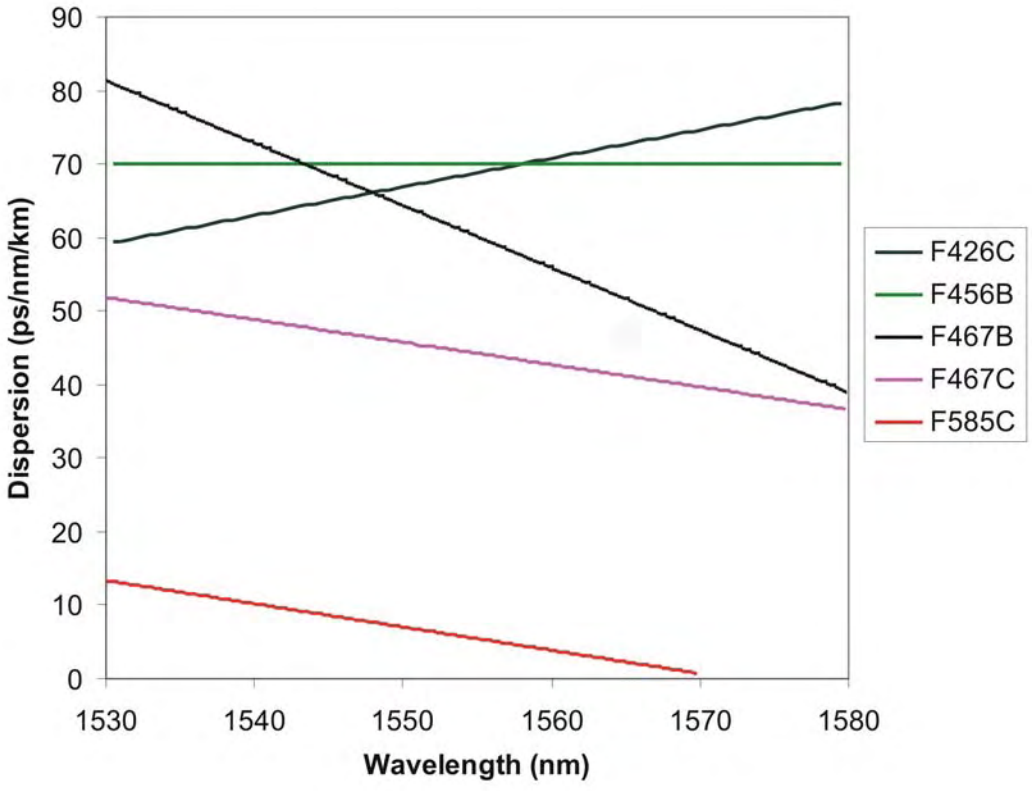

Fig. 4.10. Measured dispersion profiles for 'F426C', 'F456B', 'F467B', 'F467C' and 'F585C'.

4.4.2 Fibre loss measurement

A white light cut-back loss measurement was carried out for 'F467B'. The light was coupled into the fibre with a high NA lens. An estimated loss value of ~45 dB/km at 1.55μm was found; which is acceptable for short fibre length applications. 'F426B' and 'F456A' had losses of ~31 dB/km and ~41 dB/km at 1.55 μm, respectively. Fig. 4.11 shows a typical white light attenuation spectrum measured for these fibres.

The cut-back loss measurements for 'F585B' and F585C' were carried out by splicing to a single wavelength source at 1557nm, and a loss of ~67 dB/km was found. These results confirmed that there was an increase in confinement loss as the pitch decreases.

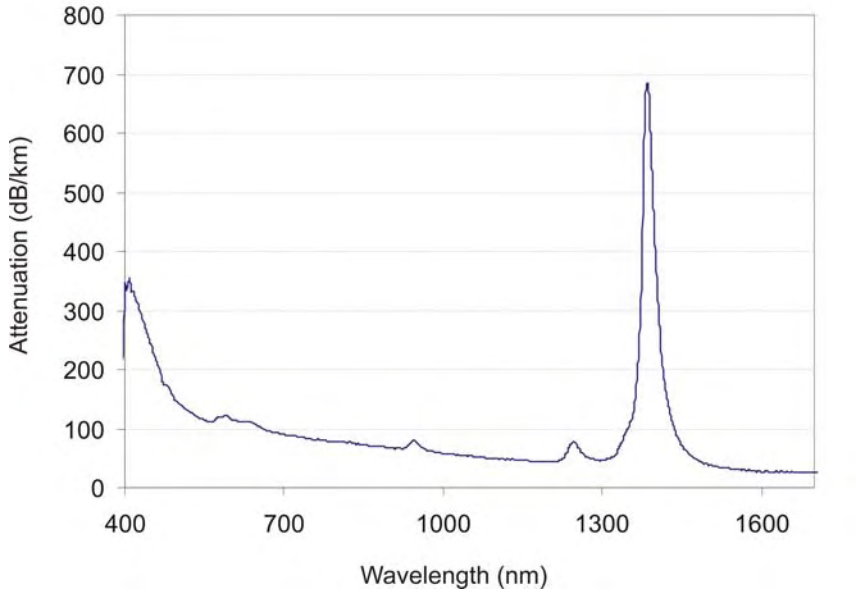

Fig. 4.11. The attenuation spectrum for fibre 'F426B'

4.4.3 Birefringence measurement

A birefringence measurement was carried out for fibres 'F426C' and 'F585C' (jointly measured by S. Asimakis). An indirect method was used, instead of observing the beat length directly from the side of the fibre [Dyott, 1995] or using an elasto-optic method [Dyott, 1995, Takada, 1985].

Light from a tunable laser, polarised at 45^0 to the principal axes, was launched into 27 mm of fibre 'F426C' and 100 mm of 'F585C' and the output polarisation state, as a function of wavelength was monitored, a polarizer was placed at the output end with its transmission axis aligned at 45^0 to the axes of the fibre and the wavelength was scanned in small increments [Ortigosa-Blanch, 2000]. The result from the scans is shown in Fig. 4.12; the polarisation beating period can be seen. The corresponding beat length was calculated to be ~7.5 mm for

'F426C' and ~6 mm for 'F585C', which is unexpectedly long since the core of the fibres appears to be quite elliptical.

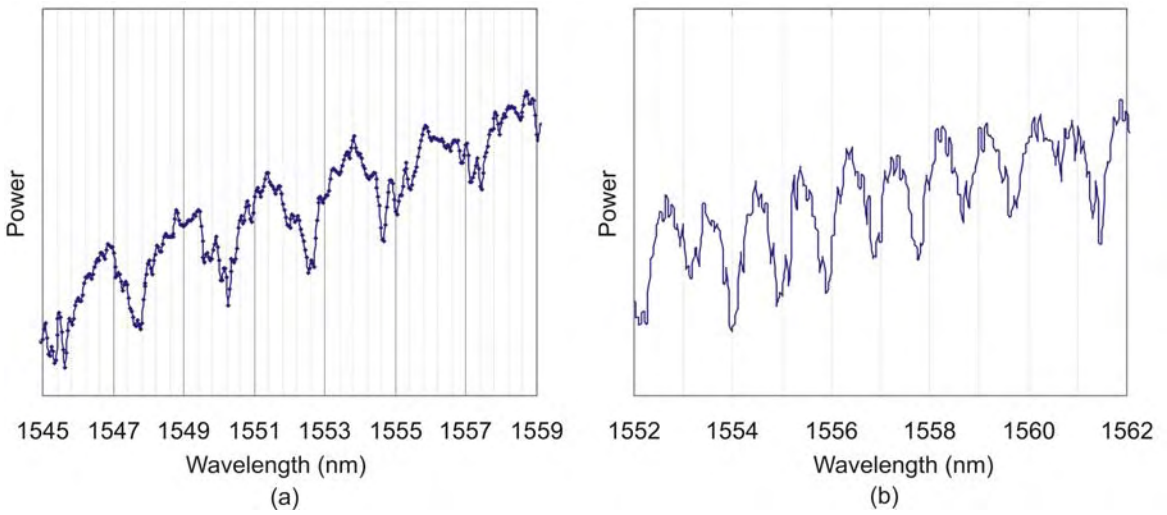

Fig. 4.12. A plot of the signal showing the polarisation beatings of fibre (a) 'F426C' and (b) 'F585C'.

4.4.4 Nonlinearity measurement

Measurements were made to find the nonlinearity for fibre 'F456B' (jointly measured by S. Asimakis). It was based on the measurement of the nonlinear phase shift induced through the self-phase modulation effect, with a cw dual-frequency beat signal used as a pump signal [Chernikov, 1996, Boskovic, 1996]. The nonlinear phase shift, φ, is a function of the ratio of the intensities of the zero- and first-order harmonics, I_0 and I_1 respectively,

$$\frac{I_0}{I_1} = \frac{J_0^{\,2}(\varphi/2) + J_1^{\,2}(\varphi/2)}{J_1^{\,2}(\varphi/2) + J_2^{\,2}(\varphi/2)} \qquad \text{Eqn. 4.4:1}$$

This ratio was measured using a similar experimental set-up to that described in [Chernikov, 1996]. Thus, the nonlinear phase shift is found for different input powers. The nonlinear phase shift is given as,

$$\varphi = \frac{2 \cdot \omega_0 \cdot n_2 \cdot L \cdot P}{c \cdot A_{eff}} \qquad \text{Eqn. 4.4:2}$$

where n_2 is the nonlinear coefficient, L is the length of the fibre, P is the output power, and A_{eff} is the effective area. Therefore, by plotting φ vs. P (Fig. 4.13), and taking the value of n_2 as 2.16×10^{-20} m^2/W for silica, the effective area can be calculated, and it was found to be ~23 μm^2 (the geometric core area ~18 μm^2, and pitch ~3.2 μm). This value seems to be large for a

small core holey fibre, this suggests that the fibres have a relatively low nonlinearity; however the fibre is far from the target design. Furthermore, one of the trade-offs for achieving a dispersion-flattened profile with this particular design was the slight lowering of nonlinearity.

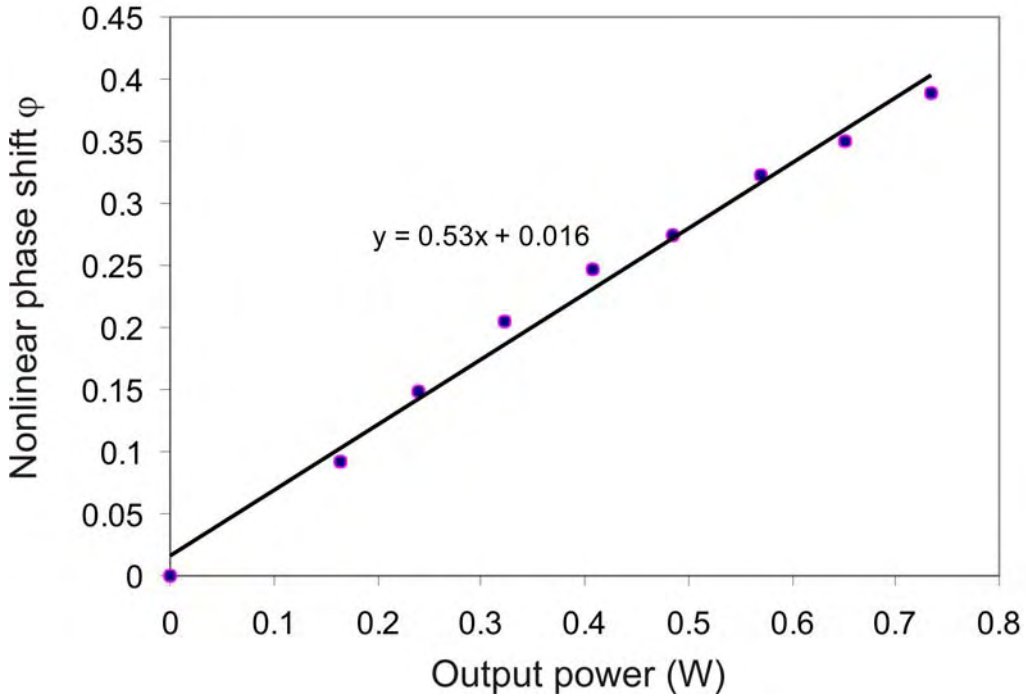

Fig. 4.13. Nonlinear phase shift verse output power with a linear fit for fibre 'F456B'.

4.5 Tolerance analysis

After two iterations, it was found that there were gross structural distortions; therefore the fabricated fibres were far from the target design. In this Section, the modelling work done by F. Poletti on the tolerance level between the structural dimensions and the dispersive property is presented. This work indicates how accurate the real fibre needs to be to achieve the designed dispersion flattened property, and whether or not the target fibre can be produced using the current technology.

A novel modelling method was used to design dispersion-flattened, small-core, holey fibres with five-ring structures [Poletti, 2005]. A Genetic Algorithm was employed to optimise the dispersion of the small-core holey fibre in the 1.5-1.6 μm wavelength range. It showed that a fibre design, similar to the target fibre in Section 4.2, would have a nonlinearity $\gamma \sim 10 W^{-1} km^{-1}$. The modal properties of the target design were also investigated, and it was found that it could have a multimode design; the pictures of the three calculated higher order modes are shown in Figure 4.14. Unusual modes were found between the first and second rings, and the 1st order mode was the most likely to be coupled with the fundamental mode. Indeed, the power fluctuations found when characterising fibre 'F585C', may have been due to the presence of

higher order modes. However, it is worth pointing out that the calculated confinement loss for the first order mode was more than one order of magnitude greater than that of the fundamental mode.

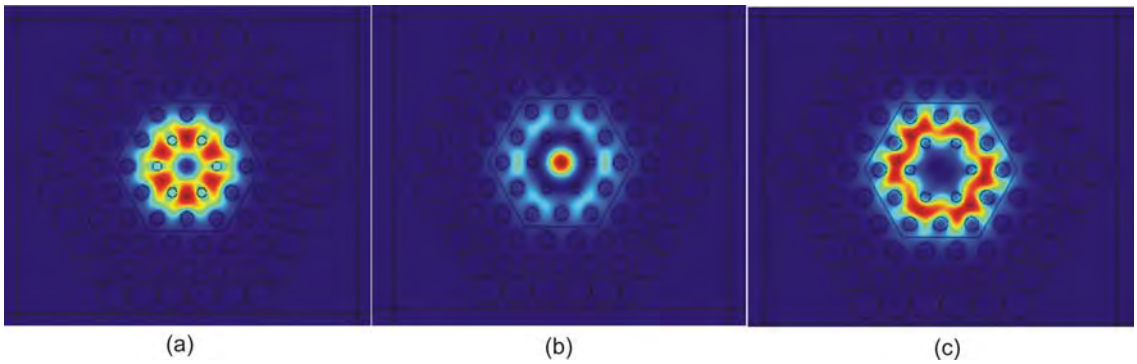

Fig. 4.14. Modal information of the target design (by F. Poletti): (a) 1st higher order mode, (b) 2nd higher order mode, and (c) 3rd higher order mode.

The sensitivity of the dispersion to fabrication inaccuracies was analyzed for various five-ring structures. It was found that the first two rings are the most crucial, and that less than 2% structural variation is desirable (see Fig. 4.15). Changes in pitch size would shift the dispersion magnitude, while variations in d/Λ of the first ring would alter the dispersion slope dramatically. Changes in the second ring hole-size would also significantly shift the dispersion magnitude, whereas changes in the third ring hole-size have less effect and there is even less effect for changes in ring 4 and 5.

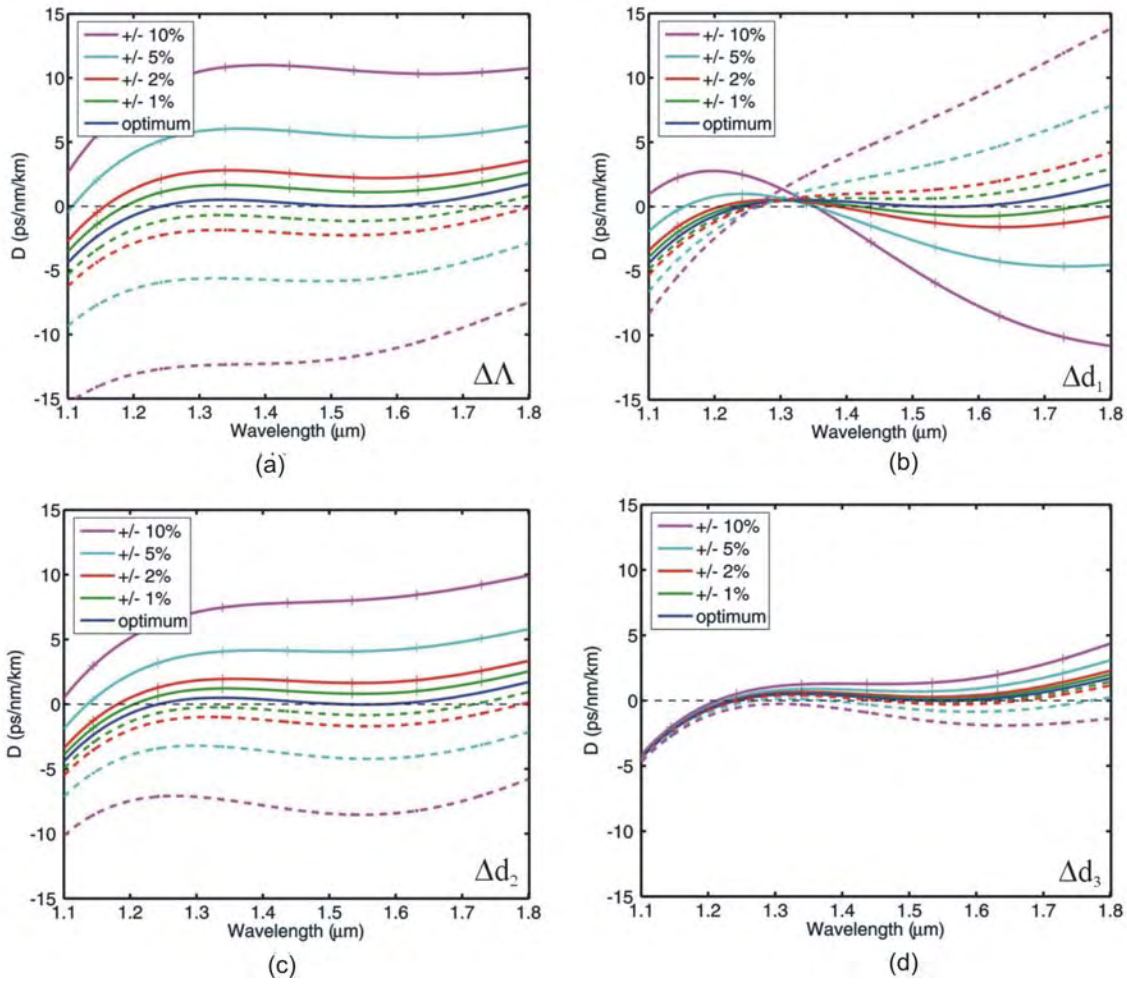

Fig. 4.15. Effect on the dispersion of error in (a) the pitch, and in (b) the first, (c) second and (d) third ring of holes. After reference [Poletti, 2005].

4.6 Structural distortion investigation by varying fabrication techniques

4.6.1 Introduction

In the Section 4.3.3, I identified some of the key obstacles preventing successful production of the target dispersion-flattened holey fibre with five rings of graded hole-size. The major problem was the pitch variation during fibre draw, mainly due to the different air pressure in the holes. The other was the production of elliptical fibres; this contributed additional distortion to the fibres and may have altered the dispersion properties. All the fibres produced so far were elliptical; because a non-centralised fibre drawing method was used. In this section, I will provide a few simple solutions to this problem, and investigate some relatively straightforward fabrication techniques for improvement in the pitch variation distortion.

The aim of this experiment was to investigate different fibre drawing techniques and the corresponding structural distortions for each case. Four different fabrication techniques were investigated; two of which were similar to the typical method used so far, and the other two involve a secondary stack at the fibre drawing stage with the cane inside the jacket tube. The basic ideas are summarised in Fig. 4.16; it shows the scale drawings of the cross-section of a typical cane and jacket arrangement, a secondary stack with rods arrangement and a secondary stack with capillaries arrangement.

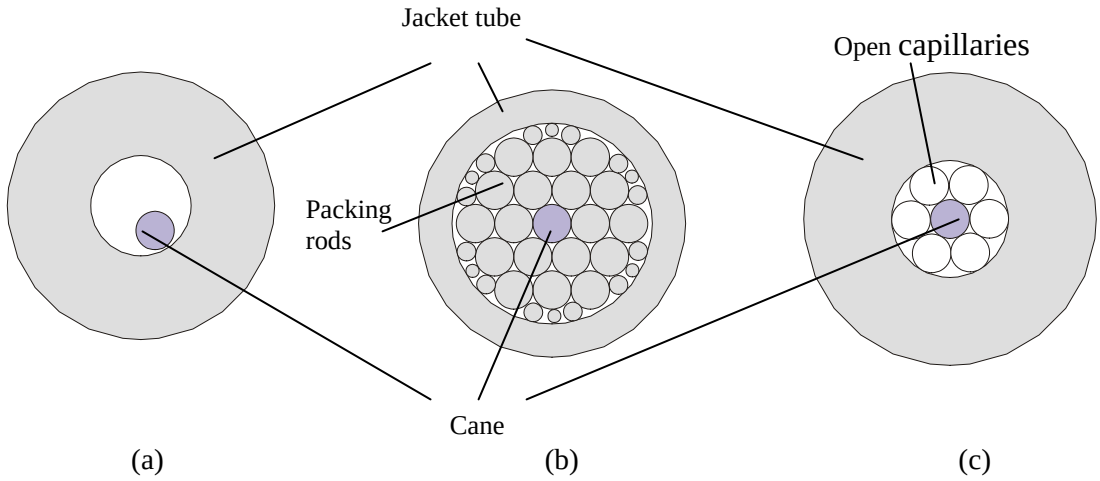

Fig. 4.16. Cross-sectional arrangements of (a) Typical cane and jacket (old method), (b) Cane, packing rods and jacket, and (c) Cane, packing capillaries and jacket.

4.6.2 Old fibre drawing techniques

The jacket tube was prepared as outlined in Section 3.6.1, except an extra small neck was created at the drop end of the jacket to hold the cane roughly in the centre of the preform. The cane was then sealed the same way as before. This was to investigate whether a cane pulled initially at the centre of the preform would preserve a more circular structure than a fibre pulled from the rest of the preform.

Fibres were pulled using this technique, with a cane made from the stack chosen in the second iteration in Section 4.3.2. A SEM micrograph was taken and the fibre (‘F635’) dimensions were measured. The result showed a typical fibre drawn from this technique with no improvement in circular structure preservation was observed from fibres pulled this way. An alternate method is suggested shown in Fig. 4.17, where an artificial holding mount is created in the start-up tube, or in the top end of the jacket tube, to hold and suspend the cane in the centre of the preform. This method is for future reference only and is not reviewed in this report.

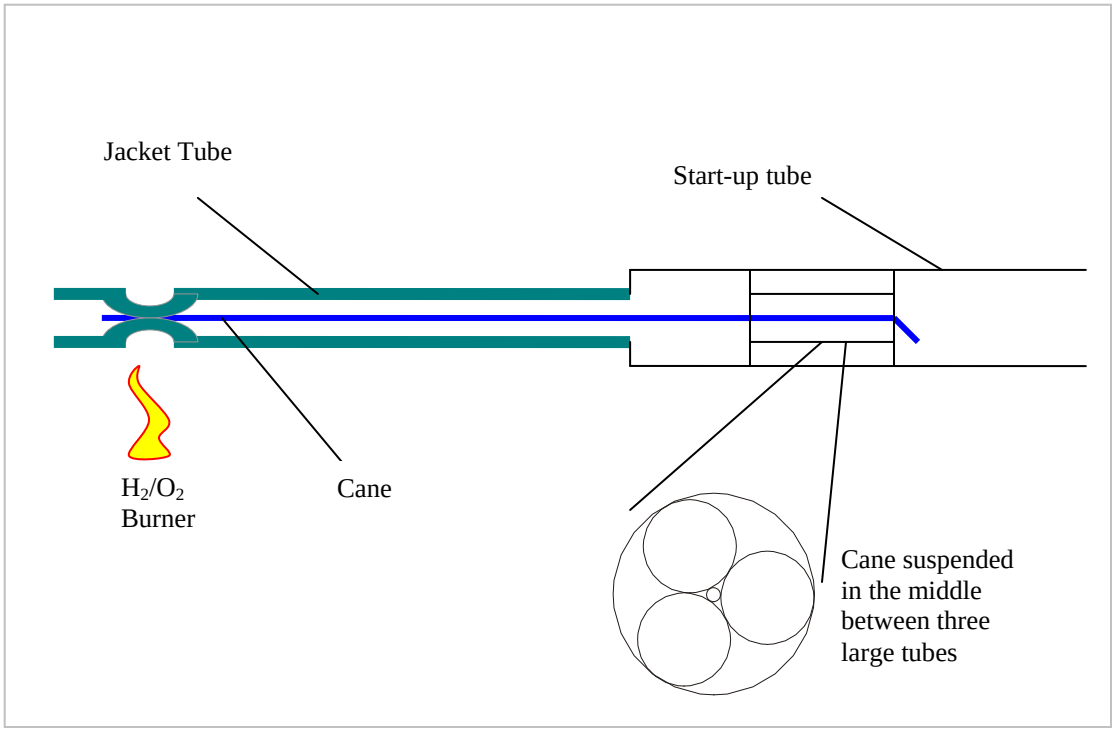

Fig. 4.17. Jacket tube and cane setup with an additional neck on preform and simple stack in the holding tube.

Next, still following the 'old method' shown in Fig. 4.16(a), a jacket tube was made to a dimension so that the diameter of the cane would fit tightly to the inner diameter of the jacket. Ideally a tube with ratio (OD : ID) = (8.5 : 1.35) mm would make a good fit to a cane of diameter ~1.15 mm and produces fibres with reasonable OD. Unfortunately, a tube with such a ratio was unavailable, and it needs to be made alternatively. It was done as follows: firstly by stretching a (12 : 4.83) mm tube to (4.75 : 1.9) mm, see Fig. 3.5(ii) and 4.18(i), it was cut and cleaned. Next, inserting it back into another clean (12 : 4.84) mm tube, then by vacuum collapsing to merge the two together to create a (11.85 : 1.72) mm tube, see Fig. 4.18(ii), it was cut and cleaned again. This was then stretched again, and the final result was a jacket tube of ratio (9 : 1.26) mm, see Fig. 4.18(iii). Canes of diameter 1.15 mm from the second iteration in Section 4.3.2 would not fit into this jacket tube, therefore a cane with diameter of 1.14 mm from the first iteration was selected.

During this fibre draw, it was found that it was not possible to retain a five ring structure, even at the lowest drawable temperature (110 ^{0}C below drop temp.), without the fibre breaking. The SEM micrograph shows that indeed it had a relatively circular structure, but only four rings of hole appeared. Moreover, the smallest inner ring of holes did not appear. Typically, by lowering the draw temperature the inner most ring would appear, but for this case it was not possible to lower the temperature further without breaking of the fibre. For this method to work, the dimensions of the initial capillaries may need to be re-chosen.

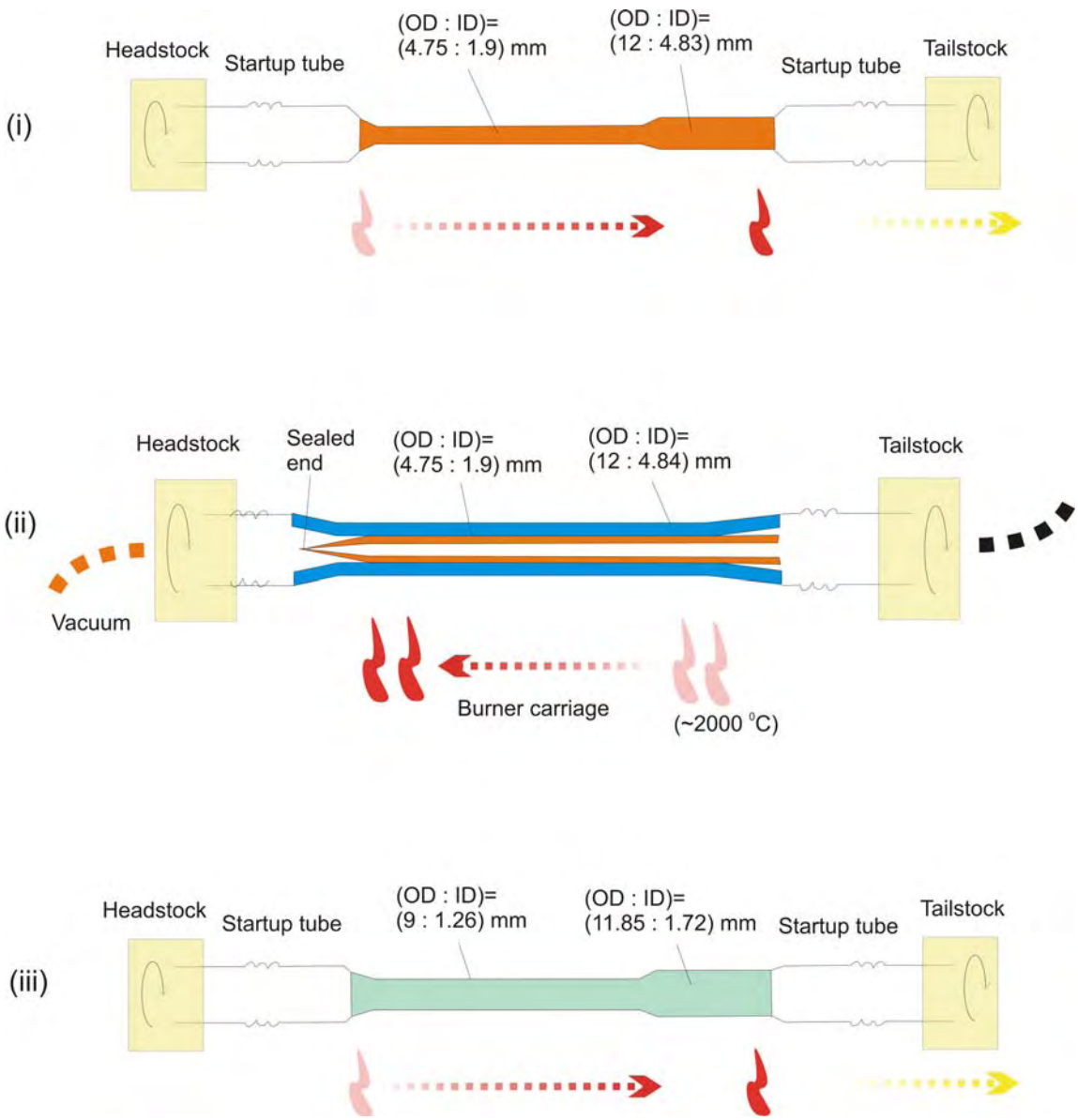

Fig. 4.18. Schematics to show the vacuum collapse procedures for creating a jacket tube to fit the cane.

4.6.3 Secondary stacking techniques

4.6.3.1 Stacking with rods

The stacking arrangement of the cane and rods inside a jacket tube is shown in Fig 4.16(b). The required inner diameter of the jacket tube is ~6 mm if a 1.15 mm cane was used; this was achieved by stretching a (OD : ID) = (20 : 16) mm tube to 8 mm OD, the final ratio of the tube was (OD : ID) = (7.85 : 5.98) mm.

Packing rods of >300mm long were used, thus making a preform of at least ~300mm in length. The selected cane was stacked together with 18 rods, all of the same diameter, and the excess space between jacket and stack was filled with smaller sized packing rods. The new preform was then cleaned again by the oxygen treatment, similar process to the one mentioned in Section 3.4.3. Here, care needed to be taken to ensure the cane and preform are setup correctly on the lathe. The 'startup' tubes were attached to the jacket tube with consideration of the extended length of the cane (illustrated in Fig. 4.19). The final side-view arrangement of the preform is shown in Fig. 4.19(d); the cane was again extended into the start-up tube and sealed in the same way as before, thus mimicking the sealed position.

Fibres were drawn at the lowest temperature (~110 ^{0}C below drop temp.) possible without fibre breakage. The SEM micrograph of the resultant fibre ('F621') structure is shown in Fig. 4.20, which also shows high circularity.

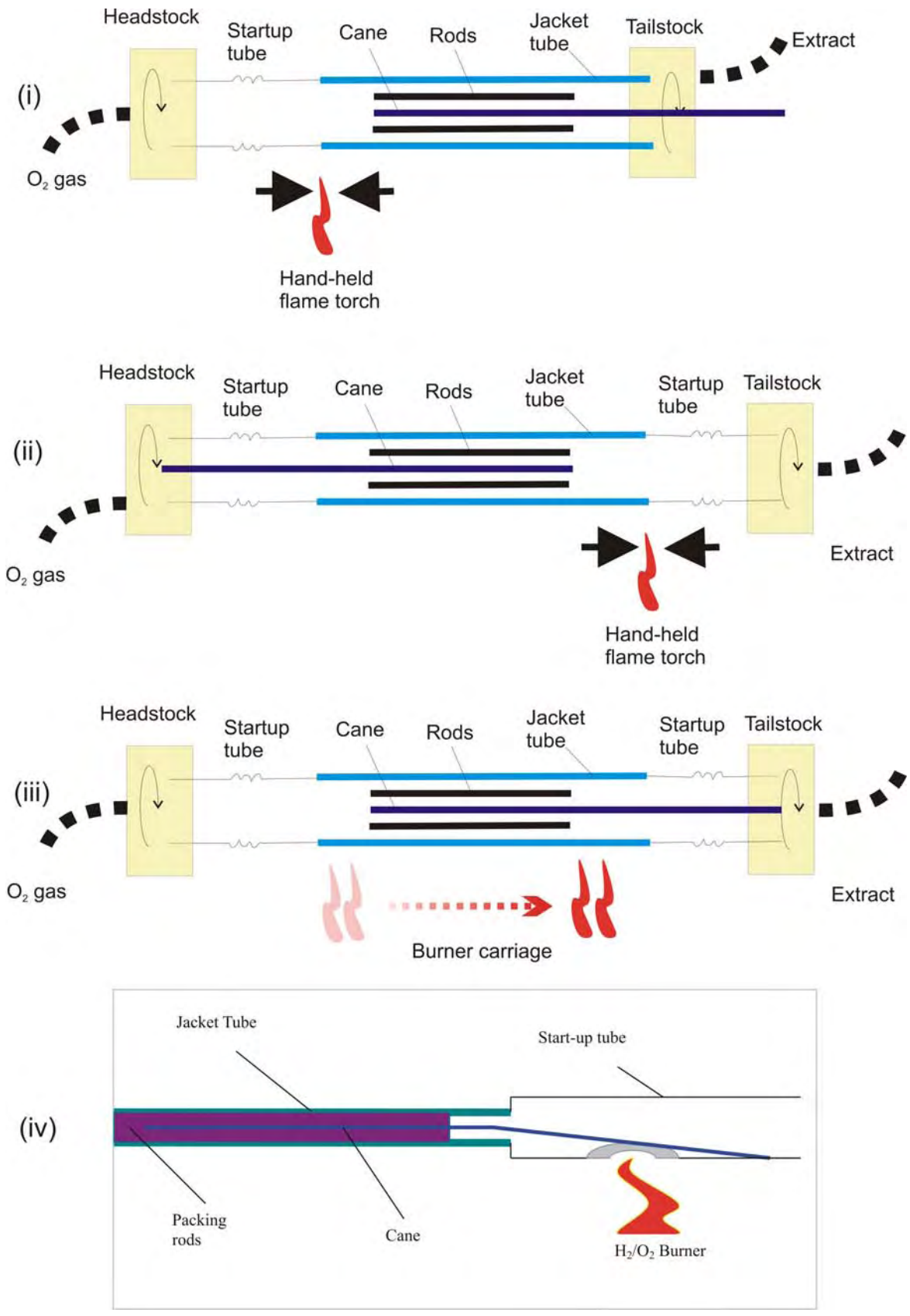

Fig. 4.19. Schematics to show the setup for jacket tube and secondary stacked cane with packing rods.

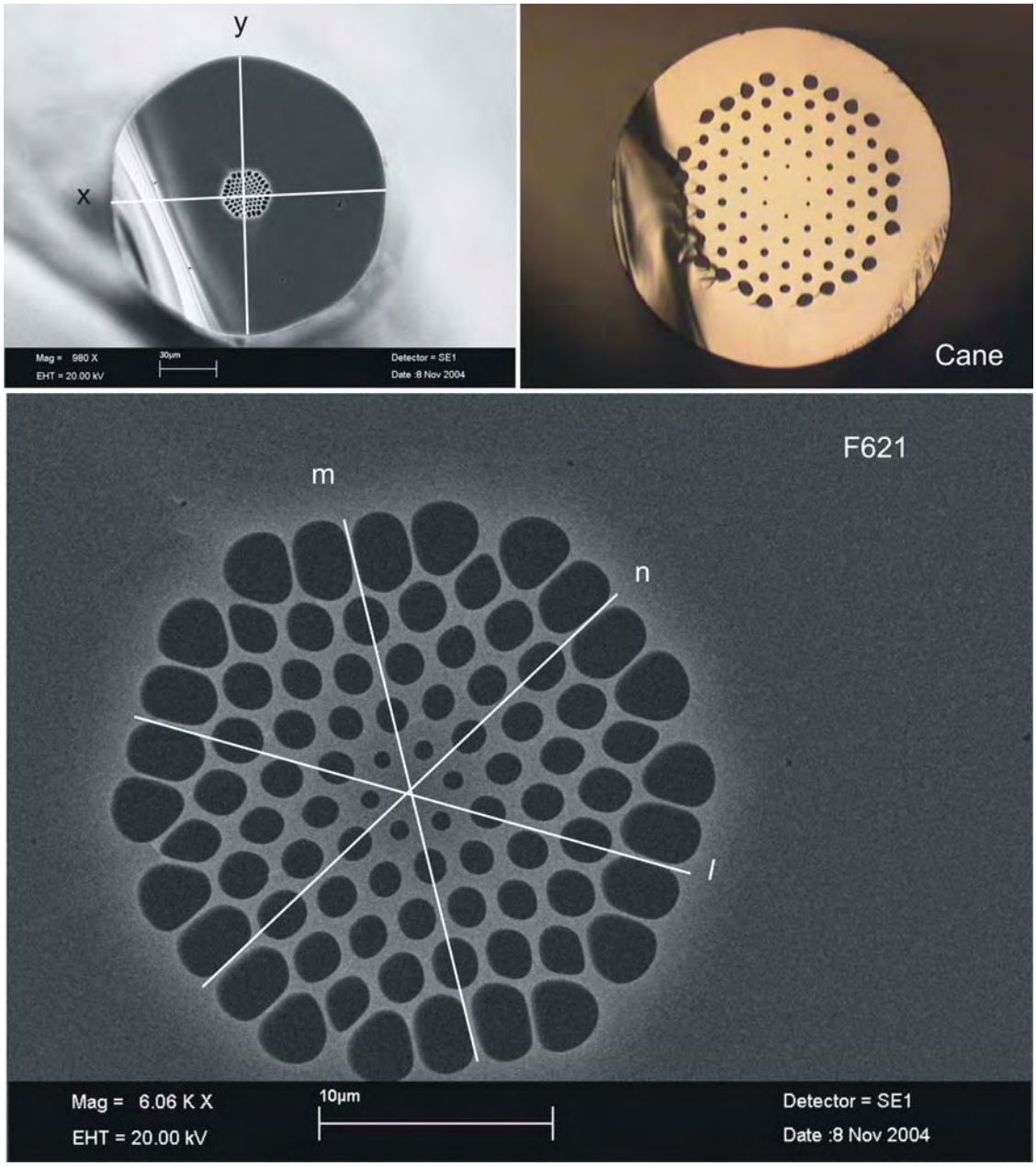

Fig. 4.20. SEM micrograph of fibre 'F621', (x : y) = (1.02 : 1) and (m : n : *l*) = (1.02 : 1.02 :1). Plus a optical microscope image of the cane used.

4.6.3.2 Stacking with capillaries

The stacking arrangement of cane and capillaries inside a jacket tube is shown in Fig. 4.16(c). The required inner diameter of the jacket tube is ~3.5 mm, if 1.15 mm cane is used; this is achieved by stretching a (OD : ID) = (12 : 4.8) mm tube to 8.75 mm OD, the final ratio of the tube was (OD : ID) = (9.15 : 3.65) mm. Packing capillaries with a large air ratio, d/D= 0.84, were used, and they were all open ended; the purpose of the six capillaries was solely to hold the cane in the middle of the preform. After the stacking, this assembly was then cleaned again by the oxygen treatment. The final side-view arrangement of the preform was similar to the

one shown in Fig. 4.19, but with packing capillaries instead of packing rods; the cane was again extended into the start-up tube and sealed in the same way as before.

Fibres were drawn at the lowest temperature (~110 ^{0}C below drop temp.) possible without fibre breakage. The SEM micrograph of the resultant fibre ('F639') shows a slightly elliptical structure. This may be due to a loosely stacked cane, since a jacket with 3.65 mm ID was used instead of a 3.5 mm ID. However, with a properly fitted stack, a more circular structure is expected.

Additionally, the evolution of the microstructured region during this fibre pull from an unstable condition to a stable condition was captured and presented in Fig 4.21. This particular fibre draw required an unusually long time for the stable structure to appear; the furnace hot zone, or the neck down region, was thought to be ~20-25 mm long, and this draw required ~45 mm of preform for the selected temperature to become effective. The possible reasons were that the preform was not in the central position in the hot zone, or because of a slightly different draw down ratio than before (the OD of the preform was slightly larger here, thus a slower feed speed was used).

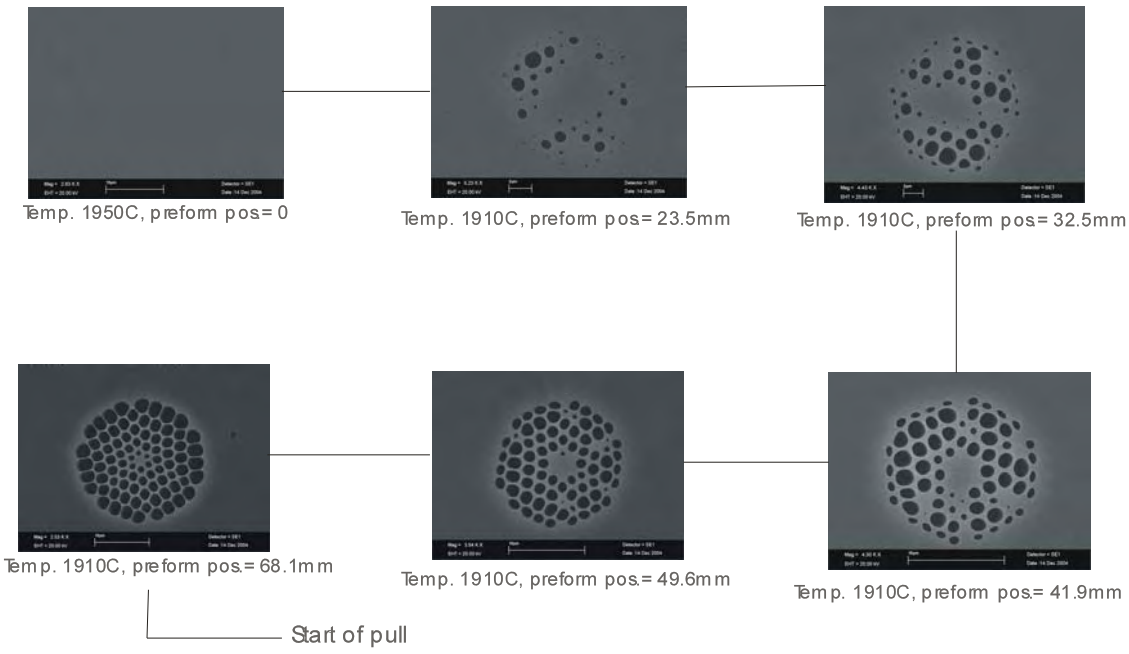

Fig. 4.21. Evolution steps of the microstructured region during the fibre draw of 'F639'

4.6.4 Structure analysis

The fibre produced with the 'tight-fit' method seemed to have the most circular structure; the three edge-to-edge axes were measured to have less than 1% variation. The fibres produced by the secondary stacking methods had good circularity, and the measured axis varied by no more than 3%. Whilst fibres produced by the typical method can have axis variation of up to 6%;

this is significant when <5% of structural variation is required in the final fibre for achievement of reasonable dispersion-flattened behaviour according to the tolerance analysis in Section 4.5. Any of the three additional fabrication methods would be appropriate; however, the secondary stacking method with open capillaries required the least fabrication steps.

The average hole size, pitch size and d/Λ in each ring for fibre 'F635', 'F621' and 'F639' are summarised in Table 4.4, the fibre produced using the tight-fit method ('F631') was discarded in the following analysis as no stable drawing condition was reached. However, a crude inspection on the SEM of the best attempted fibre shows that, this method made no significant improvement on the preservation of the pitch scaling. Moreover, the vacuum used during the fibre draw was minimal; the cane should not expand as much as before, therefore I would expect a more uniform pitch size. More work is required to investigate the effect of this fabrication technique.

		Average hole size (μm)	Standard deviation of hole size (μm)	(STDdev. /average) hole size	Average pitch size (μm)	Standard deviation of pitch size (μm)	(STDdev. /average) pitch size
F585C (old method)	Ring1	0.37	0.01	0.03	1.40	0.08	0.06
	Ring2	0.91	0.05	0.05	1.49	0.07	0.05
F635 (old method + neck at drop end)	Ring1	0.27	0.01	0.04	1.38	0.04	0.03
	Ring2	0.73	0.02	0.03	1.47	0.05	0.03
F621 (2^{nd} stack with rods)	Ring1	0.84	0.05	0.06	1.81	0.01	0.01
	Ring2	1.50	0.07	0.05	2.02	0.04	0.02
F639 (2^{nd} stack with capillaries)	Ring1	0.80	0.07	0.09	1.50	0.05	0.03
	Ring2	1.33	0.03	0.02	1.72	0.04	0.02

Table 4.4. Average hole and pitch size for ring 1 and 2 and the standard deviation.

As expected, fibre 'F635' has the closest structural profile to the ideal design (see Fig. 4.22), because it was drawn with a method closest to the typical method, and the resultant fibres were very similar to fibre 'F585' (note that it was still far from reaching the tolerance level required). Moreover, by comparing the pitch variation of the three fibres (Fig. 4.22(a)), the typical drawing method ('F635') seems to offer the best result, where the lowest gradient is

found. This may again be due to the fact that the initial capillary dimensions chosen for this particular cane were engineered to coincide with the typical drawing method.

The standard deviation of the hole size and pitch size were calculated using the standard Excel worksheet formula ("STDEVP"), for the first two rings separately for fibres 'F585C', 'F635', 'F621' and 'F639'. These measurements were made using standard computer graphics tools (see Chapter 5), the true values were limited by the resolution of the pictures taken by the SEM (Leo430) and the number of pixels used in output pictures. The theoretical value of the SEM resolution was ~10 nm and the image resolution was 1024 × 768 pixels. The scale bar in the SEM pictures and the feature sizes were measured first in pixels, and then converted into microns. The results are shown in Table 4.4; this shows that there was no significant difference in the feature sizes within each ring between the different techniques. On average, there is <5% variation within each ring, and this was already limited by the image resolution.

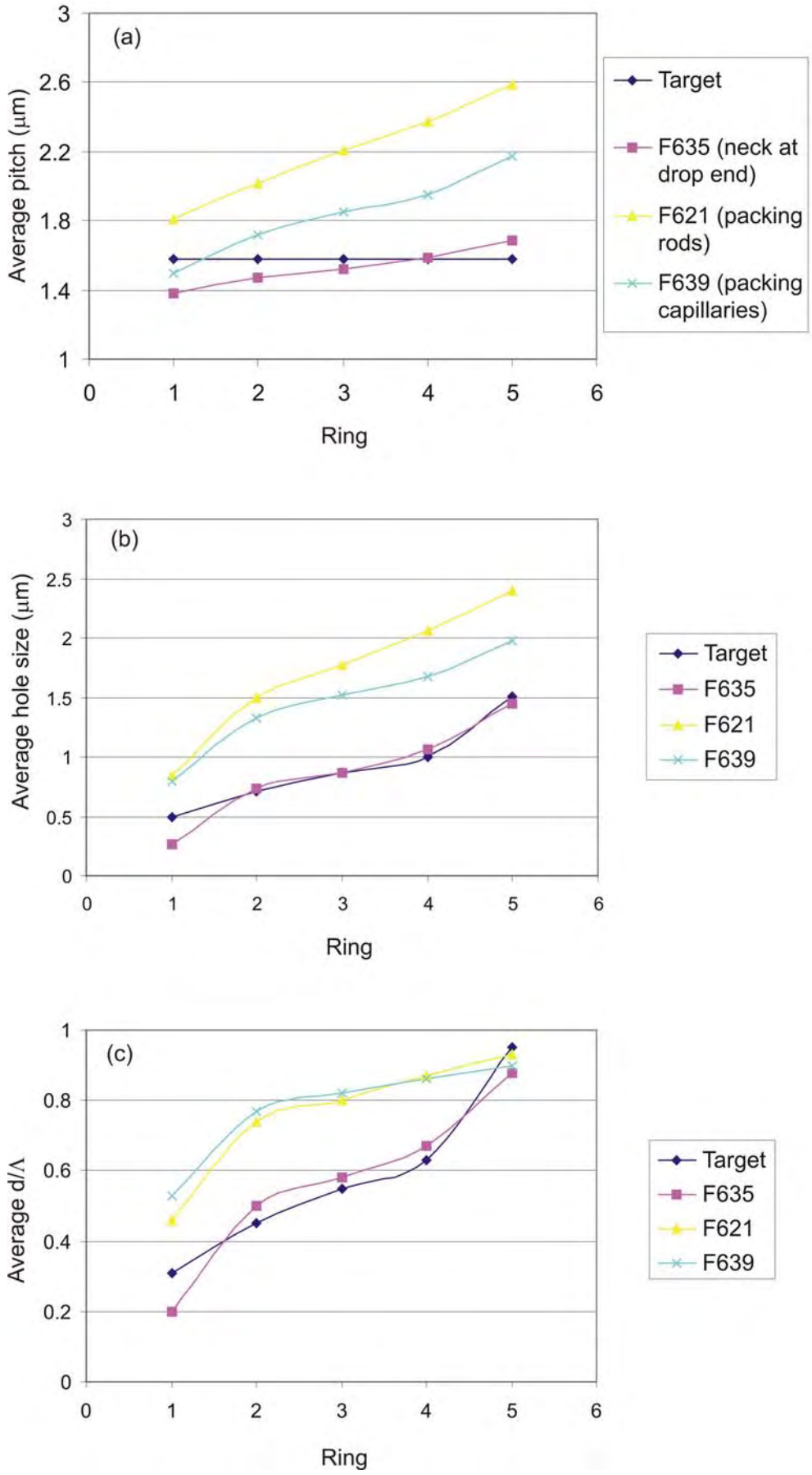

Fig. 4.22. (a) Average pitch size, (b) hole size, (c) d/Λ for each ring in fibres ‘F635’, ‘F621’ and ‘F639’.

Since the difficulty lies in the final cane-to-fibre process, the average percentage expansion of d/Λ for each ring of the lattice in the fibres was measured. Fig. 4.23 shows the results for the fibres produced in the first two iterations and in the secondary stacked. As mentioned before, the smaller the d/Λ in the canes the greater it expands in the fibre.

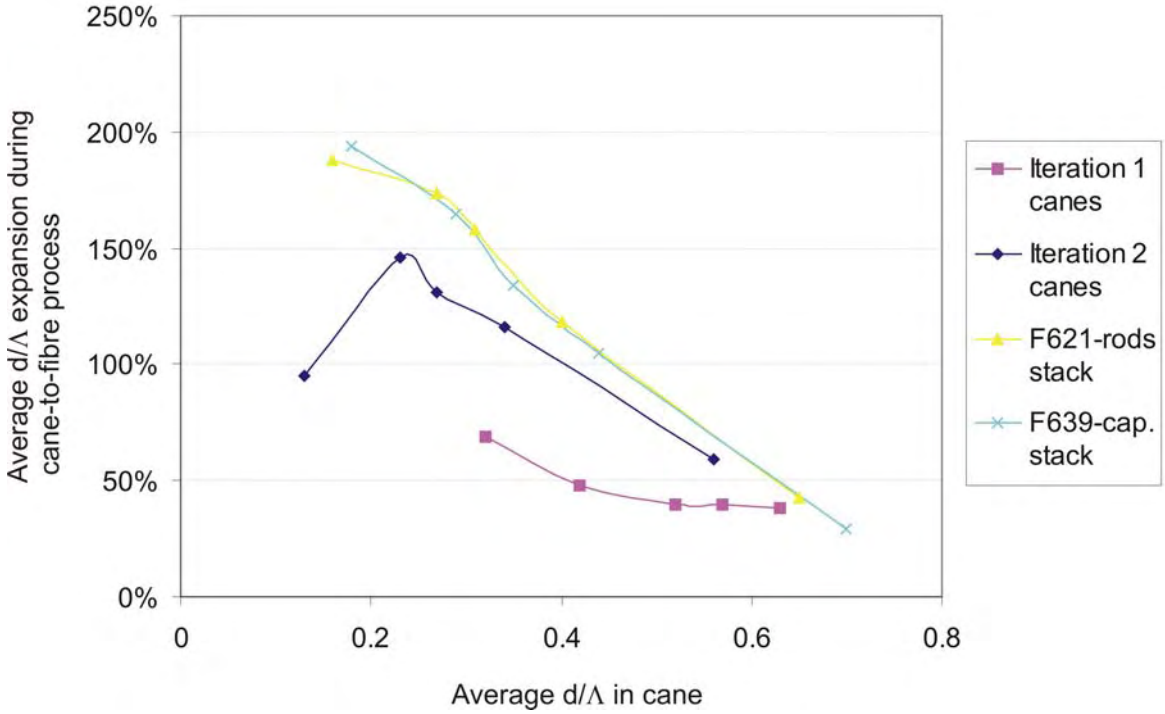

Fig. 4.23. The average percentage expansion of d/Λ during the cane-to-fibre process for different fibres.

The next logical step is to alter the initial capillary dimensions according to the d/Λ expansion graph of 'F621' and/or 'F639' in Fig. 5.23 instead of following the percentage hole expansion of each ring. Furthermore, a one-stage pulling process may be considered, but additional fabrication challenges would arise, for example, much smaller capillary stacking elements and higher drawing speed would be required, thus a higher drawing tower may be needed. However, the most sensible approach is to target a simpler holey fibre design that required less hole-size variation.

4.6.5 Improved designs

A good progress have been made towards fabricating the fibre with the target design, but it was clear that a very complex dynamical problem is involved with very demanding tolerances as identified in Section 4.5. Therefore, I decided to target some simpler structures and fabrication targets operating at 1 μm, before revisiting the dispersion-flattened case at 1.55 μm.

4.6.5.1 Three small holes design for 1 μm operation

For the continuation of the investigation into the fabrication of varying hole-size structures, it was logical to aim for a new design target, other than the one mentioned above, that was less challenging. Modelling by F. Poletti revealed a design with only 3 smaller holes adopted from a regular structure that provided dispersion-flattened behaviour operating at 1.05 μm [Poletti, 2007]. This design exploits the novel properties of microstructured fibres, where anomalous dispersion was achieved at wavelengths below 1.3 μm, moreover, dispersion flattened designs with two zero-dispersion wavelengths were possible. This was significant from the applications perspective, which is demonstrated in Chapters 5, 6 and 7, for supercontinuum generation and soliton compression at 1 μm. The regular hole-size version shown in Fig. 4.24(b) was fabricated successfully and is reported in Chapter 5.

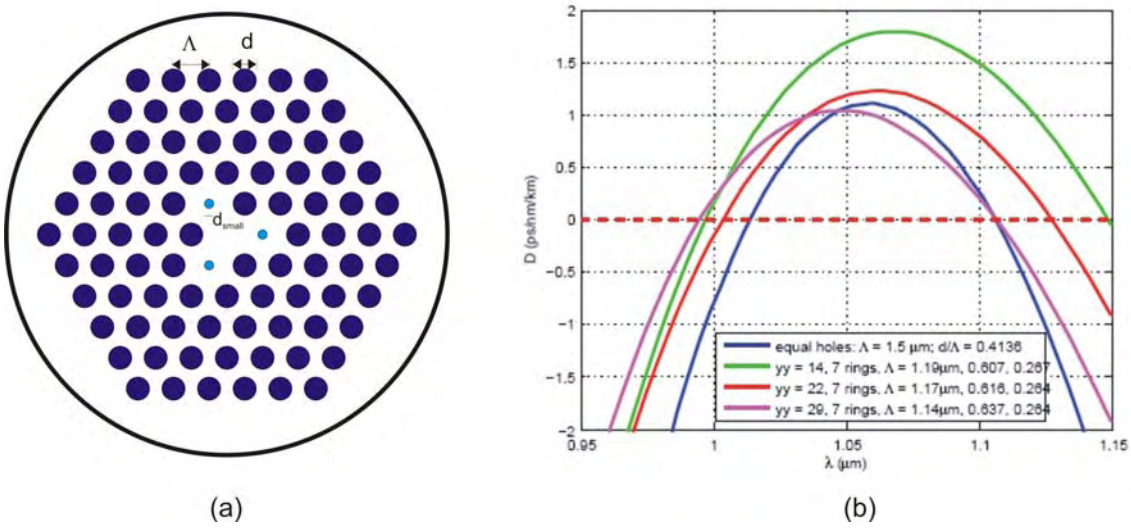

Fig. 4.24. (a) The schematic of the proposed 3 smaller holes structural arrangement, and (b) the corresponding dispersion. The blue curve represents the optimum dispersion profile for a regular hole size design. The green, red and purple curves represent slightly different dispersion profiles for designs with three smaller holes in the first ring. The optimized three small holes design (red) has Λ~1.17 μm, d/Λ~ 0.637 and d_{small}/Λ~ 0.264. After reference [Poletti, 2007].

The schematic of the proposed 3 smaller holes structural arrangement is shown in Fig. 4.24(a), and the corresponding dispersion profiles are shown in Fig. 4.25(b). The optimized design has pitch, Λ~ 1.17 μm, air-filling fraction, d/Λ~ 0.637 and d_{small}/Λ~ 0.264, which offers dispersions between ±1.2 ps/nm/km over the wavelength range between 0.956 and 1.16 μm with two zero-dispersion wavelengths and A_{eff}~3 μm^2.

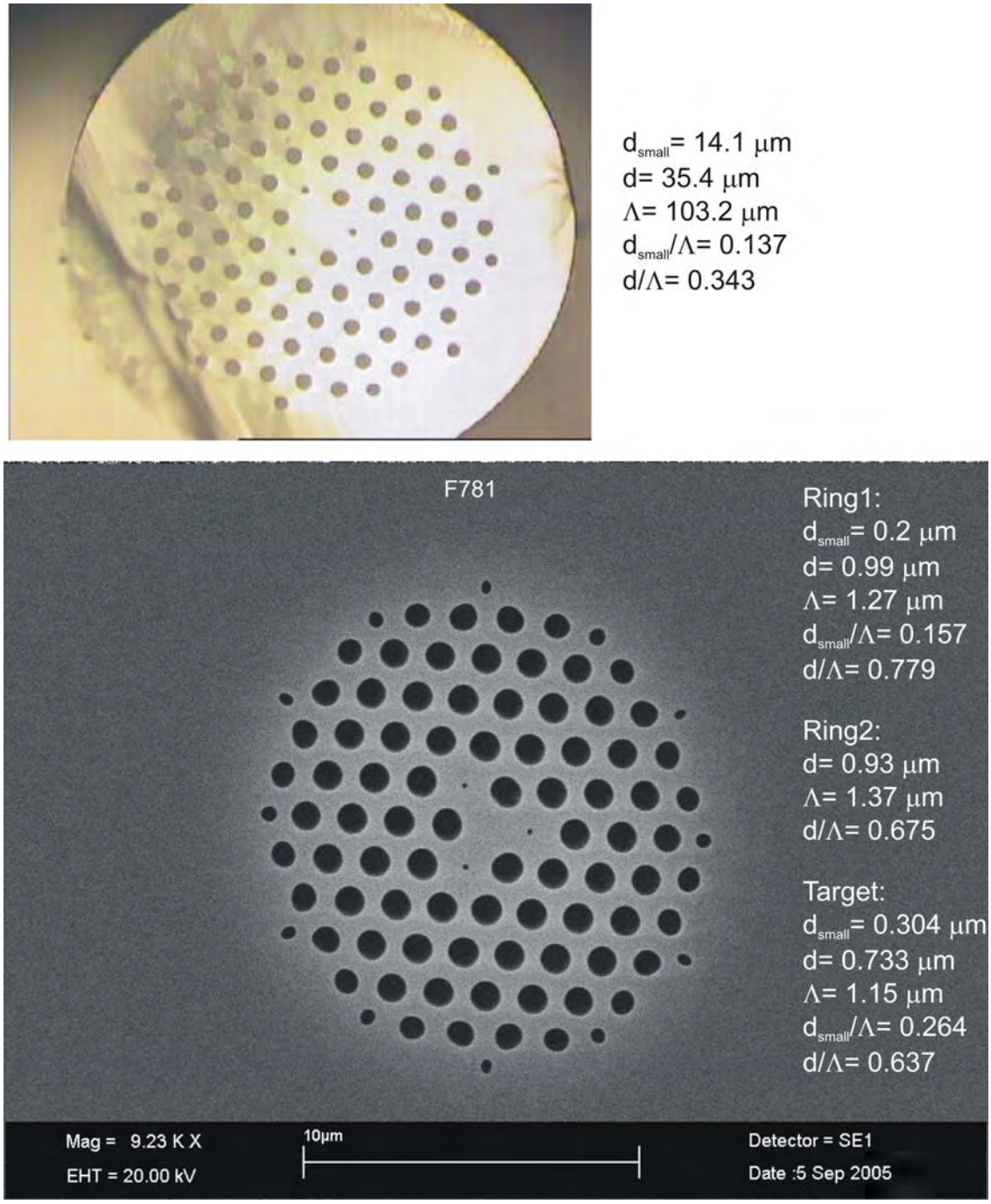

Fig. 4.25. A picture of the cane (top left), and the SEM picture of the 3-small holes fibre ('F781') and the corresponding feature size measurements for the first two rings.

A fibre with 3-small holes had been fabricated. The fabrication method for this fibre is given in Chapter 5. The capillaries stacked in this preform had OD= 1.44 mm, ID/OD= 0.44, and ID_{small}/OD= 0.18. A picture of the cane, the SEM picture of the fibre and the corresponding feature size measurements for the first two rings are presented in Fig. 4.25. Here, the d/Λ expanded by 85% and d_{small}/Λ expanded by 14.6% from the cane-to-fibre process, which was predicted from theories in Chapter 3, where larger holes have large expansion. More significantly, this was different to that found in the graded hole-size fibres. However, it still

possessed the major problem of pitch variation, noticeable even with the measurements of the first two rings only.

A further iteration on this design was carried out, with improvement toward achieving the target dimensions. Unfortunately, both of these fibres were destroyed in the Mountbatten fire, before I could do any further analysis. Initial observation of the fibre showed that, the pitch variation distortion was unavoidable when holes with different sizes are required in the cladding structure.

4.6.5.2 A defected-core design

The simplest design to date that offer the same performance as the five-ring graded hole-size design is the single defect core design by Saitoh and co workers [Saitoh, 2005(b)]. In this design, the control of the chromatic dispersion and dispersion slope is achieved by using a simple structure with a defect-core, see Fig. 4.26(a). By adjusting the size of the central air-hole defect, the design can offer an ultra-flattened dispersion profile, see Fig. 4.26(b), with low confinement losses, small effective area and effectively single mode operation. It offers dispersion of 0.2±0.2 ps/nm/km between the wavelength range between 1.14 μm and 1.7 μm. A typical variation of the design parameter d_c by ±1 % will result in a change of dispersion curve of about ±2 ps/nm/km. This is very attractive from the fabrication point of view; although the dispersion is very sensitive to the design parameter, it is compensated by the simplicity of the design. However, due to the defected core, there is a possibility of low coupling efficiency when splicing to standard single mode fibers, and the mode would extended into the cladding more strongly in comparison with the non-defected core holey fibre.

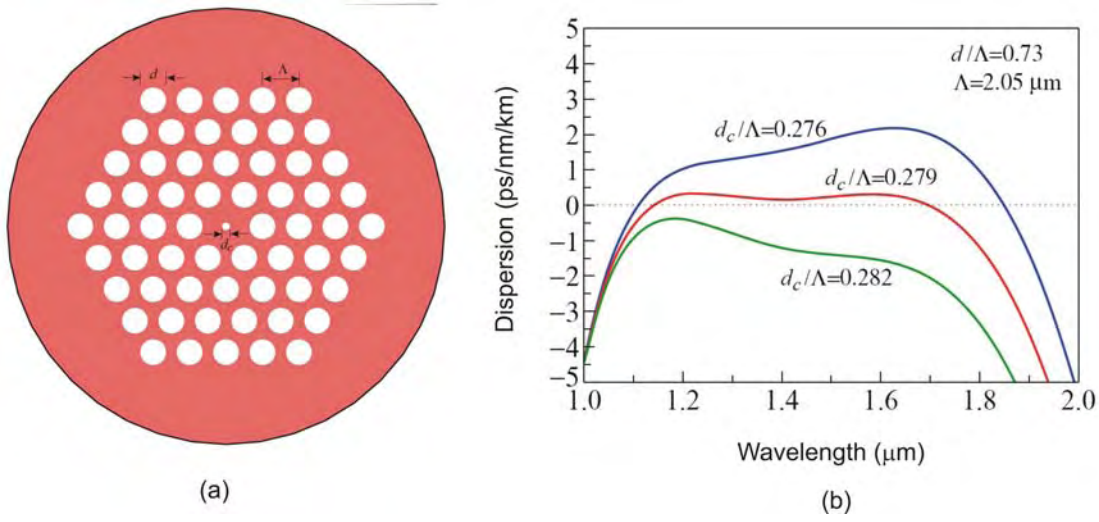

Fig. 4.26 (a) Schematic of the proposed dispersion-flattened structure. (b) The dispersion profile of the optimized design (d_c/Λ= 0.279) and the corresponding profiles with a small variation in the diameter of the defected central air-hole. After reference [Saitoh, 2005(b)].

4.7 Conclusions

The fabrication of graded hole-size microstructured fibres was reported. When air holes with many different dimensions were required in one structure, the behaviour of the hole shrinkage and expansion were found to be unpredictable during the fibre draw. Moreover, fibres drawn from the typical fabrication method always produced elliptical fibres, which added further complication. (Note that, the cane expansion inside the jacket tube, assisted by vacuum, is necessary for the opening of small holes in the structure during the fibre draw. Recall the 'tight fit' cane-in-jacket case, it was not possible to prevent the complete collapse of the smallest inner most ring of holes.)

Different fibre pulling methods were investigated for both fibre circularity preservation and feature size variation. The pitch variation was identified as the main obstacle for obtaining the ideal design. It was found that there were no significant improvements by using different drawing methods, with a similar set of canes as before. A lower draw temperature would help slightly to suppress the pitch variation between each ring of holes. It is doubtful whether it is possible to produce a varying hole-size fibre to have a structure with better than 2% deviation from the ideal design using the traditional two-stage process. With the current two-stage fabrication technology available for graded hole-size fibres, the pitch variation between the first two rings is ~6% at best. Even when the values of d/Λ of the first two rings were carefully engineered to meet the precise requirements, according to the tolerance analysis, it may not be possible to obtain a near zero dispersion flattened profile; a low flatness, low dispersion profile would be a more realistic target using this design concept and current fabrication techniques.

As for the problem of the elliptical distortion, it was tackled by using different techniques to hold the cane in the centre of the preform. The 'tight-fit' method was found to produce the most circular structure, but the two secondary stacking methods were not far from producing an essentially circular structure

The exact dispersion-flattened design was not achieved. However, measurements showed that low dispersion or, in one case, large and flat dispersion over a narrow band were obtainable from the fabricated graded hole-size fibres. I had also fabricated a simpler '3-smaller holes' design for 1 μm operation. Overall good progress had been made for all of these fibres, however, I would ultimately moved back to address progressively more complex structures if I had not lost the fabrication capability.

An even simpler fibre design should be targeted to achieve the dispersion-flattened characteristic, such as the defect-core design mentioned in Section 4.6.5.2. Ideally, the ability to directly access the individual holes for applying pressure in the cane during fibre draw; would provide a better real time controllability of the feature sizes. However, this technology

is currently unavailable, and it is likely to be very cumbersome even if it is possible to do. I propose a novel scheme (see Appendix A), which may or may not work, but which will involve a complicated fabrication setup.

Finally, it had been my intention to revisit this problem within my PhD had the fire not wiped out the ORC fibre fabrication facilities.

Chapter 5 Dispersion-flattened fibres and supercontinuum generation at 1.06 μm

5.1 Introduction

Spectral broadening and new frequency components can be generated when optical pulses propagate through an optical fibre. The temporal and spectral evolution is affected by a multitude of nonlinear and dispersive effects, some of which are described in Chapter 2. For sufficiently intense pulses, the pulse spectrum may extend over a frequency range exceeding 100 THz. Such extreme spectral broadening is referred to as supercontinuum (SC) generation; it was first reported by Alfano and Shapiro, [Alfano, 1970], in bulk glass, and has since been the subject of numerous investigations in a wide variety of nonlinear media, including solids, organic and inorganic liquids, gases, and various types of waveguide. SC generation in a bandwidth of 280 nm with intensity fluctuation less than 15 dB has been experimentally observed in conventional dispersion-flattened and decreasing fibre [Okuno, 1998].

Supercontinuum generation in holey fibres (HFs) is now an established technique for producing broadband light sources [Ranka, 2000, Rulkov, 2005]. A review of this topic is found in [Dudley, 2006]. SC generation in HFs has revolutionized the field of frequency metrology and has opened up a host of new and significant applications in areas such as medical imaging, telecommunications and sensing.

Typically, bulky and expensive Ti:Sapphire-based femtosecond pump sources operating at wavelengths around 780 nm have been used for investigations of SC generation and, therefore, most HFs are designed for use at this pump wavelength. However, there is rapidly growing interest in the development of more practical and efficient pump lasers to facilitate more widespread deployment of SC technology [Harbold, 2002]. High average power excitation of HFs can be realized by employing Yb-doped fibre lasers operating near 1.06 μm, which offer high optical efficiencies and the capability to generate pulses with durations ranging from <100 fs through to the CW regime. Moreover, the holey fibre can be spliced directly to the laser output to make a robust fully-integrated fibre-based SC source. There is thus a great demand for HFs with optimized parameters for SC generation in the vicinity of this wavelength.

From earlier work performed at wavelengths around 780 nm it is clear that pumping in the anomalous dispersion regime and controlling the position of the zero-dispersion wavelength(s) (ZDW) relative to the pump wavelength can be used to tailor the extent of the spectral

broadening, as well as the detailed spectral shape of the SC radiation [Husakou, 2001, Genty, 2004, Hilligsøe, 2004, Andersen, 2004, Frosz, 2005, Falk, 2005].

In this chapter, the fabrication of HFs with flattened dispersion characteristics around 1.06 μm is reported. The SC generation characteristics through a combination of self-phase modulation (SPM), soliton formation, Raman soliton self-frequency shifting (SSFS), and parametric processes of these fibres are investigated both experimentally and theoretically. In particular, the differences in both the dominant physical mechanisms and the shape of the generated spectra depending on the spacing between the ZDWs and the corresponding phase matching conditions for four-wave mixing (FWM) processes is investigated. The results highlight the flexibility for tailoring SC properties, which can be achieved by specifically designed dispersion flattened holey fibres. This shows the feasibility of all-fibre SC sources with specific spectral behaviour, e.g., maximum spectral coverage, high spectral flatness, high spectral coherence, tolerance to source wavelength drift etc.

This chapter is organised as follows. In Section 5.2, the designs for the fibres used for the SC generation are presented. Section 5.3 describes the detailed procedures for the fabrication of the fibres. Section 5.4 describes the method used to measure the dimensions of the microstructured region of the fibres. The experimental and numerical results of the SC generation in the fibres are presented in Section 5.5 and discussed in Section 5.6. Conclusions are presented in Section 5.7.

5.2 Fibre Designs

The fibre design was based on a regular hexagonal geometry, offering a flattened dispersion profile in the vicinity of 1.06 μm. In Fig. 5.1, a contour map (modelled by F. Poletti) of the dependence of dispersion D, dispersion slope D_s, and effective mode area A_{eff} on hole-to-hole spacing Λ and air-filling fraction d/Λ of holey fibres at 1.05 μm is presented. The zero dispersion, D= 0 ps/nm/km, and the zero dispersion slope, D_s= 0 ps/nm^2/km, contour lines are emphasized on the map. The optimum fibre parameters are at the coordinate where the D= 0 and D_s= 0 lines cross: pitch, Λ= 1.5 μm and air-filling fraction, d/Λ= 0.414. Thus the target fibres had the parameters close to that of the optimum design.

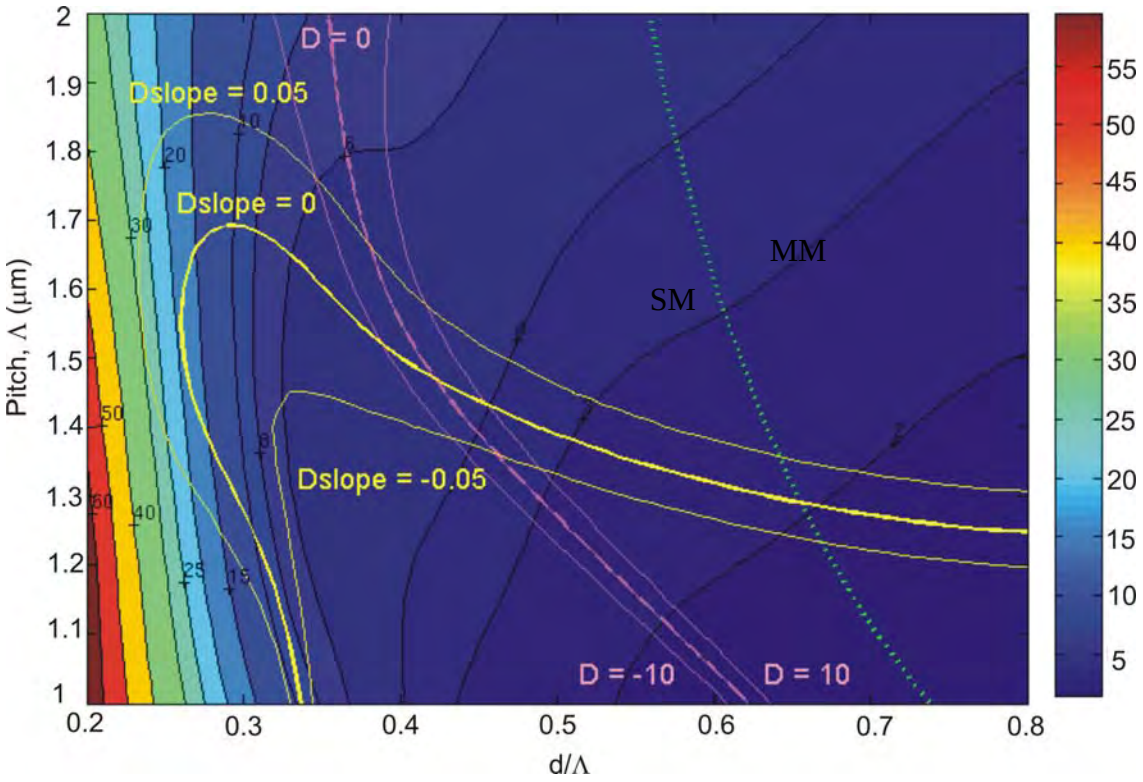

Fig. 5.1. Contour map for dispersion (units of ps/(nm km)), dispersion slope (ps/(nm^{2}km)) and effective area (Shaded colour; μm^2) versus pitch Λ and d/Λ for holey fibres of hexagonal geometry at 1.05 μm wavelength. (Dotted green line indicates single mode and multi mode boundary)

The imprecision introduced during the fabrication process and its effects on the final dispersion profile were investigated. In Chapter 4, a study was carried out into the accuracy achieved in terms of hole size definition and positioning using the stack and draw procedures. Here, the dispersion profiles were calculated to show the tolerance levels in the deviation of d/Λ and Λ from the optimum design. The dispersion varied moderately by either varying d/Λ and/or Λ. The parameters were modified by ±1%, ±2%, ±5% and ±10% from the optimum value, based on a 7 rings structure. The corresponding dispersion profiles are shown in Fig. 5.2. Similar work has been done at 1.55 μm, which is not included here, [F. Poletti, 2005].

Fig. 5.2 shows that the magnitude of the dispersion variation, when the value of particular fibre parameters are slightly modified. The fibres still provide good dispersion flatness at 1.05 μm. The aim was to target fibres with a range of dispersion profiles during the fibre drawing process of a single preform. It is possible to get a range of samples due to the inherent structural variation that occurs along a fibre in the fibre drawing stage. The internal pressure of the air in the holes was allowed to reduce naturally during the draw to produce a reduction in hole size, d, along the fibre length. The slow changes in structure produce sections of fibre with different dispersion-flattened profiles. The pitch Λ (and the effective mode area A_{eff}) are nearly constant along the fibre. SC experiments were then performed using sections of fibres. These were short samples at different positions along the single fibre drawn, with nominally

uniform properties along the samples. By studying the spectra generated in sections of fibres with different dispersion profiles, the dominant nonlinear and dispersive effects can be identified.

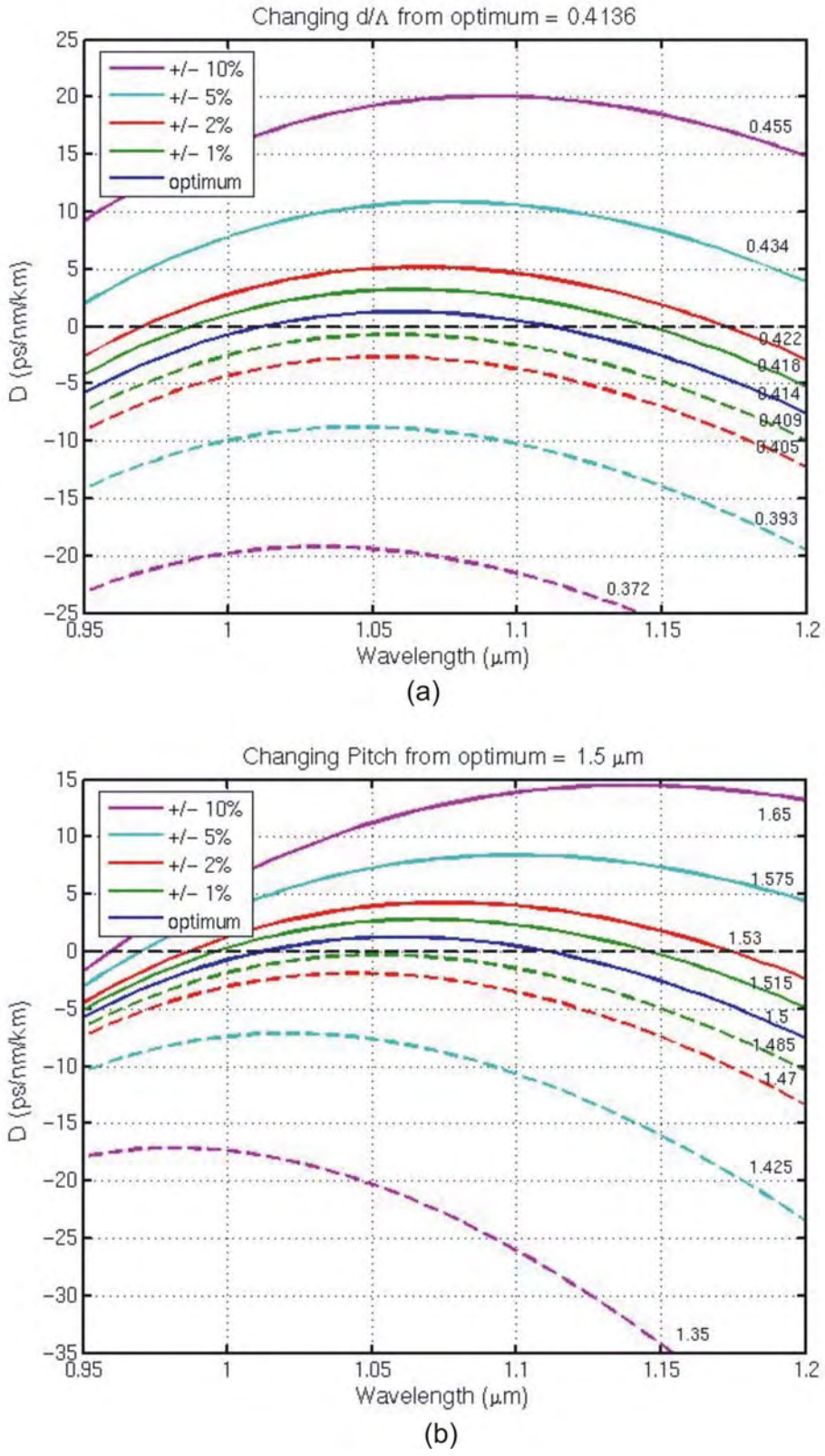

Fig. 5.2. Dispersion graphs to show the tolerance levels of deviation in (a) d/Λ and (b) Λ from the optimum dispersion-flattened design. (Provided by F. Poletti)

5.3 Fibre fabrication

5.3.1 Preform Stacking

The fibre was fabricated using the stack and draw process, described in Chapter 3. Based on Fig. 5.2(a), a change of a few percent in d/Λ is required to produce fibres with a range of dispersion curves of different profile.

The capillaries required for this preform had a hole size inner diameter, ID= 0.33 mm and outer diameter of the capillaries, OD= 0.95 mm, thus, ID/OD= 0.35. In order to reduce the confinement loss to 0.0008 dB/m, at least 7 rings of regular holes were required. To correctly seal capillaries with such small ID/OD ratio can be difficult, and therefore time consuming when a large number of elements are needed.

I stacked 198 capillary elements in a 20:16 (OD:ID) mm holding tube, to form a 7 ½ rings structure, where the 8^{th} ring had holes missing at the corners. A simpler technique was used here to produce each element with the dimensions required. Fig. 5.3 shows a sleeve 'Russian doll' method to produce each element. I stacked and arranged 198 open capillaries in the usual manner, then sealed one end of the same amount of smaller capillaries, which had an OD just smaller than the ID of the open capillaries. The sealed end can now be slightly larger than its OD without affecting the over all structural arrangement (see Fig. 5.3), therefore the sealing process was less labour intensive. After the open capillaries were properly arranged, the smaller, sealed capillaries were inserted as shown in Fig. 5.3. The space between the open capillary and the sealed capillary is closed up naturally during the caning process, assisted by applying moderate vacuum.

The length of each element and hence the length of the stacked preform was ~300 mm, of which ~200 mm was collapsed into canes. The chosen cane was around ½ m in length, OD= 1.55 mm, hole-to-hole spacing, Λ= 67 μm, hole diameter, d= 17.5 μm and d/Λ= 0.26. The picture of the cane is shown in Fig. 5.6.

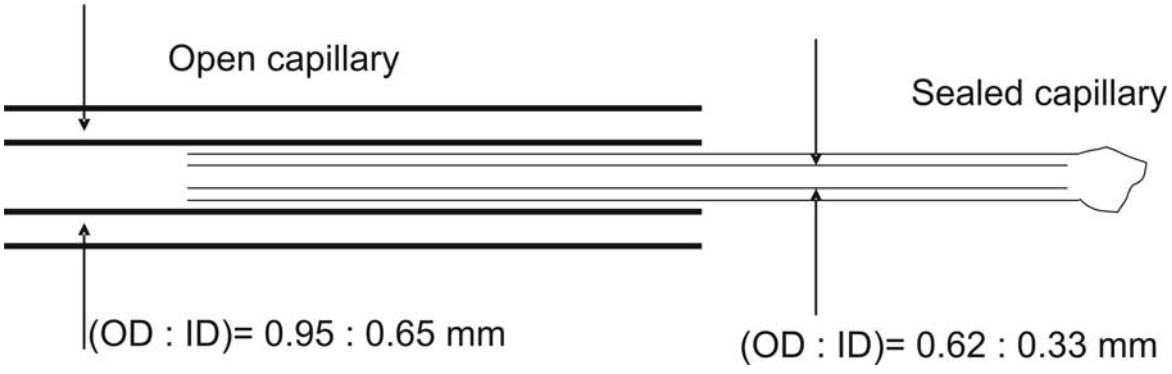

Fig. 5.3. The schematic of each element in the stack using the sleeve 'Russian doll' technique.

5.3.2 Jacket tube preparation

A few alterations were made to the standard ‘cane-in-jacket’ assembly procedures described in Chapter 3; this is the second stage of the ‘two-stage pulling process’. To prepare the jacket tube for the final preform, a 12:4.8 mm tube was stretched into a 8:3.2 mm tube, the procedures were as follows: Starting with a 400 mm long 12:4.8 mm ‘F300’ tube, ‘start up’ tubes were attached at both ends on the lathe (Fig. 6.4(i)) and fire-polished at ~1650 ^{0}C (Fig. 6.4(ii)) as before. At the tailstock end of the lathe, a marker was placed on the ‘F300’ tube where at least 150 mm would be left unstretched (Fig. 6.4(iii)). This was the length between the top of the furnace and the hot zone in the middle of the furnace. Using the appropriate burner temperature, burner carriage and tailstock speeds, the tube was stretched, starting from the headstock end of the lathe. The process was stopped just before the burner reached the marker (Fig. 6.4(iv)). The tubes were taken out of the lathe carefully in one piece. Using a diamond-coated glass saw, the ‘start up’ tube was cut off from the unstretched portion of the ‘F300’ tube. The stretched (jacket) tube was washed with de-ionised water and acetone (Fig. 6.4(v)). The detached ‘start up’ tube was also washed and kept. At this point the jacket tube was ready for the cane to be inserted.

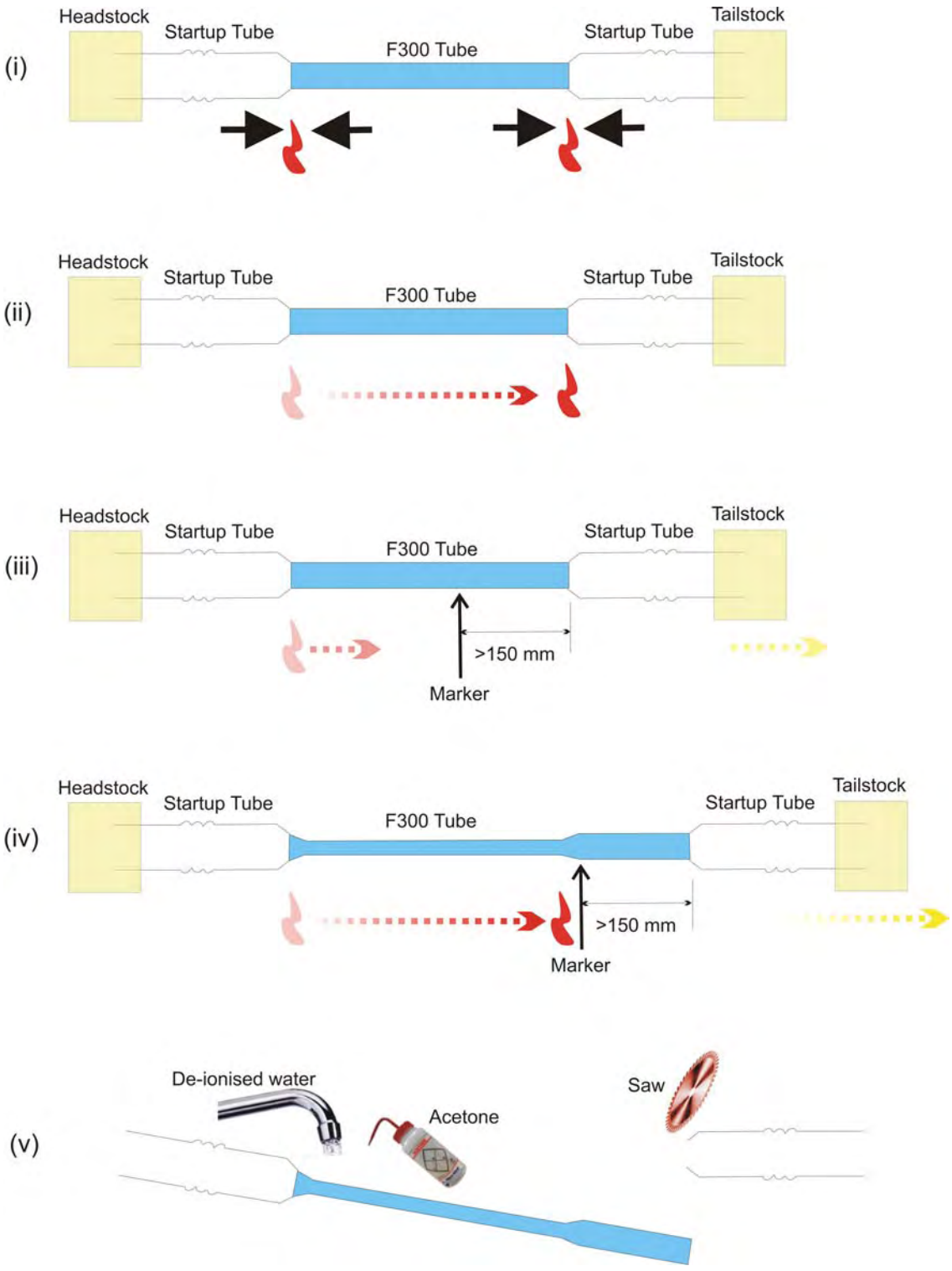

Fig. 5.4. Step-by-step schematics to show the procedures to stretch a 12 mm OD 'F300' tube into a jacket tube.

5.3.3 Cane in jacket assembly

The cane is sealed at one end, and inserted along with six short (~50 mm) capillaries or scrapped canes of the same OD, into the unstretched end of the jacket tube, as shown in Fig. 5.5. The six capillaries were stacked around the cane to ensure that the cane was held in the

centre of the preform. They were kept short to ensure the cane can be drawn up to the last 120 to 150 mm during the fibre pulling process. The holes in the cane started to reduce in size in a slow, continuous and stable manner in the last 200 mm of the cane.

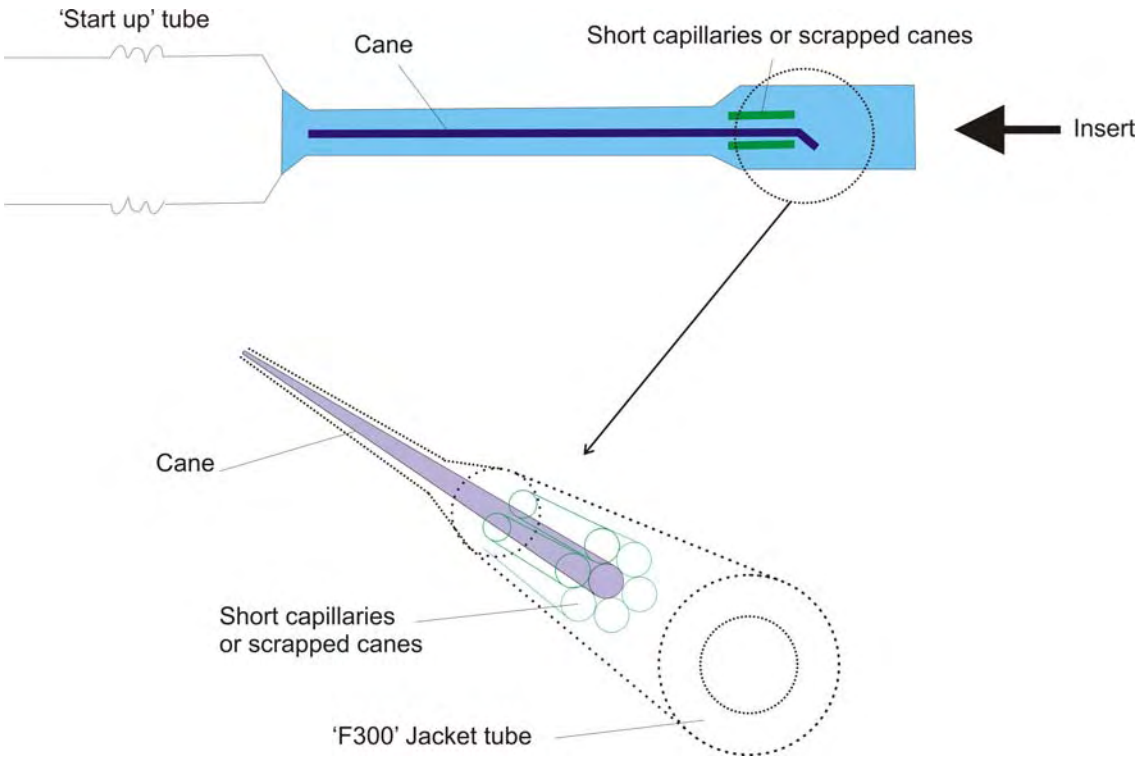

Fig. 5.5. Schematic to show the cane-in-jacket assembly procedures.

The 'start up' tube was re-attached to the preform on the lathe using a hand-held burner, this served as a handle, where the preform was hold by the feeder on the fibre draw tower. The schematic of the preform setup on the drawing tower is shown in Fig. 5.6. Note that only 70.5 mm of preform towards the latter part of the cane was drawn into useful fibre where the holes in the structure reduced in size naturally along its length. Once a long fibre was drawn, it was selectively cut into 1 m pieces for the SC experiment. Each piece provided a slightly different dispersion profile. The fibres drawn from the earlier part of the preform, which had uniform hole sizes, were either scrapped or kept for other applications.

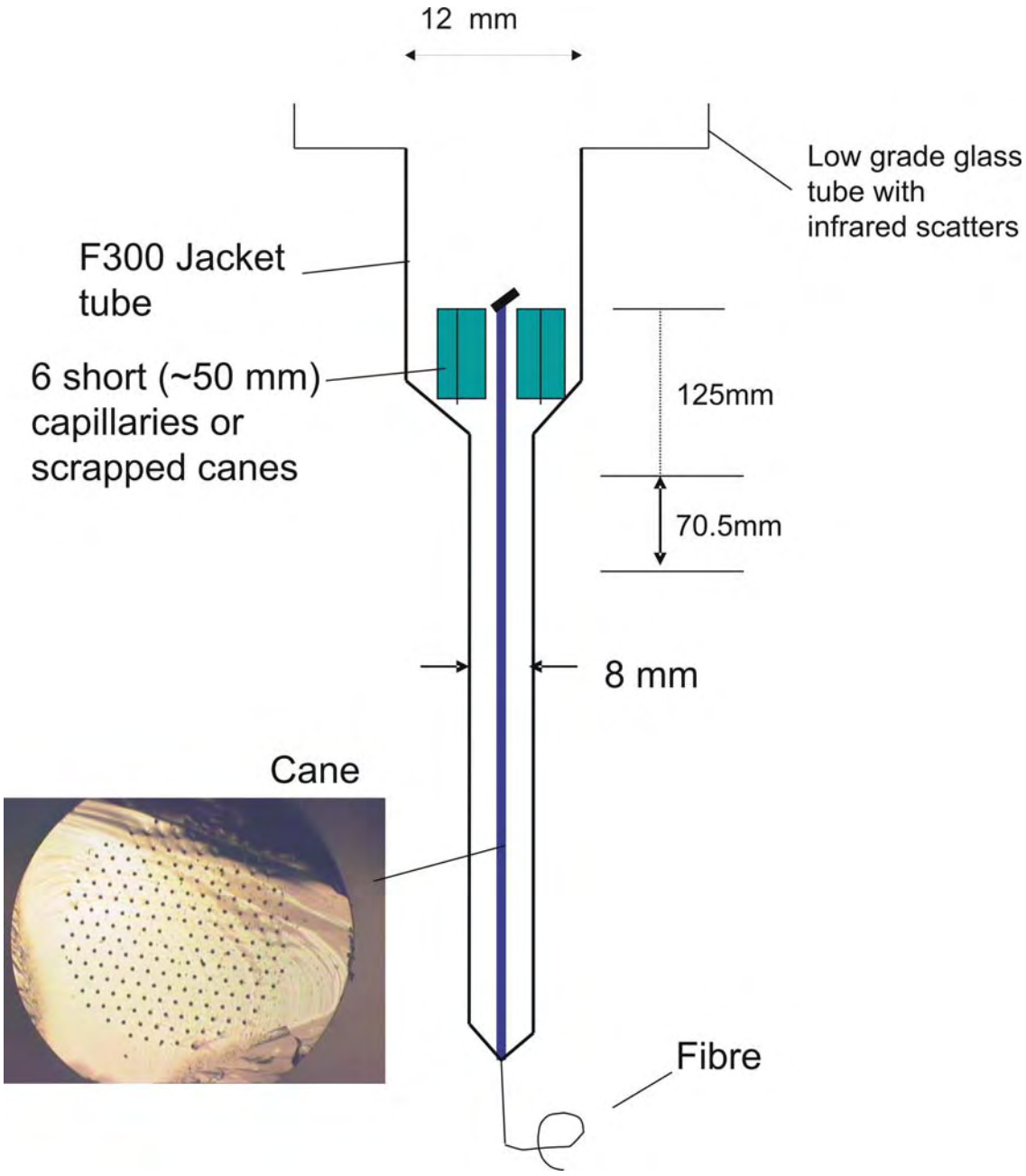

Fig. 5.6. Schematic of the cane-in-jacket preform assembly (not in scale). *Inset*: Picture of the cane structure taken under an optical microscope in the transmission setting.

5.4 Fibre structure measurements & dispersion profiles

I cut the fibre into 10 sections, and for each section I examined the dimensions of the features in the fibre structure by measuring the hole size and pitch from the SEM pictures. The initial estimated dispersion profiles were calculated using these measurements. In Section 5.5, these

results are compared with the SC experimental and numerical results, in order to identify a "correction factor" in the dispersion calculation.

The fibre ('F738b') was 193 m in length, OD~ 145 μm and d/Λ varied from 0.584 to 0.380. The SEM pictures taken from the Start-of-Pull (SOP) and End-of-Pull (EOP) of the fibre are shown in Fig. 5.7. Here, a difference in hole size can be seen clearly between the two ends of the fibre. However, this was not the case when the fibre was cut into 8 to 10 m long pieces where the difference in hole size between the pieces can be very small. Therefore, the structural feature dimensions were measured from the SEM pictures using an imaging software ('Scion Image' by Scion Corporation, downloaded from [Scion Corporation]). Beginning from the EOP, the fibre was cut and had SEM pictures taken at 20 metres from end-of-pull (mfeop), then at 30, 40, 50, 60, 70, 78, 88, 98 and 184 mfeop.

The fibre samples were gold coated for the SEM imaging, and the pictures of the microstructured region were taken using minimal current, typically 5 to 10 pA, to prevent over charging. The pictures were recorded with 1024 × 768 pixels, and then imported into the 'Scion Image' software. The procedures for measuring the dimensions of the fibre structures are as follows: In the Scion window, zoom in to the scale bar of the picture (Fig. 5.8(i)), and measure its length in pixels. Set the scale from the 'Analyze' drop down menu in microns (Fig. 5.8(ii)). Then choose the measurement options; the required options are 'X-Y Centre', 'Ellipse Major Axis', 'Ellipse Minor Axis' and 'Wand Auto-Measure' (Fig. 5.8(iii)). These generate outputs of the (x, y) coordinates of the air holes relative to the top left corner of the SEM picture, and the measured diameters of the major and minor axes of each air hole. Next, convert the picture into binary black and white image (Fig. 5.8(iv)), and adjust the contrast slightly if necessary (Fig. 5.8(v)). Care needs to be taken to ensure the hole sizes are unchanged. Then use the 'magic wand' tool to select the holes (Fig 5.8(vi)). Check the hole selections in the original image, to ensure the program reads the holes correctly (Fig 5.8(vii)). Also check the analysed results by selecting 'show results' in the 'Analyze' drop down menu (Fig 5.8(viii)). A window displays the required measurement data in microns, and they can be copied ('copy measurements') and pasted to an Excel spreadsheet. Finally, note the coordinate of the centre of the microstructure (Fig 5.8(ix)).

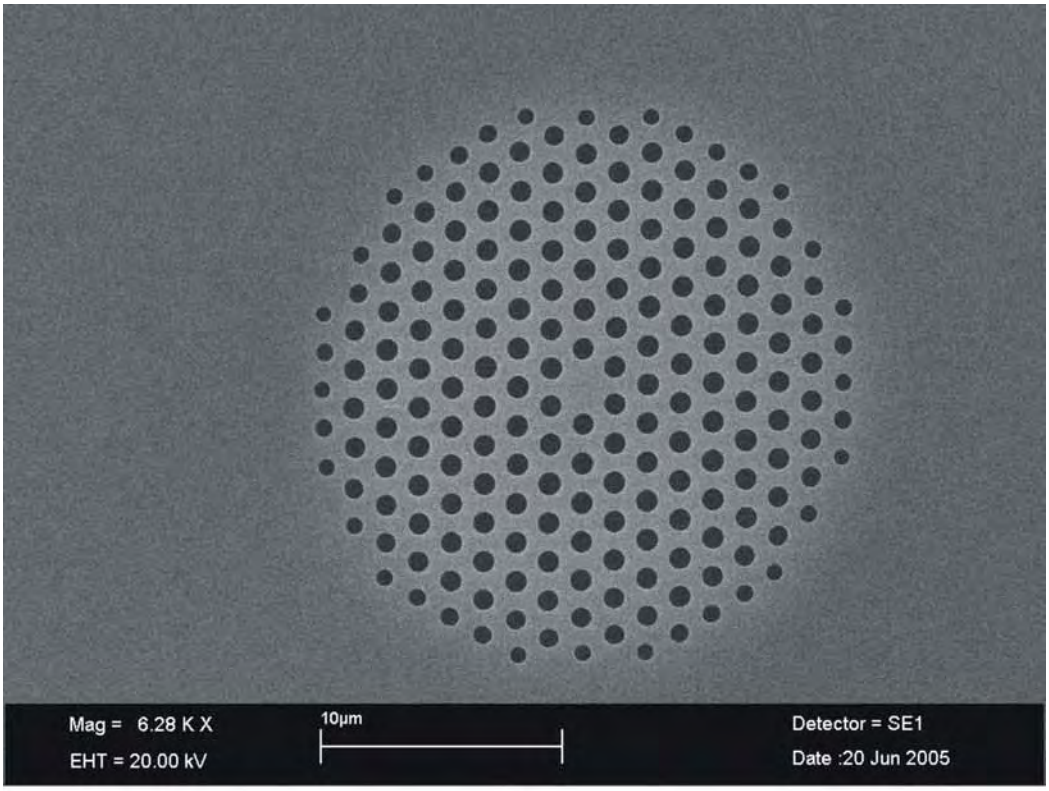

(a)

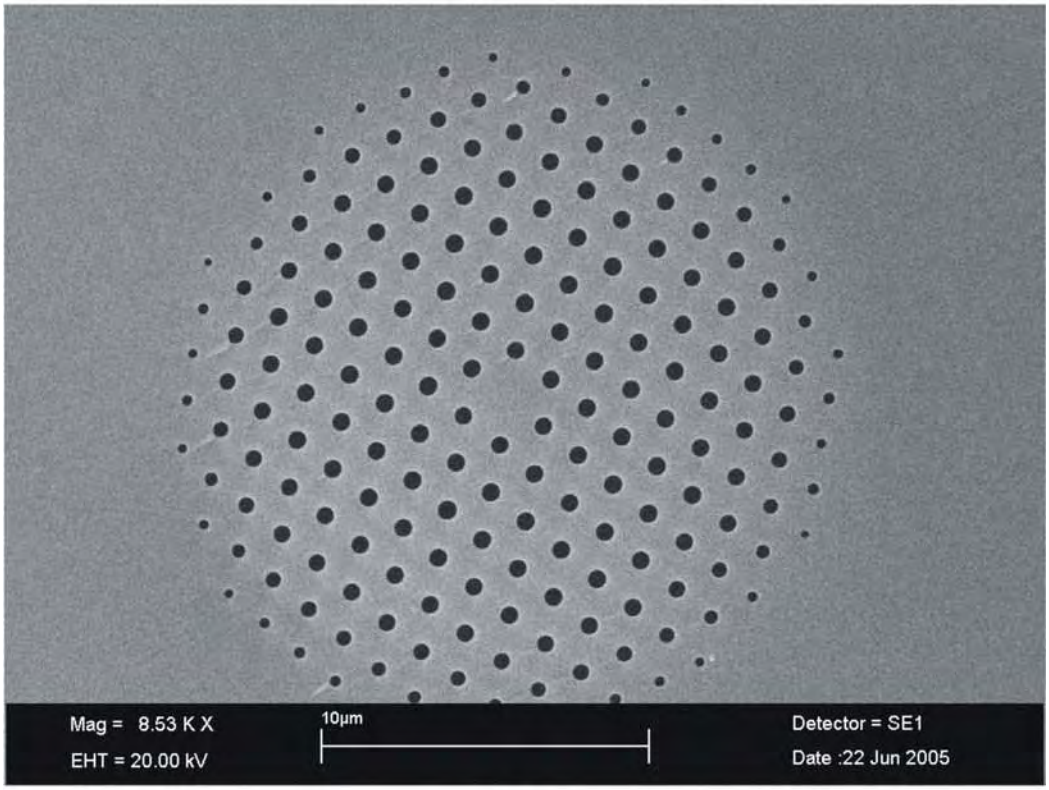

(b)

Fig. 5.7. SEM micrographs of fibre ‘F738b’ at (a) SOP and (b) EOP.

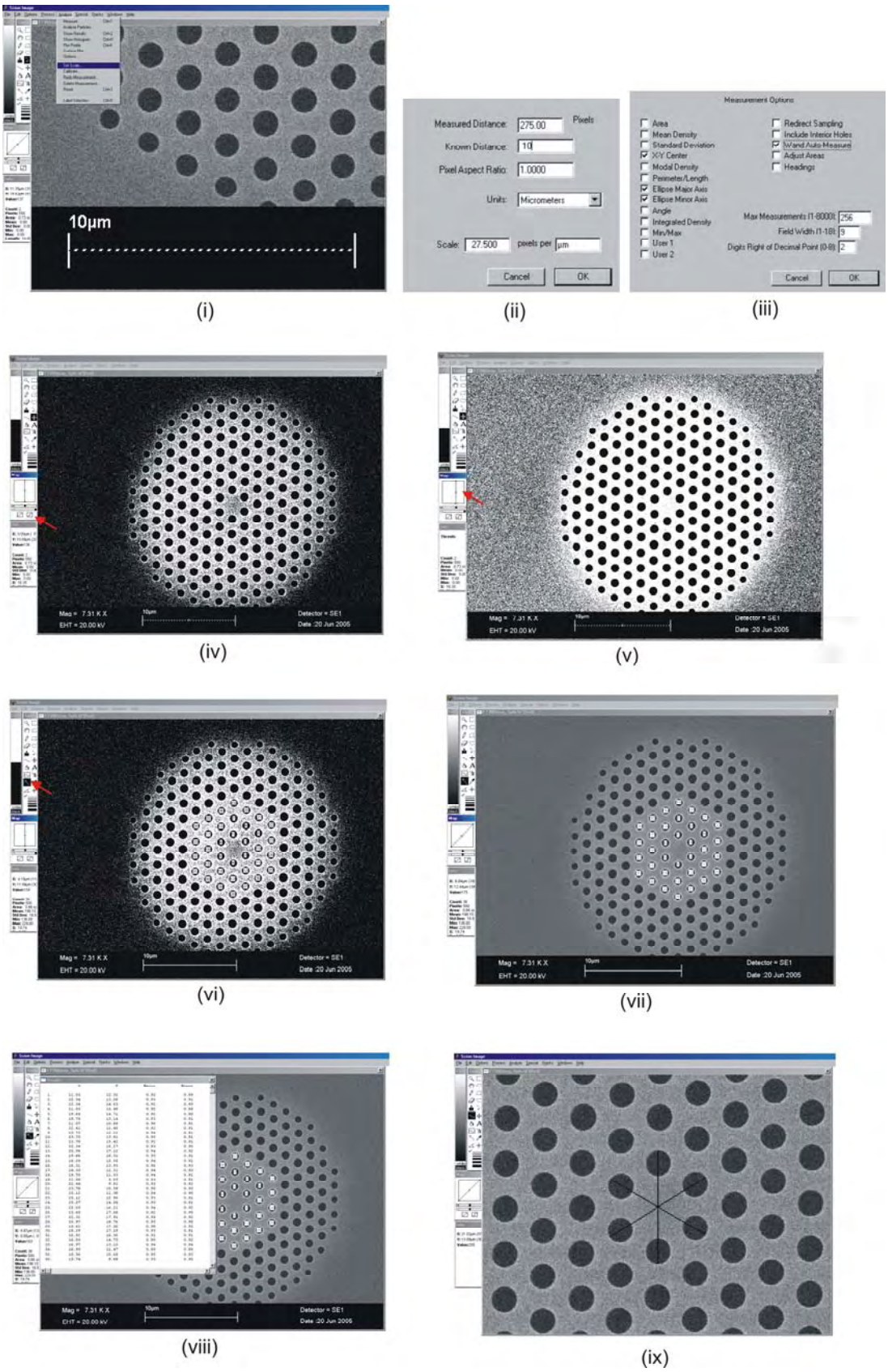

Fig. 5.8. A Step-by-step guide to measure the hole positions and sizes using the 'Scion Image' program. (See text page 88 for a detailed description.)

From this data, the averages of individual hole size and pitch were calculated for the first six rings. The results are summarised in Table 5.1 to 5.12, the standard deviations were calculated using the 'STDEV' command in Excel.

Statistics - F738(b)eop		PITCH (μm)			
	av. dist. of the six corner holes from centre	av. pitch betwwen corner holes and centre	av. pitch in a ring	av. d (μm)	av. d/Λ
1st ring					
average	1.435		1.435	0.546	0.380
st. dev.	0.049		0.022	0.018	
2nd ring					
average	2.869	1.434	1.434	0.561	0.391
st. dev.	0.211	0.105	0.033	0.014	
3rd ring					
average	4.312	1.437	1.437	0.563	0.392
st. dev.	0.263	0.088	0.033	0.015	
4th ring					
average	5.743	1.436	1.436	0.559	0.389
st. dev.	0.312	0.078	0.031	0.015	
5th ring					
average	7.163	1.433	1.433	0.550	0.384
st. dev.	0.363	0.073	0.030	0.015	
6th ring					
average	8.557	1.426	1.427	0.527	0.369
st. dev.	0.407	0.068	0.031	0.023	

Table 5.1. Summary of structure dimensions for F738b eop

Statistics - F738(b)20mfromeop		PITCH (μm)			
	av. dist. of the six corner holes from centre	av. pitch betwwen corner holes and centre	av. pitch in a ring	av. d (μm)	av. d/Λ
1st ring					
average	1.435		1.435	0.573	0.399
st. dev.	0.035		0.027	0.016	
2nd ring					
average	2.869	1.434	1.434	0.590	0.411
st. dev.	0.207	0.103	0.036	0.013	
3rd ring					
average	4.309	1.436	1.436	0.587	0.409
st. dev.	0.261	0.087	0.033	0.015	
4th ring					
average	5.745	1.436	1.436	0.584	0.407
st. dev.	0.312	0.078	0.031	0.011	
5th ring					
average	7.167	1.433	1.434	0.578	0.403
st. dev.	0.363	0.073	0.029	0.012	
6th ring					
average	8.561	1.427	1.427	0.556	0.389
st. dev.	0.407	0.068	0.030	0.021	

Table 5.2. Summary of structure dimensions for F738b 20mfeop

Statistics - F738(b)30mfromeop		PITCH (μm)			
	av. dist. of the six corner holes from centre	av. pitch betwwen corner holes and centre	av. pitch in a ring	av. d (μm)	av. d/Λ
1st ring					
average	1.441		1.441	0.563	0.391
st. dev.	0.062		0.038	0.028	
2nd ring					
average	2.890	1.445	1.445	0.588	0.407
st. dev.	0.220	0.110	0.047	0.016	
3rd ring					
average	4.337	1.446	1.446	0.583	0.403
st. dev.	0.275	0.092	0.044	0.022	
4th ring					
average	5.784	1.446	1.446	0.581	0.402
st. dev.	0.333	0.083	0.042	0.019	
5th ring					
average	7.215	1.443	1.443	0.572	0.397
st. dev.	0.387	0.077	0.040	0.021	
6th ring					
average	8.617	1.436	1.437	0.547	0.381
st. dev.	0.436	0.073	0.043	0.025	

Table 5.3. Summary of structure dimensions for F738b 30mfeop

Statistics - F738(b)40mfromeop		PITCH (μm)			
	av. dist. of the six corner holes from centre	av. pitch betwwen corner holes and centre	av. pitch in a ring	av. d (μm)	av. d/Λ
1st ring					
average	1.435		1.435	0.564	0.393
st. dev.	0.046		0.031	0.020	
2nd ring					
average	2.868	1.434	1.434	0.584	0.407
st. dev.	0.210	0.105	0.043	0.016	
3rd ring					
average	4.313	1.438	1.438	0.580	0.404
st. dev.	0.268	0.089	0.040	0.021	
4th ring					
average	5.743	1.436	1.436	0.580	0.404
st. dev.	0.321	0.080	0.037	0.017	
5th ring					
average	7.172	1.434	1.435	0.574	0.400
st. dev.	0.377	0.075	0.036	0.014	
6th ring					
average	8.568	1.428	1.429	0.552	0.386
st. dev.	0.425	0.071	0.037	0.019	

Table 5.4. Summary of structure dimensions for F738b 40mfeop

Statistics - F738(b)50mfromeop		PITCH (μm)			
	av. dist. of the six corner holes from centre	av. pitch betwwen corner holes and centre	av. pitch in a ring	av. d (μm)	av. d/Λ
1st ring					
average	1.449		1.449	0.607	0.419
st. dev.	0.030		0.029	0.016	
2nd ring					
average	2.909	1.454	1.454	0.623	0.428
st. dev.	0.210	0.105	0.036	0.016	
3rd ring					
average	4.369	1.456	1.456	0.623	0.428
st. dev.	0.263	0.088	0.032	0.017	
4th ring					
average	5.823	1.456	1.456	0.624	0.428
st. dev.	0.315	0.079	0.030	0.013	
5th ring					
average	7.269	1.454	1.454	0.615	0.423
st. dev.	0.367	0.073	0.030	0.012	
6th ring					
average	8.686	1.448	1.448	0.596	0.411
st. dev.	0.412	0.069	0.030	0.020	

Table 5.5. Summary of structures dimension for F738b 50mfeop

Statistics - F738(b)60mfromeop		PITCH (μm)			
	av. dist. of the six corner holes from centre	av. pitch betwwen corner holes and centre	av. pitch in a ring	av. d (μm)	av. d/Λ
1st ring					
average	1.453		1.453	0.610	0.420
st. dev.	0.037		0.029	0.015	
2nd ring					
average	2.917	1.458	1.458	0.630	0.432
st. dev.	0.211	0.105	0.036	0.018	
3rd ring					
average	4.384	1.461	1.461	0.631	0.432
st. dev.	0.264	0.088	0.033	0.017	
4th ring					
average	5.840	1.460	1.460	0.627	0.429
st. dev.	0.316	0.079	0.030	0.016	
5th ring					
average	7.291	1.458	1.458	0.622	0.426
st. dev.	0.368	0.074	0.030	0.013	
6th ring					
average	8.715	1.452	1.453	0.604	0.416
st. dev.	0.415	0.069	0.031	0.020	

Table 5.6. Summary of structure dimensions for F738b 60mfeop

Statistics - F738(b)70mfromeop					
		PITCH (μm)			
	av. dist. of the six corner holes from centre	av. pitch betwwen corner holes and centre	av. pitch in a ring	av. d (μm)	av. d/Λ
1st ring					
average	1.457		1.457	0.630	0.432
st. dev.	0.063		0.033	0.023	
2nd ring					
average	2.930	1.465	1.465	0.648	0.442
st. dev.	0.222	0.111	0.044	0.017	
3rd ring					
average	4.395	1.465	1.465	0.647	0.442
st. dev.	0.276	0.092	0.040	0.019	
4th ring					
average	5.866	1.466	1.467	0.648	0.442
st. dev.	0.332	0.083	0.039	0.019	
5th ring					
average	7.320	1.464	1.464	0.639	0.437
st. dev.	0.386	0.077	0.037	0.017	
6th ring					
average	8.748	1.458	1.458	0.622	0.426
st. dev.	0.437	0.073	0.039	0.021	

Table 5.7. Summary of structure dimensions for F738b 70mfeop

Statistics - F738(b)78mfromeop					
		PITCH (μm)			
	av. dist. of the six corner holes from centre	av. pitch betwwen corner holes and centre	av. pitch in a ring	av. d (μm)	av. d/Λ
1st ring					
average	1.445		1.445	0.646	0.447
st. dev.	0.046		0.030	0.020	
2nd ring					
average	2.910	1.455	1.455	0.662	0.455
st. dev.	0.217	0.108	0.041	0.017	
3rd ring					
average	4.374	1.458	1.458	0.664	0.455
st. dev.	0.270	0.090	0.037	0.018	
4th ring					
average	5.834	1.458	1.459	0.662	0.454
st. dev.	0.327	0.082	0.036	0.017	
5th ring					
average	7.281	1.456	1.456	0.656	0.451
st. dev.	0.381	0.076	0.035	0.016	
6th ring					
average	8.702	1.450	1.451	0.638	0.440
st. dev.	0.430	0.072	0.035	0.020	

Table 5.8. Summary of structure dimensions for F738b 78mfeop

Statistics - F738(b)88mfromeop					
		PITCH (μm)			
	av. dist. of the six corner holes from centre	av. pitch betwwen corner holes and centre	av. pitch in a ring	av. d (μm)	av. d/Λ
1st ring					
average	1.455		1.455	0.663	0.455
st. dev.	0.052		0.034	0.022	
2nd ring					
average	2.929	1.464	1.464	0.678	0.463
st. dev.	0.219	0.110	0.042	0.021	
3rd ring					
average	4.401	1.467	1.467	0.681	0.464
st. dev.	0.275	0.092	0.042	0.020	
4th ring					
average	5.871	1.468	1.468	0.679	0.462
st. dev.	0.332	0.083	0.039	0.018	
5th ring					
average	7.329	1.466	1.466	0.670	0.457
st. dev.	0.389	0.078	0.039	0.019	
6th ring					
average	8.760	1.460	1.460	0.655	0.449
st. dev.	0.439	0.073	0.040	0.021	

Table 5.9. Summary of structure dimensions for F738b 88mfeop

Statistics - F738(b)98mfromeop					
		PITCH (μm)			
	av. dist. of the six corner holes from centre	av. pitch betwwen corner holes and centre	av. pitch in a ring	av. d (μm)	av. d/Λ
1st ring					
average	1.468		1.469	0.667	0.454
st. dev.	0.041		0.030	0.018	
2nd ring					
average	2.967	1.483	1.483	0.680	0.459
st. dev.	0.220	0.110	0.040	0.014	
3rd ring					
average	4.458	1.486	1.486	0.683	0.460
st. dev.	0.275	0.092	0.042	0.017	
4th ring					
average	5.947	1.487	1.487	0.683	0.459
st. dev.	0.332	0.083	0.038	0.014	
5th ring					
average	7.424	1.485	1.485	0.677	0.456
st. dev.	0.388	0.078	0.037	0.014	
6th ring					
average	8.871	1.478	1.479	0.661	0.447
st. dev.	0.438	0.073	0.038	0.018	

Table 5.10. Summary of structure dimensions for F738b 98mfeop

Statistics - F738(b)9mfromsop					
		PITCH (μm)			
	av. dist. of the six corner holes from centre	av. pitch betwwen corner holes and centre	av. pitch in a ring	av. d (μm)	av. d/Λ
1st ring					
average	1.532		1.532	0.840	0.548
st. dev.	0.033		0.031	0.022	
2nd ring					
average	3.114	1.557	1.557	0.857	0.550
st. dev.	0.230	0.115	0.042	0.021	
3rd ring					
average	4.692	1.564	1.564	0.859	0.549
st. dev.	0.289	0.096	0.039	0.024	
4th ring					
average	6.262	1.565	1.566	0.856	0.547
st. dev.	0.346	0.087	0.036	0.021	
5th ring					
average	7.819	1.564	1.564	0.851	0.544
st. dev.	0.403	0.081	0.036	0.020	
6th ring					
average	9.353	1.559	1.559	0.840	0.539
st. dev.	0.456	0.076	0.037	0.023	

Table 5.11. Summary of structure dimensions for F738b 184mfeop

Statistics - F738(b)sop					
		PITCH (μm)			
	av. dist. of the six corner holes from centre	av. pitch betwwen corner holes and centre	av. pitch in a ring	av. d (μm)	av. d/Λ
1st ring					
average	1.543		1.543	0.901	0.584
st. dev.	0.043		0.027	0.019	
2nd ring					
average	3.158	1.579	1.579	0.918	0.582
st. dev.	0.232	0.116	0.032	0.017	
3rd ring					
average	4.765	1.588	1.589	0.919	0.579
st. dev.	0.288	0.096	0.030	0.021	
4th ring					
average	6.351	1.588	1.588	0.917	0.578
st. dev.	0.337	0.084	0.026	0.016	
5th ring					
average	7.937	1.587	1.587	0.910	0.573
st. dev.	0.392	0.078	0.026	0.015	
6th ring					
average	9.494	1.582	1.583	0.897	0.567
st. dev.	0.442	0.074	0.028	0.020	

Table 5.12. Summary of structure dimensions for F738b sop

At the EOP, for the worst case scenario, the standard deviation of the pitch was 2.1% of the average in the 6th ring, and that for the hole size was 4.4%. They were much better than the accuracy level achieved in the fabrication of fibre with graded hole sizes. Indeed the deviations were even smaller in the first two rings. These results set the standard of the accuracy for the current technology in fabrication of small core holey fibres with regular hole size. The average

hole size, pitch and d/Λ of the first three rings along the fibre are shown in Fig. 5.9 (a), (b) and (c) respectively.

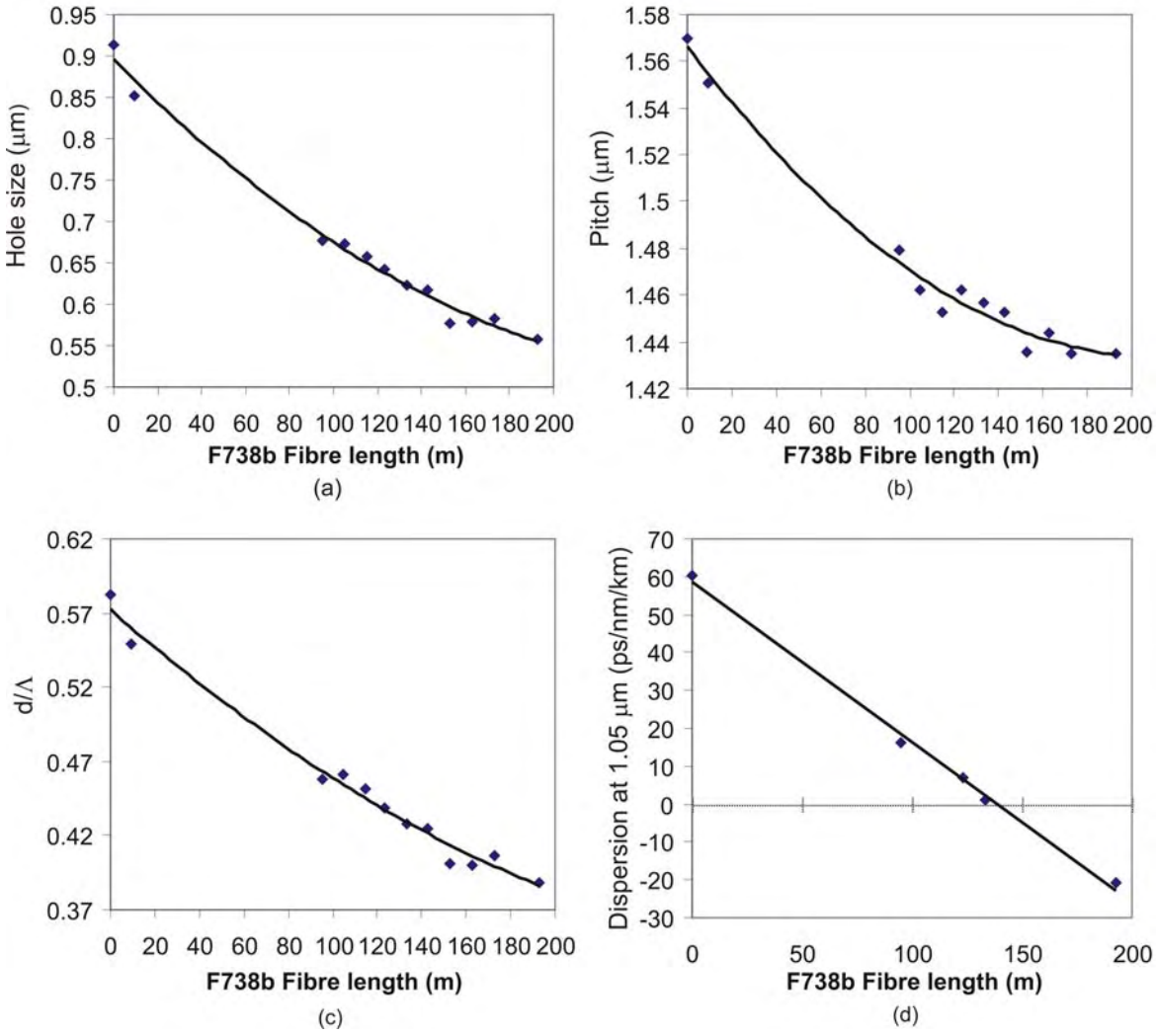

Fig. 5.9. The average (a) hole size, (b) pitch and (c) d/Λ of the first three rings along fibre 'F738b'. (d) The calculated dispersion at 1.05 μm along the same fibre. The polynomials least-squares fits are included in the graphs (black lines) (Calculated by F. Poletti).

Fig. 5.9(d) shows the calculated dispersion at 1.05 μm using the data in Table 5.1 to 5.12. It shows that the dispersion decreased almost linearly along the fibre. The calculated dispersion profiles of the different pieces of the fibre are shown in Fig. 5.10. However, these calculations were done without any correction factor applied to compensate for any systematic error in the measurement of the structure dimensions.

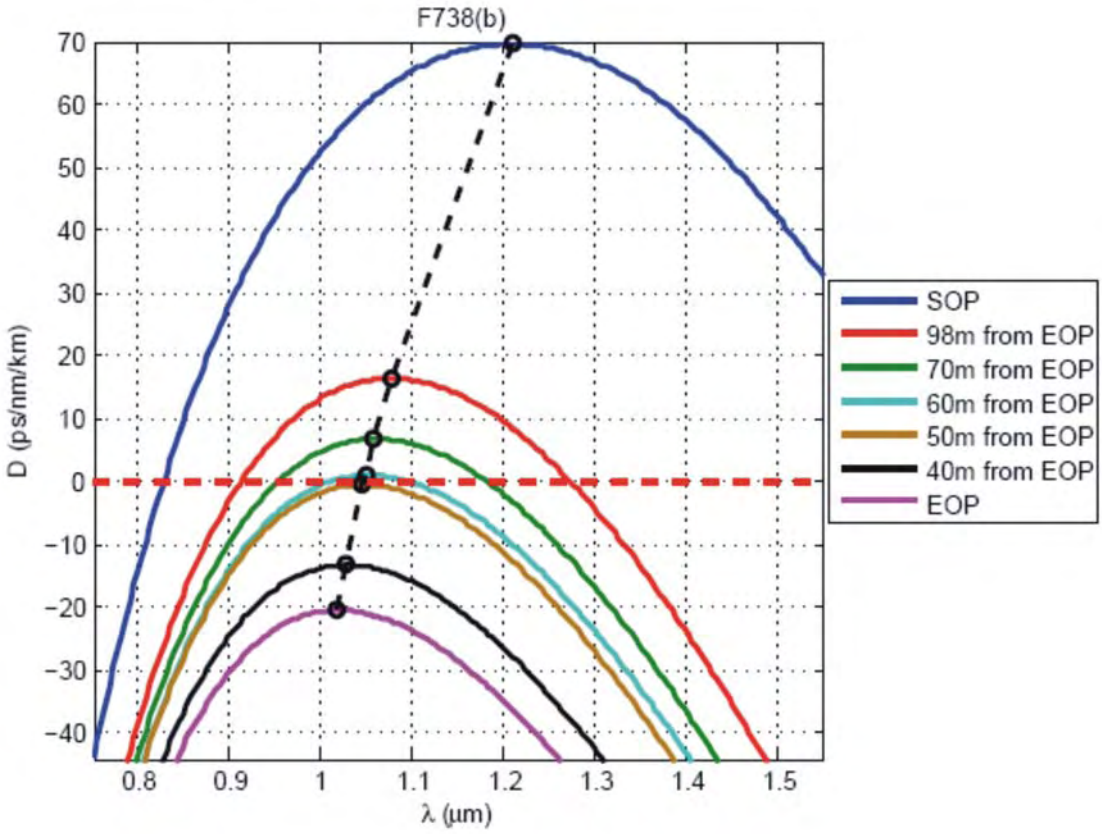

Fig. 5.10. The calculated dispersion profiles at different point along fibre 'F738b' without the correction factor (Calculated by F. Poletti).

The quality of the SEM pictures and the accuracy of the imaging program gave rise to errors. For example, in Fig. 5.8, all of the SEM pictures were recorded with 1024 × 768 pixels, and the scale was set to be 27.5 pixels per micron. Therefore if the error of the program automatic drawing tools was one pixel, then a minimum error of 0.036 μm should be accounted for when a hole size was measured. One way to improve the accuracy is to zoom-in to individual holes when taking the SEM pictures, where the scale would have a large number of pixels per micron. An example is shown in Fig. 5.11, the SEM picture at the top is the same as the one shown in Fig. 5.8 and had the same scale. The picture at the bottom was taken from the same structure but zoomed in, and had a more accurate scale. It shows visually the accuracy of the measurement, when the tool attempts to draw the circles around the circumference of the holes, the lines are smoother with more pixels in the bottom picture, therefore more accurately drawn. However, to take good quality hole-by-hole SEM pictures can be challenging and labour intensive, charging effects dominate the structure, and therefore only pictures with poor contrast are usually produced. This blurring effect due to the static-electrical charging prevents producing pictures with well defined edges. Moreover, a systematic error occurred from the thickness of the gold coating itself. It was estimated that the coating thickness was around 20 nm, thus the diameter of a hole in the samples is ~0.04 μm smaller than the real value.

According to Fig. 5.2(a), a few percent change in hole size can produce quite different dispersion profiles, smaller holes would in general produce lower dispersion.

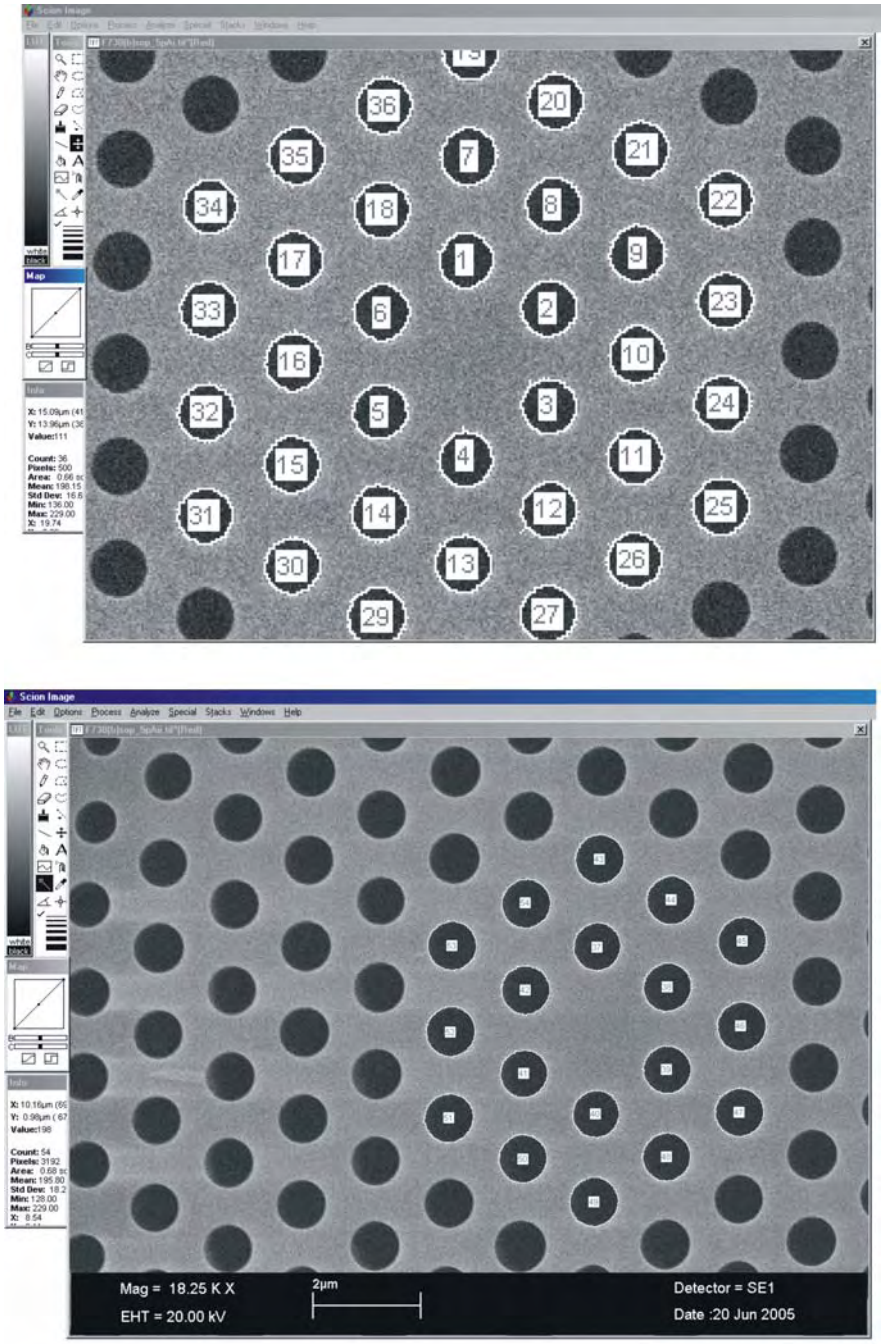

Fig. 5.11. Shows the drawing tool in 'Scion Image' for F738(b)sop with scale (Top) 27.5 pixels per micron and (bottom) 68.5 pixels per micron.

In the next section, with the support of the SC experimental and numerical data, it was found that the corrected dispersion curves were similar to the ones shown in Fig. 5.10, but shifted up by 30 m, i.e. for the curve labelled '70m from EOP' in Fig. 5.10, was in fact, the corrected dispersion profile at 40 mfeop.

5.5 Supercontinuum Experiments

5.5.1 Experimental setup

A mode-locked Nd:glass laser ('Time-bandwidth Products, Inc.') operating at 1.06 μm was used to generate fs pulses. The laser operated at a repetition rate of 80MHz and was able to generate a maximum average output power of 250mW. A pulse width of 378fs was measured just before entering the fibres using an SHG based autocorrelator (many thanks to Dr. J. H. V. Price and Dr. A. Malinowski for the initial setup). The schematic of the setup is shown in Fig. 5.12. An isolator ('Electro-Optics Technology, Inc.') was used to prevent unwanted feedback into the laser. And a ½-wave plate in conjunction with the polarising isolator was used to control the launch power. A 60× microscope objective was used to couple the light into various pieces (1 m) of fibres cut from 'F738b', with input coupling efficiencies in the range 13-30%. The fast and slow axes of the HFs were determined by inspecting the maximum and minimum nonlinear effects seen in the spectral domain, and the experiments were carried out with light launched on those axes. The results for the two axes were slightly different, suggesting that there was a small discrepancy in the dispersion between the two axes, however the overall conclusions were the same.

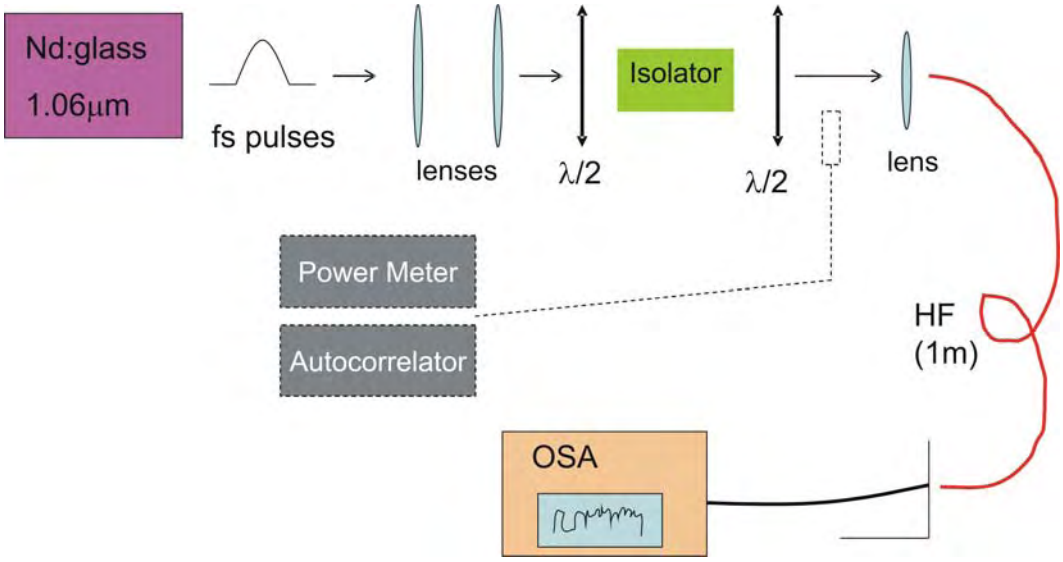

Fig. 5.12. A schematic of the supercontinuum experimental setup.

The spectra generated in eight pieces of fibres (98, 70, 60, 50, 40, 30 mfeop, SOP and EOP of 'F738b') were measured at various pump power levels. Due to poor coupling efficiency, the results for the SOP and 30 mfeop pieces are not included in this thesis. The overall experimental and numerical results are presented in the next section for fibre pieces at 98, 70, 60, 50, 40 mfeop and EOP, which are labelled Fibre A, B, C, D, E and F respectively. The discussions of the results are in Section 5.6.

5.5.2 Experimental and numerical results

The fibres had core diameters of ~2 μm. The measured average pitch, Λ, and air-filling fraction, d/Λ, for the first 6 rings are summarised in Table 5.13.

Fibres	Pitch, Λ (μm)	Air-filling fraction, d/Λ (μm)
A	1.482	0.456
B	1.463	0.437
C	1.457	0.426
D	1.453	0.423
E	1.435	0.399
F	1.434	0.384

Table 5.13. The measured average pitch, Λ, and air-filling fraction, d/Λ, for the first 6 rings of fibre A-F.

The spectra for Fibre B, D, E and F were recorded and saved from the OSA with 2 nm resolution over 3001 sample points. For Fibre A, 5 nm resolution over 1001 sample points were recorded, and for Fibre C, 0.5 nm resolution over 7001 sample points were recorded. The overall SC spectra generated in these fibres at different pump power levels are depicted in Fig. 5.13.

In order to understand the dominant nonlinear processes during pulse propagation in the fibres, I performed numerical simulations as described in Chapter 2, of the corresponding generalized nonlinear Schrödinger equation using a standard split-step Fourier tool [Paschotta] (many thanks to Dr. R. Paschotta for providing the software, and Dr. P. Horak for simulation assistance), which takes into account the full dispersion profile as well as nonlinear Kerr and Raman effects. A nonlinear refractive index n_2 of 2.5×10^{-20} m^2W^{-1} and effective mode area A_{eff} of 4 μm^2 were used as an input to these simulations (measured A_{eff} = 3.8 μm^2 (Fibre A) and 4.8 μm^2 (Fibre F), respectively). The simulations were carried out for 2048 points over a spectral range of 1200 nm, from 500 nm to 1700 nm wavelength, which also provides good coverage and resolution for the observation of the spectral evolution of the pulses. Examples of the simulated spectra together with the corresponding spectra taken from the experiments are shown in Fig. 5.14, and they showed good agreement.

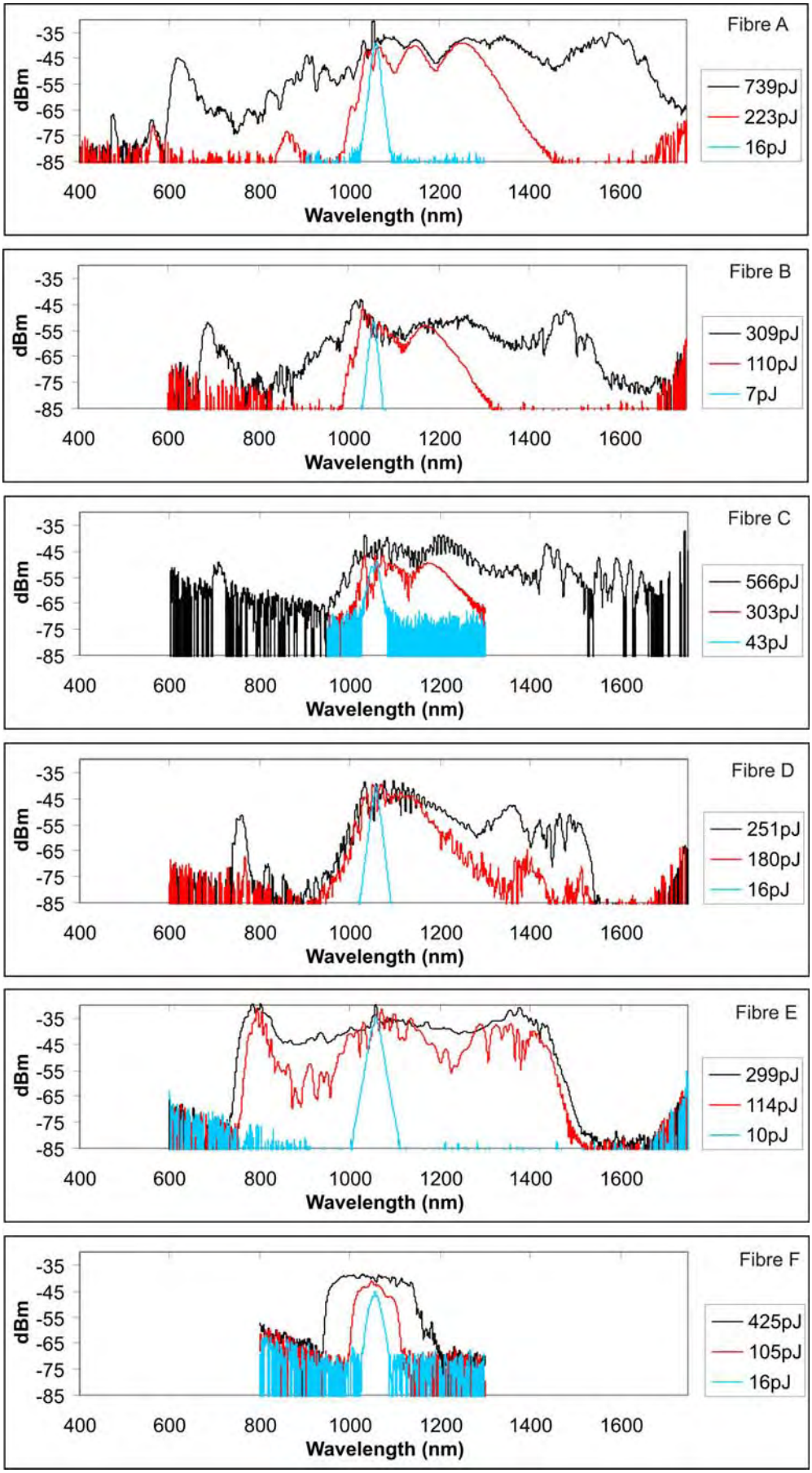

Fig. 5.13. The SC spectra generated in Fibres A-F at different pump power levels.

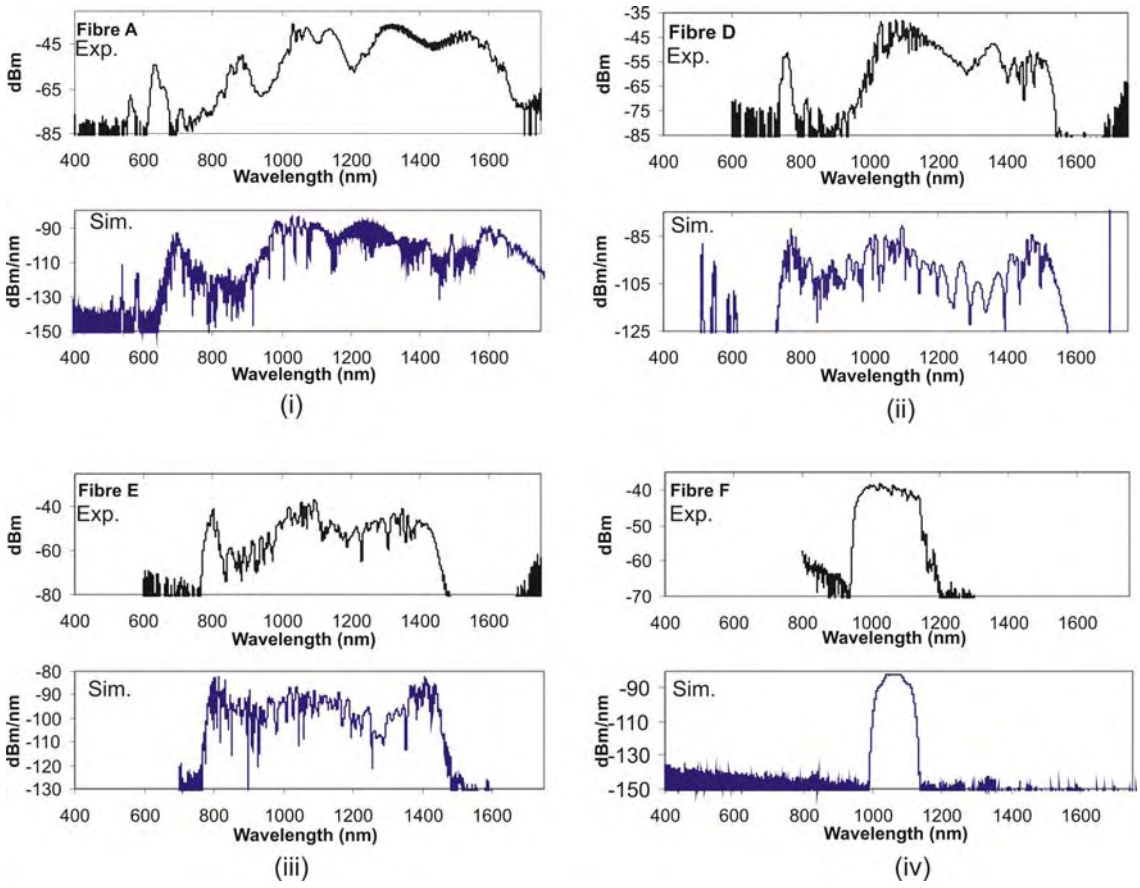

Fig. 5.14. The comparison of the simulated (blue, lower) and experimental (black, upper) spectra for (i) Fibre A, taken at 409 pJ in the experiment and 400 pJ in the simulation, (ii) Fibre D, taken at 251 pJ in the experiment and 240 pJ in the simulation, (iii) Fibre E, taken at 446 pJ in the experiment and 400 pJ in the simulation, and (iv) Fibre F, taken at 425 pJ in the experiment and 400 pJ in the simulation.

From the results shown in Fig. 5.13 and 5.14, a correction factor for the dispersion profiles was found. By inspecting the peak components and the dips in the spectra, a good estimation of the zero-dispersion wavelengths, and thus the dispersion profiles were made. The dispersion profiles calculated in Fig. 5.10 turned out to be slightly too low, mainly due to the imperfection of the fabrication, and the limited accuracy of the measurement of the features sizes in the fibre structures. From the experimental results and the slight rescaling with the correction factor mentioned in Section 5.4, the prediction of the corrected dispersion profiles were made. The corrected dispersion profiles are shown in Fig. 5.15. This was further reinforced in the next section when the phase matching curves of the fibres were calculated.

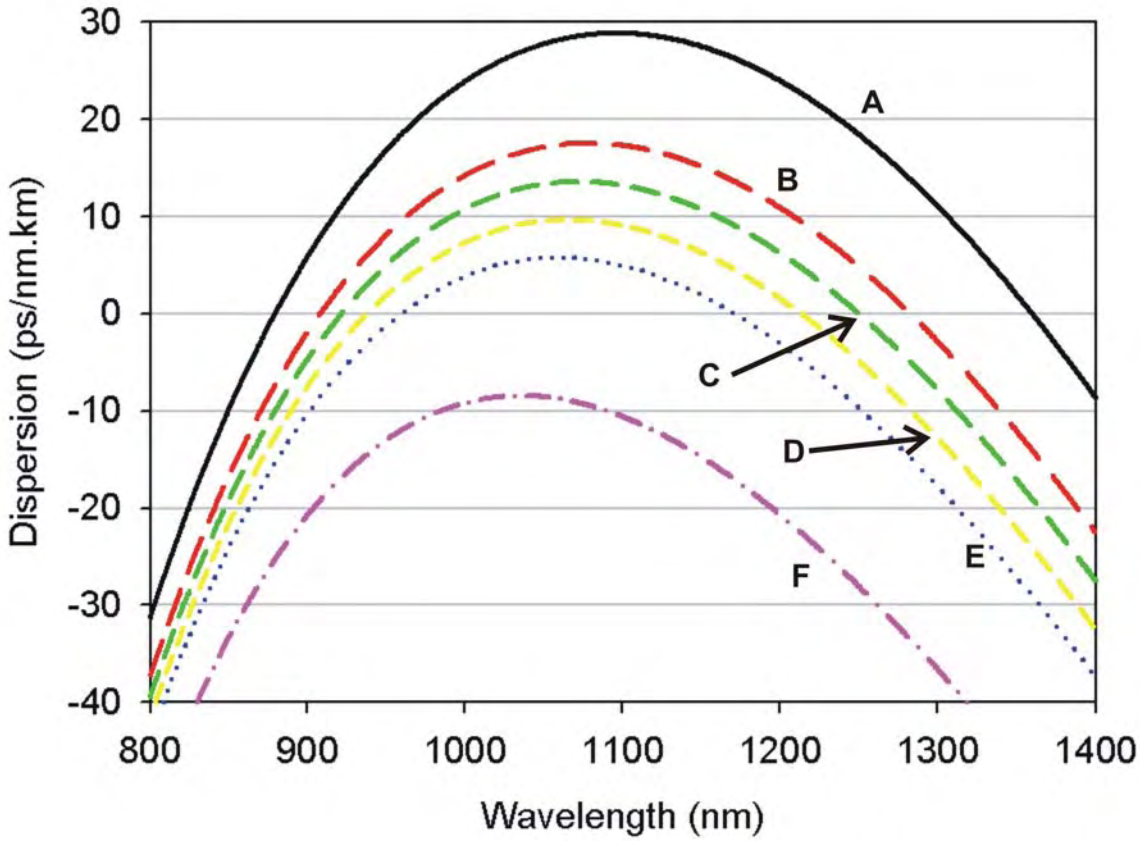

Fig. 5.15. The corrected dispersion profiles for Fibre A to F.

5.6 Discussions

5.6.1 Phase matching curves

For the interpretation of the observed spectra, the properties of the FWM processes were investigated. Pumping the fibres in the anomalous dispersion regime can lead to the phase-matched generation of long and short wavelength bands via FWM [Andersen 2004]. The generated components were calculated directly from the dispersion profiles (by Dr. P. Horak). The phase matching curves at low pump power for Fibres A to E are shown in Fig. 5.16 and the corresponding phase matched ranges are shown in Fig. 5.17.

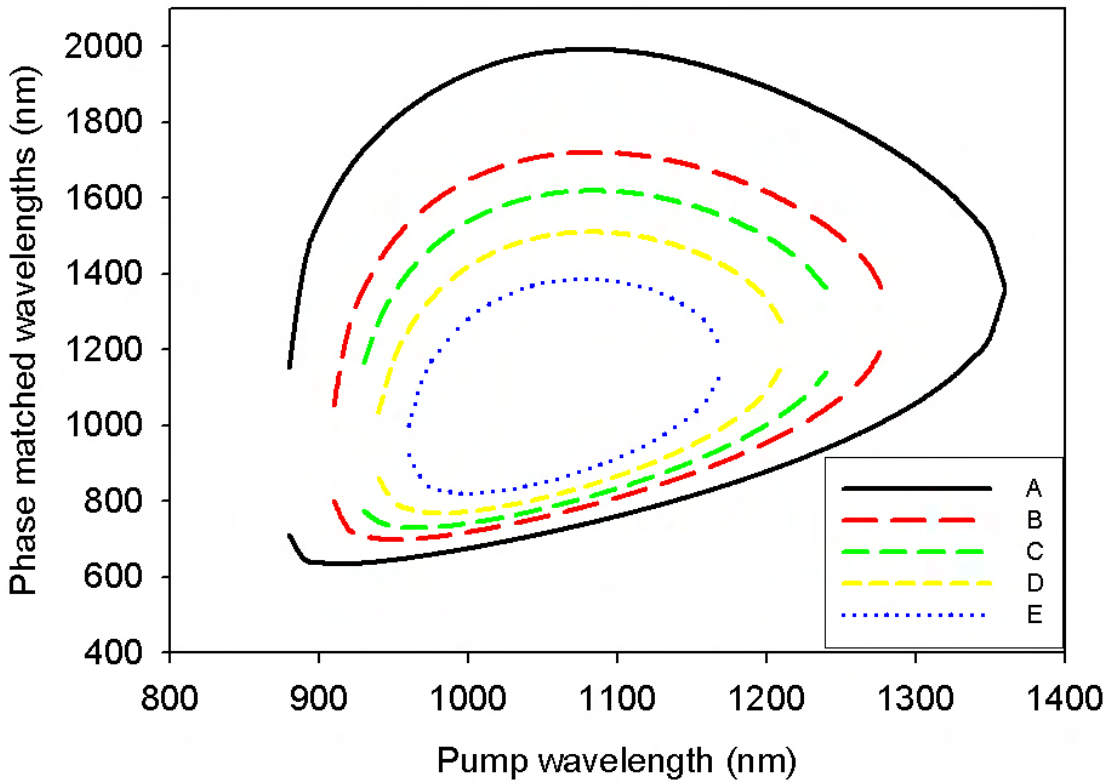

Fig. 5.16 Phase matching curves for Fibre A to E.

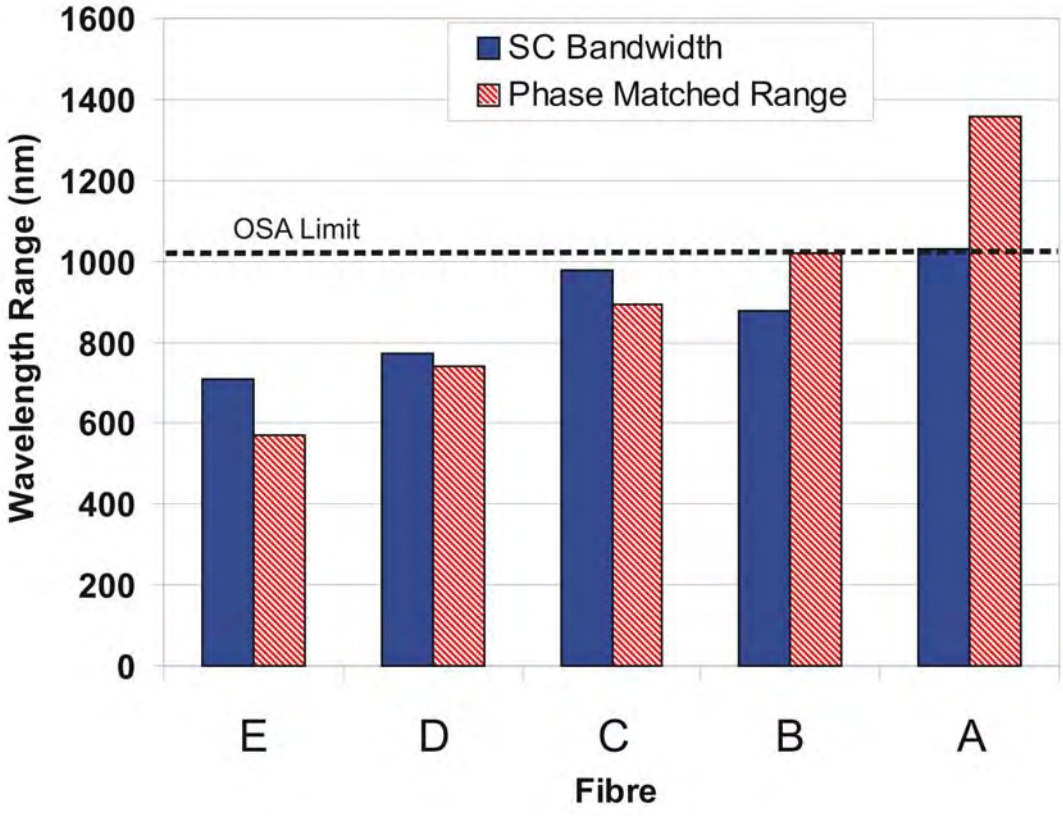

Fig. 5.17 The SC bandwidth (at maximum launched power) and the phase matched range for Fibre A to E.

When the separation of the two zero-dispersion wavelengths increases, i.e., the width of anomalous dispersion region, the resulting phase matched wavelength range also increases, see Fig. 5.15, 5.16 and 5.17. Here, the phase matched range is taken from the longest and the shortest wavelengths generated by FWM processes when pumped inside the anomalous dispersion regime. For example, for Fibre A the longest Stokes band is around 1990 nm for pumping at 1080 nm, and the shortest anti-Stokes band is around 630 nm for pumping at 910 nm, which implies a phase matched range of ~1360 nm. Note also that the phase matching curves allow us to interpret some pairs of peaks found in the SC spectra of Fig. 5.14 by FWM.

The SC bandwidths at maximum pump power for Fibres B, C, D, E, and F were measured. All bandwidths were taken at the 20 dB level in order to include all wavelength components independent of experimental power constraints. The results are shown along with the phase matched range in Fig. 5.17. Good agreement was found for Fibres B, C, D, and E. For Fibre F, no phase-matched range exists and the observed broadening is due to other mechanisms. For completeness we have included the data for Fibre A in Fig. 5.17. However, for this fibre the experimental measurement of the SC bandwidth was limited to a maximum value of ~1000 nm by the 1650 nm long wavelength cut-off of the spectrum analyzer rendering the comparison with theory somewhat meaningless.

5.6.2 Dominant nonlinear phenomena

The SC spectra for Fibres A to F were measured at various pump power levels and the results were compared with numerical simulations to identify the relevant nonlinear mechanisms. Taken together, these results provide a consistent picture of SC generation in dispersion flattened fibres, which are discussed in the following using the examples of the fibres with the longest anomalous dispersion range (Fibre A) and the shortest range (Fibre E). The experimental SC spectra at different pulse energy levels in Fibre A and E are shown in Figs. 5.18 and 5.19, respectively, to show the evolution of the SC generation.

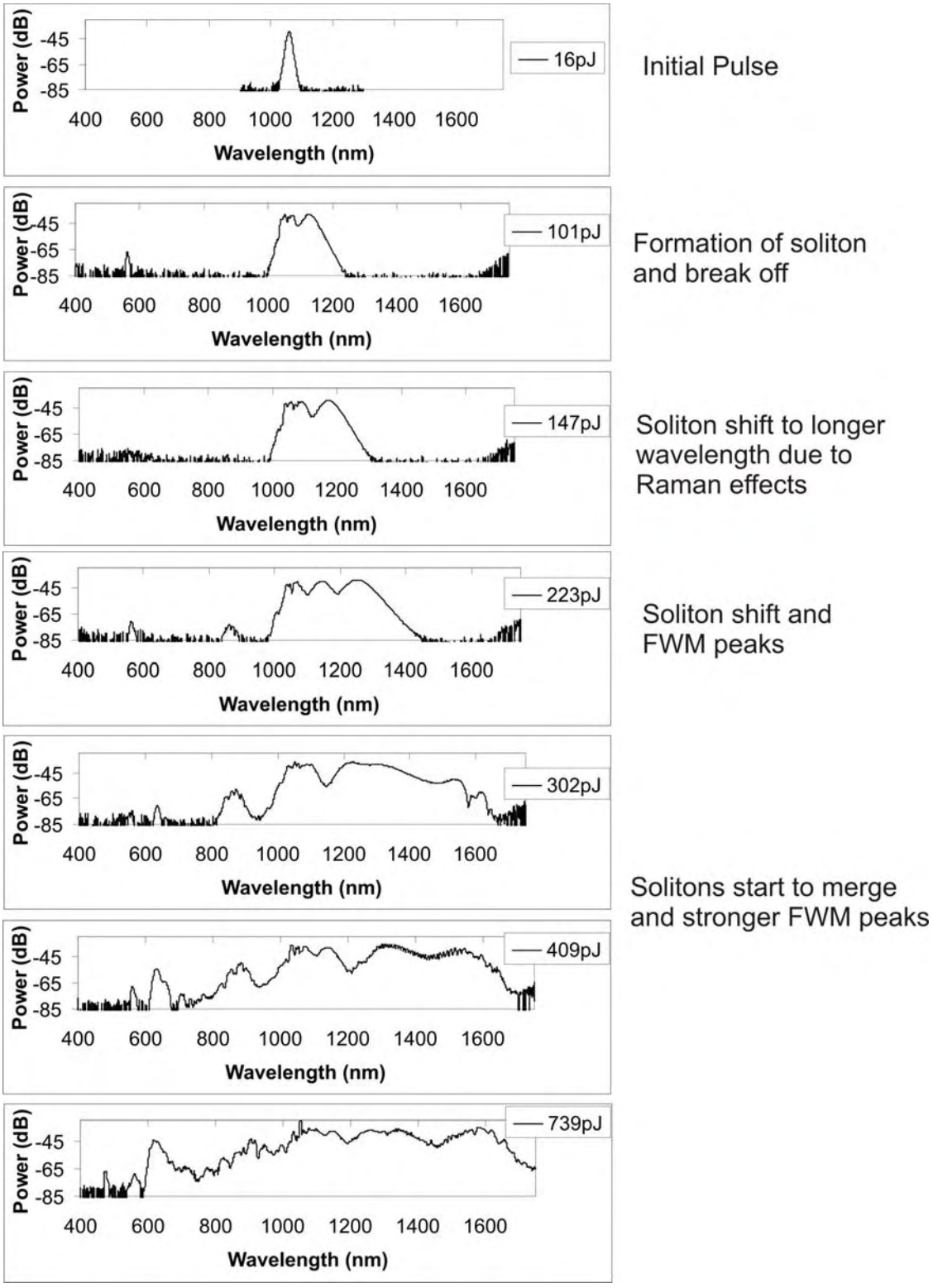

Fig. 5.18. The supercontinuum spectral evolution at increasing launched power in Fibre A.

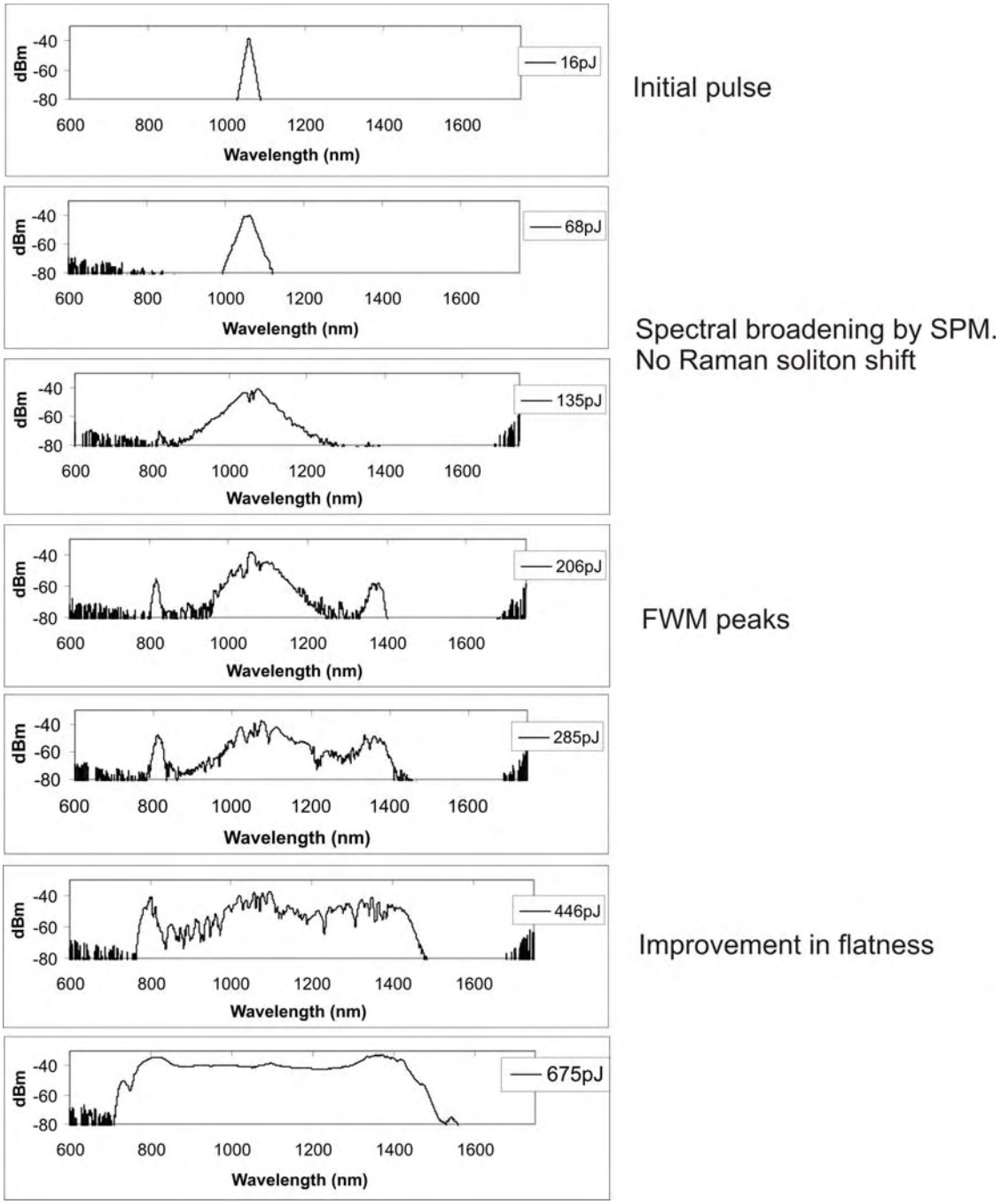

Fig. 5.19. The supercontinuum spectral evolution at increasing launched power in Fibre E.

Fibre A exhibits a wide anomalous dispersion region with a separation of the two ZDWs of ~470 nm. Here, SC generation at low powers starts with the formation of fundamental solitons which are subsequently shifted to longer wavelengths by SSFS, as observed by the soliton peak at ~1200 nm in Fig. 5.18 at 147 pJ. Numerically, I found that this leads to nearly linear broadening of the SC spectrum with increasing pump power below 300 pJ. At pump powers of 300-400 pJ, these soliton effects shift power into most of the anomalous dispersion wavelength range, and thus FWM processes start to generate frequency components outside this range, see Fig. 5.18 at 409 pJ. Fig. 5.20(a) shows the measured SC bandwidth together with results of simulations with constant anomalous dispersion, where no phase-matched FWM processes can

occur [Frosz, 2005]. In this case only the linear broadening due to SSFS is observed but no sudden increase for higher powers. For pump powers exceeding ~400 pJ, the measured SC bandwidth appears approximately constant at ~1000 nm (Fig. 5.18, at 739 pJ, and Fig. 5.20), although this measurement is again limited by our OSA.

Different mechanisms can be observed in the fibres with narrower anomalous dispersion regions, e.g, for Fibre E which exhibits a narrow anomalous dispersion region with a spacing of the two ZDWs of ~230 nm. This fibre generates a symmetrical spectrum with sharp edges, see Fig. 5.19. The measured SC bandwidth as a function of pump power in this case is shown in Fig. 5.20(b) together with corresponding simulation results. For this fibre, the spectra show no evidence of soliton formation at any power level. Instead, SC generation is dominated by SPM and FWM processes [Hilligsøe, 2004]. At low power levels, the spectrum is slightly broadened by SPM (Fig. 5.19, 68 pJ and 135 pJ). At input pulse energies of ~200 pJ, FWM processes set in, which leads to a sudden increase in bandwidth to a near maximum value. Two main phase-matched wavelength components are observed at ~800 nm and ~1400 nm together with the residual pump peak at ~1060 nm. At maximum input power, the spectrum becomes more uniform and the flatness improves to ~10 dB (Fig. 5.19, at 675pJ). This has to be compared to a flatness of ~20 dB for Fibre A. The maximum span of the spectrum of Fibre E is narrower than that of Fibre A, but much lower pump energies are required to reach the maximum bandwidth. Therefore, the spectral shape of the SC is determined primarily by the fibre characteristics and is essentially independent of the specific characteristics of the pump laser itself [Hilligsøe, 2004].

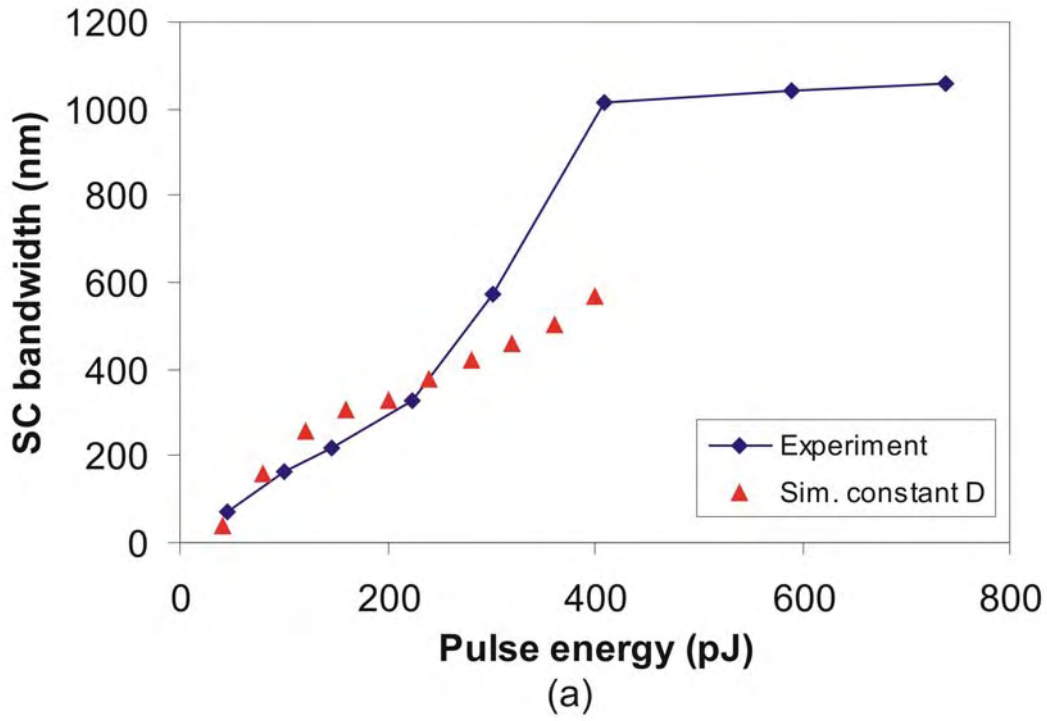

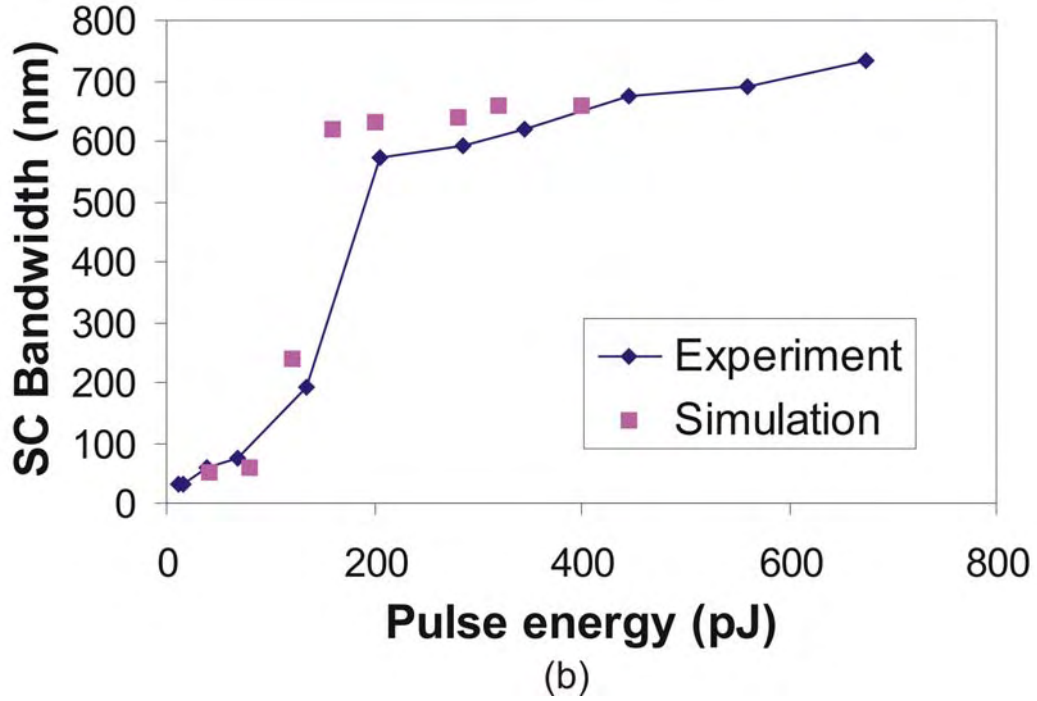

Fig. 5.20. SC bandwidth at different input pulse energy levels for (a) Fibre A, and (b) Fibre E.

The different behaviour of supercontinuum generation in fibres with narrow and broad anomalous dispersion regions, respectively, can be understood by the following considerations. The fibres with broad anomalous dispersion exhibit comparably large dispersion at the pump wavelength of 1060 nm. The dispersion length L_D [Agrawal, 2007] is thus short enough that dispersion effects play a significant role in the pulse dynamics within the 1 m length of the fibres, a requirement for soliton formation. Simultaneously, the large dispersion and the large

wavelength difference between the frequency components generated by FWM (1990 nm and 720 nm for a 1060 nm pump in Fibre A) lead to spatial walk-off within 1 cm of propagation. This effect strongly suppresses the FWM gain. For fibres with narrow anomalous dispersion regions, on the other hand, the dispersion at the pump wavelength is small. Therefore, nonlinear effects dominate over dispersion effects and no solitons can be formed within 1 m of fibre. Moreover, spatial walk-off between the FWM components at 1380 nm and 860 nm created from the 1060 nm pump in Fibre E occurs only after 20 cm of propagation and therefore the FWM gain is much larger in this fibre and the sudden increase in SC bandwidth, as shown in Fig. 5.20(b), occurs at lower pump powers.

Finally, for a fibre with wholly normal dispersion (Fibre F), no solitons can be formed and no phase-matched FWM processes can occur. The observed spectrum, see Fig. 5.13, shows some residual broadening due to SPM, but no supercontinuum is observed. However, the resulting spectrum has a flatness of <5dB due to the absence of Modulation Instability in the normal dispersion regime [Falk, 2005].

5.7 Conclusions

A detailed procedure for the fabrication of dispersion-flattened holey fibres with two zero-dispersion wavelengths at 1 μm has been presented. The structural variation and the measurement of the structural dimensions has been discussed for such regular hole size HFs, with the fabrication accuracy set to a few percents variation for the hole size and pitch size. The same fabrication method can be used for producing dispersion-decreasing holey fibre, which is studied in the next chapter.

The generation of supercontinuum light in a range of small-core holey fibres with flattened dispersion profiles has been systematically investigated, using 380 fs pump pulses at 1.06 μm. The phase matched wavelength ranges for each fibre has been calculated, and it has been shown that this accurately predicts the maximum SC bandwidth [Schreiber, 2005]. By measuring the SC bandwidths at varying pulse power and comparing the results with numerically simulated spectra, the different nonlinear processes which are dominating the SC generation in each parameter regime has been identified. Wider anomalous dispersion regions give rise to broader supercontinua, however, at the cost of reduced flatness and higher pump powers. The most uniform spectra with improved stability against laser power and frequency fluctuations were found in fibres with two closely spaced zero-dispersion wavelengths. For examples, simulation shows that for fibre E with pump pulses at 1 μm, 1.08 μm, 1.1 μm and 1.12 μm, the generated spectra are very similar to those found when pumped at 1.06 μm.

Chapter 6 Pulse compression at 1.06 μm in dispersion-decreasing holey fibres

6.1 Introduction

Tapered holey fibres have been used over the past few years in a variety of applications ranging from mode conversion, [Town, 2001] to UV-to-IR supercontinuum generation, [Kudlinski]. Very recently, their potential for compression of ps pulses has been pointed out, [Hu, 2006]. This Chapter describes compression of low-power fs pulses at 1.06 μm in a dispersion-decreasing holey fibre (DDHF).

Optical pulse compression techniques are important for the generation of ultrashort pulses. Applications include measurement of ultrafast physical processes, [Auston, 1988], optoelectronic terahertz time domain spectroscopy, [Hu, 1995], optoelectronic sampling, [Nagatsuma, 1994], and ultrahigh-data-rate optical communications. Compression of soliton pulses propagating in conventional dispersion decreasing optical fibres (DDF) is a well-established technique, [Chernikov, 1991]. Early demonstrations at 1.55 μm wavelength already showed compression from 630 fs to 115 fs in a 100 m DDF and from 3.5 ps down to 230 fs in a 1.6 km DDF, [Chernikov, 1993].

An optical soliton is the result of the cancellation of pulse broadening due to second order dispersion by the material refractive index nonlinearity (see Chapter 2). A small variation in the dispersion has a similar perturbative effect as an amplification or loss, [Bogatyrev, 1991, Mamyshev, 1991], since such a variation perturbs the equilibrium between the dispersion and nonlinearity in such a way that when, for example, the dispersion decreases, the soliton pulse is compressed. Hence, the use of fibres with variable dispersion is viewed as an effective method to control optical solitons in soliton communication systems. DDF's have been recognized to be useful for high-quality, stable, adiabatic soliton pulse compression and soliton train generation, [Mamyshev, 1991, Ivanov, 1992]. Conventional DDF's are fabricated where the core diameter of a single-mode fibre is varied through tapering the fibre during the drawing process, and hence changing the waveguide contribution to the second-order dispersion.

The dispersion is monotonically and smoothly decreased from an initial value to a smaller value at the end of the length according to some specified profile. Provided the dispersion variation in the DDF is sufficiently gradual, soliton compression can be an adiabatic process where an input fundamental soliton pulse can be ideally compressed as it propagates, while retaining its soliton character and conserving the energy. However, the scheme requires

anomalous dispersion and is therefore limited to wavelengths beyond 1.2 μm in conventional silica fibres.

The increased design flexibility provided by holey fibres allows anomalous dispersion to be achieved for a wide range of wavelengths, e.g., at 1.06 μm, which is attractive because of the availability of efficient Yb-doped fibre lasers. Moreover, because of the small effective mode area and corresponding large nonlinearity of such holey fibres, soliton energies can be as low as 1 pJ, with ~100 fs pulse duration.

This chapter is organised as follows. In Section 6.2 we study the fibre design and fabrication requirements for soliton compression at 1.06 μm in DDHF. The experimental results are presented in Section 6.3, and discussed in Section 6.4. Conclusions are in Section 6.5.

6.2 Fibre design and fabrication

6.2.1 Fibre design

The DDHF design was based on a hexagonal geometry, offering a flattened dispersion profile in the vicinity of 1.06 μm, see Chapter 5. In Fig. 6.1, the fibre design for such a dispersion profile is presented again, and the corresponding profiles to show the tolerance levels in the deviation of d/Λ and Λ from the optimum design. Here, I used the tolerance graphs to design the dispersion-decreasing holey fibre. Fig. 6.1 shows that at 1.06 μm wavelength, the dispersion varied moderately by either varying d/Λ and/or Λ, and still preserved a flat dispersion profile throughout. The fibre should have a high initial value of D at the input end, to a small value at the output end.

Starting with the soliton definition $N^2 = L_D / L_{NL}$, where $N = 1$ for a fundamental soliton, and L_D and L_{NL} are the dispersion length and nonlinear length respectively. They can be written as follows, [Agrawal, 2007],

$$L_D = \frac{\tau_0^2}{|\beta_2|} = \frac{2\pi c \tau_0^2}{D\lambda^2} \qquad \text{Eqn. 6.2:1}$$

$$L_{NL} = \frac{1}{\gamma P_{sol}} = \frac{\lambda A_{eff}}{2\pi n_2 P_{sol}} = \frac{\tau_0 \lambda A_{eff}}{\pi n_2 E_{sol}} \qquad \text{Eqn. 6.2:2}$$

where τ_0 is the soliton width, c is the speed of light, λ is the wavelength, n_2 is the nonlinear-index coefficient and E_{sol} is the pulse energy. Thus,

$$N^2 = \frac{L_D}{L_{NL}} = \frac{2\pi^2 c n_2 \tau_0 E_{sol}}{\lambda^3 D A_{eff}} \qquad \text{Eqn.6.2:3}$$

Therefore, for given fibre parameters, the full width at half maximum (FWHM), τ, of a fundamental soliton is

$$\tau = 1.76 \frac{\lambda^3 D A_{eff}}{2\pi^2 c n_2 E_{sol}} \qquad \text{Eqn. 6.2:4}$$

For adiabatic soliton compression in a lossless fibre, E_{sol} stays constant and the pulse width is proportional to dispersion and effective area. In practice, E_{sol} is reduced by the fibre loss during pulse propagation.

The history of this project is as follows. A fibre with D= 10 to 1 ps/nm/km was set as the initial target, which would provided a pulse compression factor of 10. This corresponds to a reduction of ~5% in d/Λ, from ~ 0.43 to 0.41, and Λ= 1.5 μm, see Fig. 6.1(a). However, in the Section 6.2.2, it was found that, in order to achieve a compression factor of 10 from 380 fs input soliton (the readily available and reliable high power light source), low propagation loss in the fibre was required. Therefore, extra capillary polishing steps were needed on top of the standard fibre fabrication processes described in Chapter 3. For this reason, a DDHF with D~ 6 to 2 was set as the first realistic fabrication target, and a shorter input soliton was used in the experiment; with the view to improve to the initial target in the second iteration. Unfortunately, during the preparation of the preform in my second attempt, all of the glass-works were lost in the Mountbatten building fire.

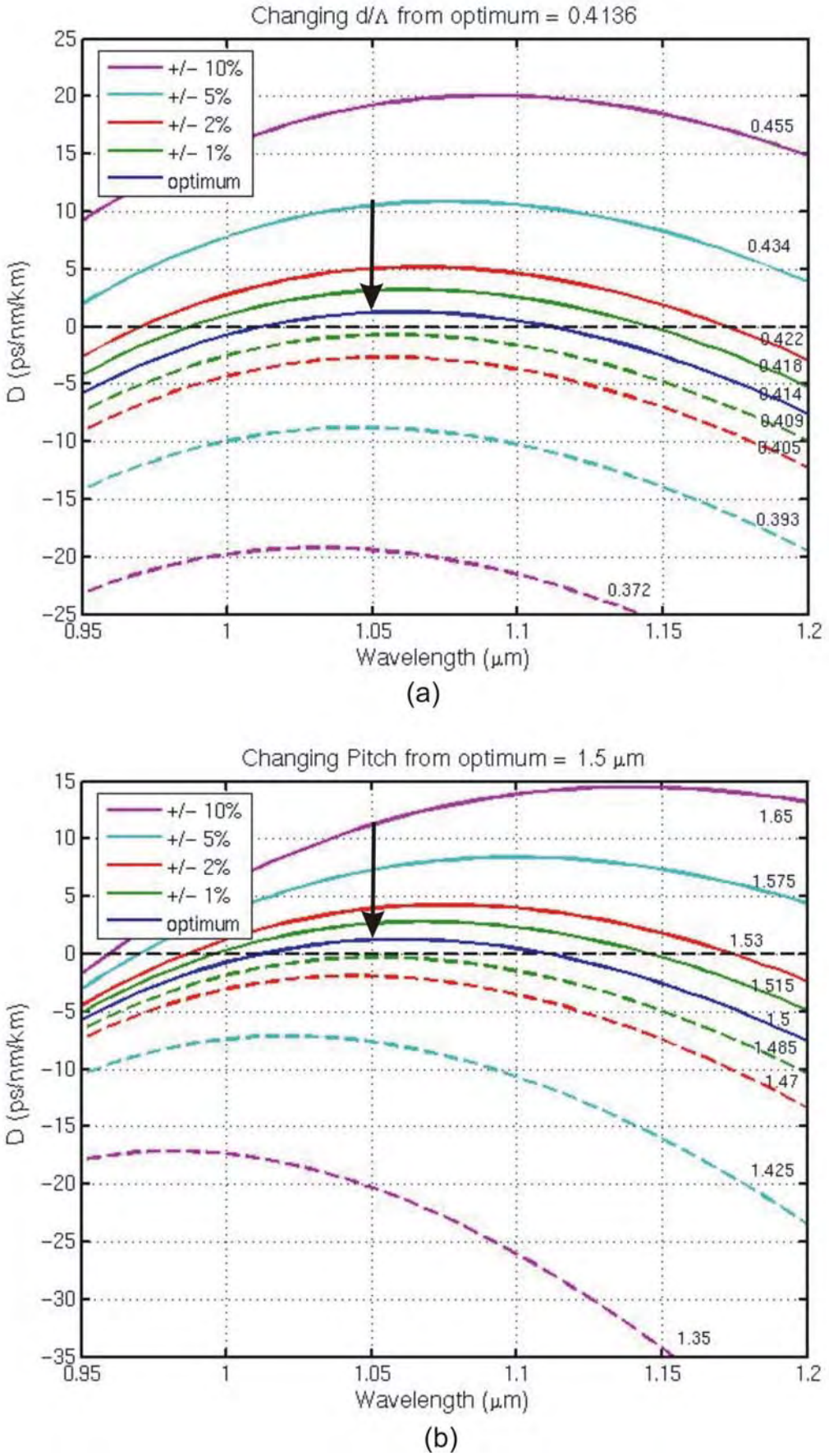

Fig. 6.1. Dispersion graphs to show the tolerance levels of deviation in (a) d/Λ and (b) Λ from the optimum dispersion-flattened design.

6.2.2 Fibre loss versus fibre length

Fibre loss is a limiting factor for adiabatic compression as it leads to soliton broadening; shorter fibres may therefore improve compression. However, there is a trade-off in adiabaticity, as the dispersion variation in the DDHF may not be sufficiently gradual. In this section, I investigate the variation of soliton pulse widths in DDHFs with certain dispersion decreasing ratios and losses, and identify the optimum fibre length for each case.

I performed numerical simulations of the generalized nonlinear Schrödinger equation described in Chapter 2, which takes into account higher-order dispersion as well as nonlinear Kerr and Raman effects. To solve the propagation equation, a standard split-step Fourier tool [Paschotta] was used. I simulate 2048 points over a spectral range of 500 nm, from 0.82 μm to 1.32 μm wavelength, which also provides good coverage for the pulses in the temporal domain. For each DDHF, the fibre was divided into small length increments, and the FWHM pulse widths and spectra were recorded in each step. It was found that 20 steps were sufficient for accurate pulse width simulations. Fig. 6.2 shows the comparison of pulse width simulations with different numbers of steps for the same fibres and inputs. Similar results were found for 100, 50 and 20 steps, whereas simulations with only 5 steps were not sufficiently accurate. A nonlinear refractive index n_2 of 2.5×10^{-20} m^2/W and a constant effective mode area A_{eff} of 4 μm^2 were used for these simulations.

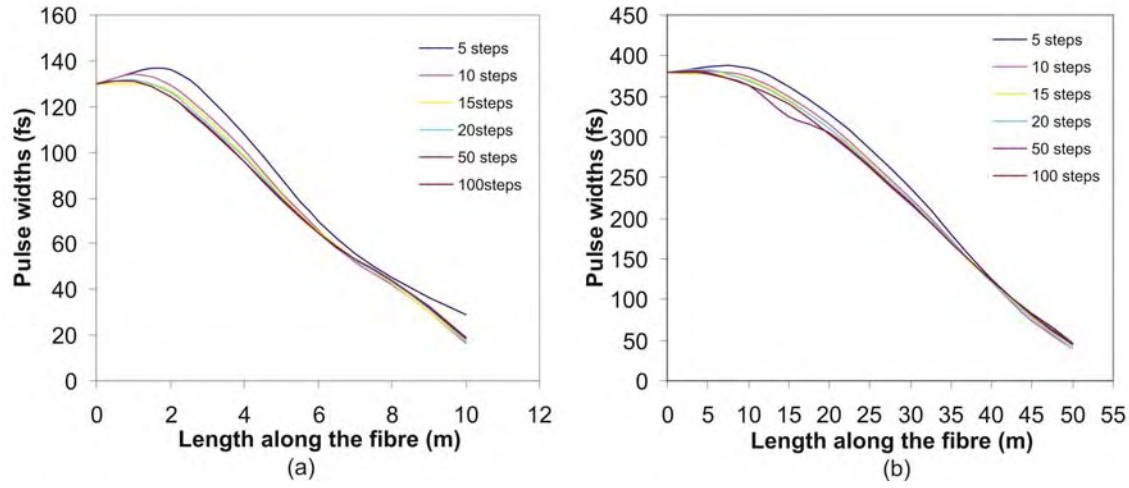

Fig. 6.2. (a) Simulation of pulse width along 10 m of DDHF with D= 10 to 1 ps/nm/km and 130 fs soliton input, and with different number of step increments. (b) Simulation of pulse width along 50 m of DDHF with D= 10 to 1 ps/nm/km and 380 fs soliton input, and with different number of step increments.

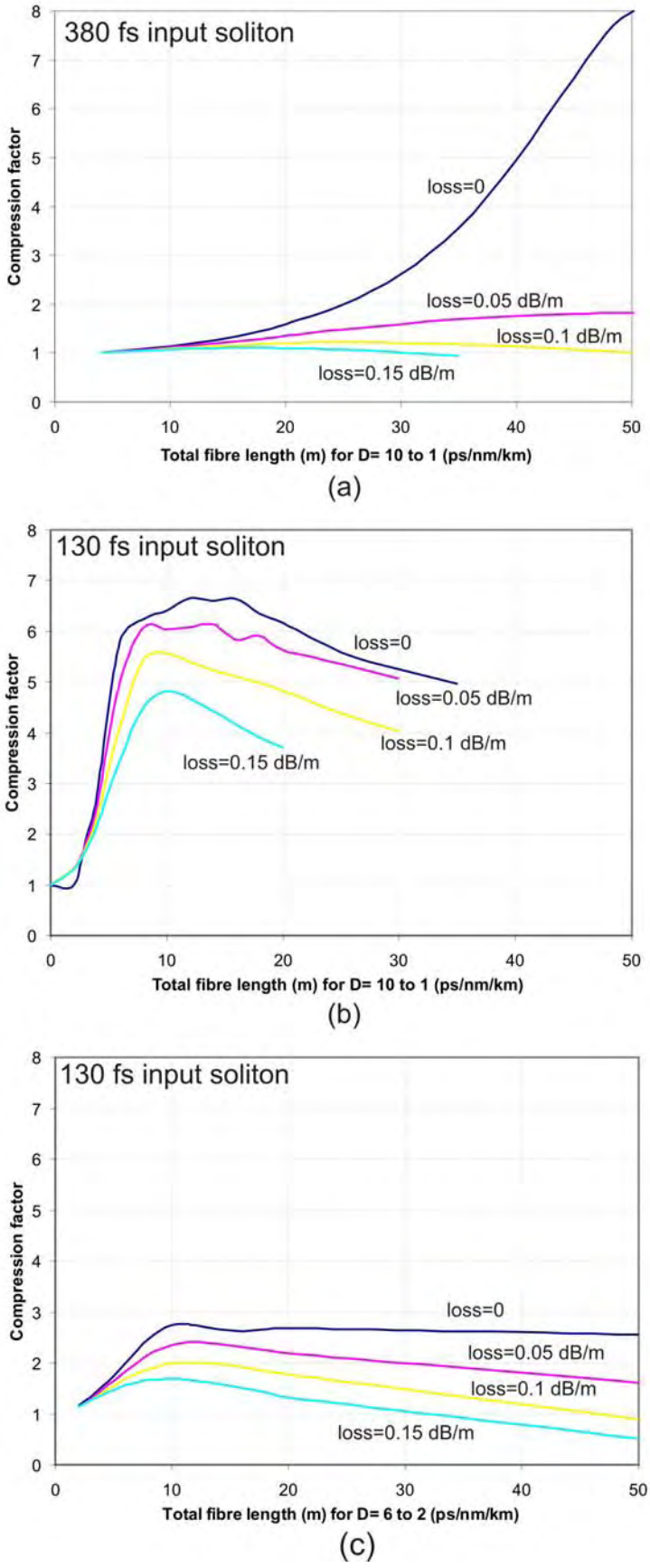

Fig. 6.3. Simulated compression factor (1= pulse unchange) for different fibre lengths and losses with (a) D= 10 to 1 ps/nm/km, 380 fs input soliton, (b) D= 10 to 1 ps/nm/km, 130 fs input soliton, (c) D= 6 to 2 ps/nm/km, 130 fs input soliton.

First, I simulated for an input soliton of 380 fs, propagating along DDHFs with D= 10 ps/nm/km at the input end, decreased linearly to 1 ps/nm/km at the output end at 1.06 μm wavelength. For simplicity, the dispersion slope is set to zero, thus the dispersion profiles were truly flat in the spectral domain, and throughout the fibre. The total fibre length was varied while keeping D=10 to 1 ps/nm/km in each case, for different values of fibre loss. Fig. 6.3(a) shows that for a given propagation loss, the highest pulse compression factor is found in a fibre with the optimum fibre length, that balances the pulse broadening effect of loss in long lengths, and the reduction of adiabaticity in short lengths. Similarly for an input soliton of 130 fs (Fig. 6.3(b)), the optimum length is around 8 to 10 m, with fibre loss up to 0.15 dB/m (achievable without extra polishing steps). In both cases, a lower compression factor was found in fibres with higher losses.

Since the dispersion length is proportional to the width of the soliton, longer input pulses required longer fibre for adiabatic compression. In order to achieve a compression factor of greater than two with an input soliton of 380 fs, the fibre required a loss lower than 0.05 dB/m. This was difficult to achieve with the available technology. However, for an input soliton of 130 fs, compression factor of 5 or more was found in fibres with loss lower than 0.15 dB/m. Therefore, pulse duration of 130 fs was used as an input in the experiment.

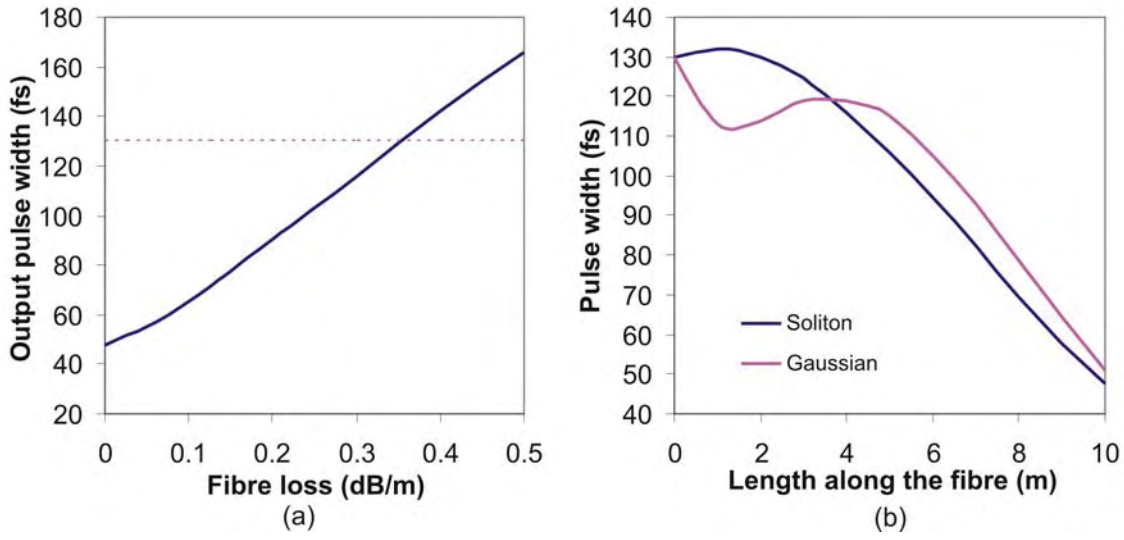

Fig. 6.4. (a) The output pulse widths at different losses for the 10 m fibre length, D= 6 to 2 ps/nm/km (dotted line indicates 130 fs soliton input). (b) Shows the pulse widths along the fibre with loss=0, for 130 fs soliton and Gaussian inputs.

To decrease the dispersion from 10 to 1 ps/nm/km in just 10 m of fibre was a challenging and ambitious target for the first fabrication attempt using the standard technique. Therefore, fibre with D= 6 to 2 ps/nm/km was chosen for the experiment. The simulation of pulse width versus fibre loss and length were carried out for this profile with 130 fs soliton input, and the result is shown in Fig. 6.3(c). Again the optimum length is around 8 to 10 m, and a compression factor

of ~2 is found for the case of loss= 0.15 dB/m. Fig. 6.4(a) shows the output pulse widths at different losses for 10 m fibre length; here, the variation is close to linear.

Note that for Gaussian input pulses, the changes in pulse width when compressed in a DDHF, were different to that found with soliton input pulses of the same initial width, see Fig. 6.4 (b). In general, the compression factor was smaller with Gaussian input pulses, and the compression in the initial part of the fibre was very different to the case of soliton inputs. In the experiment, Gaussian input pulses were used, and the impact on the pulse compression is discussed further in Section 6.3 and 6.4.

Finally, I incorporated the real dispersion profiles similar to that shown in Fig. 6.6, into the pulse compression simulations, instead of the truly flat dispersion profiles that had been used so far. The output pulse widths for different input pulse widths were simulated for two fibres, both with D= 6 to 2 ps/nm/km at 1.06 μm of length 11 m, one had the real dispersion profile, thus including the higher dispersion effect, the other had a flat dispersion profile. The corresponding results are presented in Fig. 6.5. It shows that with input soliton widths shorter than 150 fs, there is a small difference in the output between the real and flat dispersion profiles. And for input soliton longer than 150 fs, the compression is essentially identical. The higher order dispersion effect is discussed further in Section 6.4.

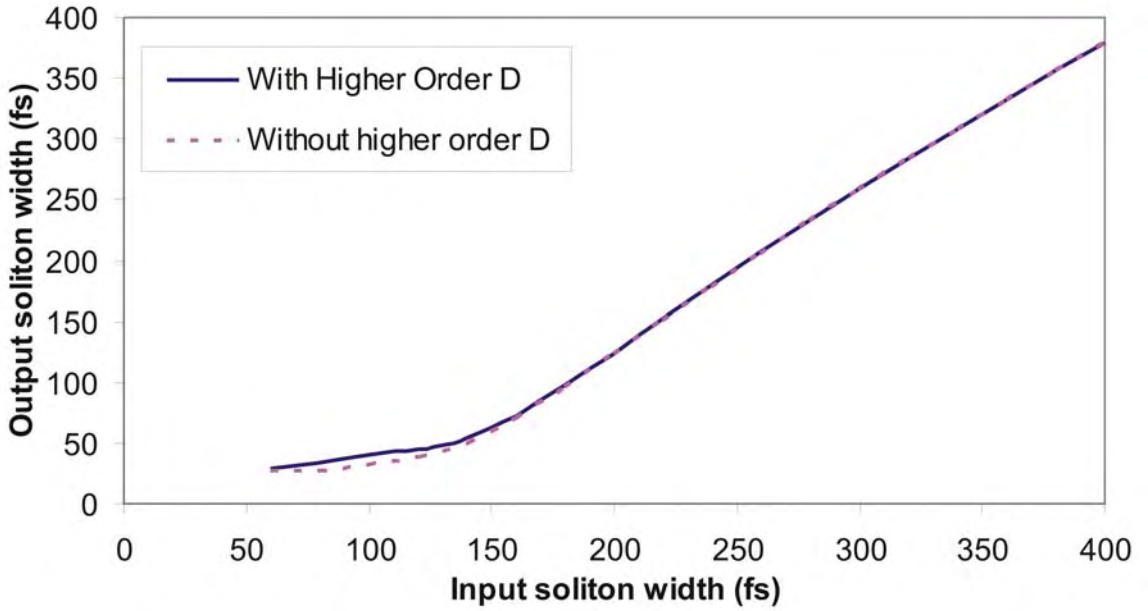

Fig. 6.5. Soliton compression results for different input soliton widths in fibres with D= 6 to 2 at 1.06 μm, 11m in length, loss=0, where higher order dispersion effect is included.

6.2.3 Fibre fabrication & dispersion profiles

The DDHF was fabricated as part of the fibres produced for the supercontinuum experiment described in Chapter 5; it was drawn from the same preform with the same technique. Based on the designs discussed in previous Sections, the internal pressure of the air in the holes was

reduced during the draw to produce a reduction in hole size, d, along its length. The change in structure produces the dispersion-decreasing characteristic. The pitch Λ and the effective mode area A_{eff} were nearly constant along the fibre. Here, ~10 m of fibre was kept, which had the dispersion characteristic closest to the target. Part of the fibre was taken for the SC experiment, and samples were taken for producing the SEM images (Fig. 6.6) of the structures at both end. The remaining part of the fibre was 8.1 m in length, the dispersion at 1.06 μm decreased from 5.4 to 2.3 ps/nm/km. The calculated dispersion profiles at the input and output end of the fibre are shown in Fig. 6.6. The calculations were done using a combination of the SC experiment results, [Tse, 2006(a)], and the measured pitch and hole sizes by 'Scion measurement' from the SEMs (see Chapter 5). A fibre loss of 0.15 dB/m at 1.06 μm was measured using the cut-back technique.

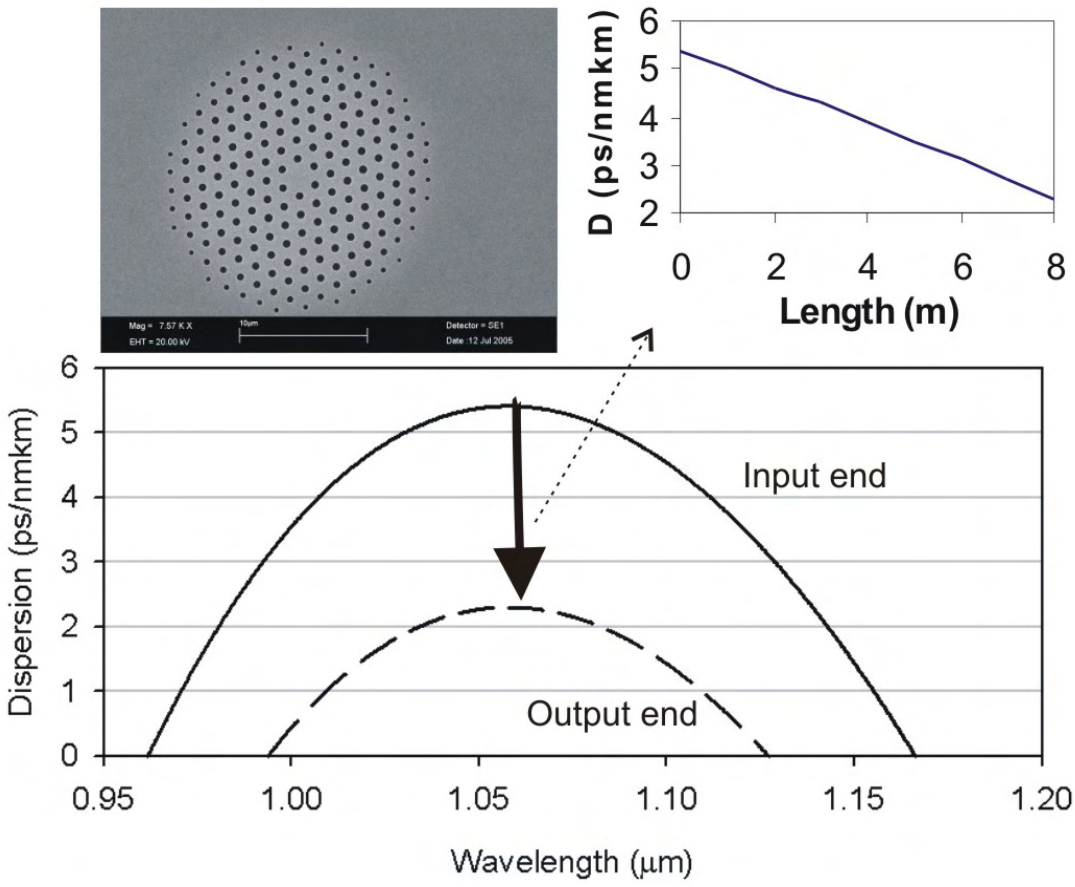

Fig. 6.6. Dispersion profiles used for numerical simulations for the input and output end of the fibre. *Inset*: SEM of the microstructure region of the fibre, and the dispersion at 1.06 μm along the fibre.

6.3 Soliton compression experiment

6.3.1 Experimental setup

I employed a mode-locked fibre laser operating at 1.06 μm, producing 130 fs pulses, [Lefort, 2002] (Setup by Dr. J. H. V. Price and F. He). The light is butt-coupled into the DDHF, with input coupling efficiency of 20%. The output pulse width was measured using a second-harmonic-generation based autocorrelator ('Femtochrome Research, INC. FR-103') and the output spectra were recorded using an optical spectral analyzer, OSA. The schematic of the setup is shown in Fig. 6.7.

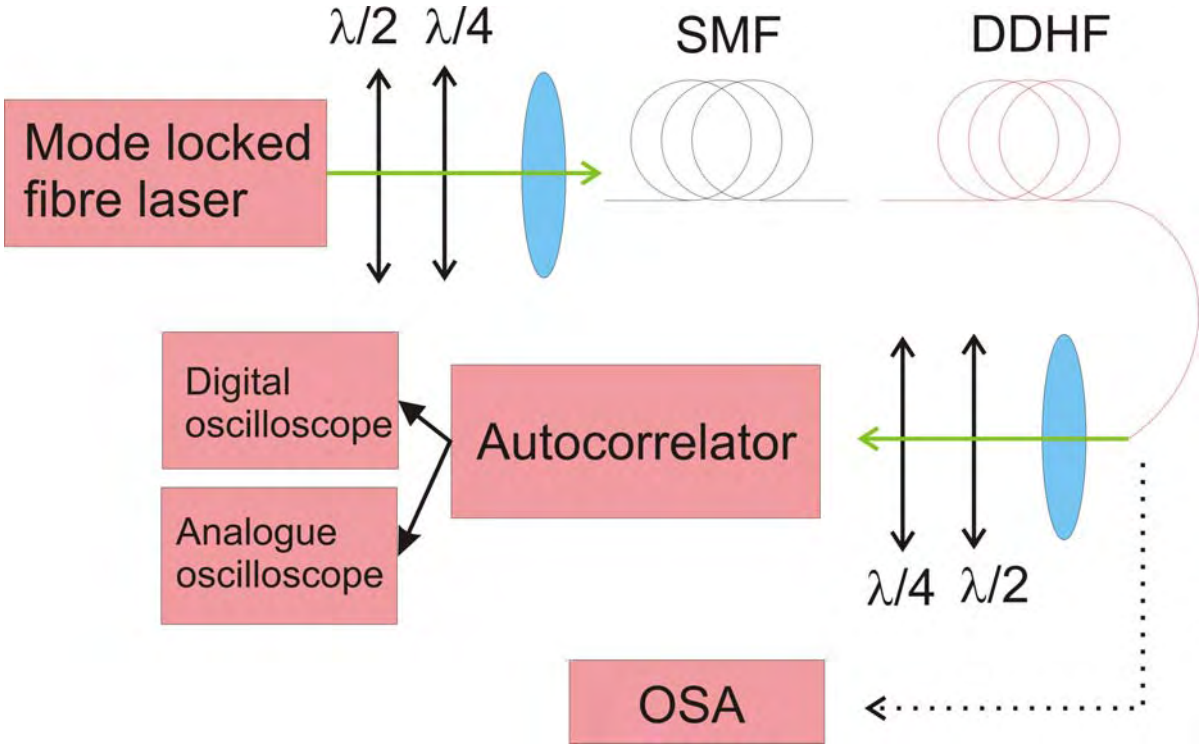

Fig. 6.7. Schematic of the experimental setup for pulse compression in DDHF

Since the experiment was carried out using only a few pJ of pulse energy, the autocorrelation signal was weak. Every effort was made to direct all the power of the output beam into the autocorrelator, and the signal was recorded from a digital oscilloscope ('Tektronix, TDS 3012'). For each power level, the signal duration was taken over different sample averages: 4, 8, 16, 64 and by eye inspection. A further average was calculated from the best readings, to give the resultant autocorrelation function width. This was then converted into real pulse duration using the appropriate factor according to the pulse shape. Next, the spectrum was recorded for the same power level by connecting the output end of the DDHF to the OSA. Although, at this point, the alignment of the output beam and the autocorrelator was temporarily lost; but with practice, it was easily aligned again for the subsequent power level readings.

6.3.2 Experiment and Results

The λ/2- and λ/4-plates before the SMF control the linearly polarised light and the orientation of the input beam into the DDHF. The fast and slow axes of the DDHF were determined by inspecting the nonlinear effects seen in the spectral domain, and carried out the experiment in those axes. The results of the two axes were slightly different, suggesting there was a discrepancy in the dispersion between the two axes. In the first axis, the compression followed closely with the predictions, in the other axis, a smaller compression ratio was found. In the following, I report and discuss the results of the experiment from the first axis in full. The result in the second axis is shown in Fig. 6.8(a) for comparison.

The results of the pulse width measurement at the DDHF output and the simulation results are shown in Fig. 6.8. The width of the autocorrelation function was converted into a pulse duration using a Gaussian conversion factor for energies below the soliton energy (2.3 pJ for a 130 fs soliton at the fibre input). For larger energies, a sech^2-pulse conversion factor was used. The root-mean-square (rms) spectral bandwidths from experiment and simulation are shown in Fig. 6.8(b). The rms widths were calculated using the following equation:

$$Std\_Dev = \sqrt{\frac{\sum \left(x - \bar{x}\right)^2}{n}} \qquad \text{Eqn. 6.3:1}$$

where x is the wavelength, $\bar{x}$ is the wavelength at the maximum, and n is the number of wavelength samples.

Figure 6.8(a) also shows an analytic prediction of the soliton width as discussed in the following. The 3dB soliton pulse duration τ_0 is given by Eqn. 6.2:4. For the fibre used, the total loss is ~25% which increases the pulse length by ~1/3 according to the equation. Therefore a compression factor of about two was expected, which was confirmed by the observed compression from 130 fs to 60 fs. The dashed curve in Fig. 6.8(a) is given by Eqn. 6.2:4 and taking fibre loss into account. The remaining difference between the predicted width and the measured and simulated results therefore suggests slightly non-adiabatic compression, i.e., a fraction of the pulse energy was shed into non-soliton radiation during soliton formation and propagation. This conclusion was also supported by the fact that the discrepancy was smaller at higher powers where the nonlinear pulse shaping occurs over shorter fibre lengths and thus the adiabaticity condition was more easily fulfilled.

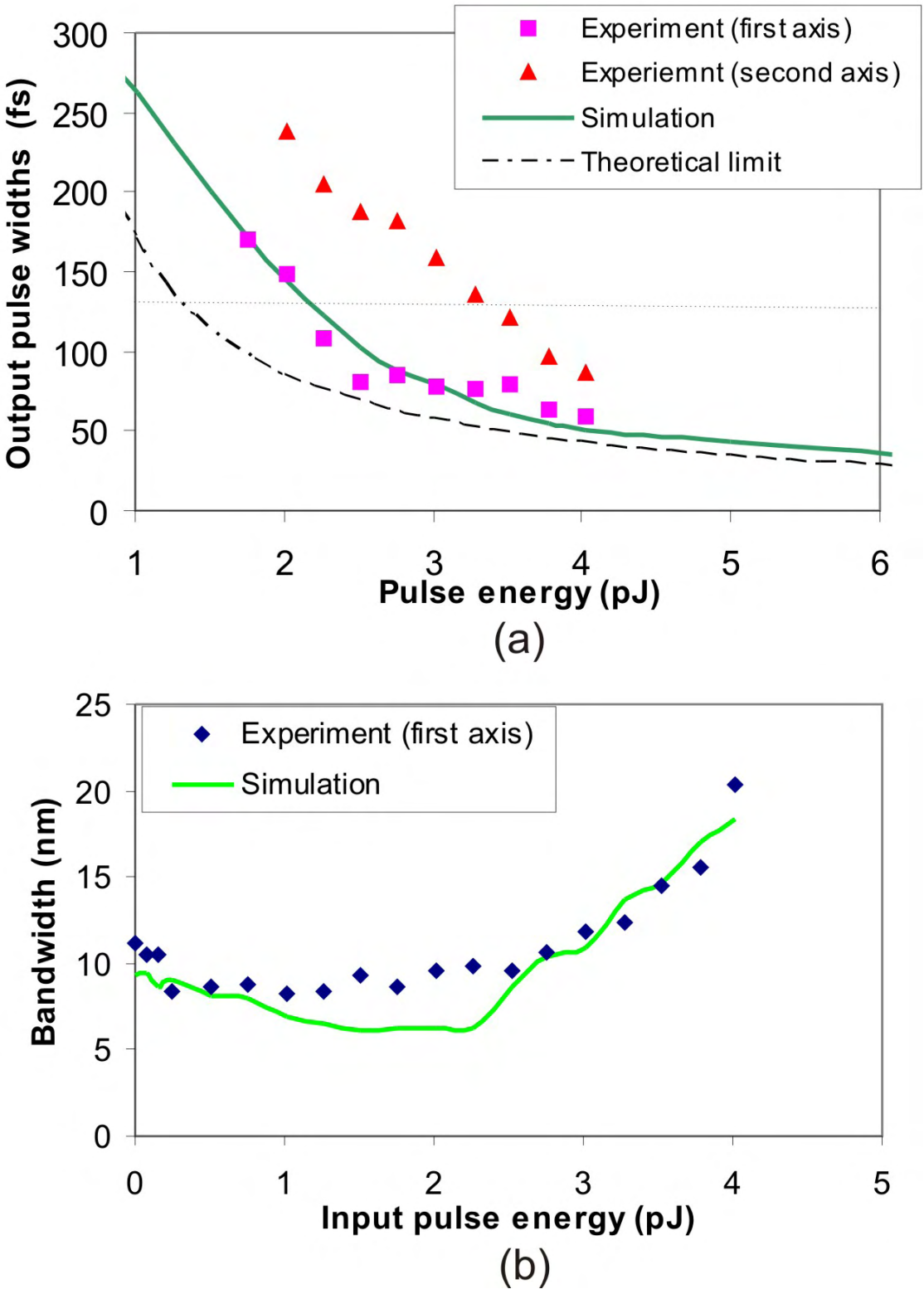

Fig. 6.8. (a) 3dB output pulse duration for different input pulse energies from experiment and simulations with an initial Gaussian pulse of 130 fs. The dashed curve shows the theoretical limit for adiabatic compression. (b) rms bandwidth from experiment and simulation.

In order to investigate these non-adiabatic effects in more detail, the output spectra were measured at various input power levels. These are shown in Fig. 6.9. I overlay these results with the simulation results, and find good agreement in all cases.

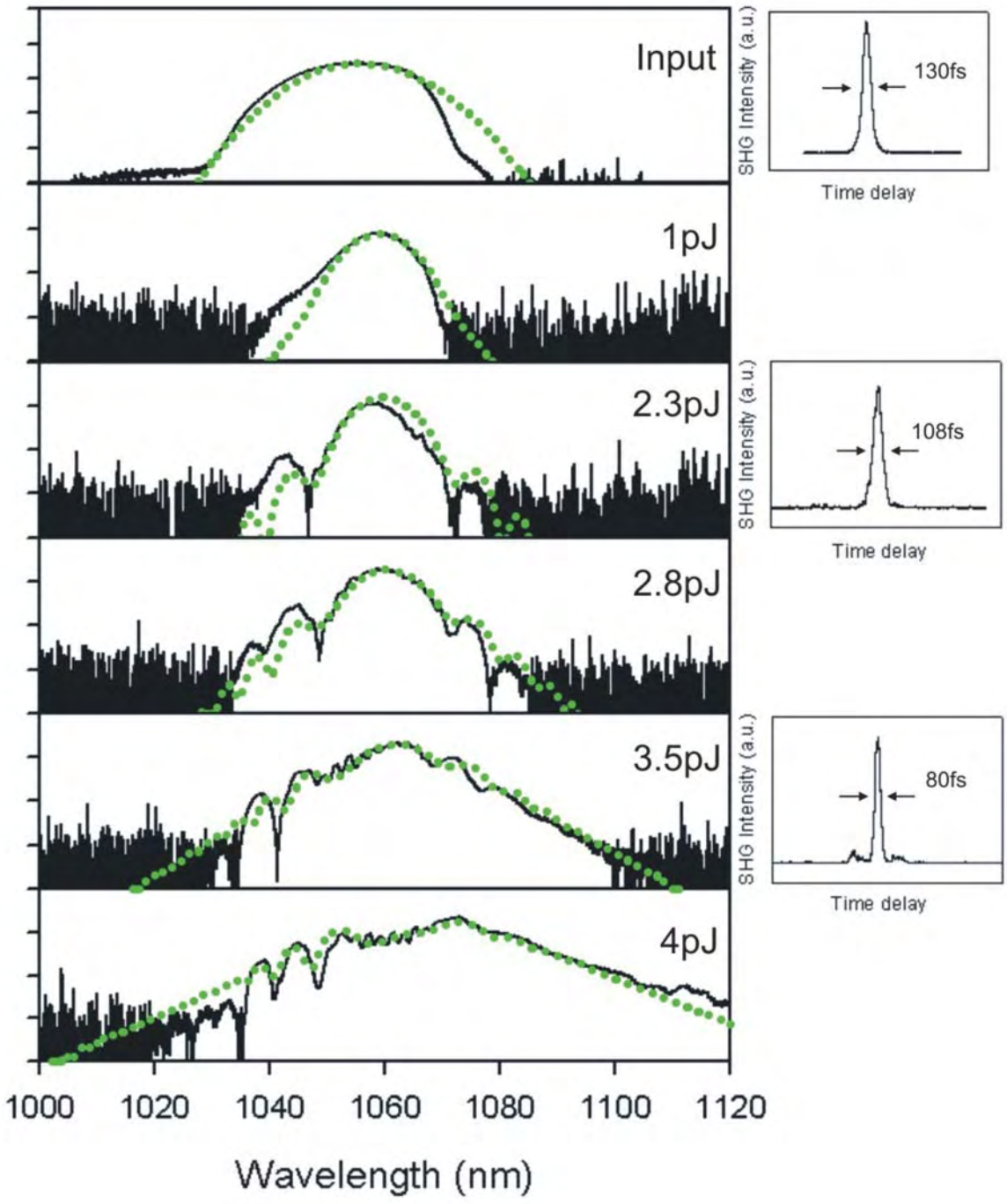

Fig. 6.9. Left: Experimental (solid black line) and simulated (dotted green line) spectra (10 dBm/div.) at different input pulse energies. Right: Selected autocorrelation functions and pulse widths.

At very low power (not shown) the output bandwidth was the same as the input bandwidth with no nonlinear effect observed, but the pulse broadens temporally because of dispersion. The slight spectral asymmetry originates from the pump source. As the input energy increased the pulse broadening was initially accompanied by spectral narrowing which was attributed to a small chirp (1e25 Hz/s) of the input pulse (Fig. 6.9, 1 pJ), this was included in the simulations presented here. I also compared the compression results with input pulse of different initial chirps, see Fig. 6.10. It shows that the initial pulses with chirp ±1e25 Hz/s

have little effect on the pulse compression, and with a larger amount of chirp would still produce similar amount of compression but required different input pulse energy.

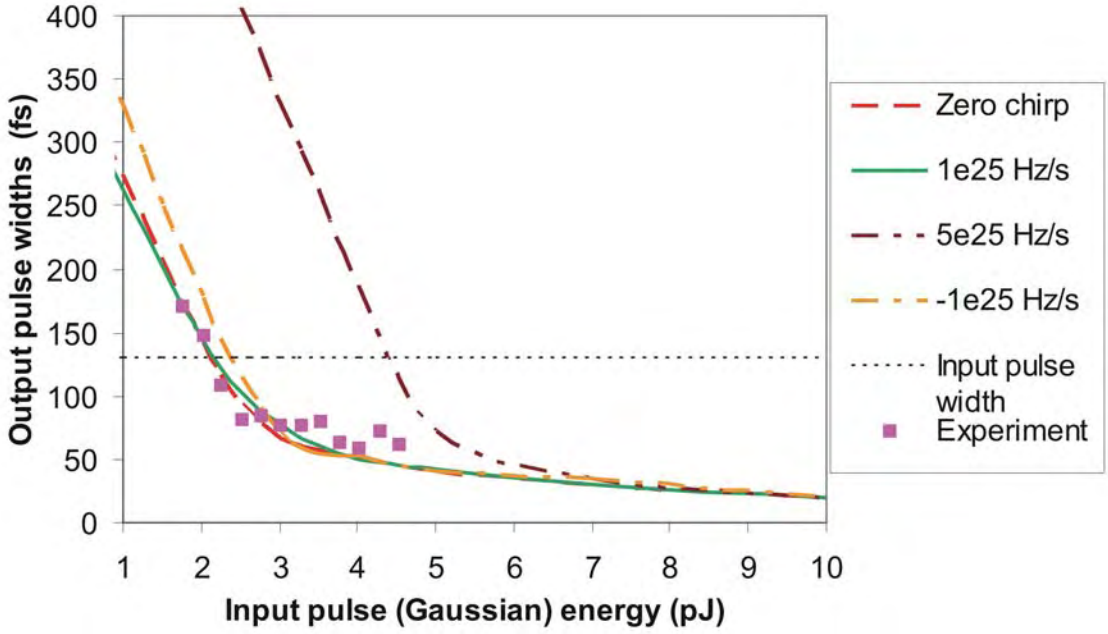

Fig. 6.10. 3dB output pulse duration for different input pulse energies from experiment and simulations with an initial Gaussian pulse of 130 fs with different initial chirps.

When the soliton energy was reached, the balance of self-phase modulation and dispersion effects led to the formation of a fundamental soliton (Fig. 6.9, 2.3 pJ) that was subsequently compressed when propagating along the DDHF. At higher power levels, further compression of the soliton was found, and the Raman soliton self-frequency shifting effect was observed (Fig. 6.9, 4 pJ). There was no evidence of higher order dispersion effects in this experiment as the fibre had a dispersion flattened profile close to 1.06 μm. Simulations showed that above ~2 pJ the small initial chirp and pulse asymmetry had no significant effect on the output pulse.

Experiments and simulations exhibited some spectral sidelobes as well as temporal satellite peaks, see Fig. 6.9. These features were even more apparent in a spectrogram, i.e., a plot of temporally resolved spectra, as shown in Fig. 6.11 for an input energy of 3.5 pJ. The spectrogram clearly associates the spectral sidelobes with the minor peaks seen at the output in the time domain. I compare this spectrogram with that of a 63 fs soliton (Fig. 6.11, right), corresponding to the output pulse width expected under truly adiabatic conditions. This showed that the sidelobes and satellite peaks originate from energy being shed during the soliton formation and propagation and that these features were therefore an indication of non-adiabatic processes. Note, however, that Fig. 6.11 is on a logarithmic scale and that the actual amount of lost power, and hence the deviation from adiabaticity, was relatively small, as already seen in Fig. 6.8.

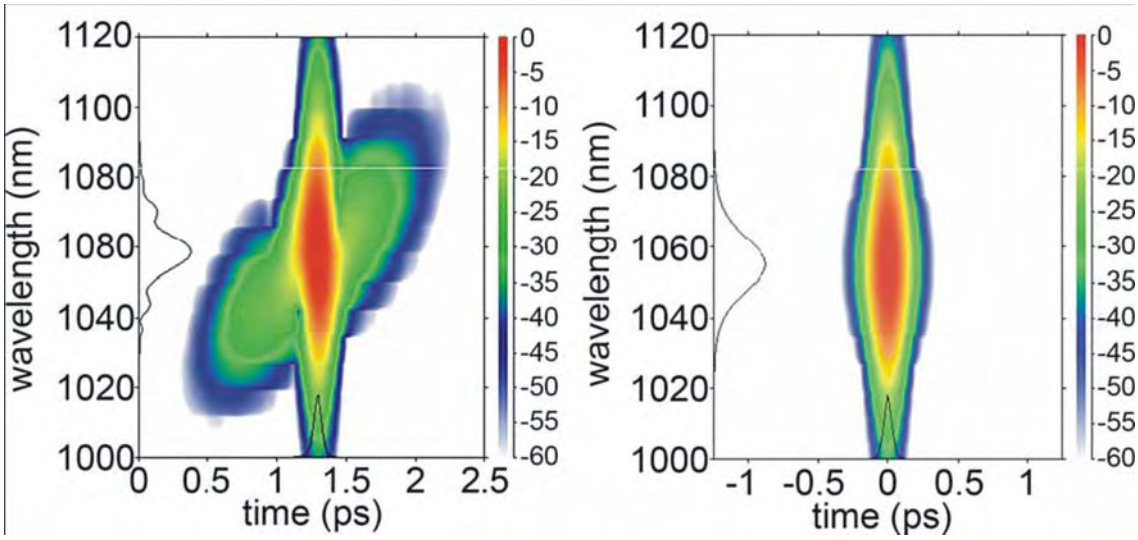

Fig. 6.11. Left: Simulated output spectrogram (logarithmic scale, time resolution = 0.1 ps) of a 3.5 pJ input pulse. Right: Spectrogram of a 63 fs soliton.

6.4 Discussion

For the current DDHF and for the range of pulse parameters investigated here, the maximum compression factor was about two. In the following, I will discuss various limiting factors and options for improvement.

(i) *Ratio of input and output dispersion*. For the fibre used, this was ~2.3 and it is the limiting factor for soliton compression. For further compression, a larger ratio is required which can be achieved by a longer fibre or a larger dispersion gradient. This work was put back by the fire delay.

(ii) *Adiabaticity*. For a 130 fs soliton, the dispersion length L_D is 1.7 m at fibre input, and after compression to 60 fs L_D decreases to 0.7 m. This confirms that compression by a factor of two over 8.1 m fibre length is near adiabatic. Longer fibre would improve adiabaticity, but in real fibre, propagation loss would be counterproductive.

(iii) *Fibre loss*. As already discussed, this is a limiting factor for adiabatic compression as it leads to soliton broadening. Shorter fibres and corresponding larger dispersion gradients may therefore improve compression. However, there is a trade-off in adiabaticity. For 130 fs input pulses, a DDHF of ~8 m is close to the optimum length balancing fibre loss and adiabaticity, see Fig. 6.3(c).

(iv) *Input power*. Figures 6.8 and 6.9 show that larger input powers provide larger compression factors. This is due to the fact that 130 fs Gaussian input pulses are converted to shorter solitons for higher powers in the initial stages of pulse propagation, according to Eqn 6.2:4, and thus effectively pulse compression starts at already reduced pulse widths. However, if the input energy reaches the threshold for the creation of 2nd order solitons (~9 pJ), this

initial compression stops as these solitons tend to break up into two fundamental solitons under perturbations, [Husakou, 2001]. Output widths are therefore limited to ~15 fs.

(v) *Higher order dispersion*. This is expected to limit the maximum compression factor if the linear dispersion at the fibre end approaches zero. For example, Fig. 6.6 shows that if the output dispersion at 1.06 μm is reduced to 1.3 ps/nm/km, the width of the anomalous dispersion region shrinks to ~100 nm, which corresponds to a pulse width of the order of 20 fs and therefore limits the maximum compression factor to about six. Hence, larger compression factors can only be achieved by increasing the dispersion at the fibre input, but with the cost of using higher input powers.

6.5 Conclusions

I have designed and fabricated a dispersion decreasing holey fibre for soliton compression at 1.06 μm. And demonstrated pulse compression from 130 fs down to 60 fs in a DDHF at pJ pulse energies. This was to my knowledge the first reported experimental demonstration of soliton compression in DDHF. These results were in good agreement with numerical simulations and analytic predictions. An analysis of the limiting processes suggests that compression factors of 10 can be achieved for pulses with less than 10 pJ energy by modest changes of fibre parameters, in particular a reduction of fibre loss and a larger ratio of input and output dispersion.

In the next chapter, holey fibres that simultaneously decrease in dispersion and mode area for soliton compression are studied numerically.

Chapter 7 Designing tapered holey fibre for soliton compression

7.1 Introduction

In this chapter, I investigate numerically the compression of femtosecond solitons at 1.55 μm wavelength propagating in holey fibres which exhibit simultaneously decreasing dispersion and effective mode area.

Compression of soliton pulses propagating in conventional dispersion decreasing optical fibres (DDF) is a well-established technique, [Chernikov, 1991]. Pulse compression of higher order solitons in DDF with factors greater than 50 was also demonstrated, [Pelusi, 1997]. The effect of the dispersion profile along the fibre on the performance of pulse compression in DDF was investigated in [Mostofi, 1997] and the effects of higher-order dispersion in [Chan, 2000]. A variant of the scheme using dispersion-decreasing fibre in a nonlinear optical loop mirror has been proposed for the compression of longer (picosecond) pulses, [Wai, 2003].

Microstructured holey fibres offer the flexibility to extend adiabatic soliton compression to a much wider range of wavelengths and pulse energies than accessible with conventional optical fibres, [Hu, 2006]. Firstly, the large refractive index contrast between fibre core and cladding, that is possible in holey fibres, leads to large waveguide dispersion which can be used to compensate for the normal material dispersion at wavelengths below 1.3 μm in silica fibres. Anomalous dispersion and hence soliton propagation can be easily achieved, for example, at 1.06 μm where efficient Yb-doped fibre laser sources exist, see Chapter 5 [Tse, 2006(a)]. Secondly, because of the small core size and thus high nonlinearity possible within holey fibres, compression already occurs at very low soliton energies and over short lengths of fibre. Compression of femtosecond solitons with pico-Joule energies at 1.06 μm has been demonstrated in Chapter 6, [Tse, 2006(b)]. Finally, in contrast to conventional fibres, holey fibres can be fabricated with simultaneously significant decreasing dispersion *and* effective mode area leading to enhanced compression factors. Dispersion- and mode-area decreasing holey fibres (DMDHFs) can be fabricated by varying the drawing conditions during the fibre draw, which in general allows for the variation of fibre parameters on a length scale as short as 10 m, [Kudlinski, 2006]. For faster parameter variations along shorter lengths of fibre, a holey fibre has to be tapered on a specialized rig similarly to fibres fabricated for supercontinuum generation at short wavelengths, [Foster, 2005, Falk, 2005, Leon-Saval, 2004]. Tapered holey fibres have also been used as a coupler to waveguides, [Moss, 2005], to generate soliton self-

frequency shifts, [Liu, 2001], to convert spot-size, [Town, 2001] and to make photonic wires, [Lizé, 2004].

This chapter is organised as follows. In Section 7.2, I analyze holey fibre dispersion and effective mode area versus fibre design parameters and model the resulting soliton compression in DMDHFs under fully adiabatic conditions. In Section 7.3, I compare these theoretical results with numerical simulations taking into account a variety of nonlinear effects and higher order dispersion. The compression factor for different fibre lengths is investigated and the minimum length required for near-adiabatic conditions is discussed. In Section 7.4, nonadiabatic compression in short lengths of DMDHFs is discussed. Section 7.5 deals with the important issues of fibre loss and in Section 7.6 fibre fabrication is described. Finally, the results are summarized in Section 7.7.

7.2 Holey fibre design and contour map

A contour map (modelled by F. Poletti) of the dependence of dispersion D, dispersion slope D_s, and effective mode area A_{eff} on hole-to-hole spacing Λ and air-filling fraction d/Λ of holey fibres with regular hexagonal geometry at 1.55 μm is shown in Fig. 7.1. The map has been calculated by simulating a number of fibres on a regular (d/Λ, Λ) grid with a full vector Finite Element Method solver and by applying a subsequent 2D spline to create smooth contours. The choice of a dense enough grid of 17 x 13 points ensures that the accuracy of each point on the map is equal to or better than the accuracy practically achievable during the fibre fabrication. The map was obtained for fibres with 8 rings of air-holes; however it was found that, in the design region of interest for this study, both D and A_{eff} are not significantly affected by an increase in the number of rings. By appropriate fibre fabrication and/or fibre tapering, a large variation of both D and A_{eff} can be achieved along the length of a single fibre. Here, the main objective is optimizing the corresponding rate of parameter change along the fibre with respect to soliton compression.

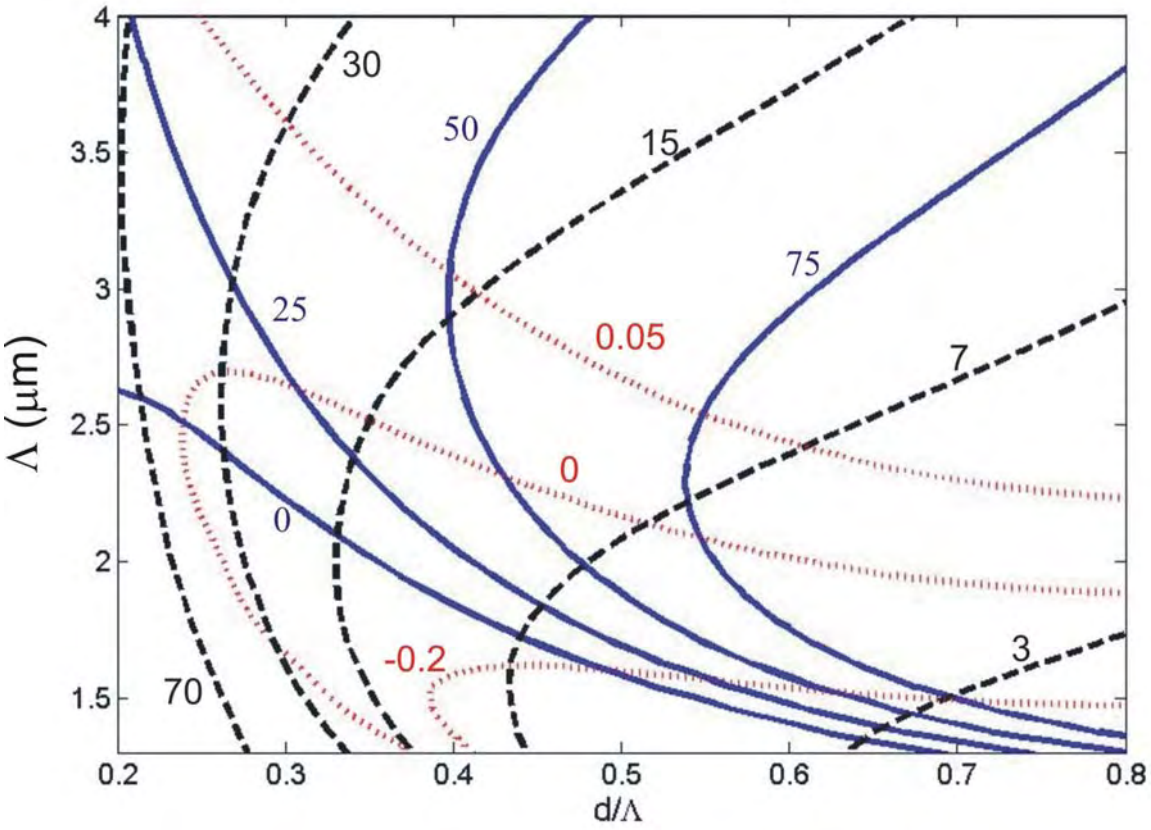

Fig. 7.1. Contour map for dispersion (blue solid line; units of ps/nm/km)), dispersion slope (red dotted line; ps/nm^2/km) and effective area (black dashed line; μm^2) versus pitch Λ and d/Λ for holey fibres of hexagonal geometry at 1.55 μm wavelength.

7.2.1 Ideal adiabatic compression

For given fibre parameters, the full width at half maximum (FWHM) of a fundamental soliton is given in Eqn. 6.2:4. In the idealized case of a lossless fibre and an arbitrarily slow change of D and A_{eff} along the fibre, E_{sol} stays constant, the pulse compression is adiabatic, and therefore the pulse width is proportional to the product $D*A_{eff}$. In real fibres however, fibre loss, the delayed nonlinear Raman response, and higher-order dispersion affect the soliton propagation and achievable compression. These effects will be discussed in the following sections, but are neglected here.

Based on Eqn. 6.2:4, the contour map of the adiabatic compression factor is obtained, see Fig. 7.2, corresponding to the map of fibre parameters in Fig. 7.1. Figure 7.2 is normalized to the top left corner of the figure which has the largest value of $D*A_{eff}$. A tapered fibre with parameters changing from that point to any other point on the map will result in compression of a soliton at 1.55 μm by the factor shown in the figure, provided that changes of fibre parameters over one local dispersion length are small. Note that compression factors of 20 and higher are possible, in theory, if the end point of the holey fibre is close to the zero-dispersion line of Fig. 7.1.

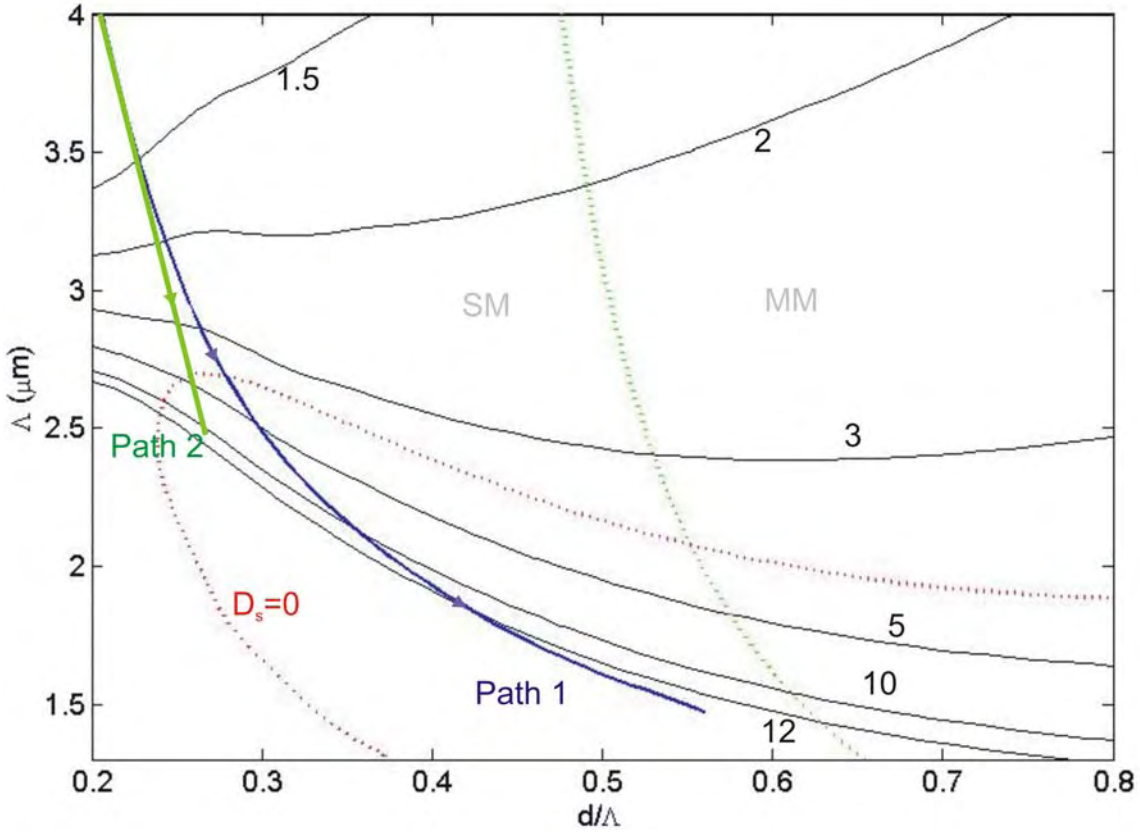

Fig. 7.2. Contour map for adiabatic compression factors corresponding to the Fig. 8.1. (green dotted line represents the single mode 'SM' and multi-mode 'MM' boundary)

7.3 Adiabatic compression in long fibres

I performed numerical simulations of the generalized nonlinear Schrödinger equation described in Chapter 2, which takes into account higher-order dispersion as well as nonlinear Kerr and Raman effects. To solve the propagation equation, a standard split-step Fourier tool [Paschotta] is used. Here, 2048 points were simulated over a spectral range of 2 μm, from 1 μm to 3 μm wavelength, which allows the observation of nonlinear effects such as SPM, Raman shifts and dispersive wave generation. At the same time it provides coverage for the pulses in the temporal domain. For each DMDHF, 500 steps were simulated, thus the fibre was divided into 500 small length increments, the FWHM pulse widths and spectra were recorded in each step.

Simulations were done for fibres with parameters following different paths on the contour map, two of the paths were shown in Fig. 7.2. Fibre loss was neglected in the following, but will be discussed later in Section 7.5. Furthermore, input solitons of 400 fs duration were used, which on one hand provides a short dispersion length of L_D~5 m such that fibre propagation losses were small over this scale, but which on the other hand, was long enough to avoid excessive spectral bandwidths.

This section describes the analyses of pulse compression in DMDHFs of 50 m length, which is long compared to L_D~5 m, and fibre parameters in the top left corner of Fig. 7.1. At first, a path was chosen in Fig. 7.1 that gives a large decrease of dispersion *and* mode area, while the fibre remains both single mode and in the anomalous dispersion regime. This is indicated as Path 1 in Fig. 7.2. Here, D is decreasing by a factor of ~5 and A_{eff} is decreasing by a factor of ~10 from the top left corner of the map to a point close to D=0 ps/nm/km. The profiles of D and A_{eff} along the length of the fibre are shown in Fig. 7.3(a).

The simulated FWHM for Path 1 is shown in Fig. 7.4. While adiabatic compression was expected for these parameters, I instead observe that after ~20 m of fibre the width deviates from that found by the analytic expression 6.2:4. A closer analysis revealed that two effects prevent further compression at this point.

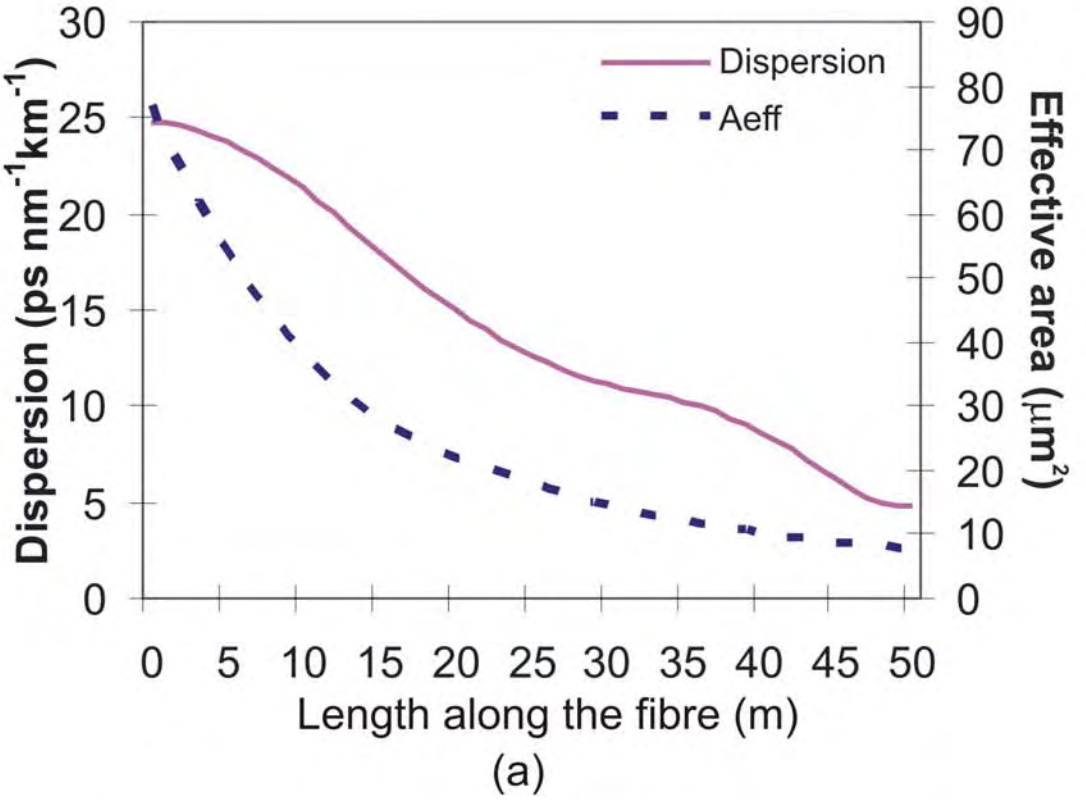

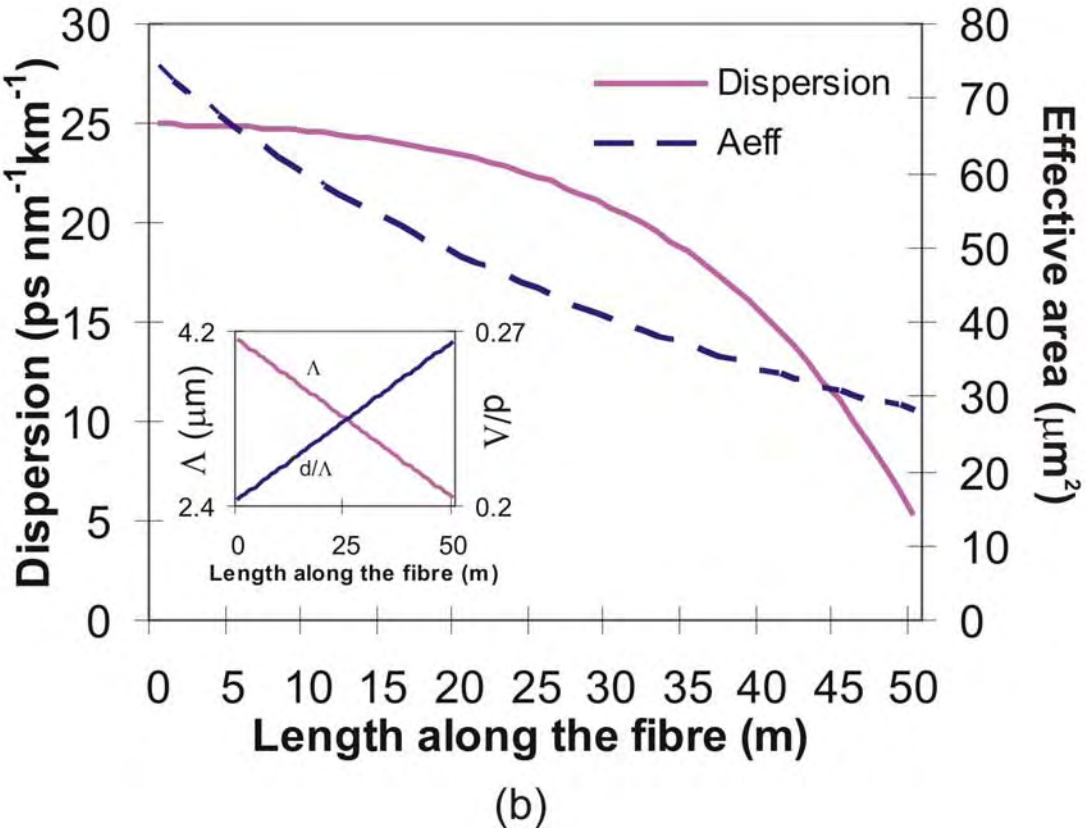

Fig. 7.3. Dispersion and effective area profiles along a 50 m fibre for (a) Path 1 and (b) Path 2 of Fig. 7.2. Inset: In both cases the fibre parameters Λ and d/Λ vary linearly along the fibre from (d/Λ= 0.20, Λ= 4.12) to (d/Λ= 0.27, Λ= 2.48).

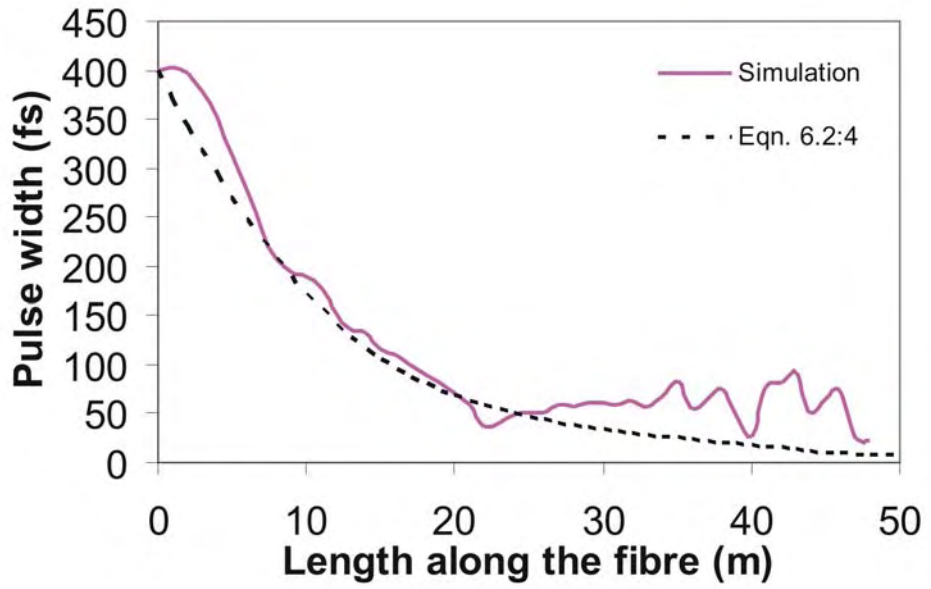

Fig. 7.4. Simulated pulse width (FWHM) in the fibre with dispersion and effective area profiles along Path 1.

Firstly, the dispersion slope decreased from 0.046 ps/nm^2/km to -0.267 ps/nm^2/km along the fibre. Thus, during the second half of the fibre the zero-dispersion wavelength shifts continuously towards the soliton wavelength. When the zero-dispersion wavelength was found close to the soliton wavelength, the soliton started to shed energy into dispersive waves, [Husakou, 2001]. This effect was clearly observed in the simulated spectra at different positions along the fibre, shown in Fig. 7.5(a). The first dispersive wave appeared at ~2 μm wavelength after 23 m of propagation. Subsequently more new components were generated below 2 μm as the zero-dispersion wavelength continues to move to shorter wavelengths. Note that this problem can be avoided with longer input pulses of, e.g. 1 ps or 2 ps, which lead to smaller output bandwidths. However, a much longer fibre with very low loss is needed in this case for adiabatic compression as the dispersion length is of the order of tens of metres.

Secondly, the large decrease in A_{eff} and the corresponding increase in the nonlinearity led to temporal broadening by Raman soliton self-frequency shifting (SSFS), [Mitschke, 1986]. This effect was clearly observed in the spectra, Fig. 7.5(b). Note that for this simulation I kept D_s=0 ps/nm^2/km throughout the fibre.

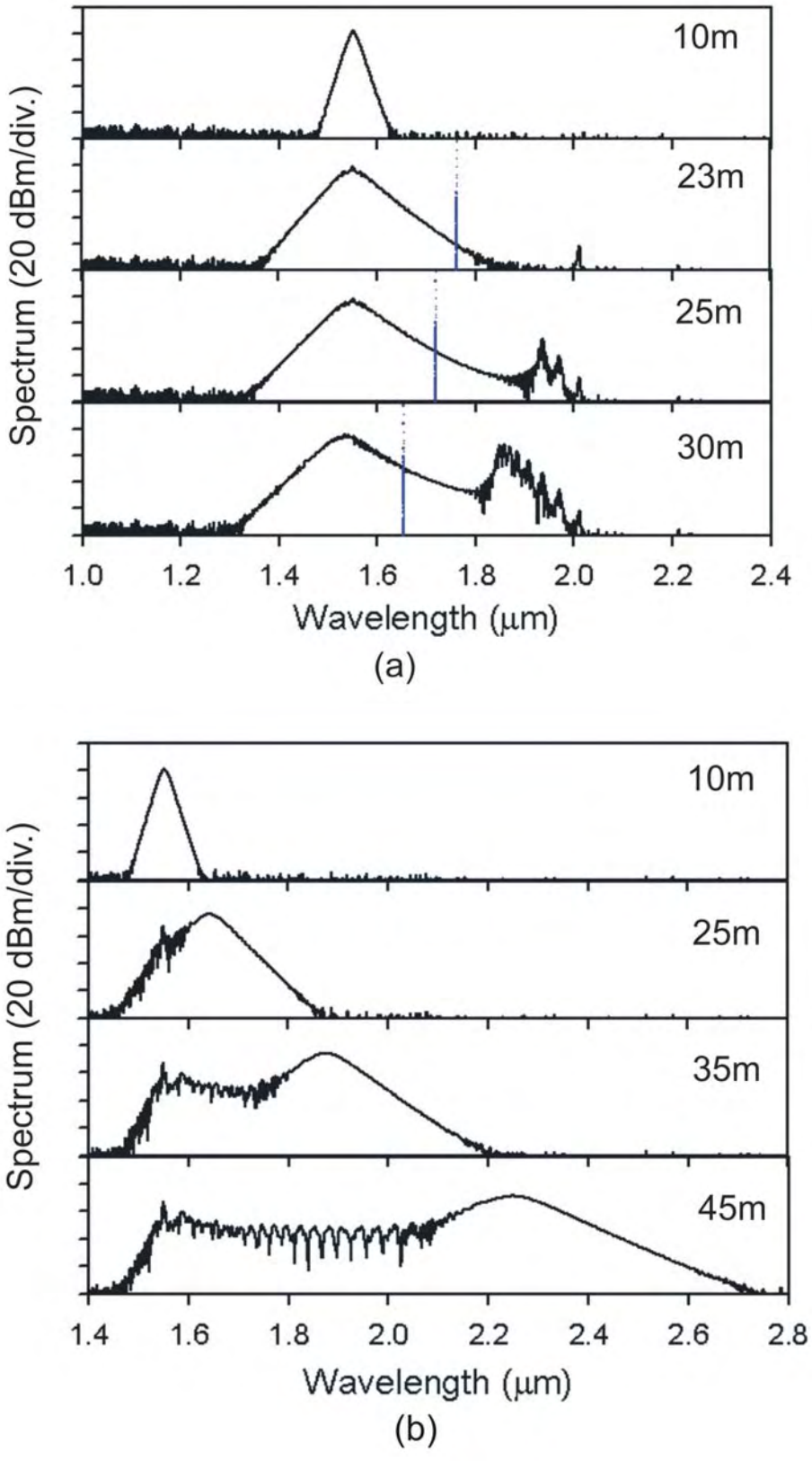

Fig. 7.5. Simulated spectra at different distances along the fibre (Path 1), (a) showing the effects of dispersion slope when Raman effects are neglected in the simulation (blue dotted lines indicate zero dispersion wavelengths), (b) showing the effects of Raman shifting when D_s=0 for the entire length.

These results imposed certain restrictions on fibre parameters which led to high soliton compression factors. First, the fibre should have an end point near the crossing point of the line of zero dispersion, D=0 ps/nm/km, and the line of zero dispersion slope, D_s=0 ps/nm^2/km, [Tamura, 1999] to avoid the resonant generation of dispersive waves. Second, the effective area, A_{eff}, can only be reduced by a certain fraction to reduce SSFS. For D and A_{eff} to be either constant or decreasing along the fibre, holey fibre parameters must therefore be chosen in the top left area of the map in Fig, 7.1. Path 2 of Fig. 7.2 represents such a choice. Here, D decreases by a factor of ~5 (from 25 ps/nm/km to 5 ps/nm/km) and A_{eff} by a factor of ~2.5 (from 75 μm^2 to 30 μm^2) along the fibre. The corresponding profiles are shown in Fig. 7.3(b), the fibre parameters Λ and d/Λ were varied linearly with length (inset). The simulated pulse width in this case is shown in Fig. 7.6. Now, there was excellent agreement with the analytic approximation, Eqn. 7.2:3, which suggested that the soliton compression was indeed adiabatic. A small SSFS was still observed in the corresponding spectrum but no dispersive waves were generated. A 400 fs soliton pulse was compressed down to 33 fs, a compression factor of ~12.

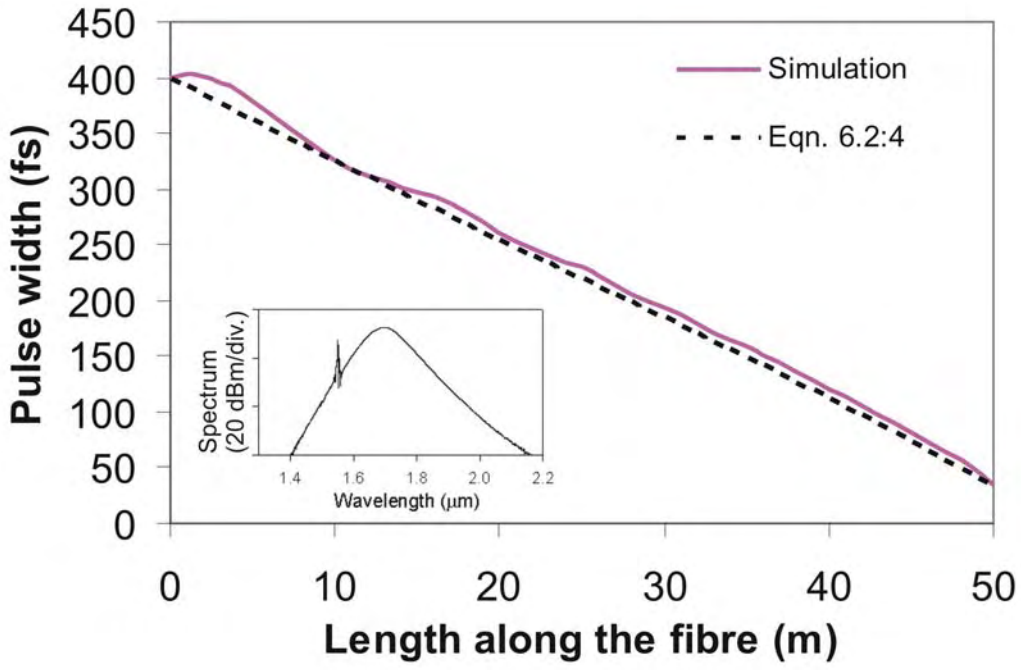

Fig. 7.6. Simulated pulse width (FWHM) in the fibre with dispersion and effective area profiles along Path 2. Inset: the output spectrum showing a small SSFS.

I also investigated fibres that have the same start and end points as Path 2 but alternative routes in between. The top left region of the map (Fig. 7.1) is again shown in Fig. 7.7(a). Two new paths are indicated with the same end points as Path 2. Path 3 consists of a first part where A_{eff} is constant and only D is decreasing, and a second part where A_{eff} is decreasing at constant D. Path 4 exhibits the opposite behaviour. The corresponding pulse compression is shown in Fig. 7.7(b). The fact that the pulse compresses to a similar value at the output of the fibres following the three paths further confirms the adiabaticity of the soliton compression.

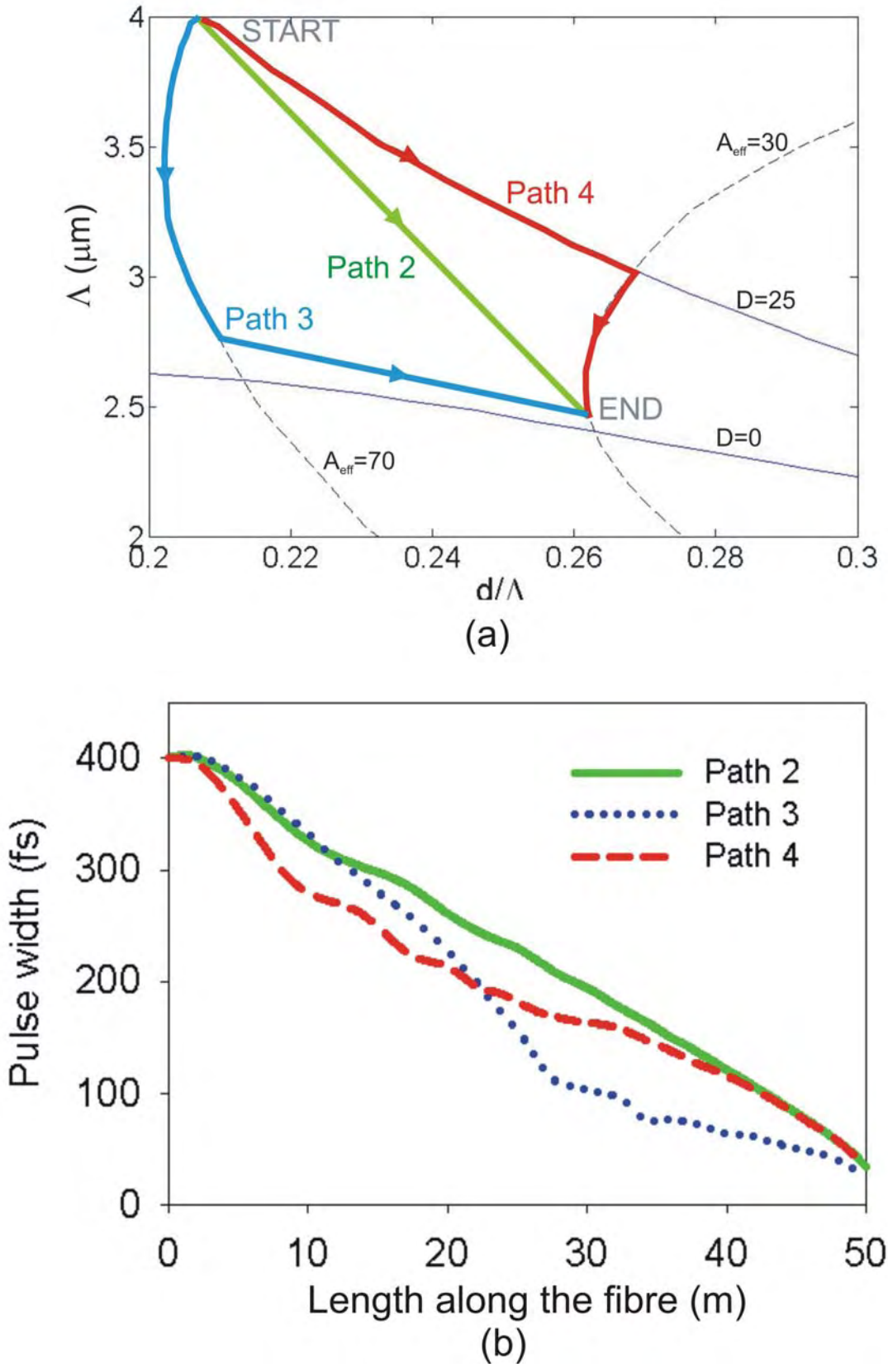

Fig. 7.7. (a) Contour map for effective area (μm^2) and dispersion (ps/nm/km) versus Λ and d/Λ for holey fibres of hexagonal geometry at 1.55 μm wavelength showing Paths 2-4. (b) Pulse width along these paths.

7.3.1 Minimised fibre length

In this section, I investigate the minimum fibre length necessary to achieve high compression factors. Fibres down to a few metres in length were studied, which could potentially be fabricated in a holey fibre tapering rig.

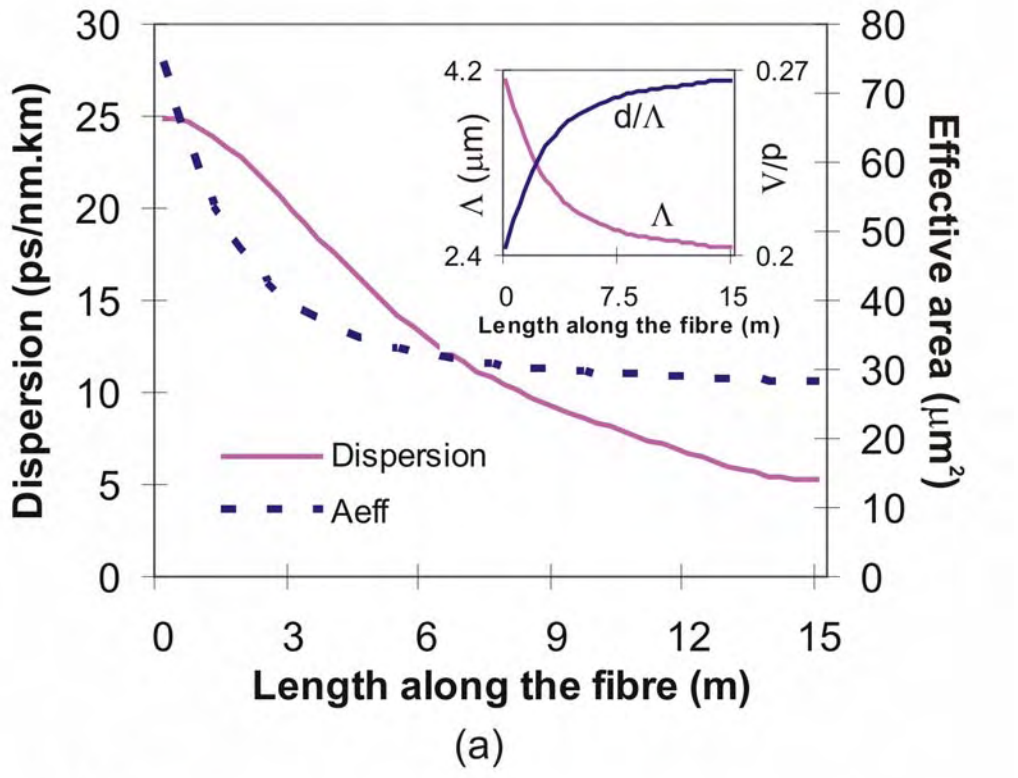

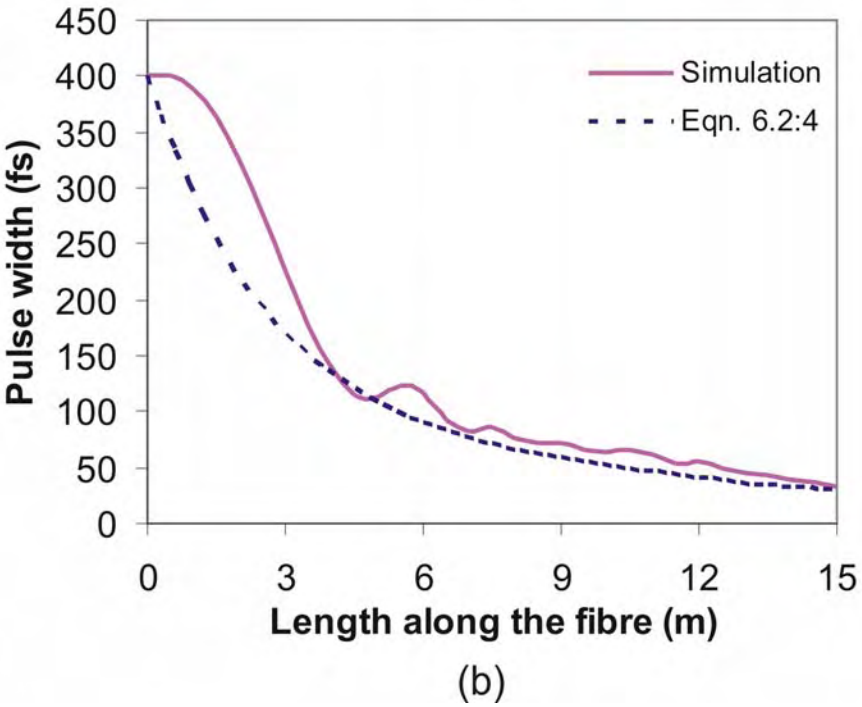

Fig. 7.8. (a) The optimized D and A_{eff} profiles for a 15 m fibre following path 2 using the constant effective gain method. Inset: the variation of Λ and d/Λ along the fibre. (b) Simulated pulse widths (FWHM) in the fibre with the optimized dispersion and effective area profiles.

I used again the fibre parameters found in Path 2 of Fig. 7.2, but now different lengths of fibre were investigated, and allowed for nonuniform changes of Λ and d/Λ along the fibre, equivalent to different profiles of D and A_{eff}, [Mostofi, 1997]. Simulations indicate that the shortest fibre length over which the maximum compression can be achieved requires constant effective gain g_{eff} along the fibre, [Bogatyrev 1991, Mamyshev, 1991]. In its dimensionless form, this condition can be written as

$$g_{eff} = -\tau_0^2 \frac{2\pi c}{\lambda^2 D}\left(\frac{1}{2D}\frac{\partial D}{\partial z_{opt}} + \frac{1}{2A_{eff}}\frac{\partial A_{eff}}{\partial z_{opt}}\right) = const \qquad \text{Eqn. 7.3:1}$$

where τ_0 is the initial soliton width and z_{opt} is the position along the optimized fibre. Since the parameter pair (Λ, d/Λ) should follow the same path (Path 2) in the contour map, z_{opt} can be mapped onto the position z of Fig. 7.3 by a function $z_{opt}(z)$. For every constant value of g_{eff}, Eqn. 7.3:1 then provides a differential equation for $z_{opt}(z)$, whose solution is the optimized profile for a fibre length $L(g_{eff})$. As an example, Fig. 7.8(a) shows the optimized D and A_{eff} profiles for a 15 m fibre, the inset shows the parameter variations along the fibre. Figure 7.8(b) depicts the corresponding simulated pulse width together with the prediction by Eqn. 6.2:4, showing that a compression factor of 12 can still be achieved with this fibre.

The same optimization routine was used for different lengths of fibre and the simulated output pulse width is plotted in Fig. 7.9, together with results obtained for non-optimized profiles where Λ and d/Λ vary linearly along the fibre. As expected, no difference was found for long fibre lengths where both profiles were adiabatic everywhere along the fibre; however there exist marked differences for fibres less than 5 m long. It was found that a compression factor of 10 can still be achieved over a length of 5 m, which was close to the dispersion length. For shorter lengths, only the optimized profiles lead to similar compression factors. However the oscillatory behaviour of the output pulse width with fibre length indicated that pulse compression was no longer fully adiabatic in this regime. The difference in adiabaticity for different fibre length can be seen more clearly when the simulated pulse width was plotted together with the prediction calculated by Eqn. 6.2:4; Fig. 7.10 shows the case for 20 m, 10 m and 5 m fibres. Here, the simulated pulse compression in the 5 m fibre deviates further from the analytical prediction than that of the 20 m fibre, especially in the first half of the fibre.

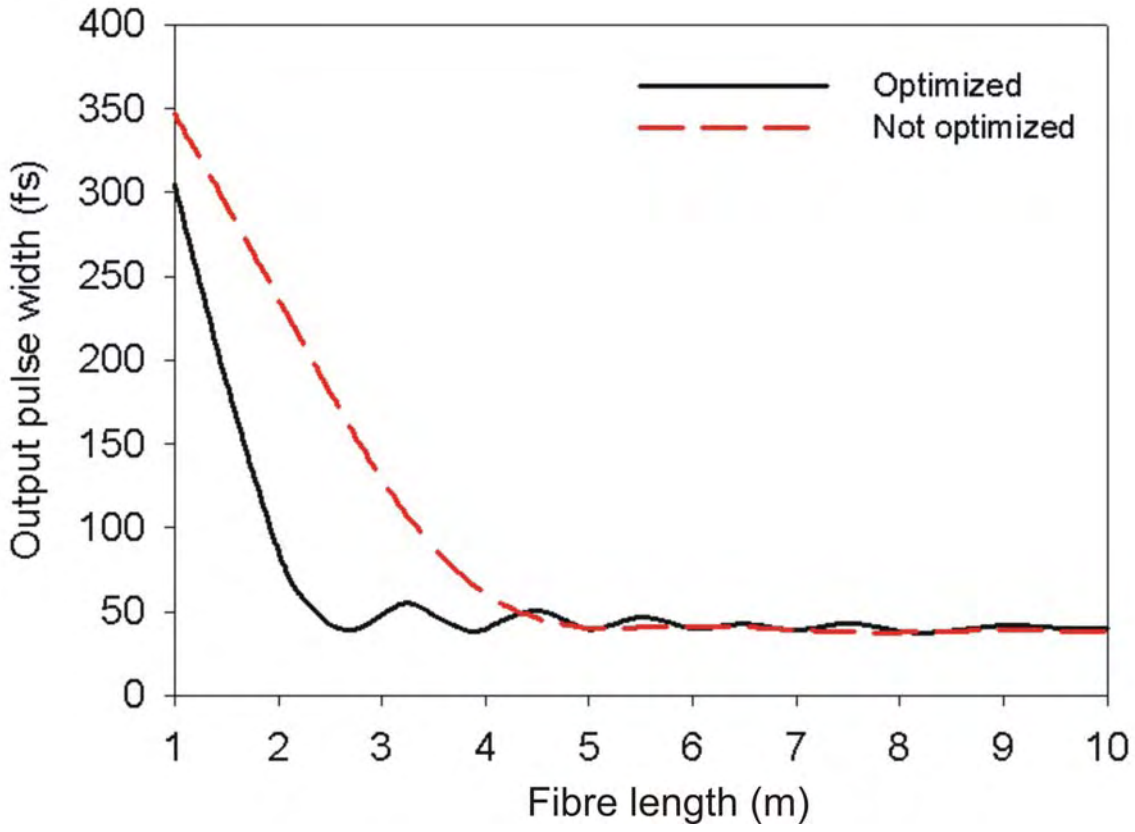

Fig. 7.9. The output pulse width for a 400 fs soliton input for fibres of different lengths following Path 2 with and without the constant effective gain (optimized) method.

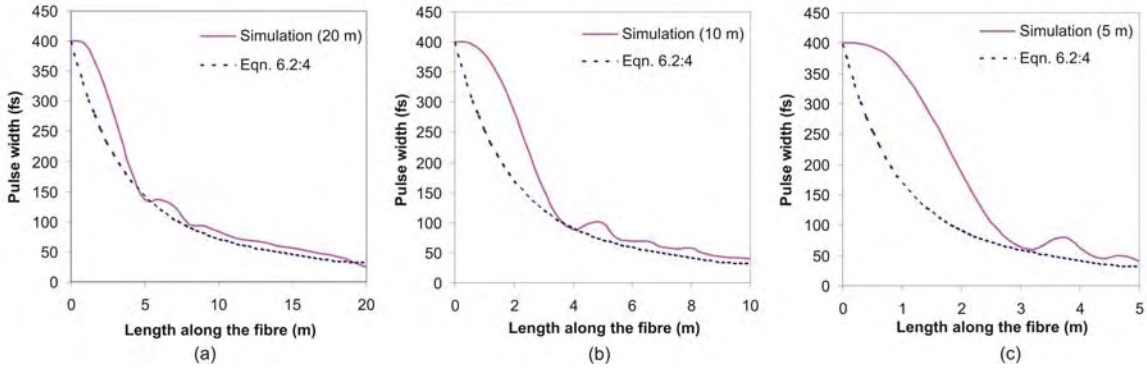

Fig. 7.10. Simulated pulse widths (FWHM) in the (a) 20 m (b) 10 m (c) 5m fibre following path 2 with the corresponding optimized dispersion and effective area profiles.

7.4 Nonadiabatic compression

Significant compression can still be observed for DMDHFs shorter than 5 m in the nonadiabatic regime, [Katemi, 2002]. As an example, I simulated the pulse propagation over only 2 m of fibre following paths 2, 3 and 4 in Fig. 7.7(a). The corresponding pulse compression is shown in Fig. 7.11, together with the results of a 5 m near-adiabatic optimized compression, as discussed in the previous section. For the short 2 m fibre, achievable compression varies significantly among different paths. The shortest pulses were found for Path 4 where A_{eff} was decreased first and D later. In this case, compression of 400 fs pulses down to 65 fs was observed, a compression factor of ~6 compared to a factor of 10 for a 5 m fibre and a factor of 12 for 15 m. By contrast, Path 3 only gave rised to a minor compression by less than a factor of two. This large difference in performance can be explained as follows. A soliton is commonly interpreted as a pulse where the broadening effect of dispersion is exactly compensated by the focusing effect of the nonlinearity. For soliton compression, I therefore expect the nonlinearity to play the major role and thus an initial decrease of the effective area (increase of nonlinearity) will lead to faster compression, in agreement with the numerical results.

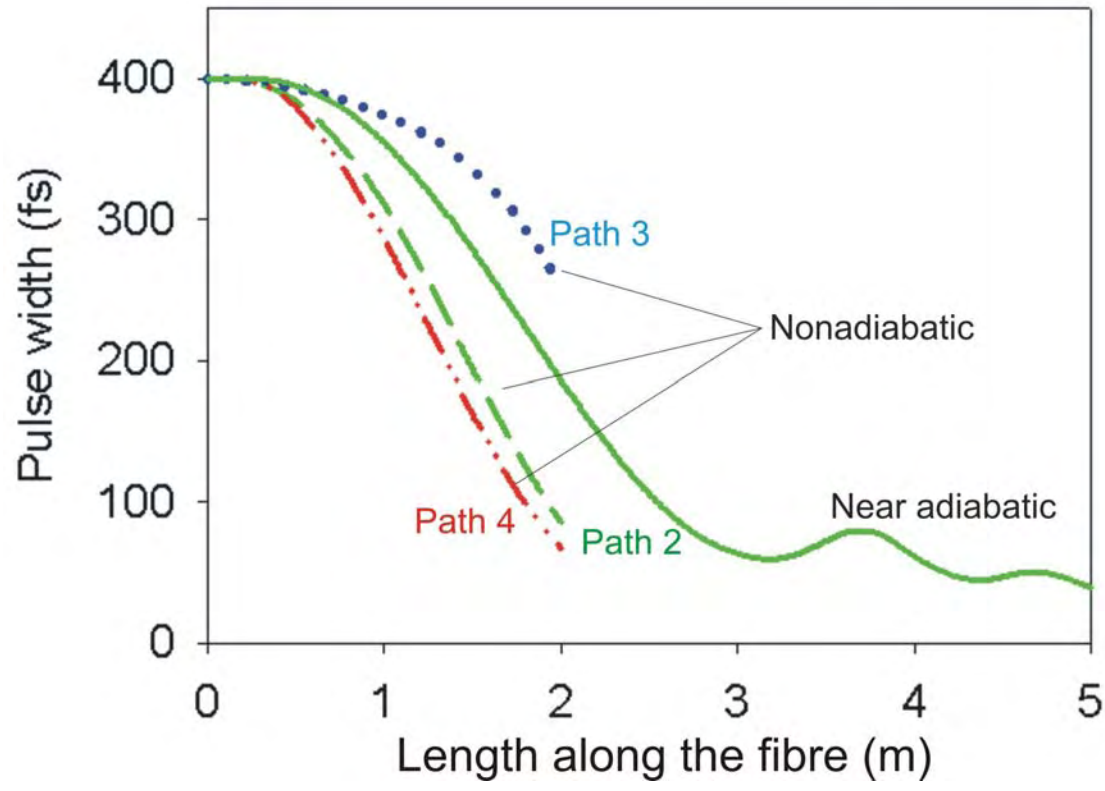

Fig. 7.11. Pulse width along paths 2, 3 and 4 under optimized near-adiabatic (5 m fibre length, path 2) and nonadiabatic (2 m fibre length) conditions.

7.5 Compression in real fibres

In real fibres, soliton compression is limited by propagation losses. In this case, the soliton energy in Eqn. 6.2:4 is not constant, but decreases exponentially with propagation length. The pulse width under ideal adiabatic conditions is thus given by

$$\tau = 1.76 \frac{\lambda^3 D A_{eff}}{2\pi^2 c n_2 E_0 \exp(-\alpha L)} \qquad \text{Eqn. 7.5:1}$$

where E_0 is the soliton energy at the input, α is the fibre loss and L is the length along the fibre. I next introduced realistic propagation losses into the numerical simulations and investigated the best fibre design and length accordingly.

If we consider again Path 2 with varying parameters Λ and d/Λ along the fibre and with the optimized D and A_{eff} profiles rescaled from Fig. 7.8(a) to various fibre lengths. The simulated output pulse widths for 400 fs soliton input, for different fibre lengths and losses, are shown in Fig. 7.12(a). The optimum length for the chosen profiles was between 3 and 10 m. For example, in the case of 0.15 dB/m fibre loss, the minimum output pulse width is 45 fs with a fibre length of ~3 m, see Fig. 7.12(b). I also observed that for long fibres the simulated output pulse widths agree very well with the analytical prediction 7.5:1, where good adiabaticity was observed.

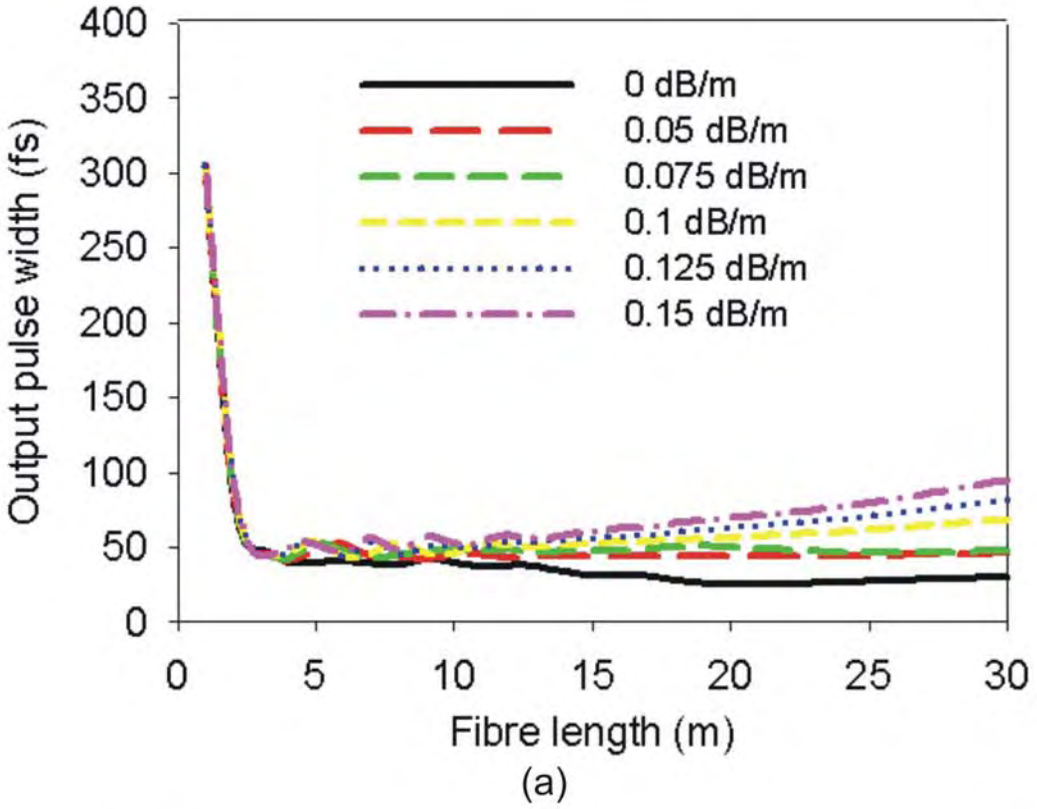

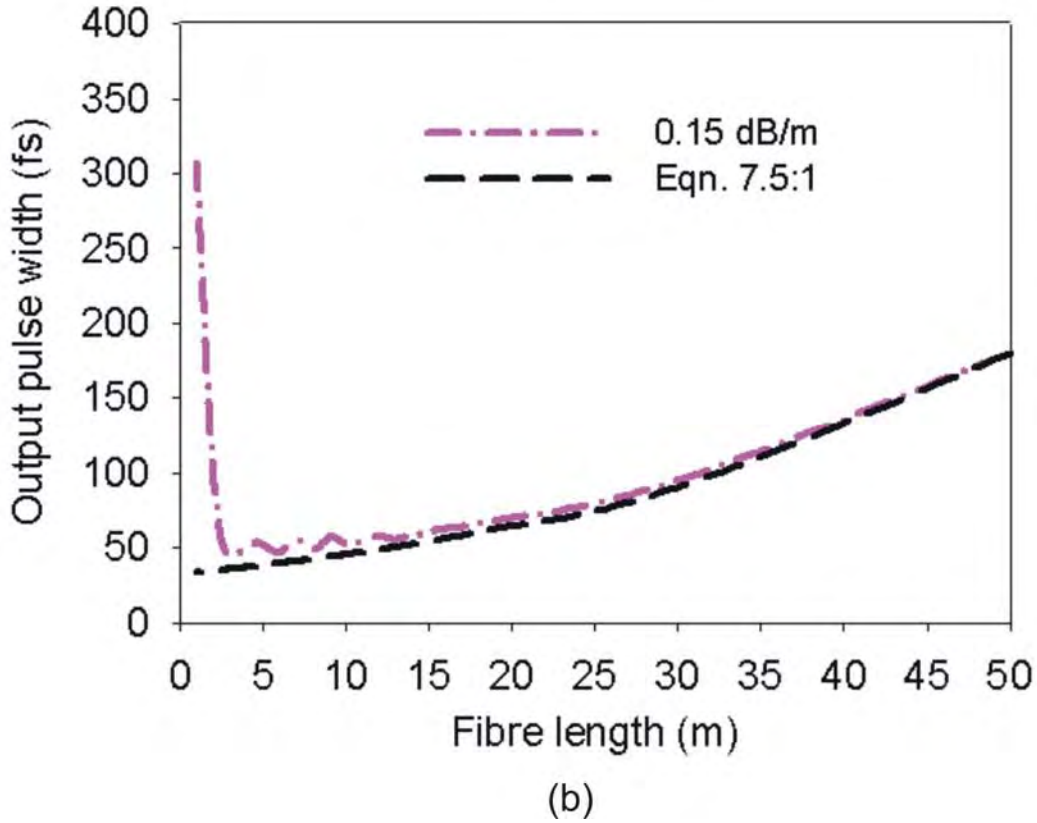

Fig. 7.12. Simulated output pulse width for fibres with D and A_{eff} profiles similar to Fig. 7.8(a) for (a) different fibre lengths and losses, (b) different fibre length and loss=0.15 dB/m, and the calculated pulse width using Eqn.7.5:1.

The fibres investigated so far require large d/Λ and small Λ, which leads to large confinement losses of the fundamental mode in such tapers, [Nguyen, 2005, Laflamme, 2007]. In order to reduce the confinement loss to an acceptable level, as many as 12 to 14 rings of identical holes are needed in this regime, see Fig. 7.13. One way to reduce the number of rings, and thus to facilitate fabrication, is to use larger hole sizes in the outer rings of the fibre structure. For example, numerical mode calculations indicate that structures with 7 rings of holes, with values for Λ and d/Λ similar to the ones found at the end point of path 2 and 2 outer rings of larger holes (d/Λ>0.7) exhibit similar dispersion profiles, see Fig. 7.14. Therefore, this should lead to similar pulse compression properties while significantly reducing confinement losses. Note, however, that the presence of different hole sizes may impede tapering of the fibres over the whole range of parameters required for efficient compression.

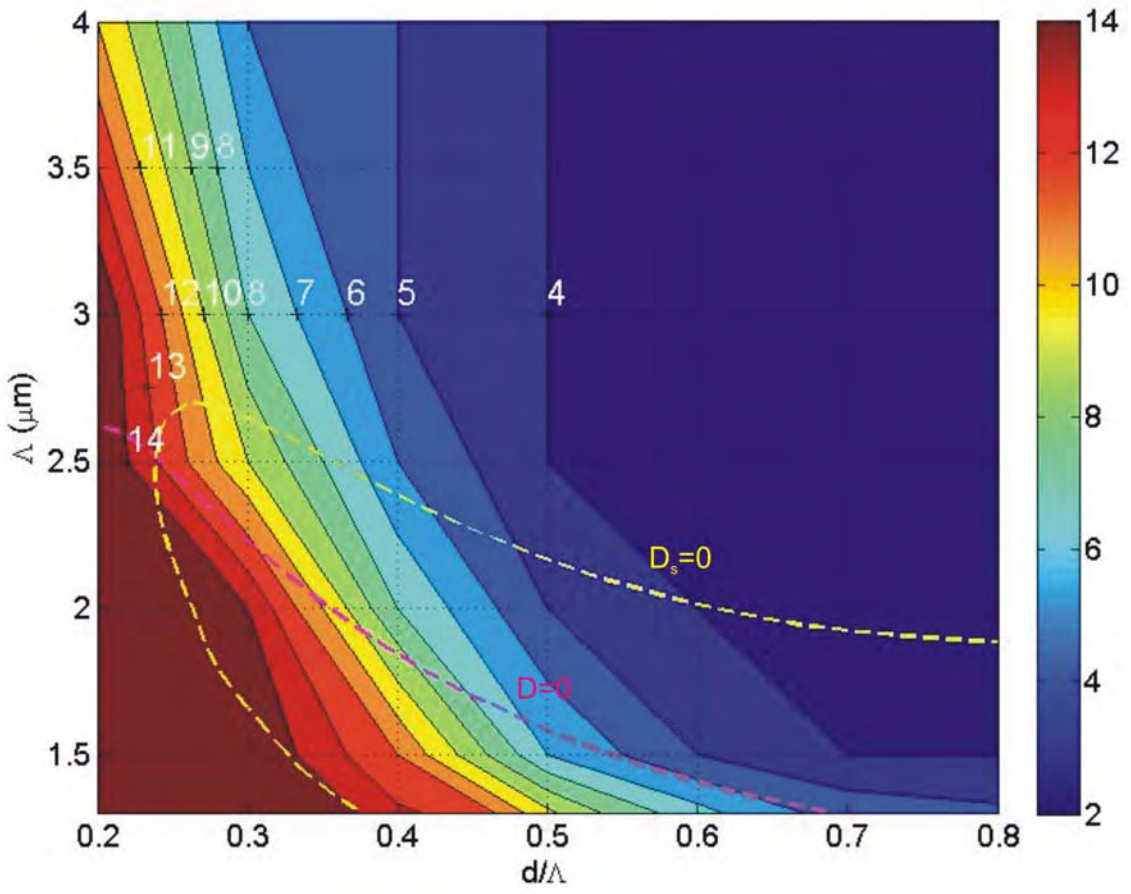

Fig. 7.13. Contour map of the number of rings of holes with regular hole size required for confinement loss <0.01 dB/m. (Provided by F. Poletti)

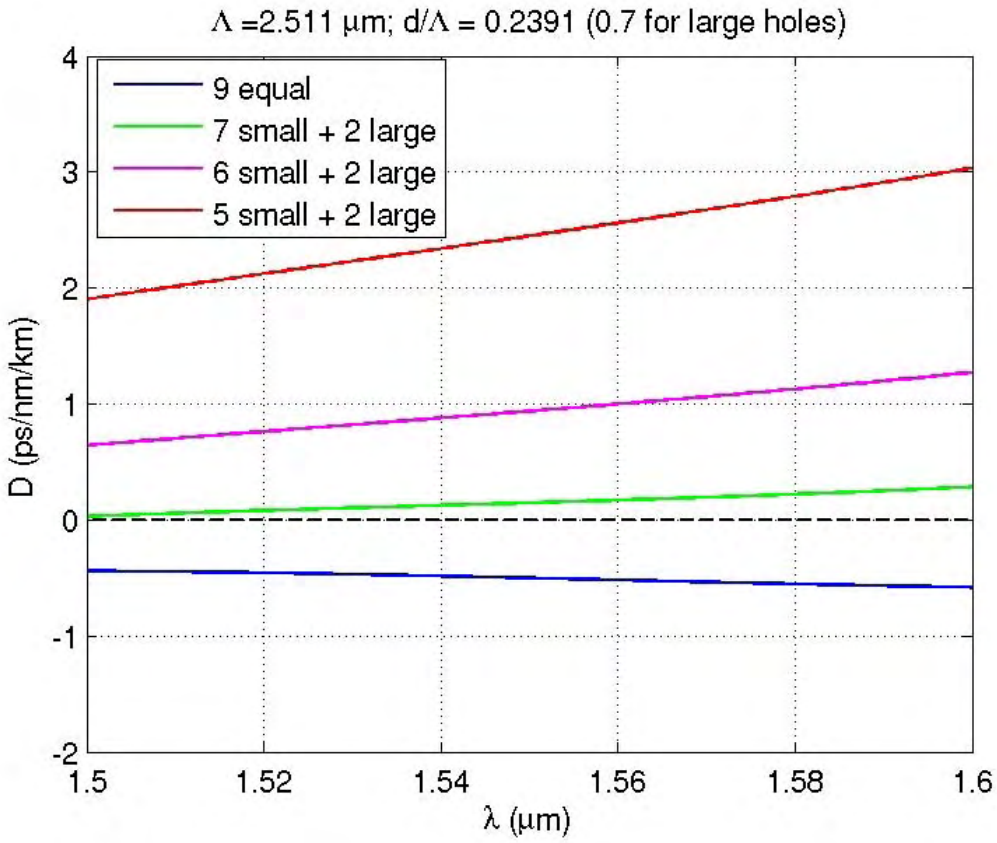

Fig. 7.14. The comparison of dispersion calculated for different numbers of rings and holes sizes, for a pair of fibre parameters similar to the end point of path 2. (Provided by F. Poletti)

7.6 Consideration of fibre fabrication

For any of the fibres investigated so far, both d/Λ and Λ were varying at the same time along the fibre, which rendered the fabrication of such fibres labour intensive and challenging. In practice, it may be desirable to find new paths in Fig. 7.1 for fibres which are more readily fabricated, even at the cost of slightly smaller compression ratios. Two possible scenarios are shown in Fig. 7.15. The first is to keep Λ constant and vary d/Λ, as indicated by Path 5, which can be achieved by varying the pressure in the air holes while simultaneously using fibre diameter feed back control during the fibre draw. However, fibres following such a path on the contour map have either D or A_{eff} decreasing but not both, which limits achievable compression factors.

The second possibility for relatively easy fabrication of DMDHFs is to keep d/Λ constant and vary Λ such as shown by Path 6 in Fig. 7.15, which can be achieved by varying the fibre drawing speed. The basic fibre drawing speed and preform size relation is given in Chapter 3, it can be written as

$$\frac{DrawSpeed_1}{DrawSpeed_2} = \left(\frac{\Lambda_2}{\Lambda_1}\right)^2 \qquad \text{Eqn. 7.6:1}$$

For example, a DMDHF that has a $\Lambda_{input}/\Lambda_{output}$ ratio of 2, the fibre drawing speed will need to increase by 4 times during a single fibre drawing process.

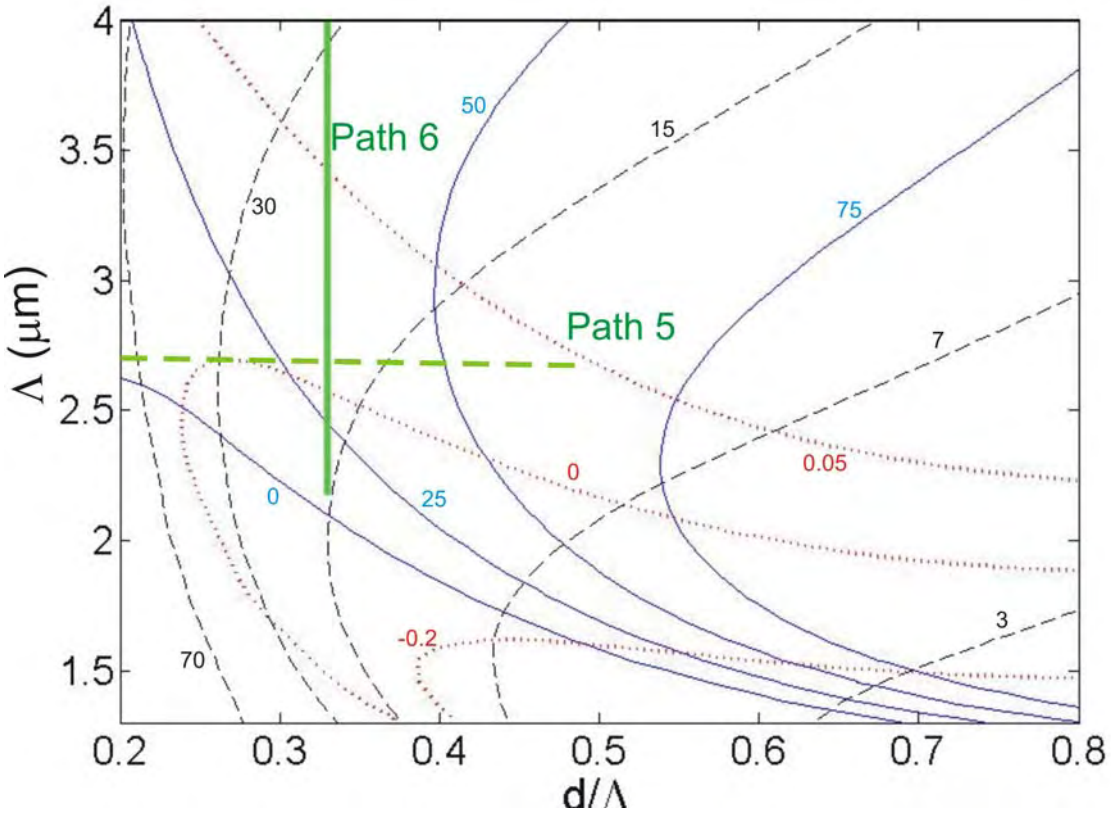

Fig. 7.15. Contour map for dispersion (blue solid line; units of ps/nm/km), dispersion slope (red dotted line; ps/nm^2/km) and effective area (black dashed line; μm^2) with paths that have either constant d/Λ or constant pitch.

Many paths with constant d/Λ offer the possibility of soliton compression, but most of the paths encounter the problems discussed in previous sections, such as Raman SSFS, large third-order dispersion, or high losses. A good option is Path 6 with d/Λ=0.33. Here, Λ decreases from 4 to 2.2 μm, D decreases from 40 to 8 ps/nm/km, and A_{eff} decreases from 30 to 15 μm^2, allowing for a compression factor of 10 in the adiabatic regime. Because of the large negative dispersion slope at the fibre end, compression of 400 fs input solitons leads to some shedding of energy into dispersive waves, but a small increase of the input soliton width to 500 fs reduces the output bandwidth sufficiently to avoid this problem.

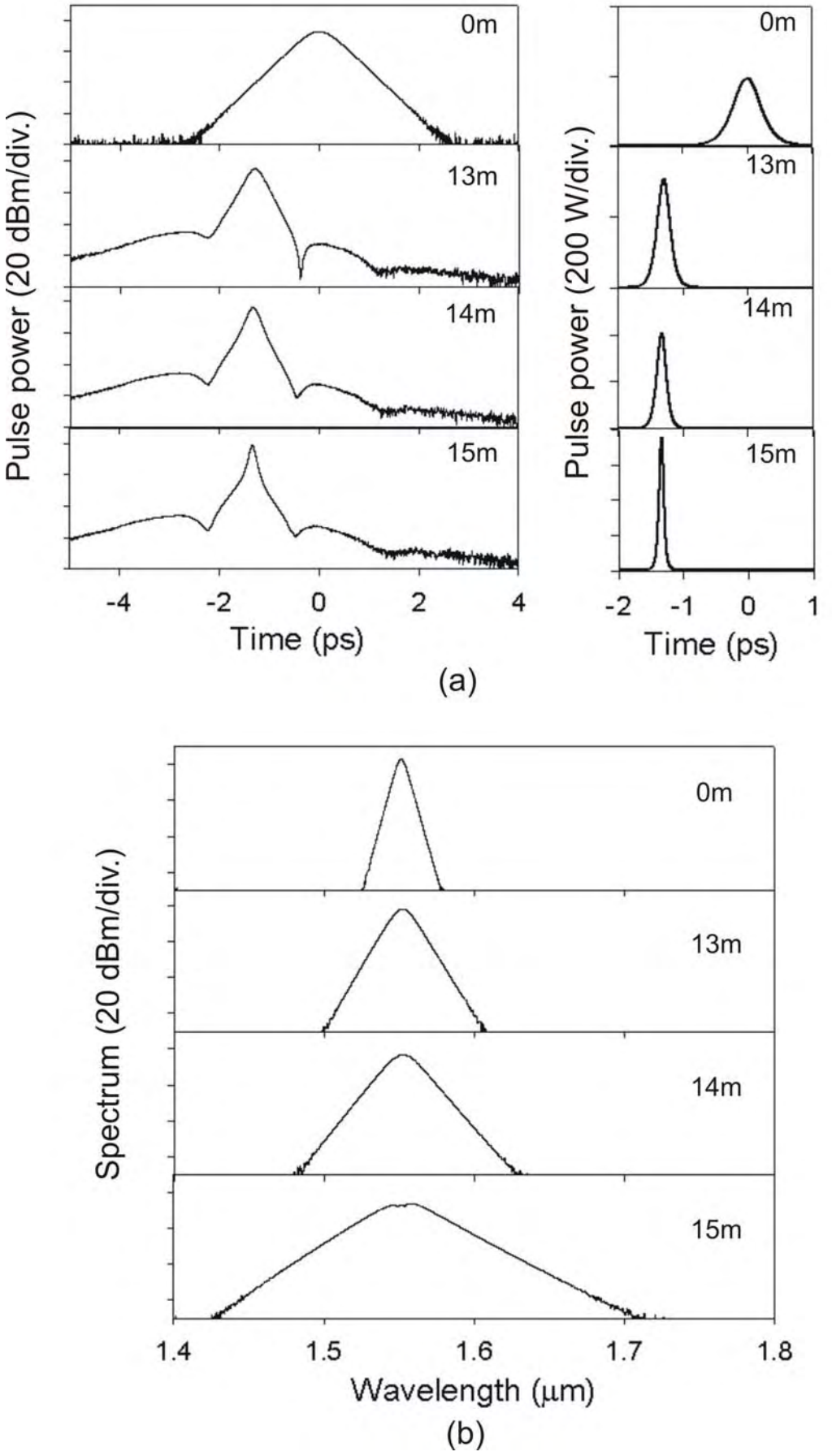

Fig 7.16. Simulated (a) pulse shape (left: logarithmic scale, right: linear scale) and (b) spectrum for a fibre (loss = 0.1 dB/m) following Path 6 with a 500 fs soliton input at different positions along the fibre.

Although 13 rings of holes are still required for low confinement loss in the latter part of the fibre, for the remaining part of the fibre only 10 or less rings are required. The resulting spectra and pulse shapes, for a 15 m fibre with a loss of 0.1 dB/m throughout are shown in Fig. 7.16. A compression factor of ~6 is found, with the output pulse maintaining high quality; pedestal-free pulses are found in both the linear scale temporal pulse shapes and the corresponding spectra.

7.7 Conclusions

Compression of femtosecond solitons in silica holey fibres of decreasing dispersion and effective mode area were investigated, which can be fabricated by changing the structural design parameters Λ and d/Λ during the fibre draw or by additional tapering. Long, low-loss, fibres with slowly changing parameters lead to adiabatic compression and the highest compression factors. In the presence of realistic fibre losses, it is essential to minimize the fibre length while maintaining high compression. It was found that the best compression over short fibre lengths was obtained in the adiabatic propagation regime if the effective gain was constant along the fibre. For even shorter fibre lengths compression is nonadiabatic but high compression factors can still be achieved by careful optimization of dispersion and effective mode area profiles along the fibre. A specific example of a fibre structure has been demonstrated which provides a compression factor of 12 in the adiabatic regime (>15 m of fibre), a factor of 10 over 5 m under optimized near-adiabatic conditions, and a factor of 6 over 2 m of nonadiabatic compression. Finally, the effects of loss and the feasibility of fabrication have been investigated. A simple fabrication design has been proposed, where adiabatic compression by a factor of ~6 can be obtained for a fibre with a loss of 0.1 dB/m.

Chapter 8

Conclusions and Future work

8.1 Conclusions

For the first part of this thesis, I investigated the fabrication procedures for dispersion controlled, small-core holey fibres of special designs. This technology plays an important role in the development of fibre based nonlinear optical devices. I found that it was not possible to accurately fabricate the fibres with a graded hole size structure by using the current two-step fibre drawing technique. Improvements have been made to reduce the structural distortion by ensuring circular fibres were being drawn. However, controlling the pitch size variation between each ring in a graded hole size structure was identified as the main obstacle for obtaining the ideal design. This variation between rings of holes was at best ~6%; this is far from the accuracy level required. Other solutions have been provided in order to achieve fibre with dispersion-flattened profiles, mainly via fibre designs of simpler structures, although it is to be appreciated that there is some associated trade off in the degree of dispersion flattening that can be achieved.

In the second part of the thesis, I focused on the study of two applications utilising the high nonlinearity and controllability of dispersion in small-core holey fibre. The supercontinuum generation phenomenon was investigated for fibres with different dispersion profiles. The systematic approach in this experiment, together with the numerical simulation, allowed me to identify the nonlinear effects that governed the spectral evolution in fibres, with one and two zero dispersion wavelengths, pumped at 1 μm. The phase matched wavelength ranges for each fibre has been calculated, and it has been shown that this accurately predicts the maximum SC bandwidth. By comparing the experimental and numerical results at different pump power levels, the different nonlinear processes which are dominating the SC generation in each parameter regime have been identified. Wider anomalous dispersion regions give rise to broader supercontinua. The most uniform spectra with improved stability against laser power and frequency fluctuations were found in fibres with two closely spaced zero-dispersion wavelengths.

Next, I demonstrated soliton compression in a dispersion-decreasing holey fibre. A compression factor of 2 was demonstrated in a 8.1 m long fibre, with low pulse energy at 1.06

μm. However, a compression factor of more than 10 is achievable using the same technique over a longer fibre with lower loss. Other limiting factors such as adiabaticity, ratio of input and output dispersion and the effects of higher order dispersion have been discussed, and the possible options for improved performance have been suggested.

The initial soliton compression experiment, which was demonstrated for the first time in a holey fibre at 1.06 μm, led to further numerical work on the topic, carried out in the final part of this thesis. The specific tapered designs are established for soliton compression from design contour maps at 1.55 μm. The work was carried out for soliton compression in the adiabatic and nonadiabatic regimes, also for fibre with and without loss. A specific example of a fibre structure has been identified which provides a compression factor of 12 in the adiabatic regime, a factor of 10 over 5 m under optimized near-adiabatic conditions, and a factor of 6 over 2 m of nonadiabatic compression. The effects of loss and the feasibility of fabrication have been investigated. A simple fabrication design has been proposed, where adiabatic compression by a factor of ~6 can be obtained in a 15 m long fibre, with a loss of 0.1 dB/m.

Overall, this thesis demonstrated the advancement of highly nonlinear microstructured fibres technology within the ORC in the past few years, with emphasis on dispersion control, demonstrated through design, fabrication and applications.

8.2 Future work

Fibres with the more simple dispersion-flattened designs were not realised due to the unfortunate event of the Mountbatten building fire. This would be the natural continuation of the work in the future, especially in developing fabrication techniques for controlling individual hole size within a holey fibre structure during fibre drawing.

The supercontinuum and the pulse compression works done in this thesis are the initial steps to achieving full control over spectral and temporal properties of light pulses via fibre design. Supercontinuum generation has been studied intensively, with over 700 publications on the subject, it continues to attract research interest. Examples of the research topics in this area in the near future are efficient SC generation in the visible and UV [Tombelaine, 2006, Kudlinski, 2006], and RGB generation [Rusu, 2005, Dupriez 2007], where extremely small core (<0.5 μm diameter) holey fibre is required.

Good quality soliton compression, with a high ratio required fibre with low propagation loss, which can be achieved by additional polishing of capillary tubes during the preform preparation steps is also worthy of continuation. Indeed, other designs on tapered holey fibre can be used. An example of a future project in this topic could be fabricating short tapered fibres from a fibre tapering rig, with the view of having more precise control of structural size.

Further modelling work can be done using larger maps and at different wavelengths, to establish a novel design (this may include extending the small core designs into large core designs), for applications such as soliton transmission [Stentz, 1995], SC generation [Tamura, 1999, Kudlinski, 2006] and an optical switch in a nonlinear optical loop mirror [Lima, 1999]. Tapering photonic bandgap fibres for high power compression would also be worthy of study.

Further investigation into improving cleaving and splicing of holey fibres would be appropriate for low-loss fibres connectivity, either between holey fibres, or between holey fibre and conventional fibre. Initial work on mode-matching between small-core holey fibres and standard single mode fibres by repeated arc discharge splicing is presented in [Xiao, 2007].

On a broader view, it is also possible to achieve dispersion and nonlinearity control in other types of holey fibres such as non-silica holey fibre [Ravi Kanth Kumar, 2003] and liquid filled holey fibre [Gundu, 2006]. They may offer a greater control and over a different wavelength range, which it is not available in an all-silica fibre and should be explored further.

Appendix A

Possible method to fabricate a graded hole-size fibre with pressure control for individual holes

In Chapter 4, I concluded that the technology for fabricating a holey fibre (HF) with a structure to have different hole-sizes to a specific design was unavailable. The main reason was the uncontrollable pitch and hole size variations during the cane-to-fibre draw process. Here, I propose a possible fabrication scheme that is designed to gain access to the individual holes in the lattice, for applying and controlling the pressure inside the holes during fibre draw.

Recently, a new method was proposed and demonstrated for making low-loss interfaces between conventional single-mode fibres (SMFs) and holey fibres [Leon-Saval, 2005]. Adapted from the fabrication of HF preforms from stacked tubes and rods, it is capable of individually coupling light into and out of all the cores of a fibre with multiple closely spaced cores, without input or output cross talk, the scheme is illustrated in Fig. A1.

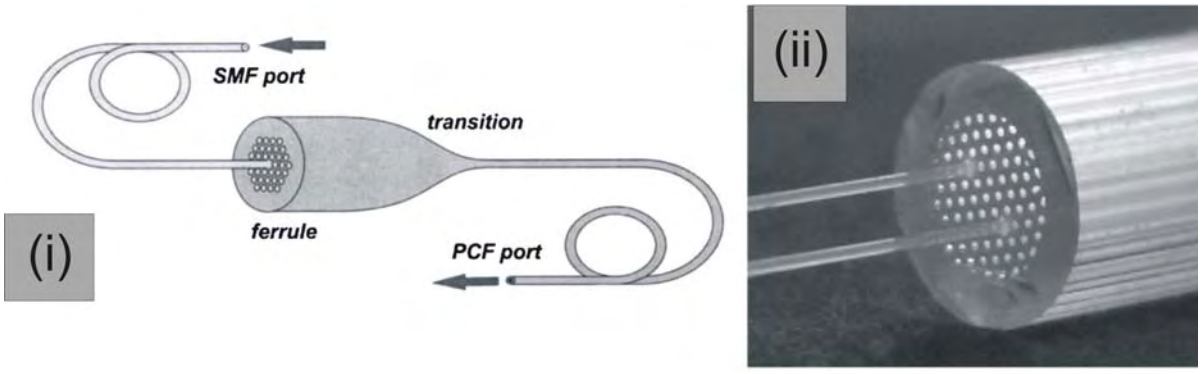

Fig. A1. (i) Schematic diagrams of a spliceless ferrule interface between a SMF and a HF. Construction of the interface by inserting a SMF into a void in the ferrule and then drawing it to a HF. The gap around the SMF in the void is collapsed by evacuation while drawing, forming a HF core from the entire SMF and some ferrule material. (ii) Photograph of the undrawn end of the ferrule containing two SMFs. Reference after [Leon-Saval, 2005].

The idea is to replace the SMF fibres with small or fibre size tubes, and connect the tubes with pressure pumps. The connections should be setup so that the pressure for each ring of holes can be altered separately, perhaps by five different pressure valve controls, one for tubes representing each ring.

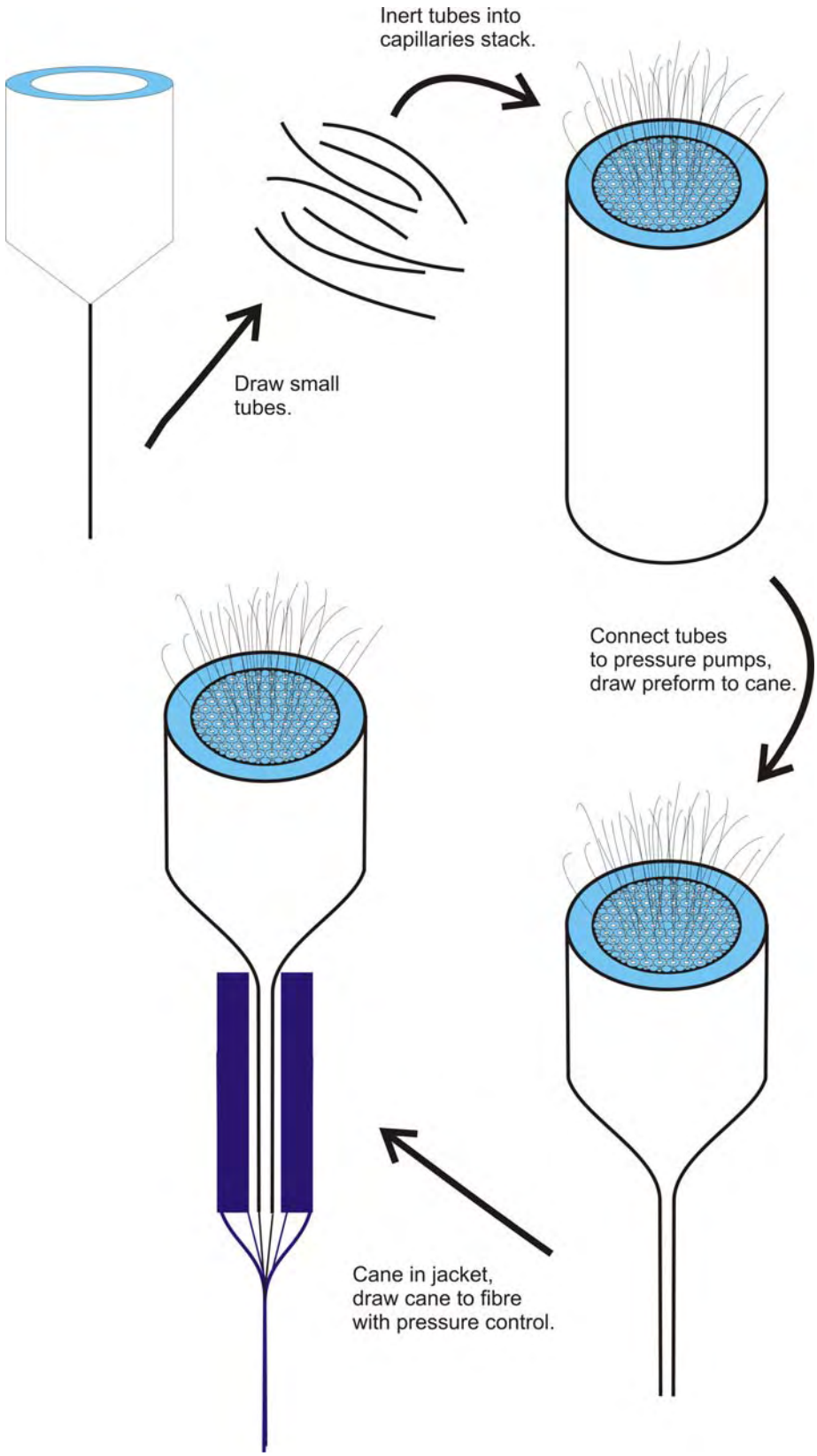

Fig. A2. Schematics to illustrate the procedures to fabricate a graded hole-size fibre with pressure control for individual holes.

The preform is stacked with open capillaries instead of using sealed ones. Next a tube is drawn down to a small size, without coating, cut it into pieces, and inserted into the stacked

capillaries. The individual tubes are connected to pressure pumps, then the preform is drawn either to a fibre while adjusting the pressure accordingly, or to a cane which is left uncut. All the holes need to be open in the cane.

Now it is possible to access individual holes in the cane. A jacket tube is fitted around the cane and this is drawn down to fibre while controlling the pressure for each ring. The scheme is shown in Fig. A2.

List of publications

Journal papers

M. L. V. Tse, P. Horak, F. Poletti, and D. J. Richardson, "Designing Tapered Holey Fibers for Soliton Compression," IEEE J. Quantum Electron. (Accepted).

M. L. V. Tse, P. Horak, J. H. V. Price, F. Poletti, F. He, and D. J. Richardson, "Pulse compression at 1.06 μm in dispersion-decreasing holey fibers," *Optics Letters*, 31 (23): 3504-3506, 2006.

M. L. V. Tse, P. Horak, F. Poletti, N. G. R. Broderick, J. H. V. Price, J. R. Hayes, and D. J. Richardson, "Supercontinuum generation at 1.06 μm in holey fibers with dispersion flattened profiles," *Optics Express* 14 (10): 4445-4451, 2006.

F. Poletti, V. Finazzi, T. M. Monro, N. G. R. Broderick, **V. Tse**, and D. J. Richardson, "Inverse design and fabrication tolerances of ultra-flattened dispersion holey fibers," *Optics. Express*, 13 (10): 3728-3736, 2005.

Conference papers

D. J. Richardson, F. Poletti, **M. L. V. Tse**, P. Horak, N. G. R. Broderick, J. Y. Y. Leong, X. Feng, K. Frampton, W. H. Loh, S. Asimakis, and P. Petropoulos, "Recent advances in highly nonlinear microstructured optical fibers," Frontiers in Optics (FiO) San Jose 16-20 Sep 2007 (Invited).

P. Horak, **M. L. V. Tse**, F. Poletti, and D. J. Richardson, "Soliton compression in short lengths of microstructured fibres," CLEO-Europe/IQEC 2007 Munich 17-22 Jun 2007.

M. L. V. Tse, P. Horak, F. Poletti, and D. J. Richardson, "Designing dispersion- and mode-area-decreasing holey fibers for soliton compression," CLEO/QELS 2007 Baltimore 6-11 May 2007.

M. L. V. Tse, P. Horak, F. Poletti, N. G. Broderick, J. H. V. Price, J. R. Hayes, and D. J. Richardson, "A systematic study of supercontinuum generation at 1.06 μm in holey fibers with dispersion flattened profiles," OFC 2006 Anaheim 5-10 Mar 2006.

P. Petropoulos, F. Poletti, J. Y. Y. Leong, T. M. Monro, H. Ebendorff-Heidepriem, V. Finazzi, **V. Tse**, X. Feng, S. Asimakis, N. G. Broderick, and D. J. Richardson, "High nonlinearity holey fibers: design fabrication and applications," CLEO/IQEC-Pacific Rim Tokyo 11-15 Jul 2005 (Invited).

D. J. Richardson, F. Poletti, J. Y. Y. Leong, X. Feng, H. Ebendorff-Heidepreim, V. Finazzi, K. E. Frampton, S. Asimakis, R. C. Moore, J. C. Baggett, J. R. Hayes, M. N. Petrovich, **M. L. Tse**, R. Amezcua, J. H. V. Price, N. G. R. Broderick, P. Petropoulos, and T. M. Monro, "Advances in microstructured fiber technology," WFOPC 2005 Palermo 22-24 Jun 2005 (Invited).

Bibliography

G. P. Agrawal and M. J. Potasek, “Nonlinear pulse distortion in single-mode optical fibers at the zero-dispersion wavelength,” Phys. Rev. A **33**, 1765-1776 (1986).

G. P. Agrawal, Nonlinear Fiber Optics, 4th ed. (Academic Press, San Diego, Ca, USA, 2007).

B. J. Ainslie and C. Day, “A review of single-mode fibers with modified dispersion characteristics,” J. Lightwave Technol. **4**, 967-979 (1986).

Y. Akasaka and Y. Suzuki, “Enlargement of effective core area on dispersion-flattened fiber and its low nonlinearity,” in Proc. OFC 1998, ThK2 (1998).

R. R. Alfano and S. L. Shapiro, “Emission in the region 4000 to 7000 Å via four-photon coupling in glass,” Phys. Rev. Lett. **24**, 584-587 (1970).

T. V. Andersen, K. M. Hilligsøe, C. K. Nielsen, J. Thøgersen, K. P. Hansen, S. R. Keiding, and J. J. Larsen, “Continuous-wave wavelength conversion in a photonic crystal fiber with two zero-dispersion wavelengths,” Opt. Express **12**, 4113-4122 (2004).

D. H. Auston and M. C. Nuss, “Electrooptic generation and detection of femtosecond electrical transients,” IEEE J. Quantum Electron.**24**, 184–197 (1988).

J. C. Baggett, T. M. Monro, K. Furusawa and D. J. Richardson, “Comparative study of bend loss in large mode holey and conventional fibers,” Opt. Lett. **26**, 1045-1047 (2001).

J. C. Baggett, T. M. Monro, K. Furusawa, V. Finazzi and D. J. Richardson, “Understanding bending losses in holey optical fibers,” Opt. Commun. **227**, 317-335 (2003).

G. Barton, M. A. van Eijkelenborg, G. Henry, M. C. J. Large, and J. Zagari, “Fabrication of microstructured polymer optical fibres,” Opt. Fiber Technol. **10**, 325-335 (2004).

P. Beaud, W. Hodel, B. Zysset and H. Weber, “Ultrashort pulse propagation, pulse breakup, and fundamental soliton formation in a single-mode optical fiber,” IEEE J. Quantum Electron. **23**, 1938-1946 (1987).

T. A. Birks, P. J. Roberts, P. St. J. Russell and D. M. Atkin, T. J. Shepherd, “Full 2-D photonic bandgaps in silica/air structures,” Electron. Lett. **31**, 1941-1943 (1995).

T. A. Birks, J. C. Knight and P. St.J. Russell, “Endlessly single-mode photonic crystal fiber,” Opt. Lett. **22**, 961-963 (1997).

T. A. Birks, D. Mogilevtsev, J. C. Knight and P. St. J. Russell, “Dispersion compensating using single-material fibers,” IEEE Photonic Tech. Lett. **11**, 674-676 (1999).

K. J. Blow and D. Wood, “Theoretical Description of Transient Stimulated Raman Scattering in Optical Fibers,” IEEE J. Quantum Electron. **25**, 2665-2673 (1989).

V. A. Bogatyrev, M. M. Bubnov, E. M. Dianov, A. S. Kurkov, P. V. Mamyshev, A. M. Prokhorov, S. D. Rumyantsev, V. A. Semenov, S. L. Semenov, A. A. Sysoliatin, S. V. Chemikov, A. N. Gur’yanov, G. G. Devyatykh, and S. I. Miroshnichenko, “A single-mode fiber with chromatic dispersion varying along the length,” J. Lightwave Technol. **9**, 561-566 (1991).

A. Boskovic, S. V. Chernikov, J. R. Taylor, L. Gruner-Nielsen and O. A. Levring, “Direct continuous-wave measurement of n2 in various types of telecommunication fiber at 1.55 μm,” Opt. Lett. **21**, 1966-1968 (1996).

N. G. R. Broderick, T. M. Monro, P. J. Bennett and D. J. Richardson, “Nonlinearity in holey optical fibers: measurement and future opportunities,” Opt. Lett. **24**, 1395-1397 (1999).

J. Broeng, D. Mogilevstev, S. E. Barkou and A. Bjarkler, “Photonic crystal fibers: A new class of optical waveguides,” Opt. Fiber Technol. **5**, 305-330 (1999) (a).

J. Broeng, T. Sondergaard, S. E. Barkou, P. M. Barbeito and A. Bjarklev, “Waveguidance by the photonic bandgap effect in optical fibres,” J. Opt. A: Pure Appl. Opt. **1**, 477-482, (1999) (b).

K.-T. Chan and W.-H. Cao, “Enhanced compression of fundamental solitons in dispersion decreasing fibers due to the combined effects of negative third-order dispersion and Raman self-scattering,” Opt. Commun. **184**, 463-474 (2000).

S. V. Chernikov and P. V. Mamyshev, “Femtosecond soliton propagation in fibers with slowly decreasing dispersion,” J. Opt. Soc. Am. B. **8**, 1633-1641 (1991).

S. V. Chernikov, E. M. Dianov, D. J. Richardson, and D. N. Payne, “Soliton pulse compression in dispersion-decreasing fiber,” Opt. Lett. **18**, 476-478 (1993).

S. V. Chernikov and J. R. Taylor, “Measurement of normalization factor of n_2 for random polarization in optical fibers,” Opt. Lett. **21**, 1559-1561 (1996).

K. K. Chow, C. Shui, C. Lin, and A. Bjarklev, “All-optical signal regeneration with wavelength multicasting using pump-modulated four-wave mixing in a nonlinear photonic crystal fiber,” in Proc. CLEO 2005, 871-872 (2005)

K. Chung, S. Kim, and A. Yin, “Design of a highly nonlinear dispersion-shifted fiber with a small effective area by use of the beam propagation method with the Gaussian approximation method,” Opt. Lett. **28**, 2031-2033 (2003).

R. F. Cregan, B. J. Mangan, J. C. Knight, T. A. Birks, P. St. J. Russell, P. J. Roberts and D. C. Allan, “Single-mode photonic band gap guidance of light in air,” Science **285**, 1537-1539 (1999).

S. A. Diddams, Th. Udem, K. R. Vogel, C. W. Oates, E. A. Curtis, R. S. Windeler, A. Bartels, J. C. Bergquist and L. Hollberg, “A compact femtosecond-laser-based optical clockwork,” in Proc. of SPIE **4269**, 77-83 (2001).

N. J. Doran and D. Wood, "Nonlinear-optical loop mirror," Opt. Lett. **13**, 56-58 (1988).

P. G. Drazin, *Soliton: An Introduction* (Cambridge University Press, Cambridge, UK, 1993).

J. M. Dudley, L. Provino, N. Grossard, H. Maillotte, R. S. Windeler, B. J. Eggleton, and S. Coen, “Supercontinuum generation in air-silica microstructured fibers with nanosecond and femtosecond pulse pumping,” J. Opt. Soc. Am. B. **19**, 765-771 (2002).

J. M. Dudley, G. Genty, and S. Coen, “Supercontinuum generation in photonic crystal fiber,” Rev. Mod. Phys. **78**, 1135-1184 (2006).

P. Dupriez, F. Poletti, P. Horak, M. N. Petrovich, Y. Jeong, J. Nilsson, D. J. Richardson, and D. N. Payne, "Efficient white light generation in secondary cores of holey fibers," Opt. Express **15**, 3729-3736 (2007).

R. B. Dyott, *Elliptical Fiber Waveguides* (Artech House, Boston, Mass., 1995).

H. Ebendorff-Heidepriem, T. Monro, M. A. Van Eijkelenborg, M. C. J. Large, "Extruded high-NA microstructured polymer optical fibre," Opt. Commun. **273**, 133-137 (2007).

P. Falk, M. Frosz, and O. Bang, "Supercontinuum generation in a photonic crystal fiber with two zero-dispersion wavelengths tapered to normal dispersion at all wavelengths," Opt. Express **13**, 7535-7540 (2005).

A. Ferrando, E. Silvestre, J. J. Miref, J. A. Monsoriu, V. M. Andres and P. St. J. Russell, "Designing a photonic crystal fibre with flattened chromatic dispersion," Electon. Lett. **35**, 325-327 (1999).

A. Ferrando, E. Silvestre, J. J. Miret and P. Andres, "Nearly zero ultraflattened dispersion in photonic crystal fibers," Opt. Lett. **25**, 790-792 (2000).

V. Finazzi, T. M. Monro and D. J. Richardson, "Small-core silica holey fibers: nonlinearity and confinement loss trade-offs," J. Opt. Soc. Am. B **20**, 1427-1436 (2003).

R. A. Fisher and W. K. Bischel, "Numerical studies of the interplay between self-phase modulation and dispersion for intense plane-wave laser pulses," J. Appl. Phys. **46**, 4921-4953 (1975).

A. D. Fitt, K. Furusawa, T. M. Monro, C. P. Please and D. J. Richardson, "The mathematical modelling of capillary drawing for holey fibre manufacture," J. Eng. Math. **43**, 201-227 (2002).

R. L. Fork, C. V. Shank, C. Herlimann, R. Yen and W. J. Tomlinson, "Femtosecond white-light continuum pulse," Opt. Lett. **8**, 1-3 (1983).

M. A. Foster and A. L. Gaeta, "Ultra-low threshold supercontinuum generation in sub-wavelength waveguides," Opt. Express **12**, 3137-3143 (2004).

M. Foster, A. Gaeta, Q. Cao, and R. Trebino, "Soliton-effect compression of supercontinuum to few-cycle durations in photonic nanowires," Opt. Express **13**, 6848-6855 (2005).

M. H. Frosz, P. Falk, and O. Bang, "The role of the second zero-dispersion wavelength in generation of supercontinua and bright-bright soliton-pairs across the zero-dispersion wavelength," Opt. Express **13**, 6181-6192 (2005).

M. Fuochi, F. Poli, S. Selleri, A. Cucinotta and L. Vincesti, "Study of Raman amplification properties in triangular photonic crystal fibers," J. Lightwave Technol. **21**, 2247-2254 (2003).

K. Furusawa, *Development of rare-earth doped microstructured optical fibres*, PhD thesis, University of Southampton, Southampton, SO17 1BJ (2003).

G. Genty, M. Lehtonen, H. Ludvigsen, and M. Kaivola, "Enhanced bandwidth of supercontinuum generated in microstructured fibers," Opt. Express **12**, 3471-3480 (2004).

A. M. Glass, D. J. DiGiovanni, T. A. Strasser, A. J. Stentz, R. E. Slusher, A. E. White, A. R. Kortan, and B. J. Eggleton, "Advances in Fiber Optics," Bell Labs Technical Journal **5**, 168-187 (2000)

J. P. Gordon, "Theory of the soliton self-frequency shift," Opt. Lett. **11**, 662-664 (1986).

D. Grischkowsky, E. Courtens and J. A. Armstrong, "Observation of self-steepening of optical pulses with possible shock formation," Phys. Rev. Let. **31**, 422-425 (1973).

R. Hainberger and S. Watanabe, "Impact of the Wavelength Dependence of the Mode Field on the Nonlinearity Coefficient of PCFs," IEEE Photonic. Tech. Lett. **17**, 70-72 (2005).

K. M. Gundu, M. Kolesik, and J. V. Moloney, "Ultra-flattened-dispersion selectively liquid-filled photonic crystal fibers," Opt. Express **14**, 6870-6878 (2006).

K. P. Hansen , "Dispersion flattened hybrid-core nonlinear photonic crystal fiber," Opt. Express **11**, 1503-1509 (2003).

J. Hansryd, P. A. Andrekson, M. Westlund, L. Jie and P.-O. Hedekvist, "Fiber-Based optical Parametric Amplifiers and Their Applications," IEEE J.Sel. Top. Quant. Electron. **8**, 506-520 (2002).

J. M. Harbold, F. Ö. Ilday, F. W. Wise, T. A. Birks, W. J. Wadsworth, and Z. Chen, "Long-wavelength continuum generation about the second dispersion zero of a tapered fiber," Opt. Lett. **27**, 1558-1560 (2002).

I. Hartl, X. D. Li, C. Chudoba, R. K. Ghanta, T. H. Ko, J. G. Fujimoto, J. K. Ranka and R. S. Windeler, "Ultrahigh-resolution optical coherence tomography using continuum generation in an air-silica microstructure optical fiber," Opt. Lett. **26**, 608-610 (2001).

J. D. Harvey, R. Leonhardt, H. C. Clark, R. Kruhlak, J. C. Knight, W. J. Wadsworth, P. St. J. Russell, "PCF based optical parametric oscillators and amplifiers," IEEE LEOS **1**, 186-187 (2003).

A. Hasegawa and Y. Kodama, "Amplification and reshaping of optical solitons in a glass fiber –I," Opt. Lett. **7**, 285-287 (1982).

H. Hasegawa and Y. Kodama, *Soliton in Optical Communications* (Oxford University Press, New York, 1995)

K. M. Hilligsøe, T. V. Andersen, H. N. Paulsen, C. K. Nielsen, K. Mølmer, S. Keiding, R. Kristiansen, K. P. Hansen, and J. J. Larsen, "Supercontinuum generation in a photonic crystal fiber with two zero dispersion wavelengths," Opt. Express **12**, 1045-1054 (2004).

Y. Horiuchi, Y. Namihira and H. Wakabayashi, "Chromatic Dispersion Measurement in 1.55 μm narrow band region using a tunable external-cavity laser," IEEE Photonic. Tech. Lett. **1**, 458-460 (1989).

B. B. Hu and M. C. Nuss, "Imaging with Terahertz waves," Opt. Lett. **20**, 1716–1718 (1995).

J. Hu, B. S. Marks, C. R. Menyuk, J. Kim, T. F. Carruthers, B. M. Wright, T. F. Taunay, and E. J. Friebele, "Pulse compression using a tapered microstructure optical fiber," Opt. Express **14**, 4026-4036 (2006).

A. V. Husakou and J. Herrmann, "Supercontinuum generation of higher-order solitons by fission in photonic crystal fibers," Phys. Rev. Lett. **87**, 203901/1- 203901/4 (2001).

A. V. Husakou and T. Herrmann, “Supercontinuum generation, four-wave mixing, and fission of higher-order solitons in photonic-crystal fibers,” J. Opt. soc. Am. B **19**, 2171-2182 (2002).

E. P. Ippen and R. H. Stolen, “Stimulated Brillouin scattering in optical fibers,” Appl. Phys. Lett. **21**, 539-541 (1972).

E. P. Ippen, C. V. Shank and T. K. Gustafson, “Self-phase modulation of picosecond pulses in optical fibers,” Appl. Phys. Lett. **24**, 190-192 (1974).

M. N. Islam, G. Sucha, I. Bar-Joseph, M. Wegener, J. P. Gordon and D. S. Chemla, “Femtosecond distributed soliton spectrum fibers”, J. Opt. Soc. Am. B **6**, 1149-1158 (1989).

H. Itoh, G. M. Davis and S. Sudo, “Continuous-wave-pumped modulational instability in an optical fiber,” Opt. Lett. **14**, 1368-1370 (1989).

L. M. Ivanov, P. P. Branzalov, and L. I. Pavlov, “Efficient compression of fundamental solitons in fibers with decreasing dispersion,” Opt. Quantum Electron. **24**, 565–573 (1992).

S. John, “Strong localization of photons in certain disordered dielectric lattices,” Phys. Rev. Lett. **58**, 2486-2489 (1987).

R. J. Jonek and R. Landauer, “Laser pulse distortion in a nonlinear dielectric,” Phys. Lett. A **24**, 228-229 (1967).

P.Kaiser and H.W.Astle, “Low-loss single-material fibers made from pure fused silica,” Bell System Tech.J. **53**, 1021-1039 (1974).

K. C. Kao and G. A. Hockham, “Dielectric-fiber surface waveguides for optical frequencies,” in Proc. IEE J. **133**, 1151-1158 (1966).

F. P. Kapron, D. B. Keck, and R. D. Maurer, “Radiation losses in glass optical waveguides,” Appl. Phys. Lett. **17**, 423-425 (1970).

F. K. Katemi, “Analysis of nonadiabatically compressed pulses from dispersion-decreasing fiber,” Opt. Lett. **27**, 1637-1639 (2002).

J. C. Knight, T. A. Birks, P. St. J. Russell and D. M. Atkin, “All-silica single mode optical fiber with photonic crystal cladding,” Opt. Lett. **21**, 1547-1549 (1996).

J. C. Knight, T. A. Birks, P. St. J. Russell and J. P. de Sandro, “Properties of photonic crystal fiber and the effective index model,” J. Opt. Soc. Am. A **15**, 748-752 (1998).

J. C. Knight, J. Arriaga, T. A. Birks, A. Ortigosa-Blanch, W. J. Wadsworth, P. St. J. Russell, “Anomalous dispersion in photonic crystal fiber,” IEEE Photonic Tech. Lett. **12**, 807-809 (2000).

C. J. Koester and E. Snitzer, “Amplification in a fiber laser,” Appl. Opt. 3, 1182-1186 (1964)

A. Kudlinski, A. K. George, J. C. Knight, J. C. Travers, A. B. Rulkov, S. V. Popov, and J. R. Taylor, “Zero-dispersion wavelength decreasing photonic crystal fibers for ultraviolet-extended supercontinuum generation,” Opt. Express **14**, 5715-5722 (2006).

S. Laflamme, S. Lacroix, J. Bures, and X. Daxhelet, “Understanding power leakage in tapered solid core microstructured fibers,” Opt. Express **15**, 387-396 (2007).

J. H. Lee, W. Belardi, K. Furusawa, P. Petropoulos, Z. Yusoff, T. M. Monro and D. J. Richardson, “Four-wave mixing based 10-Gbit/s tunable wavelength conversion using a holey fiber with a high SBS threshold,” IEEE Photonic. Tech. Lett. **15**, 440-442 (2003).

L. Lefort, J. H. V. Price, D. J. Richardson, G. J. Spühler, R. Paschotta, U. Keller, A. R. Fry and J. Weston, “Practical low-noise stretched-pulse Yb3+-doped fiber laser,” Opt. Lett. **27**, 291-293 (2002).

S. Leon-Saval, T. Birks, W. Wadsworth, P. St. J. Russell, and M. Mason, “Supercontinuum generation in submicron fibre waveguides,” Opt. Express **12**, 2864-2869 (2004).

S. G. Leon-Saval, T. A. Birks, N. Y. Joly, A. K. George, W. J. Wadsworth, G. Kakarantzas, and P. St. J. Russell, “Splice-free interfacing of photonic crystal fibers,” Opt. Lett. **30**, 1629-1631 (2005).

J.L.S. Lima and A.S.B. Sombra, “Soliton and quasi-soliton switching in nonlinear optical loop mirror constructed from dispersion decreasing fiber,” Opt. Commun. **163**, 292–300 (1999).

Y. Liu, W. B. Mattingly, D. K. Smith, C. E. Lacy, J. A. Cline and E. M. De Liso, “Design and fabrication of locally dispersion-flattened large effective area fibers,” in Proc. ECOC 1998, 37-38 (1998).

X. Liu, C. Xu, W. H. Knox, J. K. Chandalia, B. J. Eggleton, S. G. Kosinski, and R. S. Windeler “Soliton selffrequency shift in a short tapered air-silica microstructure fiber,” Opt. Lett. **26**, 358–360 (2001).

Y. K. Lizé, E. C. Mägi, V. G. Ta’eed, J. A. Bolger, P. Steinvurzel, and B. J. Eggleton, “Microstructured optical fiber photonic wires with subwavelength core diameter,” Opt. Express **12**, 3209–3217 (2004).

J. J. Lu and A. Safaai-Jazi, “Analysis and design of multi-clad single mode fibers with three zero-dispersion wavelengths,” in Proc. IEEE Southeastcon 1989, 12B5 (1989).

J. B. MacChesney, P. B. O’Connor, F. V. DiMarcello, J. R. Simpson, and P. D. Lazay, “Preparation of low-loss optical fibers using simultaneous vapour deposition and fusion,” in Proc. 10th Intl. Congress on Glass **6**, 40-44 (1974).

P. V. Mamyshev, S. V. Chernikov, and E. M. Dianov, “Generation of fundamental soliton trains for high-bit-rate optical fiber communication lines,” IEEE J. Quantum. Electron. **27**, 2347-2355 (1991).

R. J. Mears, L. Reekie, I. M. Jauncey, D. N. Payne, “Low-noise erbium-doped fibre amplifier operating at 1.54 μm,” Electron. Lett. **23**, 1026-1028 (1987).

D. Mestdagh and M. Haelterman, “Spectral super-broadening of ultra-short pulses in a nonlinear Kerr medium; effect of relaxation,” Opt. Commun. **61**, 291-295 (1987).

F. M. Mitschke and L. F. Mollenauer, “Discovery of the soliton self-frequency shift,” Opt. Lett. **11**, 659-661 (1986).

M. Miyagi and S. Nishida, “Pulse spreading in single-mode fiber due to third-order dispersion,” Appl. Opt. **18**, 678 (1979).

D. Mogilevtsev, T. A. Birks and P. St. J. Russell, “Group-velocity dispersion in photonic crystal fibers,” Opt. Lett. **23**, 1662-1664 (1998).

L. F. Mollenauer, R. H. Stolen, and J. P. Gordon, “Experimental Observation of Picosecond Pulse Narrowing and Solitons in Optical Fibers,” Phys. Rev. Lett. **45**, 1095-1098 (1980).

T. M. Monro, D. J. Richardson, N. G. R. Broderick, P. J. Bennett, “Holey optical fibers: An efficient modal model,” J. Lightwave Technol. **17**, 1093-1102 (1999).

T. M. Monro, P. J. Bennett, N. G. R. Broderick and D. J. Richardson, “Holey fibers with random cladding distributions,” Opt. Lett. **25**, 206-208 (2000).

T. M. Monro, W. Belardi, K. Furusawa, J. C. Baggett, N. G. R. Broderick and D. J. Richardson, “Sensing with microstructured optical fibres,” Meas. Sci. Technol. **12**, 854-858 (2001)

K. Mori, T. Morioka and M. Saruwatari, “Ultrawide spectral range group-velocity dispersion measurement utilizing supercontinuum in an optical fiber pumped by a 1.5 mm compact laser source,” IEEE Tran. Instrum. Meas. **44**, 712-715 (1995).

D. J. Moss, Y. Miao, V. Ta’eed, E. C. M¨agi, and B. J. Eggleton, “Coupling to high-index waveguides via tapered microstructured optical fibre,” Electron. Lett. **41**, 951–953 (2005).

A. Mostofi, H. Hatami-Hanza, and P. L. Chu, “Optimum dispersion profile for compression of fundamental solitons in dispersion decreasing fibers,” IEEE J. Quantum Electron. **33**, 620-628 (1997).

K.Mukasa, M.N.Petrovich, F.Poletti, A.Webb, J.Hayes, A.van Brakel, R.Amezcua Correa, L.Provost, J.K.Sahu, P.Petropoulos, and D.J.Richardson, “Novel fabrication method of highly-nonlinear silica holey fibres,” in Proc. CLEO 2006, CMC5 (2006).

T. Nagatsuma, M. Yaita, M. Shinagawa, K. Kato, A. Kozen, K. Iwatsuki, and K. Suzuki, “Electrooptic characterization of ultrafast photodetectors using adiabatically compressed soliton pulses,” Electron. Lett. **30**, 814–816 (1994).

V. Nagarajan, E. Johnson, P. Schellenberg, W. Parson and R. Windeler, “A compact versatile femtosecond spectrometer,” Rew. Sci. Instrum. **73**, 4145-4149 (2002).

H. Nakatsuka, D. Grischkowsky, and A. C. Balant, “Nonlinear Picosecond-Pulse Propagation through Optical Fibers with Positive Group Velocity Dispersion,” Phys. Rev. Lett. **47**, 910-913 (1981).

M. Nakazawa, K. Suzuki and Y. Kimura, “3.2-5 Gb/s, 100 km error-free soliton transmission with erbium amplifiers and repeaters,” IEEE Photon. Technol. Lett. **2**, 216-219 (1990).

M. Nakazawa, E. Yoshida, T. Yamamoto, E. Yamada and A. Sahara, “TDM single channel 640 Gbit/s transmission experiment over 60 km using 400 fs pulse train and walk-off free, dispersion flattened nonlinear optical loop mirror,” Electron. Lett. **34**, 907-908 (1998).

H. C. Nguyen, B. T. Kuhlmey, M. J. Steel, C. L. Smith, E. C. Mägi, R. C. McPhedran, and B. J. Eggleton, “Leakage of the fundamental mode in photonic crystal fiber tapers,” Opt. Lett. **30**, 1123-1125 (2005).

Y. Ni, L. Zhang, L. An, J. Peng and C. Fan, “Dual-core photonic crystal fiber for dispersion compensation,” IEEE Photonic Tech. Lett. **16**, 1516-1518 (2004).

M. D. Nielsen, N. A. Mortensen, M. Albertsen, J. R. Folkenberg and H. R. Simonsen, “Predicting macrobending loss for large-mode area photonic crystal fibers,” Opt. Express **12**, 1775-1779 (2004).

M. Oberthaler, “Spectral narrowing of ultrashort laser pulses by self-phase modulation in optical fibers,” Appl. Phys. Lett. **63**, 1017-1019 ((1993).

T. Okuno, M. Onishi, and M. Nishimura, “Generation of Ultra-Broad-Band Supercontinuum by Dispersion-Flattened and Decreasing Fiber,” IEEE Photon. Technol. Lett. **10**, 72-74 (1998).

T. Okuno, M. Onishi, T. Kashiwada, S. Ishikawa and M. Nishimura, “Silica-based functional fibers with enhanced nonlinearity and their applications,” IEEE J. Sel. Top. Quantum Electron. **5**, 1385-1391 (1999).

T. Okuno, M. Hirano, T. Kato, M. Shigematsu and M. Onishi, “Highly nonlinear and perfectly dispersion-flattened fibres for efficient optical signal processing applications,” Electron. Lett. 39, 972-974 (2003).

A. Ortigosa-Blanch, J. C. Knight, W. J. Wadsworth, J. Arriaga, B. J. Mangan, T. A. Birks and P. St. J. Russell, "Highly birefringent photonic crystal fibers," Opt. Lett. **25**, 1325-1327 (2000).

R. Paschotta, Simulation software *ProPulse*, RP Photonics Consulting GmbH, Zurich, Switzerland.

D. N. Payne, L. Reekie, R. J. Mears, S. B. Poole, I. M. Jauncey and J. T. Lin, "Rare-earth doped single-mode fiber lasers, amplifiers and devices" in Proc. CLEO 1986, FN1, 374-375 (1986).

M. D. Pelusi and H.-F. Liu, "Higher order soliton pulse compression in dispersion-decreasing optical fibers," IEEE J. Quantum Electron. **33**, 1430-1439 (1997).

P. Petropoulos, T. M. Monro, W. Belardi, K. Furusawa, J. H. Lee and D. J. Richardson, "2R-regenerative all-optical switch based on a highly nonlinear holey fiber," Opt. Lett. **26**, 1233-1235 (2001).

F. Poletti, V. Finazzi, T. M. Monro, N. G. R. Broderick, V. Tse, and D. J. Richardson, "Inverse design and fabrication tolerances of ultra-flattened dispersion holey fibers," Opt. Express **13**, 3728-3736 (2005).

F. Poletti, *Direct and inverse design of microstructured optical fibres*, PhD thesis, University of Southampton, Southampton, SO17 1BJ (2007).

F. Poli, F. Adami, M. Foroni, L. Rosa, A. Cucinotta and S. Selleri, "Optical parametric amplification in all-silica triangular-core photonic crystal fibers," Appl. Phys. B **81**, 251–255 (2005)

J. K. Ranka, R. S. Windeler, and A. J. Stentz, "Visible continuum generation in air-silica-microstructure optical fibers with anomalous dispersion at 800 nm," Opt. Lett. **25**, 25-27 (2000).

V. V. Ravi Kanth Kumar, A. K. George, W. H. Reeves, J. Knight, P. St. J. Russell, "Modified group-velocity dispersion in extruded photonic crystal fiber," in Proc. OFC 2003, WA5 (2003).

W. H. Reeves, J. C. Knight and P. St. J. Russell, “Demonstration of ultra-flattened dispersion in photonic crystal fibers,” Opt. Express **10**, 609-613 (2002).

P. J. Robert, F. Couny, H. Sabert, B. J. Mangan, T. A. Birks, J. C. Knight, and P. St. J. Russell, “Loss in solid-core photonic crystal fibers due to interface roughness scattering,” Opt. Express **13**, 7779-7793 (2005).

A. Rulkov, M. Vyatkin, S. Popov, J. Taylor, and V. Gapontsev, “High brightness picosecond all-fiber generation in 525-1800nm range with picosecond Yb pumping,” Opt. Express **13**, 377- 381(2005).

P. St. J. Russell, “Photonic-Crystal Fibers,” J. Lightwave Technol. 24, 4729-4749(2006).

M. Rusu, S. Kivistö, C. B. E. Gawith, O. G. Okhotnikov, “Red-green-blue (RGB) light generator using tapered fiber pumped with a frequency-doubled Yb-fiber laser,” Opt. Express 13, 8547-8554 (2005).

K. Saitoh and M. Koshiba, “Chromatic dispersion control in photonic crystal fibers: application to ultra-flattened dispersion,” Opt. Express **11**, 843-852 (2003).

K. Saitoh and M. Koshiba, “Numerical Modeling of Photonic Crystal Fibers,” J. Lightwave Technol. **23**, 3580-3590 (2005)(a).

K. Saitoh, N. Florous, and M. Koshiba, “Ultra-flattened chromatic dispersion controllability using a defected-core photonic crystal fiber with low confinement losses,” Opt. Express **13**, 8365-8371 (2005)(b).

T. Schreiber, T. V. Andersen, D. Schimpf, J. Limpert, and A. Tünnermann, “Supercontinuum generation by femtosecond single and dual wavelength pumping in photonic crystal fibers with two zero dispersion wavelengths,” Opt. Express **13**, 9556-9569 (2005).

Scion Corporation. Retrieved April 2007 from the World Wide Web: http://www.scioncorp.com/frames/fr_download_now.htm

J. M. Senior, *Optical Fiber Communications, Principles and Practice 2nd Edition* (Prentice Hall Europe, 1992).

Y. R. Shen, *The Principles of Nonlinear Optics* (Wiley, New Jersey, 2003) (a).

L-P. Shen, W-P. Huang and S-S. Jian, "Design of photonic crystal fibers for dispersion-related applications," J. Lightwave Technol. **21**, 1644-1651 (2003) (b).

A. I. Siahlo, L. K. Oxenlwe, K. S. Berg, A. T. Clausen, P. A. Andersen, C. Peucheret, A. Tersigni, P. Jeppesen, K. P. Hansen, and J. R. Folkenberg, "A high-speed demultiplexer based on a nonlinear optical loop mirror with a photonic crystal fiber," IEEE Photon. Technol. Lett. **15**, 1147-1149 (2003).

R. K. Sinha and S. K. Varshney, "Dispersion properties of photonic crystal fibers," Microw. Opt. Techn. Let. **37**, 129-134 (2003).

R. G. Smith, "Optical power handling capacity of low loss optical fibres as determined by stimulated Raman and Brillouin scattering," Appl. Opt. **11**, 2489 (1972).

A. W. Snyder and J. D. Love. *Optical Waveguide Theory*. (Chapman and Hall, 1996).

T. Sorensen, J. Broeng, A. Bjarklev, E. Knudsen and S. E. B. Libori, "Macro-bending loss properties of photonic crystal fibre," Electron. Lett. **37**, 287-289 (2001).

A. J. Stentz, R. W. Boyd, and A. F. Evans, "Dramatically improved transmission of ultrashort solitons through 40 km of dispersion-decreasing fiber," Opt. Lett. **20**, 1770-1772 (1995).

R. H. Stolen, E. P. Ippen and A. R. Tynes, "Raman Oscillation in Glass Optical Waveguide," Appl. Phys. Lett. **20**, 62-64 (1972).

R. H. Stolen and A. Ashkin, "Optical Kerr effect in glass waveguide," Appl. Phys. Lett. **22**, 294-296 (1973).

R. H. Stolen, "Phase-matched-stimulated four-photon mixing in silica-fiber waveguides," IEEE J. Quantum Electron. **11**, 100-103 (1975).

R. H. Stolen and C. Lin, "Self-phase-modulation in silica optical fibers," Phys. Rev. A **17**, 1448-1453 (1978).

K. Tajima, “Compensation of soliton broadening in nonlinear optical fibers with loss,” Opt. Lett. **12**, 54-56 (1987).

K. Tajima, “Low-loss photonic crystal fibers,” in Proc. OFC 2002, ThS3, 523-524 (2002).

K. Tajima, “Low loss PCF by reduction of hole surface imperfection” in Proc. ECOC 2007, PD2.1, 75-76 (2007).

K. Takada, J. Noda and R. Ulrich, “Precision measurement of modal birefringence of highly birefringent fibers by periodic lateral force,” Appl. Opt. **24**, 4387-4391 (1985).

K. R. Tamura and M. Nakazawa, “Femtosecond soliton generation over a 32 nm wavelength range using a dispersion-flattened dispersion-decreasing fiber,” IEEE Photon. Technol. Lett. **11**, 319-321 (1999).

M. Tateda, N. Shibata, and S. Seikai, “Interferometric method for chromatic dispersion measurement in single-mode optical fiber,” IEEE J. Quantum Electron. QE-**17**, 404-407 (1981).

X. Tian and X. Zhang, “Dispersion-flattened designs of the large effective-area single-mode fibers with ring index profiles,” Opt. Commu. **230**, 105-113 (2004).

V. Tombelaine, P. Leproux, V. Couderc, and A. Barthélémy, “Visible supercontinuum generation in holey fibers by dual-wavelength subnanosecond pumping,” IEEE Photon. Technol. Lett. 18, 2466-2468 (2006).

G. E. Town and J. T. Lizier, “Tapered holey fibers for spot-size and numerical-aperture conversion,” Opt. Lett. **26**, 1042–1044 (2001).

J. C. Travers, B. A. Cumberland, A. B. Rulkov, S. V. Popov, J. R. Taylor, J. M. Stone, A. K. George, and J. C. Knight, “Pulse compression in dispersion decreasing photonic crystal fiber,” in Proc. CLEO 2007, CFK1 (2007).

M. L. V. Tse, P. Horak, F. Poletti, N. G. R. Broderick, J. H. V. Price, J. R. Hayes, and D. J. Richardson, “Supercontinuum generation at 1.06 μm in holey fibers with dispersion flattened profiles,” Opt. Express **14**, 4445-4451 (2006) (a).

M. L. V. Tse, P. Horak, J. H. V. Price, F. Poletti, F. He, and D. J. Richardson, "Pulse compression at 1.06 μm in dispersion-decreasing holey fibers," Opt. Lett. **31**, 3504-3506, (2006) (b).

P. K. A. Wai and W.-H. Cao, "Ultrashort soliton generation through higher-order soliton compression in a nonlinear optical loop mirror constructed from dispersion-decreasing fiber," J. Opt. Soc. Am. B. **20**, 1346-1355 (2003).

C-Y. Wang, P. L. Baldeck, Y. Budansky, and R. R. Alfano, "15-THz pulse generation arising from modulation instability oscillation in a colliding-pulse mode-locking dye laser," Opt. Lett. **14**, 497-499 (1989).

P. S. Westbrook, J. W. Nicholson, K S. Feder, and A. D. Yablon, "Improved supercontinuum generation through UV processing of highly nonlinear fibers," J. Lightwave Technol. **23**, 13-18 (2005).

T. P. White, R. C. McPhedran, C. M. de Sterke, L. C. Botten, and M. J. Steel, "Confinement losses in microstructured optical fibers," Opt. Lett. **26**, 1660-1662 (2001).

R. S. Windeler, "Improving microstructure fibers including preform fabrication, fiber draw, splicing and postproduction dispersion tailoring," in Proceedings of the 14th international workshop on optical waveguide theory and numerical modelling, 123-135 (2005).

L. Xiao, W. Jin, and M. S. Demokan, "Low-loss splicing small-core photonic crystal fibers and single-mode fibers by repeated arc discharges," in Proc. CLEO 2007, JTuA89 (2007).

E. Yablonovitch, "Inhibited Spontaneous emission in solid-state physics and electronics," Phys. Rev. Lett. **58**, 2059-2062 (1987).

S. Yin, K. Chung, H. Liu, P. Kurta, and K. Reichard, "A new design for non-zero dispersion-shifted fiber (NZ-DSF) with a large effective area over 100 μm^2 and low bending and splice loss," Opt. Commun. **177**, 225-232 (2000).

Z. Yusoff, J. H. Lee, W. Belardi, T. M. Monro, P. C. Teh, and D. J. Richardson, "Raman effects in a highly nonlinear holey fiber: amplification and modulation," Opt. Lett. **27**, 424-426 (2002).

Y. Zhang, K. Li, L. Wang, L. Ren, W. Zhao, R. Miao, M. C. J. Large, and M. A. van Eijkelenborg, “Casting preforms for microstructured polymer optical fibre fabrication,” Opt. Express **14**, 5541-5547 (2006).

J. Zhou, K. Tajima, K. Nakajima, K. Kurokawa, C. Fukai, T. Matsui, and I. Sankawa, “Progress on low loss photonic crystal fibers,” Opt. Fiber Technol. **11**, 101–110 (2005).